Surface Transfer Doping of Diamond using Transition Metal Oxides

by

Kevin G. Crawford

Submitted in fulfilment of the requirements for the degree of Doctor of Philosophy

School of Engineering
University of Glasgow

In memory of my Grandmother

who taught patience to a stone

sowed flowers in winter

and called me sparrow

Surprising what you can dig out of books if you read long enough, isn't it?

Robert Jordan

Abstract

This thesis presents a body of work which advances the use of single crystal hydrogen terminated diamond as a semiconducting material. Surface transfer doping of intrinsic diamond is investigated, examining the current state of this technology and its limitations. New techniques for producing robust, thermally stable surface transfer doped diamond were achieved through use of transition metal oxides such as MoO_3 and V_2O_5, as demonstrated experimentally by way of Hall measurement. Through use of these materials, thermal stability was greatly increased up to temperatures of at least 300^oC. To achieve this higher temperature operation, encapsulation of MoO_3 and V_2O_5 was found to be necessary in maintaining conductivity of the diamond surface due to suspected thermally-induced loss of hydrogen termination. Similarly, long term atmospheric stability is shown to necessitate annealing of the diamond surface prior to oxide deposition and for thinner layers of oxide, down to 10 nm, encapsulation of the oxide to isolate from atmosphere is shown to be required for increased stability. As well as the improvements in stability offered by these transition metal oxides, sheet resistance of the hydrogen terminated diamond surface was also greatly reduced. Carrier densities as high as ~7.5 $\times 10^{13}$ cm^{-2} were observed for MoO_3-induced surface transfer doping, resulting in a low sheet resistance of ~ 3 kΩ/□.

In parallel to the development of oxide acceptor materials, conditioning of the diamond surface was explored using Atomic Force Microscopy (AFM). Techniques for smoothing the surface after mechanical polishing were developed by way of RIE and ICP etching using both chlorine and oxygen mixtures. Surface roughness down to 2 angstroms was demonstrated, showing a significant improvement in roughness over mechanical polishing alone. Similarly, observed defects produced by polishing induced damage were removed through use of this etching strategy. The effects of varied plasma density during hydrogen termination was explored on etched surfaces, which produced higher quality hydrogen-terminated surfaces as verified by surface conductivity and AFM measurements.

Finally, incorporation of MoO_3 into a preliminary Field Effect Transistor (FET) device on diamond was attempted. Fabrication techniques to produce a FET device on hydrogen-terminated diamond is shown with preliminary results of MoO_3 encapsulated devices. Insights into the fabrication of ohmic and gate contacts, incorporating MoO_3, is also discussed.

Acknowledgements

I would take this opportunity to print my sincere gratitude to all those who have aided me both in life and over the past four years. The work presented in this thesis is the product of countless influences which have supported and shaped me.

My gratitude to David Moran for the opportunity he gave me. A PhD is a privilege I did not feel I deserved in the first place, yet David's patience with my shortcomings gave me confidence where others may have scoffed. Our weekly interactions over the course of my PhD guided me and provided a persistent sense of affinity towards a common goal. I have no doubt he has always acted in my best interest and I hope my work ethic never disappointed. My PhD started initially with just one colleague who finished up and departed shortly after. I would like to thank Stephen for his training and shared knowledge. I was later joined by two new group members, David and Andrew. Their humour and presence no doubt prevented what otherwise would have felt a lone endeavour. I'll miss the banter and the strong coffee.

I have been fortunate enough to work in a lab maintained by a dedicated group of technical staff, my sincere thanks to them and their excellent work which keeps the cogs turning. My thanks to James Grant, who has on countless occasions taken an interest in my work, offered good advice and general encouragement. My thanks also to Helen and Susan, who with great care ran almost all my VB6 jobs. All the excellent work conducted within the James Watt Nanofabrication Centre is made possible by a combined contribution from the technical staff, the academic management and the many users who are the life blood of the facility. It is a unique place to be sure.

On a personal note, I wish to acknowledge those who support me in life. My mother has, as it is for most, been an enormous boon. Her tireless efforts to give me a life unfazed, despite what many would deem life changing illness, has brought me here. My brother has ever been a beacon of example. I once described him in a high school essay as akin to gravity. A force unaware of its own importance, it simply is. My aunt has always been an infinite dynamo of energy and enthusiasm. Her encouragement is uplifting and I consider myself a son she always had. So too has our friend Christine always been a supporting presence to me. She gives help to any who ask and many who won't. Lastly, the support and companionship from my flatmate Bhavana has made the final years of my PhD special to me. She has without doubt been my closest friend and a friend to my family. Words do not express.

Associated Publications to Date

Journal Publications

Kevin G. Crawford, Liang Cao, Dongchen Qi, Alexandre Tallaire, E. Limiti, C. Verona, Andrew T. S. Wee and David A. J. Moran
Enhanced surface transfer doping of diamond by V_2O_5 with improved thermal stability
Appl. Phys. Lett. 108, 042103 (2016)

Kevin G. Crawford, Dongchen Qi, Jessica McGlynn, Tony G. Ivanov, Pankaj B. Shah, James Weil, Alexandre Tallaire, Alexey Y. Ganin and David A. J. Moran
Thermally Stable, High Performance Transfer Doping of Diamond using Transition Metal Oxides
Under review (2017)

Kevin G. Crawford, Alexandre Tallaire, Xu Li, David A. Macdonald, Dongchen Qi and David A. J. Moran
The role of hydrogen plasma power on surface roughness and carrier transport in transfer-doped H-diamond
Under review (2017)

Stephen A. O. Russell, Liang Cao, Dongchen Qi, Alexandre Tallaire, Kevin G. Crawford, Andrew T. S. Wee and David A. J. Moran
Surface Transfer Doping of Diamond by MoO3: a combined spectroscopic and Hall measurement study
Appl. Phys. Lett. 103, 202112 (2013)

Isolda Roger, Roberta Moca, Haralampos N. Miras, Kevin G. Crawford, David A. J Moran, Alexey Y. Ganin, Mark D. Symes
The direct hydrothermal deposition of cobalt-doped MoS_2 onto fluorine-doped SnO_2 substrates for catalysis of the electrochemical hydrogen evolution reaction
J. Mater. Chem. A, 5, 1472-1480 (2017)

Conference Proceedings

Kevin G. Crawford, Dongchen Qi, Alex Tallaire, E. Limiti, C. Verona and David A. J. Moran
Surface Transfer Doping of Hydrogenated Diamond by V_2O_5 and MoO_3
Oral, The 67th Diamond Conference, Warwick, UK, July 2016

Kevin G. Crawford, Dongchen Qi, Alex Tallaire, E. Limiti, C. Verona and David A. J. Moran
Thermally Stable Surface Transfer Doping of Diamond by V_2O_5
Oral, Diamond workshop SBDD XIX, Hasselt, Belgium, February 2016

Kevin G. Crawford, Alex Tallaire and David A. J. Moran
Impact of ICP Etching on the Formation of Surface Defects on Hydrogen Terminated Diamond
Poster, MRS Fall Meeting: Materials Research Society, Boston MA, USA, 2015

Kevin G. Crawford, Stephen A. O. Russell, Dongchen Qi, Liang Cao, Alex Tallaire, Andrew T. S. Wee and David A. J. Moran
Temperature Stable Surface Transfer Doping of H-Terminated Diamond via MoO_3
Oral, Hetech European Workshop, Giessen, Germany, October 2014

Kevin G. Crawford, Stephen A. O. Russell, Dongchen Qi, Liang Cao, Alex Tallaire, and Andrew T. S. Wee and David A. J. Moran
Advancing Surface Transfer Doping of Hydrogen-Terminated Diamond via Deposition of MoO_3
Oral, Diamond workshop SBDD XIX, Hasselt, Belgium, February 2014

Kevin G. Crawford, Stephen A. O. Russell, Dongchen Qi, Liang Cao, Alex Tallaire, Andrew T. S. Wee and David A. J. Moran
Advancing Surface Transfer Doping of Hydrogen Terminated Diamond via Inorganic Materials
Oral, Hetech European Workshop, Glasgow, UK, September 2013

Contents

1 Introduction

Solid state electronics is one of the most rapidly advancing fields, in both industry and research. The drive for ever shrinking devices and for higher power and frequency operation has fuelled interest in a wide variety of materials. Of these, diamond has more recently demonstrated serious potential as a semiconductor for use in field effect transistors and other such devices. Diamond possesses many properties making it highly appealing for numerous applications, such as high-power electronics, radiation detectors, pH sensors and bioelectronics. These properties, which include radiation hardness and extremely high thermal conductivity, fundamentally derive from the structure and composition of diamond itself and often far outpace other wide bandgap semiconductors. Diamond's large bandgap of 5.47 eV enables high operating voltages due to a high electric field breakdown of 10 MV/cm. The extremely high thermal conductivity of diamond, greater than 20 W/cm, also significantly reduces thermal constraints. The robust nature of the diamond material system makes it most appealing for use in hazardous environments, such as operation in outer space. Progress in the development of diamond-based electronic components has been limited by the difficulties associated with doping of the material. Surface transfer doping of diamond offers an alternative to substitutional doping that alleviates the challenges of introducing impurity dopants into diamond's tightly packed carbon lattice.

In this thesis, primary investigation revolves around the stability and performance of surface transfer doped hydrogen terminated diamond. Chapter 2 begins with an introduction to the diamond material system and an analysis of diamond's many useful properties. Two fundamentally different doping strategies are presented along with some important properties of the diamond surface. Chapter 3 & 4 contain a review of important literature and an overview of measurement techniques used in this work. Chapter 5 details fabrication processes used in the preparation of samples, including the formation of FET devices and other such measurement structures. Chapter 6 presents a summary of hydrogen termination used in the majority of this thesis, followed by experimental work concerning

surface transfer doping of diamond. Chapter 7 contains research relating to the conditioning and preparation of diamond surfaces, including etching of the surface and improvements observed to both roughness and hydrogen termination results. Advances made in surface transfer doping are then incorporated into a FET device in Chapter 8, showing preliminary results. This body of work is concluded in Chapter 9, providing insights into what has been achieved thus far and the prospect of future work.

2 The Diamond Material System

As a material of interest, diamond possesses many properties making it useful for numerous applications. These properties fundamentally derive from the structure and composition of diamond. In this chapter, the carbon allotrope diamond is discussed in detail, such as its structure, surface, growth and importantly the question of diamond's potential as a semiconductor.

2.1 Carbon Structures

While isolated, the carbon atom consists of electronic configuration $1s^2\ 2s^2\ 2p^2$. This means it has two core electrons surrounding the nucleus in an s orbital and four valence electrons, two in an s orbital and two in p orbitals as illustrated in Figure 2.1. This places carbon as element 6 on the Periodic Table.

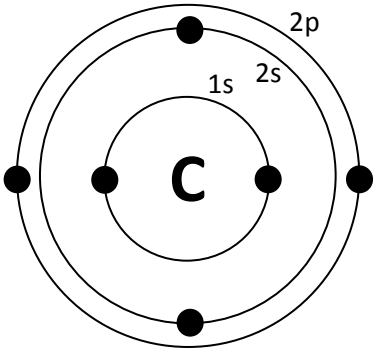

Figure 2.1 - Electron configuration of an isolated carbon atom.

Carbon when arranged together in an sp^2 bonded configuration forms graphite, the most energetically stable form of carbon at room temperature [2.1]. In this state three of the four possible bonding sites are satisfied with covalent chemical bonds to neighbouring carbon

atoms along a single two-dimensional layer, leaving the forth electron free to migrate around the plane and thus making graphite electrically conductive. These planes are held together by weak van der Waals forces which allow layers of graphite to separate or slide past each other easily. As a result of this, graphite is extremely strong in the horizontal plane while much weaker in the vertical. The sp^2 bonding model is shown in Figure 2.2.

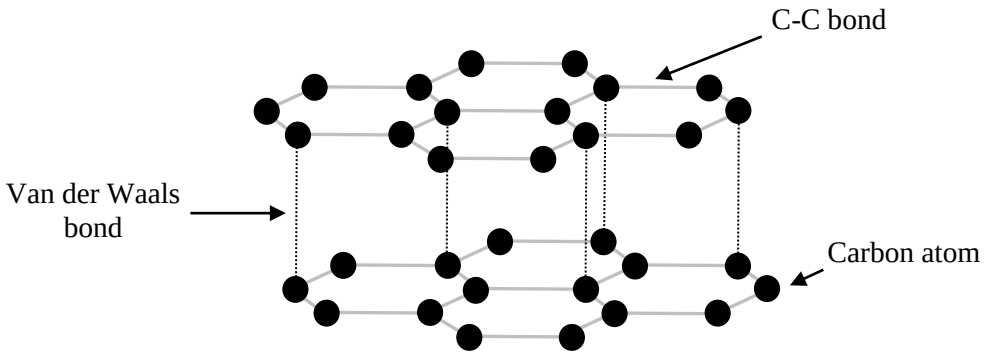

Figure 2.2 - Sp^2 bonded carbon graphite, forming two layers bonded together by van der Waals forces.

Arranged together in an sp^3 bonded configuration forms the carbon allotrope diamond. Here each of the four outer electrons form strong covalent bonds with neighbouring atoms with each bond orientated in the direction of a tetrahedron's corners. The short length of the C-C bond and three-dimensional stability of the tetrahedral bonding arrangement are responsible for diamonds extreme material hardness [2.2]. The sp^3 bonding model is shown in Figure 2.3. The crystal structure of diamond is also named after the material itself. The *diamond* structure is shared with many other materials including silicon and germanium. It is the equivalent of a face centred cubic or FCC lattice with two atoms at each lattice point, one at the coordinates 0, 0, 0 and the other at $\frac{1}{4}, \frac{1}{4}, \frac{1}{4}$ where a corner of the unit cell is origin.

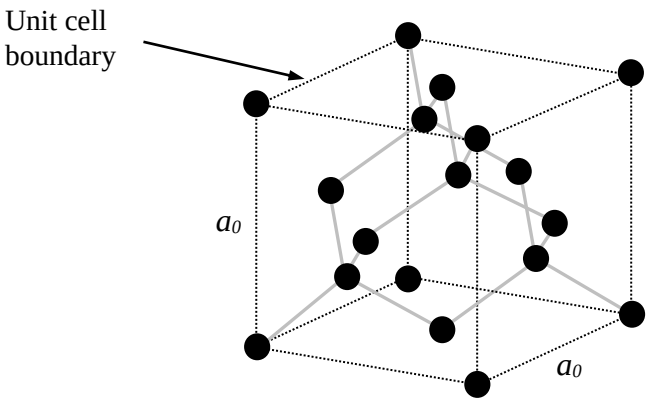

Figure 2.3 - Conventional unit cell of sp^3 bonded carbon diamond. The cubic lattice parameter a_0 equals 3.57 Å.

Due to the small size of the carbon atom they can come relatively close together before experiencing repulsive forces, giving rise to a short C-C bond length [2.3]. This results in an overlap of orbitals between adjacent atoms and in a C-C bond causes large energy separation between the bonding orbitals and the antibonding orbitals. The effect of which produces a very large gap of forbidden energy between the valence and conduction band states in bulk diamond. The bandgap of diamond is indirect, with a value of 5.47 eV at a temperature of 300 K. As such diamond is usually considered an insulator or a very wide bandgap semiconductor [2.4].

Extremely high thermal conductivity is uncommon amongst semiconductors where there is typically a lack of conduction band electrons available at room temperature to carry thermal energy through the material. This effect is bolstered even further in diamond due to its large bandgap. However, the closely packed carbon atoms and rigid covalent bonding serves to efficiently transfer atomic vibrations and makes diamond one of the best known thermally conducting solids (roughly 4 times that of copper or silver) while also electrically insulating. Likewise, the strength of the covalent bonds render diamond chemically inert (resistant to all known acids and solvents at room temperature) and hardened to the effects of irradiation [2.5].

The typical unit cell of diamond, Figure 2.3, has a lattice parameter measured to be 3.57 Å at room temperature and contains the equivalent of 8 carbon atoms. The volume density of atoms for a given unit cell can be found as

$$Atomic\ Density = \frac{8}{{a_0}^3} \approx 1.76 \times 10^{23}\ cm^3$$

This value of atomic density can be multiplied by the atomic mass of carbon to give a theoretical density for pure diamond of ≈ 3516 kg m^{-1}. However, due to the presence of impurities and crystal imperfections the measured density of practical diamond will always be lower. Each atom can be thought of as a sphere with the centre to centre bond length *d* between atoms equal to one quarter the cubic body diagonal and the radius *r* therefore equal to one-eighth the diagonal

$$r = \frac{\sqrt{3}a_0}{8} \approx 0.77\ \text{Å}$$

The atomic packaging fraction for the cubic can then be identified by the volume of spheres divided by the volume density of atoms.

$$APF = \frac{8\left(\frac{4}{3}\pi r^3\right)}{{a_0}^3} \approx 0.34 \text{ or } 34\%$$

As a result of this low packing fraction combined with the small mass of the carbon atom diamonds atomic density is one of the highest of all terrestrial materials [2.6].

2.2 CVD Growth

Chemical Vapour Deposition (CVD) is a process used often in the semiconductor industry to produce high quality solid materials of varying thickness [2.7]. CVD growth of diamond has become a well-established area of research and development over the last four decades, due to the usefulness of diamond in many applications. For single crystal diamond, a single crystal diamond substrate is required from which the new diamond material is produced by epitaxial growth, taking on the same structure and orientation of the substrate. The CVD growth process is based upon the activation of gaseous reactants, usually hydrogen and methane (H_2/CH_4), with high hydrogen concentration and normally low amounts of hydrocarbon. The decomposition of hydrocarbon required is typically achieved by thermal (hot filament) or plasma activation (DC or RF electrical discharges). An illustration of both is shown in Figure 2.4. While much of the early knowledge into diamond growth has stemmed from hot filament activation, most modern systems employ the plasma technique. One of the main challenges encountered with epitaxial growth of diamond is due to the greater thermodynamic stability of graphite. As such, a main requirement of diamond growth is the deposition of sp^3 carbon while suppressing the formation of sp^2 graphitic bonding. This is achieved with high levels of atomic hydrogen as an etchant of non-sp^3 bonded carbon. While this work does not focus on the growth aspect of diamond, the reader is directed to "Theory of Diamond Chemical Vapor Deposition" by Goodwin and Butler for its extensive review of the subject [2.8].

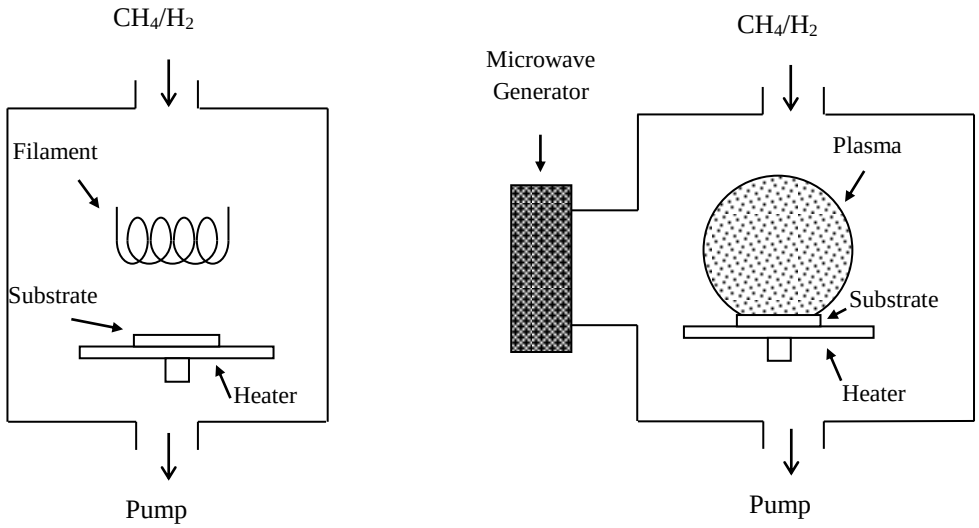

Figure 2.4 - Example diagram of common CVD growth chambers, (left) hot filament reactor (right) microwave plasma reactor.

2.3 Surface Termination

Figure 2.5 illustrates the different surface orientations of diamond. The exposed atoms at the surface of CVD diamond are most commonly those of [001] and [111] orientations due to the nature of the growth process. These two faces are the slowest growing and so remain once the other faster growing orientations cease. For the same reason, the randomly orientated material in polycrystalline diamond is dominated by [001] and [111] orientations. The [111] surface is also common due to the dominance of cleavage on the [111] plane in diamond [2.9].

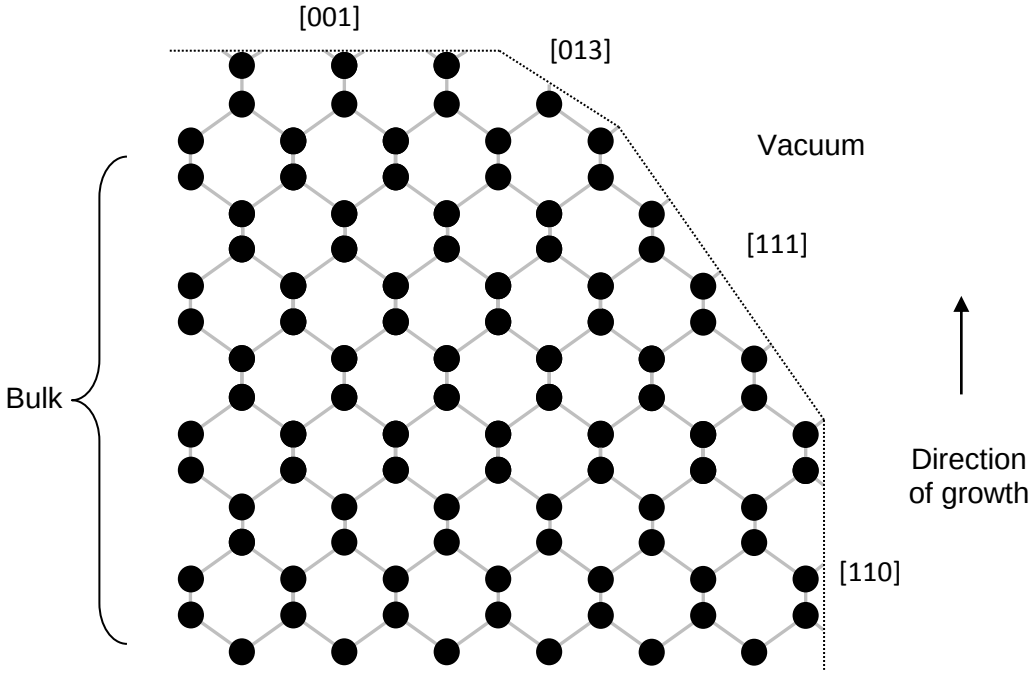

Figure 2.5 - Vertical cross section of an ideal single crystal diamond with atomic structure magnified, showing different surface orientations and the primary growth direction.

While a solid material such as diamond may be defined in terms of a base unit cell, repeated to show its ideal crystal structure, a materials surface represents a transition from ideal crystal bulk to vacuum in which the periodicity of the structure is broken. In this sense, the surface can be considered the largest defect present in any solid material. Atoms at the surface where the crystal structure is terminated will be left with energetically unsatisfied bonds called “dangling bonds” which result in increased surface energy. In an ideal crystal, the position of each individual atom is determined by the collective forces exerted upon it by neighbouring atoms. When the periodic structure is terminated along a

given plane, these forces are altered and thus the position of atoms at the surface differs in relation to those of bulk. Reducing the number of dangling bonds minimizes the surface energy and so atoms at the surface will seek to find new positions which satisfy surface bonds. This is called relaxation or reconstruction of the surface [2.10].

For a diamond surface outside of vacuum, atoms provided by available atmospheric species can further lower the total surface energy by reducing the number of dangling bonds. Figure 2.6 shows 2D representations of the [001] diamond surface ideally reconstructed and with both oxygen and hydrogen termination.

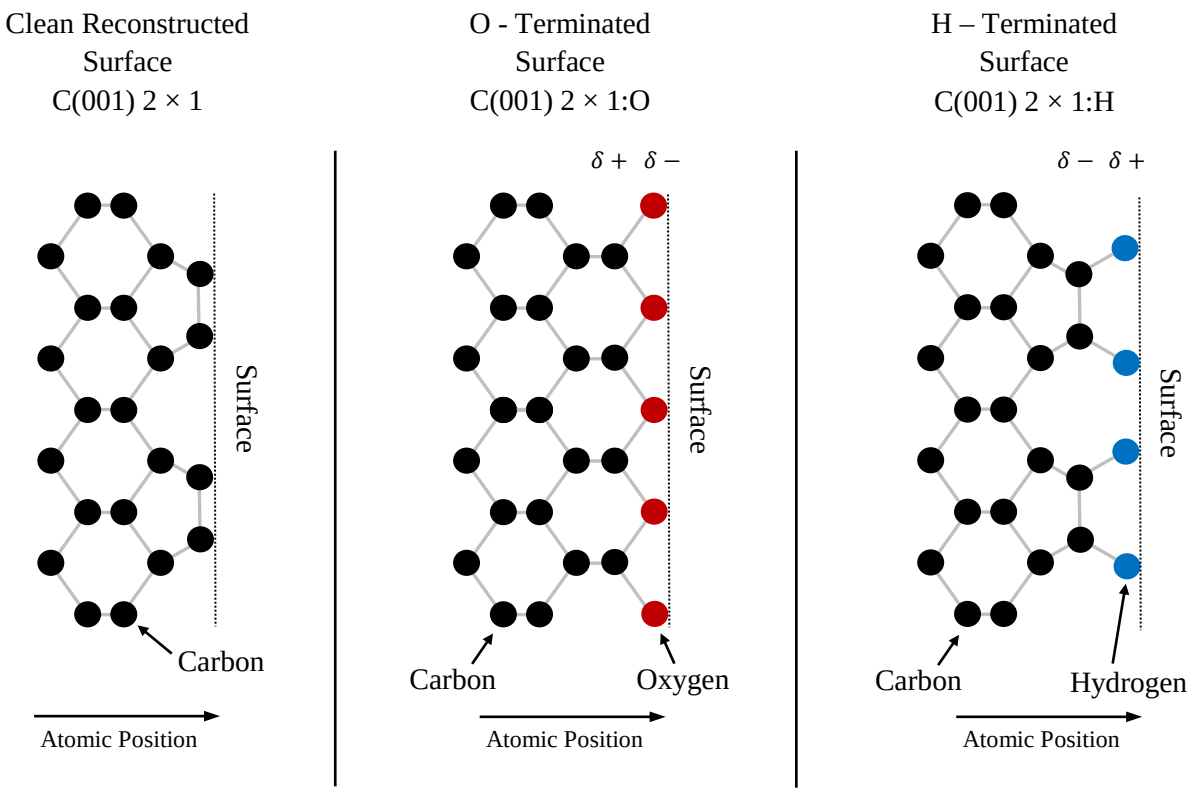

Figure 2.6 - Cross sections of a reconstructed [001] diamond surface, terminated with hydrogen and oxygen.

For a clean non-reconstructed surface, each exposed surface atom exhibits two unsatisfied dangling bonds. For a clean [001] surface in vacuum these atoms will reconstruct with neighbouring atoms to form C=C dimers in a 2 × 1 reconstruction symmetry in order to lower the total surface energy, reducing the number of dangling bonds by a factor of two. When bonded to oxygen or hydrogen the double bonds of dimers are saturated and thus the surface energy is further lowered [2.11].

It was observed by Himpsel *et al* [2.12] that diamond with a surface termination of hydrogen exhibited increased electron emission per absorbed photon. This effect was correctly attributed to Negative Electron Affinity (NEA) of the diamond surface caused by hydrogen termination. NEA occurs when the vacuum level lies below the conduction band minimum. In practice, this means electrons which reach the conduction band may escape into vacuum without experiencing an energy barrier, which explains the observed emission of electrons by Himpsel. It was further shown that the value of Electron Affinity (EA) is directly related to the coverage of hydrogen on the surface. In contrast to the effect of hydrogen, oxygen termination increases the electron affinity to positive values above that of a clean diamond surface. Figure 2.7 shows energy band diagrams for a clean diamond surface, oxygen terminated and hydrogen terminated.

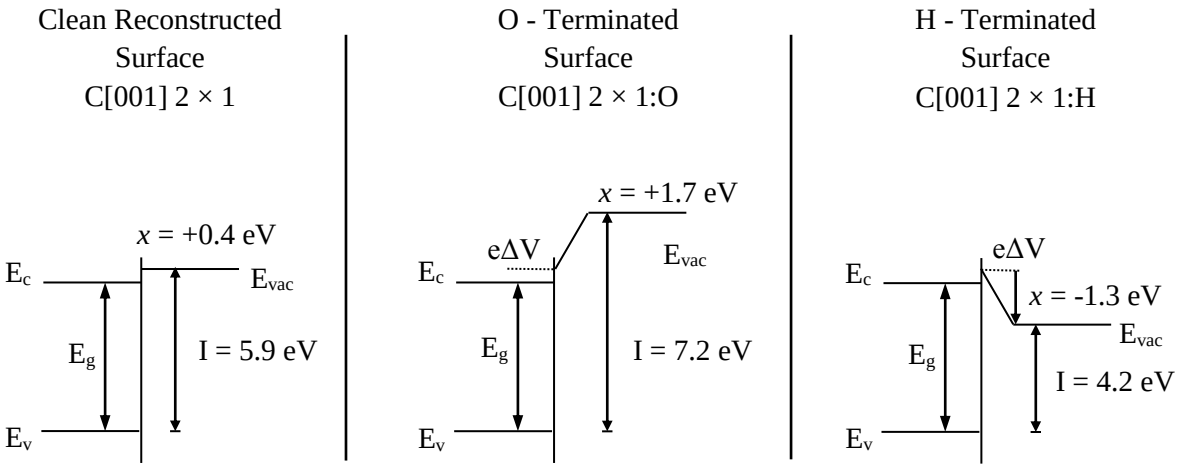

Figure 2.7 - Energy band diagrams for the clean diamond surface, terminated with hydrogen and oxygen.

Partially ionic C (δ–) - H (δ+) bonds at the diamond surface create a dipole layer causing a potential drop perpendicular to the surface over a distance equal to the C-H bond length. This results in a lowering of the vacuum energy level below the conduction band minimum and grants hydrogen terminated diamond its negative electron affinity of -1.3 eV [2.13]. The reverse is true for an oxygen terminated surface where C (δ+) - O (δ–) causes an increased potential shift resulting in a positive electron affinity of +1.7 eV, 1.3 eV greater than that of a non-terminated diamond surface. In the case of hydrogen-terminated diamond, electrons leaving the surface into vacuum do experience a small barrier, illustrated in Figure 2.8. However, this barrier is roughly 0.4 eV high and less than 0.5 Å wide and can therefore be passed with relative ease via quantum mechanical tunnelling [2.14].

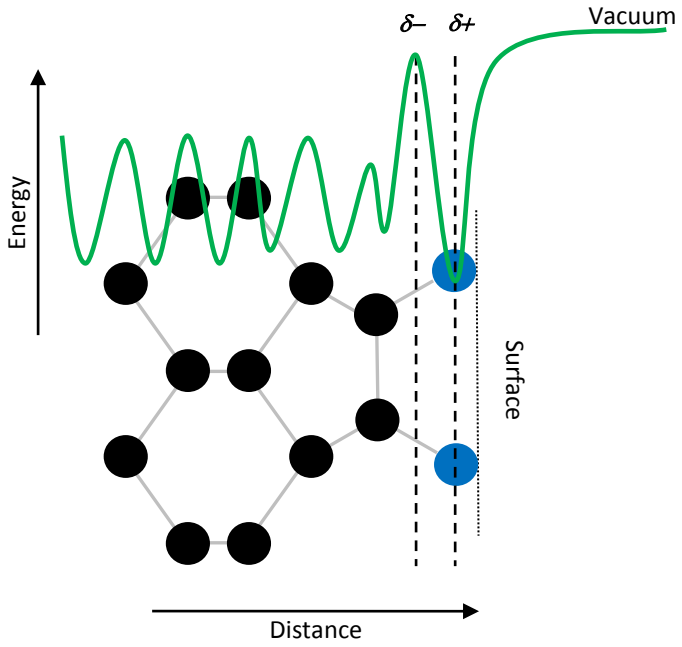

Figure 2.8 - Cross section of hydrogen terminated diamond surface with dipole electrostatic barrier.

The ionization energy of 4.2 eV for hydrogen terminated diamond is lower than most commonly used semiconductors and is made possible by the already low electron affinity of diamond. Silicon, for example, has ionization energy of 5.2 eV despite having a much smaller bandgap than diamond. Similarly, the reduction in ionisation energy by hydrogenation is possible only in diamond, for other elemental semiconductors the effect is to raise the vacuum energy level [2.15]. Oxygen-terminated diamond produces greater positive electron affinity due to the electronegativity of oxygen being greater than carbon on the Pauling scale.

Quantifying hydrogen termination of diamond surfaces is challenging, due to difficulties in detecting atomic hydrogen. Techniques typically used in the elemental analysis of surfaces, such as Energy-dispersive X-ray spectroscopy (EDX) or Auger Electron Spectroscopy (AES), cannot directly detect simple hydrogen bonds. This has led to other, more indirect, methods of observing the presence of hydrogen in the surface termination of diamond. Low Energy Electron Diffraction (LEED) has been used to observe patterns of surface reconstruction that would indicate successful hydrogen termination [2.16]. Wettability experiments may also indicate successful surface termination [2.17], due to the hydrophobic nature of a hydrogen terminated diamond surface, and measurements of negative electron affinity can also confirm hydrogen termination [2.18].

2.4 Substitutional Doping

The process of doping aims to generate additional charge carriers by introducing foreign atoms into a material's lattice structure. This can be done by various methods, such as ion implantation and or during material growth. The process makes use of elements with either less or more valence electrons than the host material. A dopant element with an abundance of electrons is called a *donor* and is used to produce n-type material, while an element with fewer electrons is deemed an *acceptor* and used to produce p-type material [2.19]. Carbon has four electrons within the valence shell. In diamond, these outer valence electrons come together to form strong covalent bonds as shown in Figure 2.9. A covalent bond involves the sharing of electron pairs between two atoms, resulting from the need to satisfy a balanced state of attractive and repulsive forces between the atoms.

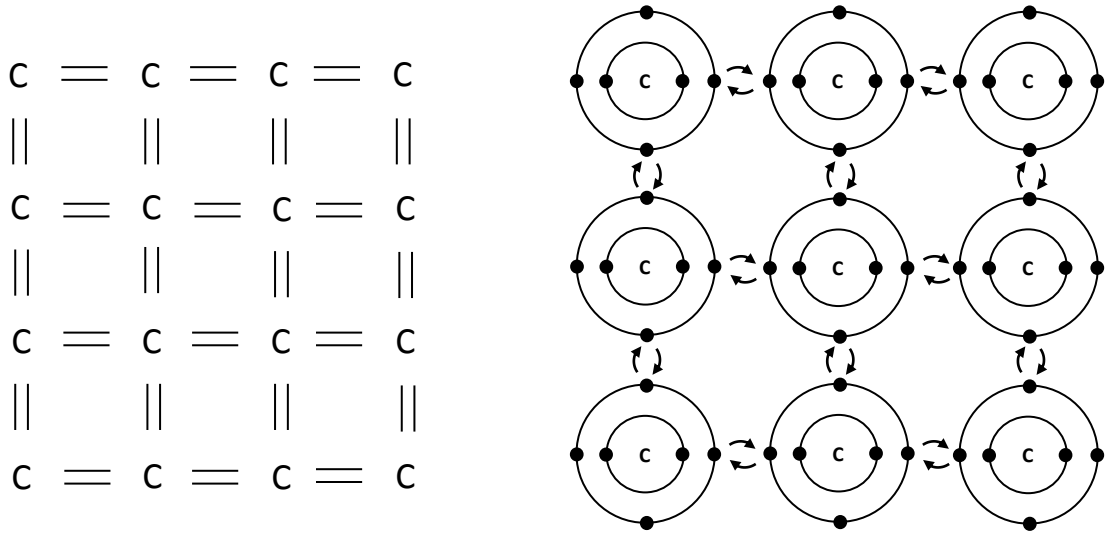

Figure 2.9 - 2D representation of the diamond lattice and the covalent bonds between outer valence electrons.

By implanting an element with one less valence electron, such as boron, a vacancy is created at the donor's energy level. This type of dopant is referred to as an acceptor, as the vacancy can now accept an electron from another atom within the lattice. Shown in Figure 2.10, one covalent bond between the boron atom and a carbon atom is missing or unsatisfied. A bound valence electron from elsewhere in the lattice with sufficient thermal energy may move to occupy this vacancy, creating a hole in the valence band without promoting an electron to the conduction band. The electron occupying this vacancy is now bound to the boron atom and has far less energy than the conduction band energy. The

thermal energy required to move a lattice electron into this vacancy is referred to as the acceptor impurities activation energy.

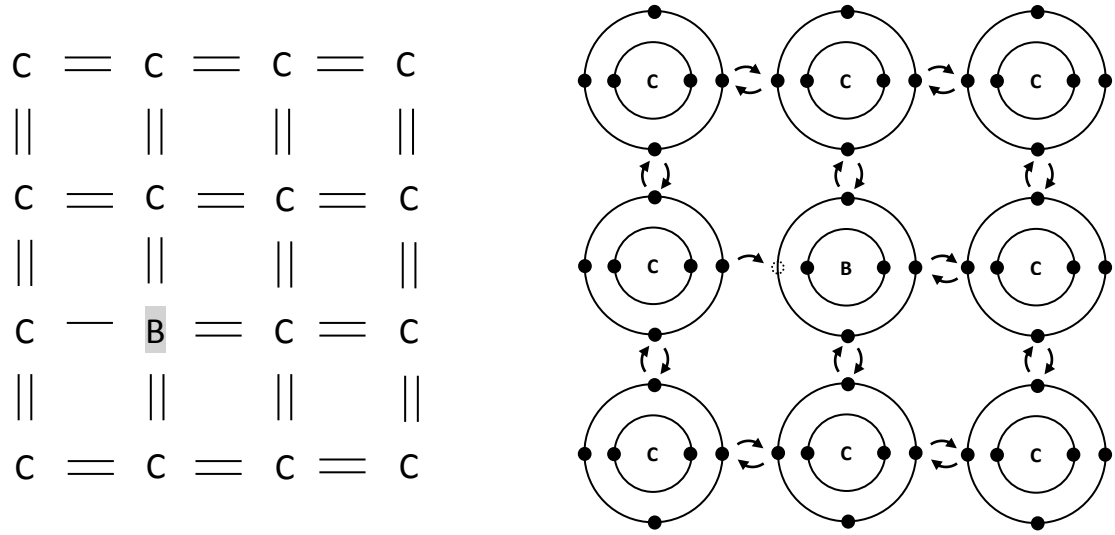

Figure 2.10 - 2D representation of the diamond lattice and the covalent bonds between outer valence electrons doped with a boron atom.

By introducing an atom with one additional electron, such as phosphorus, an extra electron is introduced within the lattice as illustrated in Figure 2.11. This 5^{th} electron is more loosely bound to the phosphorus atom and can be referred to as a *donor* electron. With the donor electron, the phosphorus atom is negatively charged. However, as this donor electron is not involved in any covalent bonding the thermal energy required to raise it to the conduction band is far less than for other bound electrons. This energy requirement is also referred to as the activation energy. Once in the conduction band the donor electron is free to move through the lattice while the now positively charged phosphorus ion is fixed in place. The effect of this donor impurity atom creates an additional electron without a corresponding hole.

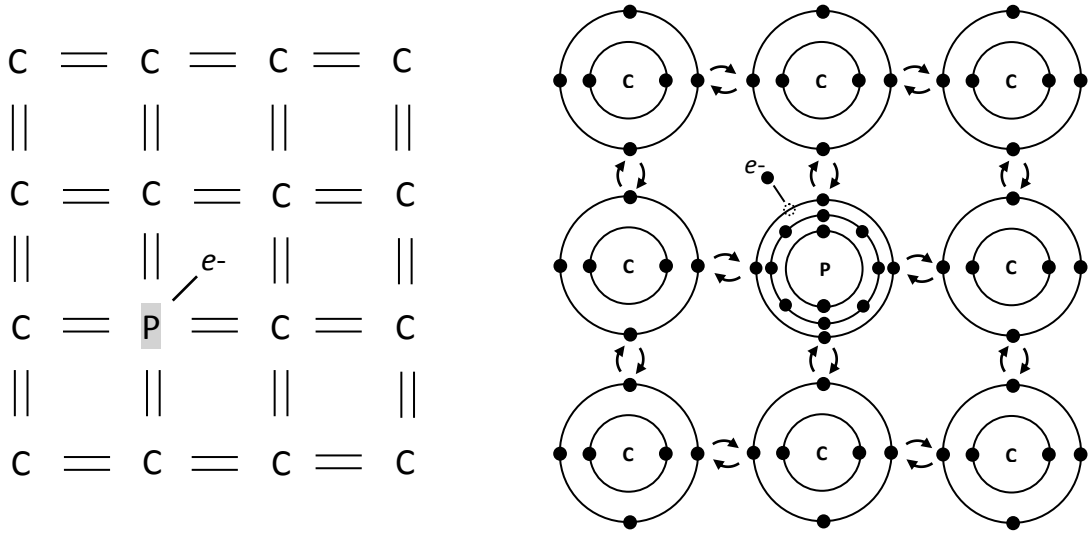

Figure 2.11 - 2D representation of the diamond lattice and the covalent bonds between outer valence electrons doped with a phosphorus atom.

Increasing the presence of dopant atoms in the host material, in general, leads to increased conductivity due to a higher density of mobile charge carriers. As is discussed further in Chapter 4, conductivity is the combination of carrier concentration (hole or electron) and the mobility of these carriers. Increased carrier concentration and or mobility will result in a greater capacity to conduct electric current. As carbon belongs to group IV of the periodic table, group III elements offer intuitive acceptor dopants while group V presents donors. When implanting dopant atoms, the ideal aim is substitution, replacing a host atom with a foreign one. In diamond, this proves difficult due to the short interatomic spacing and strong covalent bonding that gives the material its extreme strength. Alternatively, interstitial doping is possible where by the dopant is placed between original host atoms. The carbon atom is relatively small, as such any attempt to implant a significantly larger atom between the short interatomic spacing results in lattice damage [2.20]. The most soluble dopants found thus far are boron, nitrogen and phosphorus. The most commonly used p-type dopant is boron, while phosphorus and nitrogen have been used to produce n-type diamond [2.21]. Figure 2.12 below illustrates the activation energies of these 3 elements within the diamond bandgap.

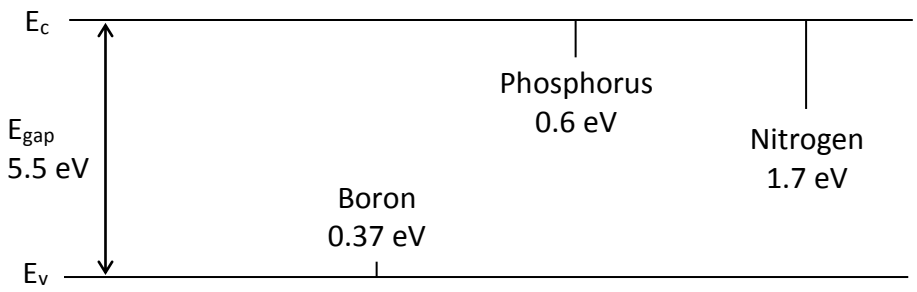

Figure 2.12 - Common donor energy levels represented within the diamond bandgap.

Boron is most commonly used due to its activation energy of 0.37 eV. While 0.37 eV is not a particularly shallow dopant energy compared with other semiconductors, it is the lowest known in diamond. By comparison, in silicon the ionisation energy of a boron dopant is 0.045 eV [2.22]. The best-known donor is phosphorus with a higher activation energy of 0.6 eV, making it of less use apart from in high temperature devices. Nitrogen is the most common impurity in diamond. While impractical for most semiconductor applications due to its high activation energy, the nitrogen vacancy centre is of great interest in storing qubits for quantum computing applications [2.23].

Boron is commonly found in natural diamond, can be implanted or introduced as part of the gas phase during growth via chemical vapour deposition which will produce boron doped polycrystalline or single crystal diamond material [2.24]. Hole mobility degrades significantly as doping concentration increases. Impurity concentrations as high as $\times 10^{20}$ cm^{-3} will induce a wide impurity band corresponding to a large spread in the energy of localised impurity centres. This manifests in a transition to hopping conduction, as impurities begin to cluster and carrier mobility suffers significantly. Above 3.9×10^{21} cm^{-3} a transition to a metallic state takes place as the acceptor band begins to overlap the valence band [2.25]. Boron doped diamond at these levels has been shown to exhibit superconductivity, the first elemental semiconductor to do so [2.26]. The transition temperature depends on the boron concentration and can be as high as 11 K. A potential solution to the issue of reduced mobility is delta doping. The principle of delta doping is to incorporate a thin layer of doped diamond into bulk, ideally one atom thick, so that the wave function of the charge carriers overlaps with that of the intrinsic diamond. Thus, the introduced charge carriers spend an appreciable amount of time outside of the doped layer and form conductivity in the intrinsic diamond. However, attempts so far at producing a boron delta doped layer in diamond have not managed to be much thinner than 2 nm, not thin enough for the technique to produce any significant number of charge carriers overlapping into the intrinsic diamond [2.27].

2.5 The Surface Transfer Doping Model

Surface transfer doping of diamond offers an appealing alternative to substitutional doping, alleviating the problems of introducing foreign dopants into diamonds tight carbon lattice. Owing to the negative electron affinity produced by a hydrogen terminated surface, diamond when in intimate contact with a suitable molecular species will develop p-type surface conductivity. This surface conductivity occurs due to electron transfer from the diamond valence band to empty acceptor levels provided by an adsorbed surface material, creating corresponding holes within the diamond which form a 2-dimensional hole gas (2DHG). The process governing this transfer relies upon the surface species offering energetically favourable electron states for the diamond valence band electrons to transfer to. For air-exposed diamond, this exchange is reportedly driven by the redox reaction $2H_3O^+ + 2e^- = H_2 + 2H_2O$, caused by the difference in chemical potential of electrons in the liquid phase (μ_e) and the diamond Fermi level (E_f). While μ_e is below E_f, electrons will be transferred from the diamond valence band to the atmospheric layer and thereby reduce H_3O^+ to H_2 and H_2O [2.28]. The resultant holes accumulating in the diamond valence band induces a potential that raises μ_e until equilibrium is reached as depicted in Figure 2.13. The reason air exposure incites this effect on hydrogen-terminated diamond was investigated further by Takagi *et al* and is discussed in detail in Chapter 3.

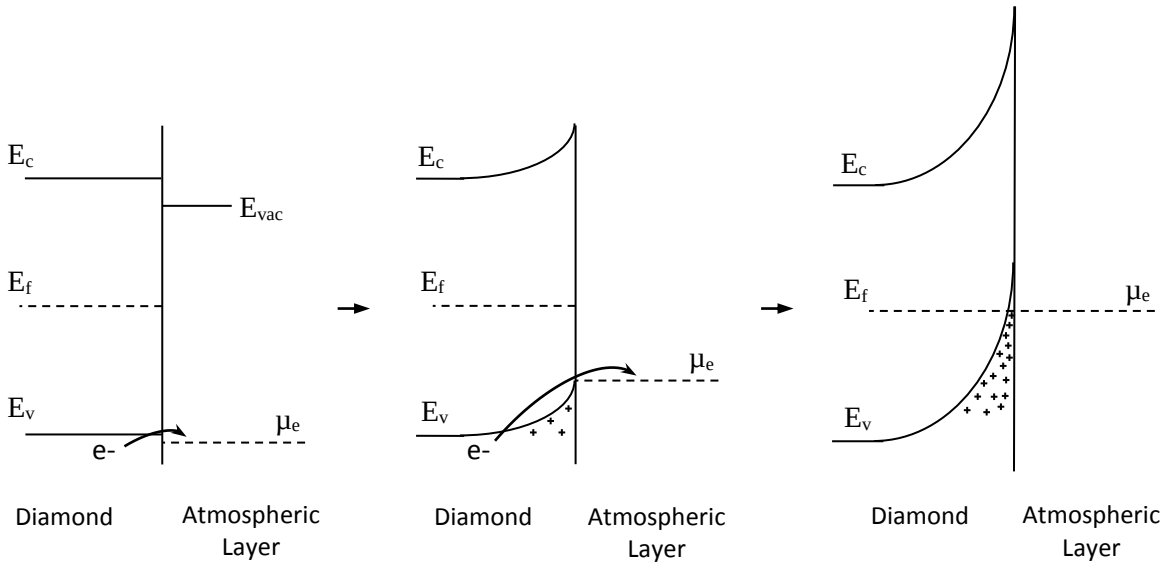

Figure 2.13 - Process of band bending during electron transfer between hydrogen terminated diamond and atmospheric molecules on the surface.

An energy band diagram for hydrogen terminated diamond in intimate contact with a solid surface acceptor material of suitably high electron affinity (qX) is illustrated in Figure 2.14. A negative electron affinity of -1.3 eV combined with the already low ionisation potential of H-diamond results in strong surface transfer doping potential when in contact with a material of electron affinity (qX) greater than 4.2 eV. Here the conduction band minimum (E_c) is positioned below the hydrogen terminated diamond valence band, providing an energetically favourable energy level within the surface materials conduction band for the transfer of electrons from the diamond valence band. The upward band bending on the diamond side will be strong enough to force E_f below the valence band maximum (E_v), forming a 2DHG within the diamond near the surface. The accumulated holes are mobile (~ 70 cm^2/Vs) parallel to the surface and are confined by the electric field generated by the interfacial charge separation. As such, this accumulated hole channel below the diamond surface most likely behaves as a quasi-2DHG with discrete quantum states [2.29]. Increasing carrier concentration will deepen the quantum well, bringing holes closer to the surface and thus possibly lowering mobility due to additional scattering from sources such as surface roughness and proximity to charge at the interface.

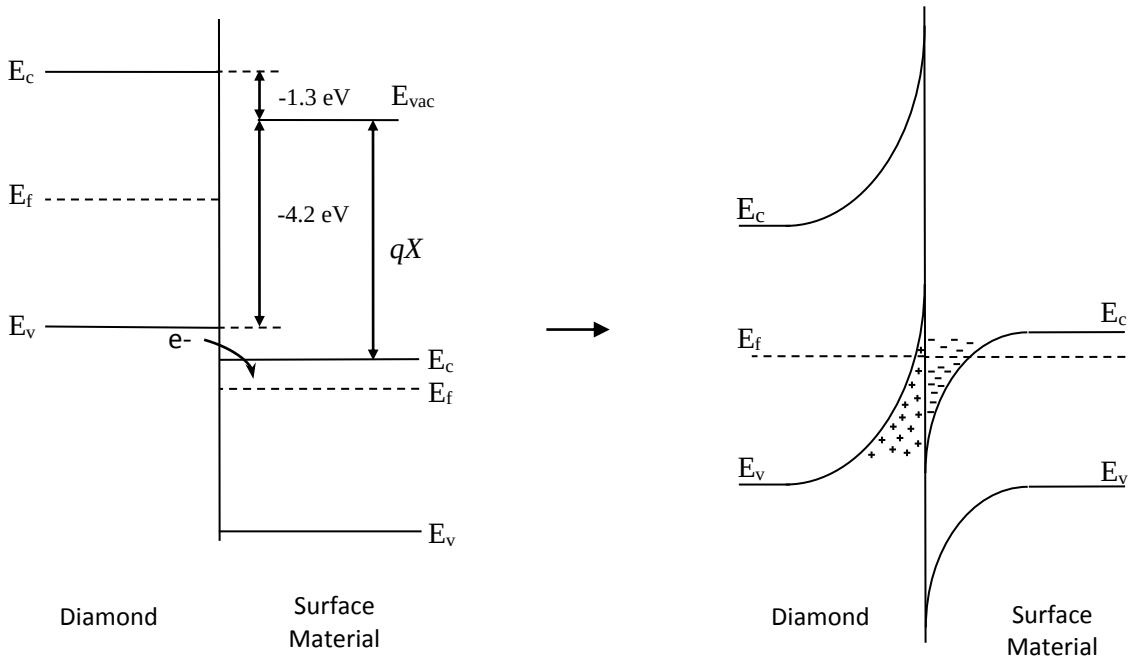

Figure 2.14 - Process of band bending during electron transfer between hydrogen terminated diamond and a surface acceptor material.

For air-exposed H-diamond, typical values for areal hole density have been found to vary between 10^{12} and 10^{13} cm^{-2} at room temperature for polycrystalline and single crystal CVD

films alike [2.30]. There are several potential candidates as a solid electron acceptor material on H-diamond. Figure 2.15 shows a diagram with the energy bands of diamond illustrated with different surface terminations as discussed previously in this chapter. Three high electron affinity materials and one with much lower electron affinity are also plotted.

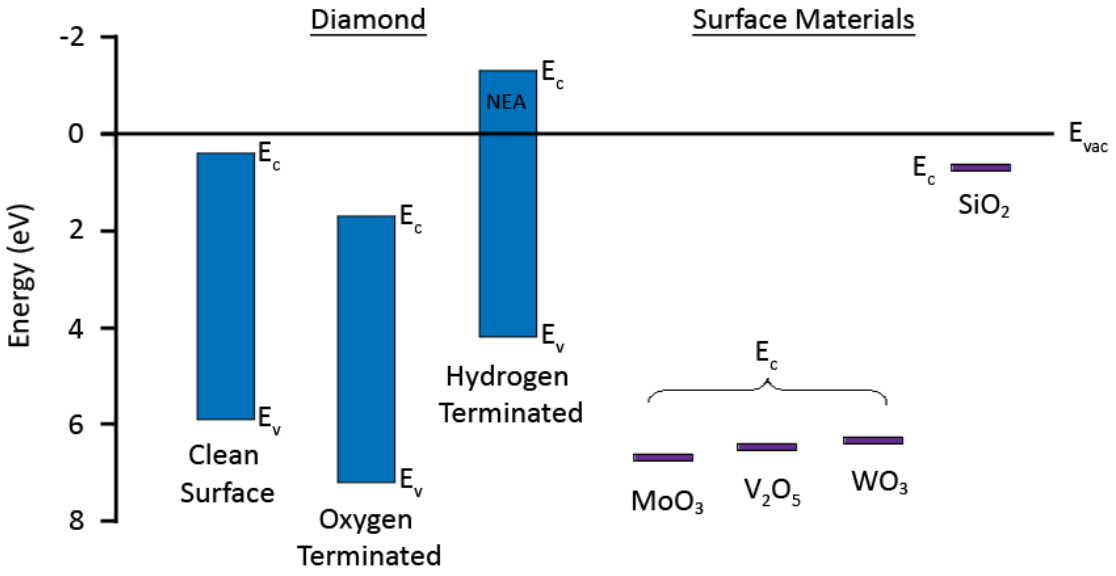

Figure 2.15 - Energy bands for diamond with different surface termination plotted alongside MoO_3, V_2O_5, WO_3 and SiO_2 to illustrate the difference between the diamond valence band and surface material conduction band.

Due to their respective high electron affinities, the transition metal oxides MoO_3, V_2O_5 and WO_3 are anticipated to induce surface transfer doping in diamond [2.31]. This is due to the EA of each material being greater than 4.2 eV, positioning their conduction band below the hydrogen terminated diamond valence band. By contrast, SiO_2 represents a surface medium that would not be expected to induce surface conductivity on diamond due to its much lower EA of 0.75 eV [2.32]. Note that while E_c of the transition metal oxides shown here are also positioned below the valence band of a clean reconstructed diamond surface, the NEA granted by hydrogen termination is still required to reduce the barrier experienced by electrons attempting to leave the diamond. This state of surface reconstruction is also not stable.

2.6 Metal-Semiconductor Interface

An integral component of any semiconductor device is the ability to make electrical connections between the semiconducting material and the external. Such connections as to allow the passage of current into and from a semiconductor are an important area of research for experimental and real-world applications.

A Schottky barrier is formed when a metal comes into contact with the surface of a semiconductor. The behaviour of the contact can be described as rectifying or non-rectifying, depending upon the height of the potential barrier formed. Figure 2.16a shows an energy diagram for a metal and an n-type semiconductor not in contact. The work function $q\Phi_m$ and $q\Phi_S$ is shown for the metal and semiconductor respectively, along with the electron affinity qX of the semiconductor.

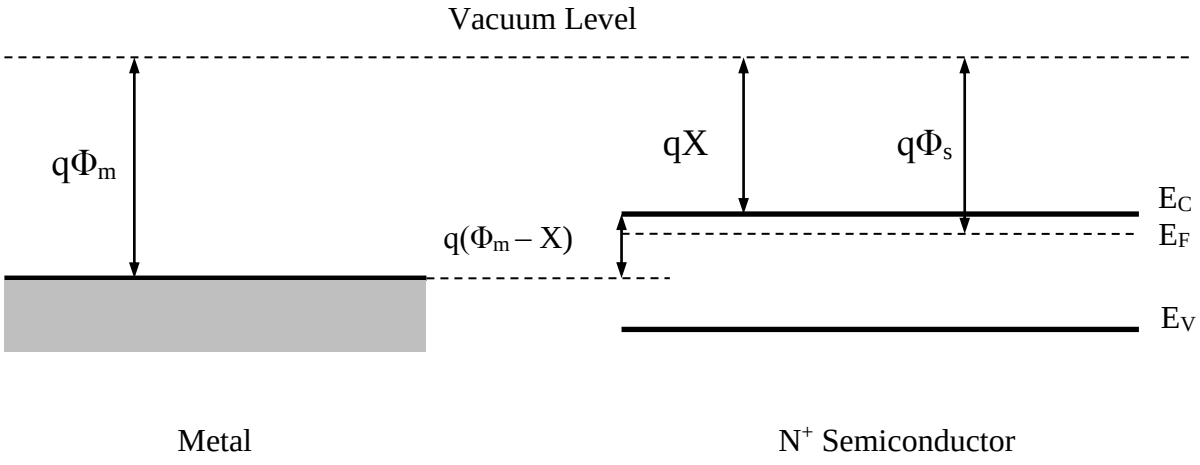

Figure 2.16a - Energy diagram of a metal and n-type semiconductor not in contact.

When brought into contact with each other the Fermi levels align as electrons diffuse between the two materials until a balanced state of charge is met, shown in Figure 2.16b. Once the depletion region is established, which opposes any further flow of electrons from the semiconductor, the energy required to excite an electron from the metal to the semiconductor is known as the barrier height qV_{Bn}. It is the difference between the semiconductor conduction band minimum and the metal Fermi level at the interface. In order for electrons to move from the semiconductor to the metal they must overcome the built in potential qV_{bi}, which is the energy difference between the conduction band at the interface and bulk.

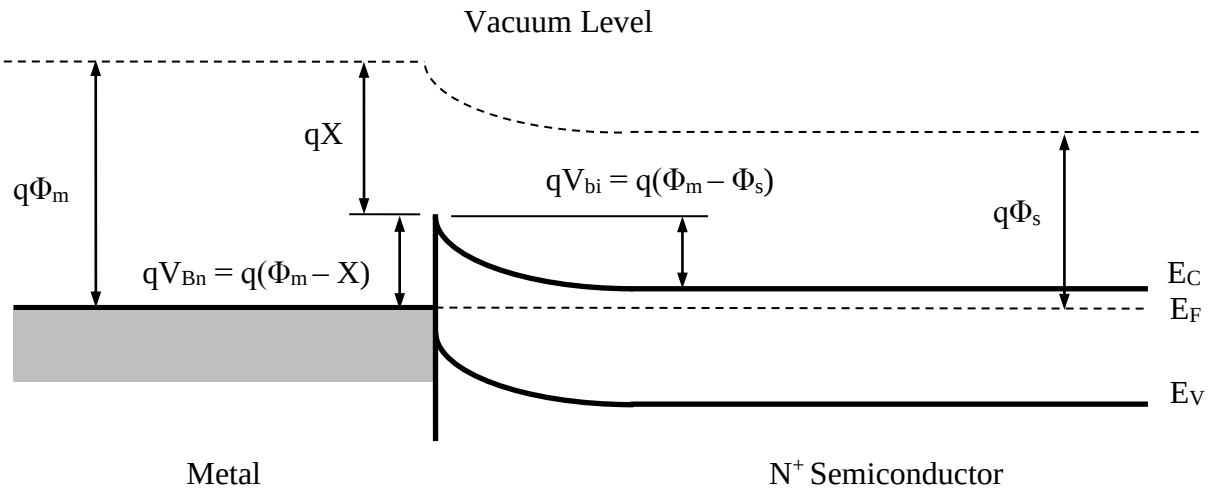

Figure 2.16b - Energy diagram of a metal and n-type semiconductor in contact after Fermi level alignment

In Figure 2.17a the semiconductor is now p-type, resulting in an increased value of $q\Phi_s$ as the Fermi level now sits closer to the valence band maximum. The semiconductor's Fermi level now sits at a lower energy than that of the metal. Note that qX remains unchanged.

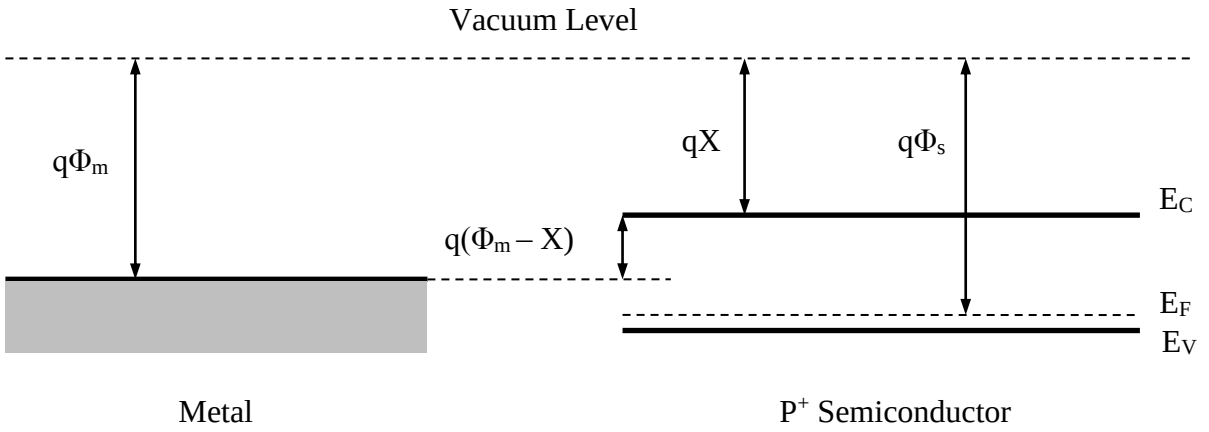

Figure 2.17a - Energy diagram of a metal and p-type semiconductor in contact

As a metal-semiconductor contact is made, bringing the Fermi levels into alignment, downward band bending occurs at the interface, illustrated in Figure 2.17b.

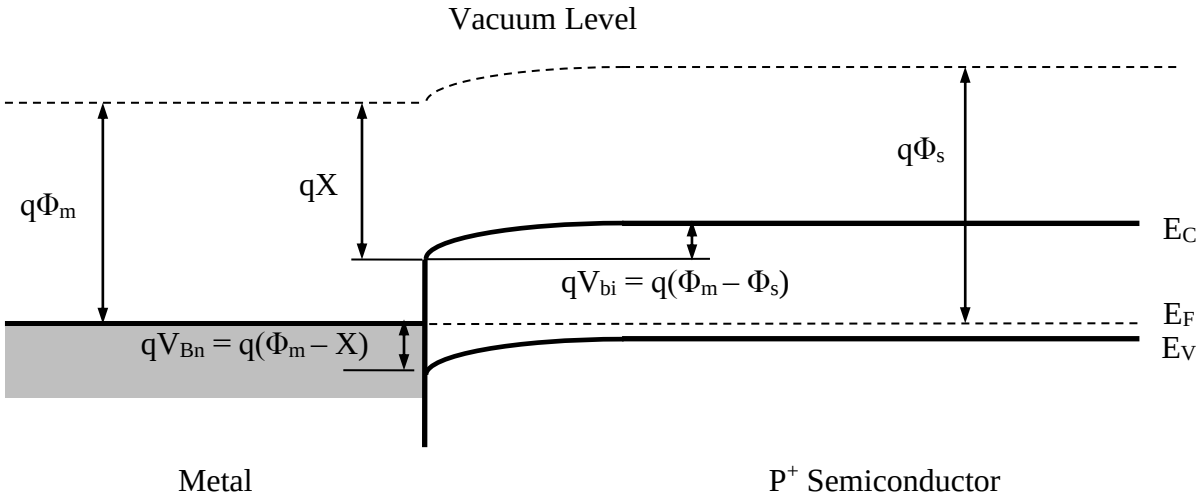

Figure 2.17b - Energy diagram of a metal and p-type semiconductor in contact after Fermi level alignment

The periodicity of the semiconductor crystal is interrupted at the interface between it and the metal contact, giving rise to surface states between the two mediums. The quantity and distribution of these surface states is influenced by various factors such as the semiconductor doping, quality of the contact and the crystal orientation of the two materials [2.33]. If the concentration of surface states is high enough, then the Fermi level may become 'pinned' at certain energies. The amount of charge required to equalize the Fermi level can be provided by these traps, causing Fermi level pinning due to the density of states at the surface. As such, the resultant barrier height will be independent of the metal work function. In the case of hydrogen terminated diamond, the surface termination leads to a reduction in surface states, making the surface sensitive to metal work function. High work function metals such as gold will form an ohmic contact on H-diamond, meaning the IV characteristics of the contact will display linear behaviour [2.34].

2.7 Chapter Summary

Diamond as a material for electronics has been explored in this chapter. The bonding configuration of carbon that produces the allotrope diamond was discussed and its associated properties detailed, such as extreme hardness, thermal conductivity and resistance to corrosive elements. Many of these appealing properties come from the

structure of diamond itself, making the material an important area of study. A method of producing synthetic diamond was presented, as well as strategies known to produce semiconducting properties in diamond. The challenges of traditional substitutional doping were explored and an alternative process known as surface transfer doping shown. While impurity doping of diamond is currently very limited, surface transfer doping shows great potential through further engineering of the diamond surface and use of surface acceptor materials. The following chapter contains a literature review of surface transfer doped diamond, from the discovery of this phenomenon to the present-day status of this technology.

References

[2.1] F. P. Bundy, "Direct Conversion of Graphite to Diamond in Static Pressure Apparatus", Journal of Chemical Physics, 38, (1963)

[2.2] F. Gao, "Theoretical model of intrinsic hardness", Physical Review B, 73 (2006)

[2.3] L. S. Bartell, "On the Length of the Carbon-Carbon Single Bond", Journal of the American Chemical Society, 81, (1959)

[2.4] G. E. Kimball, "The Electronic Structure of Diamond", Journal of Chemical Physics, 3, (1935)

[2.5] C. J. H. Wort and R. S. Balmer, "Diamond as an Electronic Material", Materials Today, 11, (2008)

[2.6] H. Pierson, "Handbook of carbon, graphite, and fullerenes: properties, processing, and applications", Noyes Publications, Park Ridge, (1993)

[2.7] K. E. Spear, J. P. Dismukes, "Synthetic Diamond: Emerging CVD Science and Technology", John Wiley & Sons, (1994)

[2.8] D. G. Goodwin, J. E. Butler, in "Handbook of Industrial Diamonds and Diamond Films", (Eds: M. A. Prelas, G. Popovici, L. K. Biglow), Marcel Dekker, Inc., NY, 527, (1997)

[2.9] B. El-Dasher, J. J. Gray, J. W. Tringe, J. Biener, A. V. Hamza, "Crystallographic Anisotropy of Wear on a Polycrystalline Diamond Surface", Applied Physics Letters, (2005)

[2.10] S. J. Harris, D. G. Goodwin, "Growth on the reconstructed diamond (100) surface", Journal of Physical Chemistry, 97, (1993)

[2.11] S. J. Sque, R. Jones and P. R. Briddon, "Structure, electronics, and interaction of hydrogen and oxygen on diamond surfaces", Physics Review Letters B, 73, (2006)

[2.12] F. J. Himpsel, J. A. Knapp, J. A VanVechten and D. E. Eastman, "Quantum Photoyield of Diamond (111) – a Stable Negative-affinity Emitter", Physical Review B, 20, (1979)

[2.13] W. Chen, D. Qi, X. Gao, A. T. S. Wee, "Surface transfer doping of semiconductors", Progress in Surface Science, 84, (2009)

[2.14] J. B. Cui, J. Ristein and L. Ley, "Electron Affinity of the Bare and Hydrogen Covered Single Crystal Diamond (111) Surface", Physics Review Letters, 81, (1998)

[2.15] F. Maier, M. Riedel, B. Mantel, J. Ristein and L. Ley, "Origin of Surface Conductivity in Diamond", Physics Review Letters, 85, (2000)

[2.16] B. D. Thoms, J. E. Butler, "HREELS and LEED of H/C(100): the 2 × 1 monohydride dimer row reconstruction" Surface Science, 328, (1995)

[2.17] Y. Kaibaraa, K. Sugataa, M. Tachikia, H. Umezawaa, H. Kawarada, "Control wettability of the hydrogen-terminated diamond surface and the oxidized diamond surface using an atomic force microscope" Diamond and Related Materials, 12, (2003)

[2.18] K. M. O'Donnell, T. L. Martin, M. T. Edmonds, A. Tadich, L. Thomsen, J. Ristein, C. I. Pakes, N. A. Fox, and L. Ley, "Photoelectron emission from lithiated Diamond", Physica Status Solidi (a), 211, (2014)

[2.19] D. A. Neamen, "Semiconductor Physics and Devices", 3rd Edition, McGraw-Hill, Page 115-135, (2003)

[2.20] M. E. Zvanut, Shigang Zhang and W. E. Carlos “A Study of Dopants in Diamond Using Electron Paramagnetic Resonance Spectroscopy”, MRS Proceedings, 416, (1995)

[2.21] A. Mainwood, “Theoretical modelling of dopants in diamond”, Journal of Materials Science: Materials in Electronics, 17, (2006)

[2.22] F. J. Morin and J. P. Maita, "Electrical Properties of Silicon Containing Arsenic and Boron", Physical Review, 96, (1954)

[2.23] D. Marcos, M. Wubs, J. M. Taylor, R. Aguado, M. D. Lukin, and A. S. Sørensen, "Coupling Nitrogen-Vacancy Centers in Diamond to Superconducting Flux Qubits", Physical Review Letters, 105, (2010)

[2.24] R. Kalish, "Doping of diamond", Carbon, 37, (1998)

[2.25] T. Yokoya, T. Nakamura, T. Matsushita, T. Muro, Y. Takano, M. Nagao, T. Takenouchi, H. Kawarada and T. Oguchi, "Origin of the Metallic Properties of Heavily Boron-doped Superconducting Diamond", Nature, 438, (2005)

[2.26] E. A. Ekimov, V. A. Sidorov, E. D. Bauer, N. N. Mel’nik, N. J. Curro, J. D. Thompson and S. M. Stishov, "Superconductivity in Diamond", Nature, 428, (2004)

[2.27] G. Chicot, T. N. Tran Thi, A. Fiori, F. Jomard, E. Gheeraert, E. Bustarret and J. Pernot, "Hole Transport in Boron Delta-Doped Diamond Structures", Applied Physics Letters, 101, (2012)

[2.28] D. Takeuchi, M. Riedel, J. Ristein, L. Ley, “Surface Band Bending and Surface Conductivity of Hydrogenated Diamond”, Physical Review B, 68, (2003)

[2.29] L. Gan, E. Baskin, C. Saguy, and R. Kalish, “Quantization of 2D Hole Gas in Conductive Hydrogenated Diamond Surfaces Observed by Electron Field Emission”, Physical Review Letters, 96, (2006)

[2.30] K. Hayashi, S. Yamanaka, H. Okushi and K. Kajimura, “Study of the Effect of Hydrogen on the Transport Properties in Chemical Vapor Deposited Diamond Films by Hall Measurements”, Applied Physics Letters, 68, (1996)

[2.31] M. T. Grenier, M. G. Helander, W-M. Tang, Z-B. Wang, J. Qiu and Z-H. Lu, “Universal energy-level alignment of molecules on metal oxides”, Nature Materials, 11, (2012)

[2.32] Nobuyuki Fujimura, Akio Ohta, Katsunori Makihara and Seiichi Miyazaki, “Evaluation of valence band top and electron affinity of SiO2 and Si-based semiconductors using X-ray photoelectron spectroscopy”, Japanese Journal of Applied Physics, 55, (2016)

[2.33] S. M. Sze, “Physics of Semiconductor Devices”, John Wiley and Sons Inc. p.273-276, (1981)

[2.34] H. Kawarada, M. Aoki and M. Ito, “Enhancement mode metal-semiconductor field effect transistors using homoepitaxial diamonds,” Applied Physics Letters, 65, (1994)

3 Literature Review

3.1 Diamond Surface Conductivity

In 1989 Landstrass and Ravi reported a conductivity of 10^{-6} Ω^{-1} cm^{-1} for CVD diamond and for single crystal IIa diamond after exposure to hydrogen plasma. Considering the intrinsic conductivity for diamond is well below this value, hydrogen was clearly closely related to whatever effect was occurring to lower the surface resistance [3.1]. Soon after, it was shown that annealing the surface to 300^{o}C in air or oxidation of the surface by acid based solution would remove the observed increase in conductivity [3.2]. Maki *et al* gave the first insight into the nature of the increased conductivity by way of Seebeck-effect measurements and the electrical characterisation of a simple MISFET (metal insulator semiconductor field effect transistor) based on hydrogen terminated diamond. Their findings suggested holes within a subsurface layer were responsible for the conductivity [3.3].

Two years later Kawarada *et al* demonstrated a FET based on H-diamond, utilising the surface conductivity by way of two gold pads forming ohmic contacts and an aluminium gate to form a Schottky contact [3.4]. A cross section of their FET design is shown in Figure 3.1. For devices based on H-diamond the hydrogen serves a double purpose. Firstly, as a crucial component of the surface conductivity but also as a means to reduce density of states at the surface to an extent at which the diamond-metal barrier interface follows the metal work function. As such, gold with its high work function of 5.1 eV has a low Schottky barrier of 0.2 eV on H-diamond, whereas aluminium with its work function of 4.2 eV forms a Schottky barrier height of 0.9 eV [3.5].

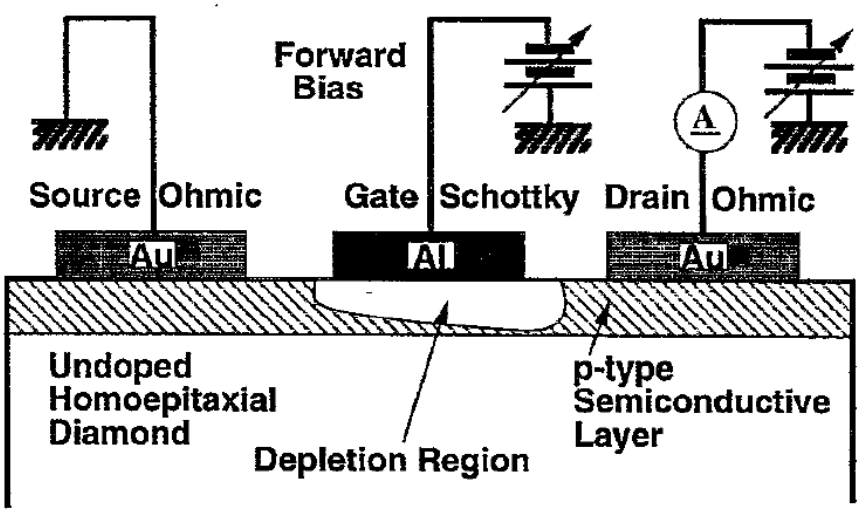

Figure 3.1 – Cross section of a MESFET using a p-type homoeptaxially grown diamond with an aluminium gate and gold source and drain (1994) [3.4].

As the reported surface conductivity of H-diamond became more pervasive, various reported values were established through Hall measurement [3.6, 3.7]. Conductivity of H-diamond was found to be in the region of 10^{-4} to 10^{-5} Ω^{-1}. Typical values for areal hole density were found to vary between 10^{12} - 10^{13} cm^{-2} and mobility with values around 30 – 70 cm^2/Vs at room temperature for polycrystalline and single crystal CVD films alike. Mobility was not merely a function of sample quality, but also highly influenced by carrier concentration; the lower the concentration the higher mobility is [3.8]. For example, a high mobility of 335 cm^2/Vs has been reported for a low carrier concentration of 7×10^{11} cm^{-2} [3.9].

The formation and origin of holes involved in surface conduction of H-diamond has been a topic of debate for a number of years. Initial theories suggested that hydrogen during the surface termination process would diffuse into the diamond and contribute shallow acceptor states [3.10, 3.11, 3.12]. However, this was contradicted by Grot *et al* who showed that removing hydrogen from the surface without attacking the diamond reversed the increased surface conductivity [3.2].

Shirafuji and Sugino were the first to propose a hole accumulation layer below the H-diamond surface as being responsible for the observed surface conductivity [3.13]. Using X-ray Photoelectron Spectroscopy (XPS) and Kelvin probe techniques they suggested electrons were transferred from the diamond to acceptor like states at the hydrogen

terminated surface, resulting in upward band bending, Figure 3.2. This would explain why after oxidation of the surface by acid based solution conductivity would be lost. Electrical characterisation of a surface channel FET on H-diamond later supported this theory by modelling the results with a two-dimensional acceptor layer at the surface extending up to 10 nm into the diamond [3.14]. Ri *et al* were to demonstrate the surface conductivity relies upon the atmosphere in which the H-diamond sample is kept [3.15, 3.16]. Exposure to acidic vapours would increase surface conductivity, whereas over other solutions it drops. From these results Ri *et al* were the first to suggest the reduction of H_3O_+ by electrons from the H-diamond as the origin of surface conductivity.

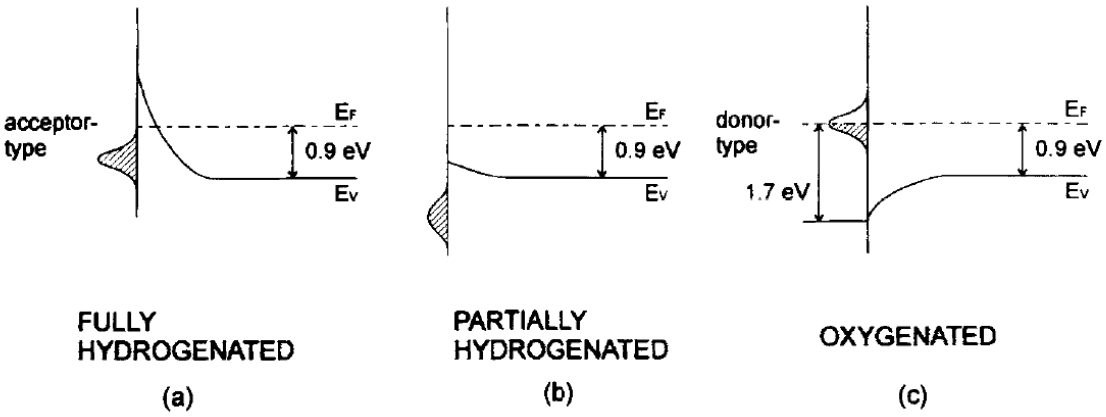

Figure 3.2 – Energy band diagrams for (a) hydrogen terminated (b) partially hydrogen terminated and (c) oxygen terminated diamond surfaces, as shown by Shirafuji and Sugino [3.13].

A vital experiment for the understanding of surface conductivity in H-diamond was published by Maier *et al* [3.17]. They placed a hydrogen terminated single crystal diamond sample in Ultra High Vacuum (UHV) where the conductivity could also be measured via two-point probe. Hydrogen termination was removed on one half of the sample by electron bombardment, simultaneously removing surface conduction on that half of the sample. Further annealing the sample at 410°C for 15 minutes also removed conductivity for the still hydrogen terminated side. The side with intact hydrogen termination was confirmed by total photoelectron yield spectroscopy. At this point the sample showed a conductance below 10^{-10} Ω^{-1} for both sides. Once the chamber was vented and the sample brought into air, the conductance of the hydrogenated half of the sample rose by 4 orders of magnitude within the first 20 minutes and reached a value similar to before of 2×10^{-5} Ω^{-1} after 3 days. In contrast, the non-hydrogen terminated half of the sample did not exhibit any change in

conductivity once exposed to air. This result clearly demonstrated both the hydrogen termination and exposure to air as vital components of the so far observed surface conductivity in H-diamond. Thus, the existence of acceptor states on the surface must be facilitated by air borne species. Maier *et al* went on to develop an electrochemical transfer doping model that was able to account for nearly all experimental findings concerning surface conductivity of H-diamond and gave an explanation as to why diamond exhibits this kind of surface conductivity. His model also identifies the role of hydrogen as a means to lower the ionisation energy of diamond, allowing the transfer doping to take place.

Once the nature of the surface transfer doping effect on H-diamond was better understood as being dependant on acceptor states introduced by an atmospheric surface layer, attempts were made to demonstrate the effect using alternative surface acceptors. The fullerene molecule C_{60} and its fluorinated variants ($C_{60}F_x$, x = 18, 36, 48) are well known to be highly oxidising, resulting in a high electron affinity. Strobel *et al* were the first to demonstrate fullerene induce surface transfer doping in H-diamond when it is evaporated onto the surface [3.18, 3.19]. The doping efficiency of $C_{60}F_{48}$ was found to be linear i.e. for each $C_{60}F_{48}$ molecule adsorbate on the surface a corresponding hole was generated up to a saturation of around 10^{13} cm^{-2} carriers, comparable in magnitude to air induced surface transfer doping.

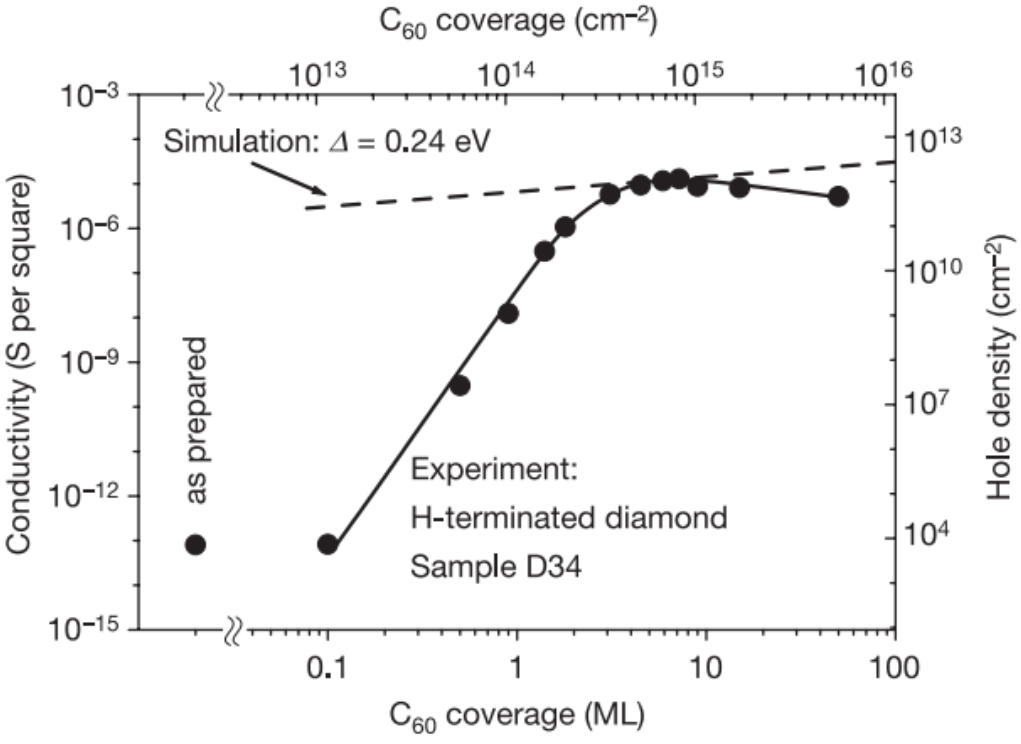

Figure 3.3 - Comparison between experiment and simulation of the two-dimensional conductivity of hydrogen-terminated diamond as a function of C_{60} coverage [3.18].

Although the electron affinity of C_{60} is measured to be only 2.7 eV [3.20], Goss *et al* and Sque *et al* showed potential for electron transfer from H-diamond to C_{60} using cluster calculation [3.21, 3.22]. Illustration of C_{60} and its fluorinated compositions are shown in Figure 3.4 alongside relative electron affinity.

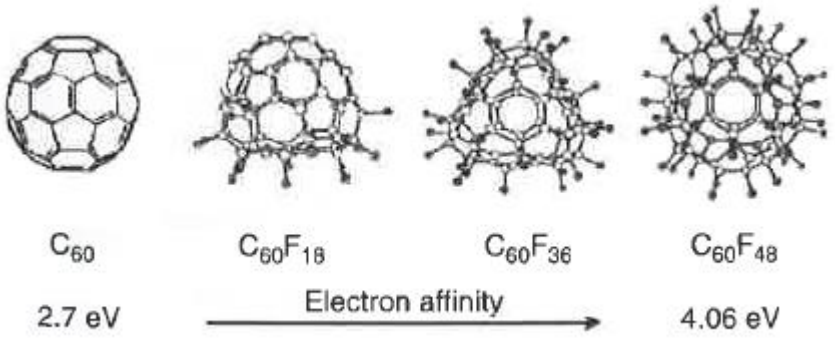

Figure 3.4 - Structure of different fluorofullerenes used to induce surface transfer doping in H-diamond. Fluorine atoms are represented by the solid spheres outside the C_{60} body, respective electron affinity increases with fluorine count [3.23].

Strobel *et al* demonstrated an H-diamond substrate annealed in vacuum at which point the sheet conductivity was below 10^{-12} Ω^{-1}. Depositing C_{60}, $C_{60}F_{18}$ and $C_{60}F_{48}$ showed, with increasing surface coverage, the diamond sheet conductivity rises by six orders of magnitude and saturates between 5×10^{-6} and 5×10^{-5} Ω^{-1} [3.19]. Depositing the fullerenes simultaneously onto an oxygen terminated diamond sample showed no increase in conductivity, demonstrating the hydrogen termination to be a necessary component while also observing no transport through the fullerene layer itself. An important result of this work showed the saturation in conductivity increases with higher electron affinity, with an order of magnitude difference between C_{60} and $C_{60}F_{48}$. Due to an EA of 4.06 eV, $C_{60}F_{48}$ shows greater doping efficiency than C_{60}, in essence a 1:1 ratio between fluorofullerenes and holes [3.24].

Dongchen *et al* further reported on high electron affinity molecules on H-diamond, investigated by Photoemission Spectroscopy (PES) [3.25]. The fluorinated derivative of Tetracyanoquinodimethane (F4-TCNQ) was chosen due to its high EA of 5.24 eV. The surface transfer doping potential was compared with another organic molecule of relatively low EA, Copper phthalocyanine (CuPc), at 2.7-2.9 eV. The diamond valence band maximum (VBM) lies well above the Lowest Unoccupied Molecular Orbital (LUMO) of

F4-TCNQ, as such electron transfer from the diamond valence band to adsorbed F4-TCNQ is thermodynamically favourable. This was confirmed by monitoring interfacial charge transfer during F4-TCNQ deposition, showing upward band bending towards the diamond surface associated with hole accumulation within the diamond to balance the negatively charged surface anion molecules. With increasing F4-TCNQ film thickness the change in work function became larger, attributed to the formation of an interface dipole. This effect was observed below 3 Å thickness, indicating the charge transfer occurs only at the diamond:F4-TCNQ interface leaving bulk largely un-charged. CuPc on the other hand with its much lower EA exhibits a LUMO 1.7-1.9 eV above the VBM of diamond. The resulting barrier should far exceed the thermal energy of electrons at room temperature (~0.026 eV) and as such surface transfer doping is not expected to occur. This was confirmed by the absence of band bending during CuPc deposition, indicating no hole accumulation at the diamond surface. Likewise, no work function shift was observed, as in the F4-TCNQ results. These organic materials, however, still demonstrated limited stability in air, despite attempts to encapsulate them [3.26].

A 2013 study by Takagi *et al* investigated the mechanism for 2DHG formation in hydrogen terminated diamond when surface transfer doped by air exposure, based on first principle calculation [3.27]. Hydrogen terminated diamond exposed to NO_2, O_3, NO and SO_2 formed sub-surface conductivity, whereas exposure to N_2O, CO_2 and N_2 had little or no effect. This relationship between adsorbed molecular species and sheet carrier concentration within the diamond relies on the electronic structure of isolated molecules, Figure 3.5. The VBM and conduction band minimum (CBM) of hydrogen terminated diamond with different surface orientation is shown alongside the Highest Occupied Molecular Orbital (HOMO) and the LUMO of isolated surface species. The group responsible for electron transfer (NO_2, O_3, NO and SO_2) have a LUMO at or below the VBM of hydrogen terminated diamond, while the LUMO of N_2O, CO_2 and N_2 falls above this threshold. This observation agreed with experimental results showing hole carrier density dependence on the species of adsorbates.

A more recent approach has demonstrated improved stability up to 550°C in air [3.28] through Atomic Layer Deposition (ALD) of Al_2O_3 on the H-diamond surface, resulting in carrier concentration between $8 \times 10^{12} – 1.5 \times 10^{13}$ cm^{-2}. Recently 1 kV operation of FETs has also been demonstrated using this Al_2O_3 passivation technique [3.29]. Similarly, Al_2O_3 has been used to encapsulate previously identified NO_2 surface accepter states, achieving higher temperature operation [3.30]. Although this work has yielded very promising device

performance, the exact mechanism responsible for the hole accumulation of diamond passivated by Al_2O_3 is still a point of investigation, due to the low EA of Al_2O_3 (~1 eV). Similar work involving ALD deposition of Al_2O_3 and HfO_2 has been explored for use in MOSFETs [3.31].

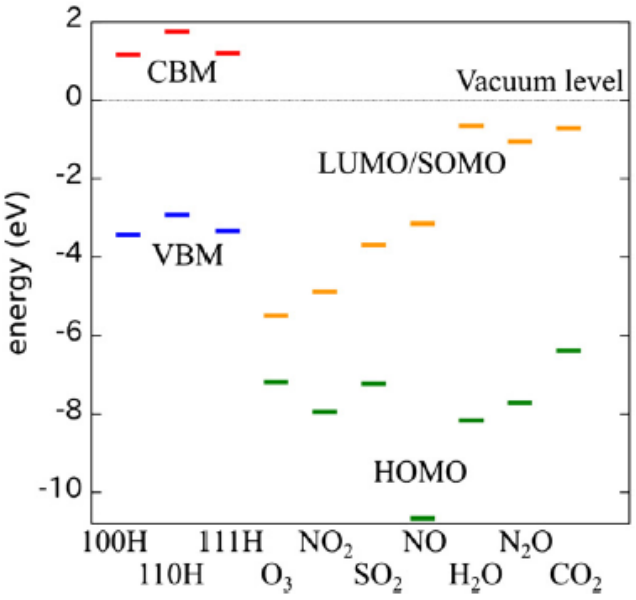

Figure 3.5 - Energy levels for the valence band maximum and conduction band minimum for H-terminated diamond with 100, 110 and 111 surfaces. HOMO and LUMO is shown for various atmospheric species [3.27].

High electron affinity transition metal oxides for surface transfer doping were first explored at the University of Glasgow as part of this work. Russell *et al* demonstrated molybdenum trioxide (MoO_3) to be a highly effective surface electron accepter material on H-diamond by way of PES and Hall measurement [3.32]. They showed thermal deposition of 100 nm MoO_3 resulted in a carrier density increase from 1 $\times 10^{13}$ to 2.16 $\times 10^{13}$ cm^{-2}, with clear charge separation across the diamond/MoO_3 interface forming a dipole with no further change beyond 1.6 nm of deposited oxide. This work was quickly followed by a similar study from Tordjman *et al* again demonstrating surface transfer doping by MoO_3 on H-diamond [3.33]. In this work varied thicknesses of oxide were observed up to 10 nm showing saturation of the increased carrier concentration occurring below 5 nm of MoO_3. As discussed in the later chapters of this thesis, vanadium pentoxide (V_2O_5) is demonstrated to be another excellent surface transfer dopant of H-diamond with similar potential to that of MoO_3 and a thermal stability upwards of 200°C *ex situ* [3.34]. A comparison study was later published by Verona *et al* investigating several high electron

affinity oxide materials, Nb_2O_5, WO_3, V_2O_5, and MoO_3 on H-diamond [3.35]. Due to the success of these transition metal oxide materials, early H-diamond FET devices have already been demonstrated using both MoO_3 and V_2O_5 as surface electron acceptors [3.36, 3.37].

3.2 Chapter Summary

Surface transfer doped diamond is a relatively new technology. Since the discovery of electrical conductivity in hydrogen terminated diamond, several attempts have been made to engineer a suitable surface acceptor which could overcome the initial limitations of the naturally occurring atmosphere exposed layer. This chapter has provided an overview of major developments in the study of surface transfer doped diamond up to the present. While still an emerging technology, the prospect of surface transfer doping in diamond using robust surface acceptor materials, such as high electron affinity oxides, shows great promise.

References

[3.1] M. I. Landstrass and K. V. Ravi, "Resistivity of chemical vapor deposited diamond films", Applied Physics Letters, 55, (1989)

[3.2] S. A. Grot, Gennady Sh. Gildenblat, C. W. Hatfield, C. R. Wronski, A. R. Badzian and Russell Messier, "The Effect of Surface Treatment on the Electrical Properties of Metal Contacts to Boron-Doped - Homoepitaxial Diamond Film" IEEE Electron Device Letters, 11, (1990)

[3.3] T. Maki, S. Shikama, M. Komori, Y. Sakaguchi, K. Sakuta and T. Kobayashi, "Hydrogenating Effect of Single-Crystal Diamond Surface", Japanese Journal of Applied Physics, 31, (1992)

[3.4] H. Kawarada, M. Aoki and M. Ito, "Enhancement mode metal semiconductor field effect transistors using homoepitaxial diamonds", Applied Physics Letters, 65, (1994)

[3.5] M. Aoki and H. Kawarada, “Electric Properties of Metal / Diamond Interfaces Utilizing Hydrogen-Terminated Surfaces of Homoepitaxial Diamonds”, Japanese Journal of Applied Physics, 33, (1994)

[3.6] K. Hayashi, S. Yamanaka, H. Okushi, and K. Kajimura, “Study of the effect of hydrogen on transport properties in chemical vapour deposited diamond films by Hall measurements”, Applied Physics Letters, 68, (1996)

[3.7] K. Hayashi, S. Yamanaka, H. Watanabe, T. Sekiguchi, H. Okushi, K. Kajimura “Investigation of the effect of hydrogen on electrical and optical properties in chemical vapour deposited on homoepitaxial diamond films”, Journal of Applied Physics, 81, (1997)

[3.8] H. J. Looi, R. B. Jackman, J. S. Foord, “High carrier mobility in polycrystalline thin film diamond”, Applied Physics letters, 72, (1998)

[3.9] B. Rezek, H. Watanabe, and C. E. Nebel, “High carrier mobility on hydrogen terminated [100] diamond surfaces”, Applied Physics Letters, 88, (2006)

[3.10] J. I. Pankove and N. M. Johnson, “Hydrogen in Semiconductors: 34 (Semiconductors and Semimetals)”, Academic Press, San Diego, (1991)

[3.11] M. I. Landstrass and K. V. Ravi, “Hydrogen passivation of electrically active defects in diamond”, Applied Physics Letters, 55, (1989)

[3.12] S. Albin, and L. Watkins, "Current-voltage characteristics of thin film and bulk diamond treated in hydrogen plasma", IEEE Electron Device Letters, 11, (1990)

[3.13] J. Shirafuji, T. Sugino, “Electrical properties of diamond surfaces”, Diamond and Related Materials, 5, (1996)

[3.14] K. Tsugawa, K. Kitatani, H. Noda, A. Hokazono, K. Hirose, M. Tajima, H. Kawarada, “High-performance diamond surface-channel field-effect transistors and their operation mechanism”, Diamond and Related Materials, 8, (1999)

[3.15] Ri S. Gi, T. Mizumasa, Y. Akiba, Y. Hirose, T. Kurosu and M. Iida, “Formation Mechanism of p-Type Surface Conductive Layer on Deposited Diamond Films”, Japanese Journal of Applied Physics, 34, (1995)

[3.16] Ri S. Gi, K. Tashiro, S. Tanaka, T. Fujisawa, H. Kimura, T. Kurosu and M. Iida, “Hall Effect Measurements of Surface Conductive Layer on Undoped Diamond Films in NO_2 and NH_3 Atmospheres”, Japanese Journal of Applied Physics, 38, (1999)

[3.17] F. Maier, M. Riedel, B. Mantel, J. Ristein and L. Ley, “Origin of Surface Conductivity in Diamond”, Physics Review Letters, 85, (2000)

[3.18] P. Strobel, M. Riedel, J. Ristein, and L. Ley, “Surface Transfer Doping of Diamond”, Nature, 430, (2004)

[3.19] P. Strobel, M. Riedel, J. Ristein, L. Ley, O. Boltalina, “Surface transfer doping of diamond by fullerene”, Diamond and Related Materials, 14, (2005)

[3.20] S. H. Yang, C. L. Pettiette, J. Conceicao, O. Cheshnovsky, R. E. Smalley “UPS of buckminsterfullerene and other large clusters of Carbon”, Chemical Physics Letters, 139, (1987)

[3.21] J. P. Goss, B. Hourahine, R. Jones, M. I. Heggie and P. R. Briddon, “P-type surface doping of diamond: a first-principles study”, Journal of Physics: Condensed Matter, 13, (2001)

[3.22] S. J. Sque, R. Jones, J. P. Goss, P. R. Briddon, S. Öberg, “First-principles study of C_{60} and $C_{60}F_{36}$ as transfer dopants for p-type diamond”, Journal of Physics: Condensed Matter, 17, (2004)

[3.23] O. V. Boltalina, and S. H. Strauss, “Encyclopedia of Nano-Science and Nanotechnology”, CRC Press, (2004)

[3.24] C. Jin, R. L. Hettich, R. N. Compton, A. Tuinman, A. Derecskei-Kovacs, D. S. Marynick, B. I. Dunlap, “Attachment of Two Electrons to C60F48: Coulomb Barriers in Doubly Charged Anions”, Physical Review Letters, 73, (1994)

[3.25] Qi, D., Chen, W., Gao, X., Wang, L., Chen, S., Loh, K. P., Wee, A. T. S. "Surface Transfer Doping of Diamond (100) by Tetrafluoro-tetracyanoquinodimethane", Journal of the American Chemical Society, 129, 8084-8085 (2007)

[3.26] P. Strobel, J. Ristein, L. Ley, K. Seppelt, I. V. Goldt, O. Boltalina, "Surface conductivity induced by fullerenes on diamond: Passivation and thermal stability" Diamond and Related Material, 15, (2006)

[3.27] T. Yoshiteru, K. Shiraishi, M. Kasu, H. Sato, "Mechanism of hole doping into hydrogen terminated diamond by the adsorption of inorganic molecule", Surface Science, 609, (2013)

[3.28] A. Daicho, T. Saito, S. Kurihara, A. Hiraiwa and H. Kawarada, "High-reliability passivation of hydrogen-terminated diamond surface by atomic layer deposition of Al_2O_3, Journal of Applied Physics, 115, (2014)

[3.29] H. Kawarada, T. Yamada, D. Xu, H. Tsuboi, T. Saito, A. Hiraiwa, "Wide temperature (10K-700K) and high voltage (~1000V) operation of C-H diamond MOSFETs for power electronics application", Electron Devices Meeting (IEDM), IEEE International, (2014)

[3.30] Kazuyuki Hirama, Hisashi Sato, Yuichi Harada, Hideki Yamamoto, and Makoto Kasu, "Thermally Stable Operation of H-Terminated Diamond FETs by NO_2 Adsorption and Al_2O_3 Passivation", IEEE Electron Device Letters, 33, (2012)

[3.31] J. W. Liu, M. Y. Liao, M. Imura, Y. Koide, "Band offsets of Al_2O_3 and HfO_2 oxides deposited by atomic layer deposition technique on hydrogenated diamond", Applied Physics Letters, 101, (2012)

[3.32] S. A. O. Russell, L. Cao, D. Qi, A. Tallaire, K. G. Crawford, A. T. S. Wee, D. A. J. Moran, "Surface transfer doping of diamond by MoO_3: A combined spectroscopic and Hall measurement study", Applied Physics Letters, 113, (2013)

[3.33] M. Tordjman, C. Saguy, A. Bolker, and R. Kalish, "Superior Surface Transfer Doping of Diamond with MoO_3", Advanced Material Interfaces, 1, (2014)

[3.34] K. G. Crawford, L. Cao, D. Qi, A. Tallaire, E. Limiti, C. Verona, A. T. S. Wee and D. A. J. Moran, "Enhanced surface transfer doping of diamond by V_2O_5 with improved thermal stability", Applied Physics Letters, 108, (2016)

[3.35] C. Verona, W. Ciccognani, S. Colangeli, E. Limiti, Marco Marinelli, and G. Verona-Rinati, "Comparative investigation of surface transfer doping of hydrogen terminated diamond by high electron affinity insulators", Journal of Applied Physics, 120, (2016)

[3.36] A. Vardi, M. Tordjman, J. A. del Alamo and R. Kalish, "A Diamond:H/MoO_3 MOSFET", IEEE Electron Device Letters, 35, (2014)

[3.37] S. Colangeli, C. Verona, W. Ciccognani, M. Marinelli, G. Verona Rinati, E. Limiti, M. Benetti, D. Cannatà, F. Di Pietrantonio, "H-Terminated Diamond MISFETs with V2O5 as Insulator", Compound Semiconductor Integrated Circuit Symposium (CSICS), IEEE (2016)

4 Characterisation and Measurement

This chapter covers the various techniques used to characterise and quantify diamond samples in this work. This includes the theory of Hall effect measurements, used to measure carrier concentration, carrier mobility and sheet resistance of substrates. Atomic force microscopy was also used extensively to inspect the diamond surface, detailed here.

4.1 Hall Measurements

The Hall Effect describes a potential voltage difference generated across an electrical conductor when in the presence of a magnetic field, discovered in 1879 by Edwin Hall [4.1]. The model consists of a flat, uniform electrically conducting material though which current can flow. By applying an external magnetic field transverse to the flow of current, charge carriers are deflected perpendicular to the field. These deflected charge carriers will accumulate along the materials edge as shown in Figure 4.1. The result is the production of a potential difference between the two edges, referred to as the Hall Voltage. This voltage (V_H) varies proportionally with the applied current and strength of the magnetic field.

The Lorentz force acting upon charge carriers in this magnetic field is expressed by

$$F_B = q(v \times B)$$

Where F_B is the force on the charge carrier; q is the charge of the electron, v is the velocity of the charge carrier and B the magnetic field strength. The cross product of the velocity and magnetic field is taken, resulting in a force vector that is perpendicular to the two.

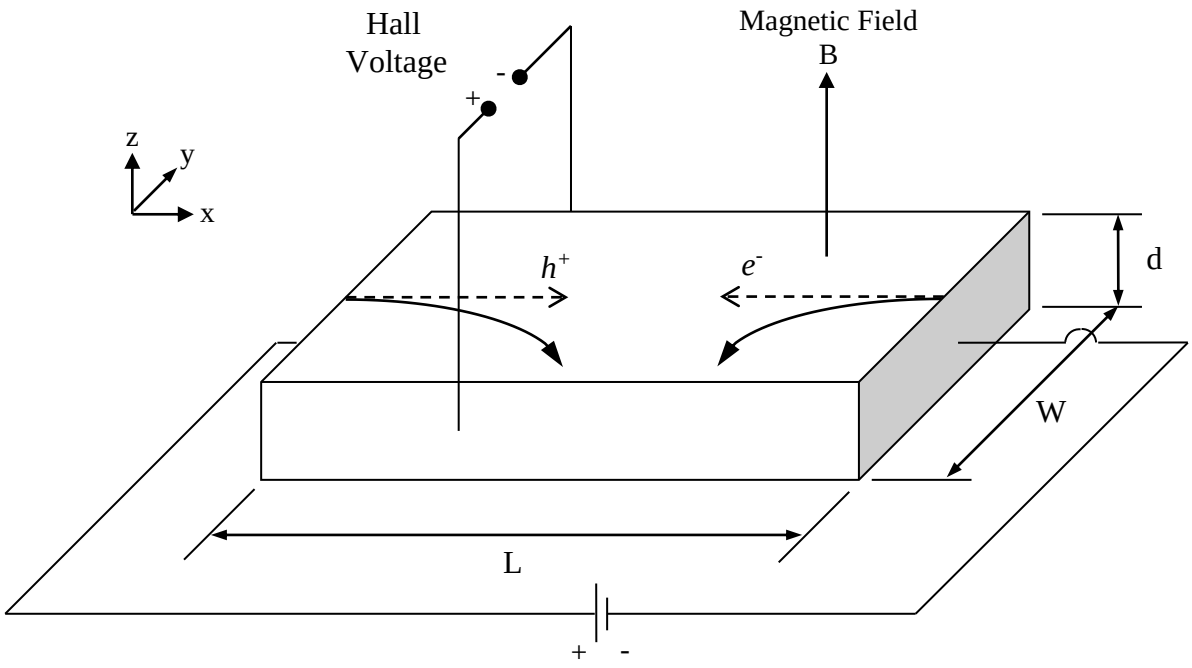

Figure 4.1 - Diagram of the Hall Effect with geometry for a semiconductor exhibiting both electron and hole carriers.

Once the accumulated charge carriers along the materials edge reach saturation i.e. charge now flows along the material without experiencing a Lorentz force, the balance may be expressed as

$$F_B = q(E + v \times B) = 0 \quad \text{or} \quad E_y = v_x B_z$$

The electric field created in the y-direction is referred to as the Hall Field E_H, which produces a voltage across the conductor called the Hall Voltage V_H

$$V_H = E_H W$$

Where W is the width of the conducting material. Combining these two equations gives

$$\frac{V_H}{W} = v_x B_z \quad \text{or} \quad V_H = v_x W B_z$$

For a p-type semiconductor the drift velocity can be written as

$$v_{dx} = \frac{J_x}{ep} = \frac{I_x}{(ep)(Wd)} \qquad \boxed{J_x = \frac{I_x}{Wd}}$$

Where p is the carrier concentration, e the electronic charge and J_x the drift current density. Combining the previous two equations gives

$$V_H = \frac{I_x\, WB_z}{(ep)(Wd)} \quad \text{or} \quad V_H = \frac{I_x B_z}{epd}$$

Solving for the hole concentration p therefore gives

$$p = \frac{I_x B_z}{edV_H}$$

For an n-type conductor both V_H and the carrier concentration n can be solved as

$$V_H = \frac{I_x B_z}{end}$$

$$n = \frac{I_x B_z}{edV_H}$$

The majority carrier mobility μ can now be calculated from the current density J

$$J = ep\mu_p E_x$$

In this example we are using a p-type conductor. Converting current density to current over dimensions and electric field to voltage over length gives

$$\frac{I}{Wd} = \frac{ep\mu_p V}{L} \qquad \boxed{E_x = \frac{V}{L}}$$

Therefore

$$\mu_p = \frac{IL}{epVWd}$$

For an n-type material, the equation is

$$\mu_n = \frac{IL}{enVWd}$$

The van der Pauw (VDP) method is a technique which makes use of the Hall effect to electrically characterise a given material, independent of its geometry so long as the sample retains a flat surface and is roughly 2-dimensional i.e. significantly thinner than it is wide [4.2]. The VDP method was first proposed by Leo J. van der Pauw in 1958 and can be used to accurately determine:

- Resistivity of the material
- Sheet charge carrier concentration
- Mobility of the majority charge carrier
- Type of majority charge carrier (holes or electrons)

The basic principle utilises four ohmic contacts of equal spacing on the material surface, producing a symmetrical measurement structure as illustrated in Figure 4.2. Due to the symmetry of the design if a current is passed between two contacts such as 1 and 2, the corresponding voltage across 3 and 4 will give rise to a resistance that is symmetrical around the structure. Typically, the four contacts are made around the edge of the sample. However, by electrically isolating around the design multiple structures can be made on the same sample.

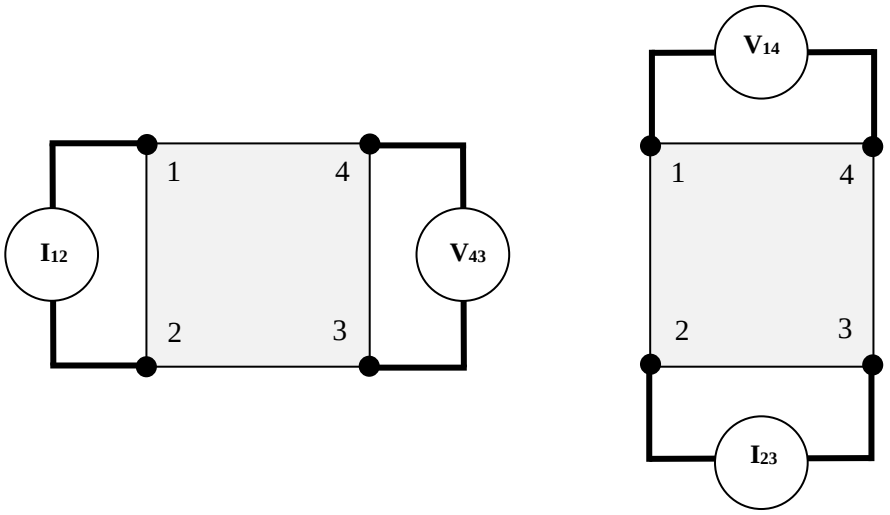

Figure 4.2 - Example numbering of VDP contacts.

Using Ohm's law

$$R = \frac{V_{43}}{I_{12}} = \frac{V_{14}}{I_{23}}$$

Where the channel thickness is known, using the van der Pauw equation resistivity ρ is then given by

$$\rho = \frac{\pi t}{2\ x\ In(2)} \left[\frac{V_{43}}{I_{12}} + \frac{V_{14}}{I_{23}}\right] \qquad \Omega\text{cm}$$

If the channel thickness is unknown, then sheet resistance ρ_{sheet} can be defined as

$$\rho_{sheet} = \rho/t \qquad \Omega\text{/square}$$

To measure the Hall Coefficient, current is applied between two non-adjacent contacts and the potential voltage difference measured between the two remaining contacts while a magnetic field, *B*, is acting perpendicular to the sample surface. This potential difference is the Hall Voltage.

$$q\ (v\ \times\ B) = qE$$

This relates the electric field *E* to the magnetic field *B* and the carrier velocity *v*. The charge of a carrier is denoted by *q*.

Current can be expressed as:

$$I = qntWv$$

where *n* is the carrier density and *W* the separation between the two non-adjacent contacts. This assumes a constant carrier distribution and velocity throughout the active layer. An illustration of the Hall effect when applied in a VDP configuration is shown in Figure 4.3.

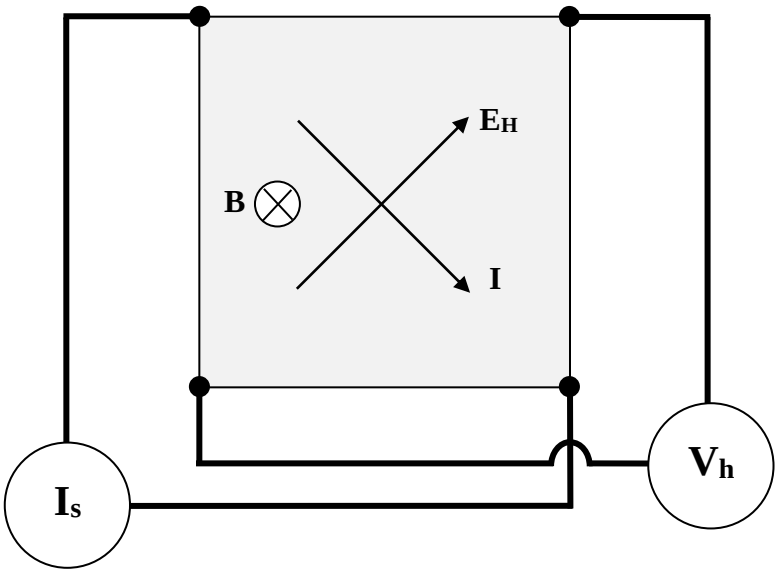

Figure 4.3 - Hall effect as applied in a VDP configuration.

The Hall Coefficient R_H can then be calculated as:

$$R_H = \frac{1}{qn} = \frac{V_H t}{IB}$$

Where V_H is the measured Hall voltage, $V_H = EW$. If the thickness of the active layer is not known then the sheet Hall Coefficient can be expressed as:

$$R_{Hs} = \frac{R_H}{t} = \frac{V_H}{IB}$$

Sheet carrier concentration n_{sheet} can then be calculated from the measured sheet Hall coefficient R_{Hs} in units cm^{-2}.

$$n_{sheet} = \frac{1}{qR_{Hs}} \qquad cm^{-2}$$

When the thickness is known, carrier concentration can be expressed in bulk as:

$$n = \frac{1}{qtR_{Hs}} \qquad cm^{-3}$$

Hall mobility μ_H is calculated from the measured values of sheet resistivity ρ_{sheet} and sheet Hall Coefficient R_{Hsheet}. The thickness of the active layer is not required to determine Hall mobility.

$$\mu_H = \frac{R_{Hs}}{\rho_s}$$

All Hall measurements carried out in this work were performed using a Nanometrics HL5500PC Hall measurement system. This four-probe system equipped with micromanipulators is rated as capable of measuring resistivity ranging from 0.1 mΩ/□ to 1 MΩ/□. The fixed magnet with field reversal has a strength of 0.32 T nominal to ±1% with uniformity over 25 mm diameter from the magnet centre. As such this Hall kit is suitable for samples up to 25 mm in diameter. The system used in this work comes with an interchangeable heated stage ranging from room temperature to 300ºC either in ambient atmosphere or in a vacuum of ~ 60 mTorr, allowing high temperature Hall measurements *in-situ*. An image of the standard measurement stage is shown in Figure 4.4.

Figure 4.4 – Image of the Nanometrics HL5500PC Hall measurement system.

Using a VDP structure the carrier concentration, mobility and thus resistivity of an arbitrary flat sample can be determined if the following conditions are true:

- The contacts are on the circumference of the sample active region
- The contacts are sufficiently small relative to the active region
- The sample active region is electrically continuous i.e. no electrically isolated areas within the active region
- The electrically active region is of uniform thickness

Two of the most common VDP geometries employ a square or a circle, however cross formations can also be effective [4.3]. Figure 4.5 shows some common VDP designs.

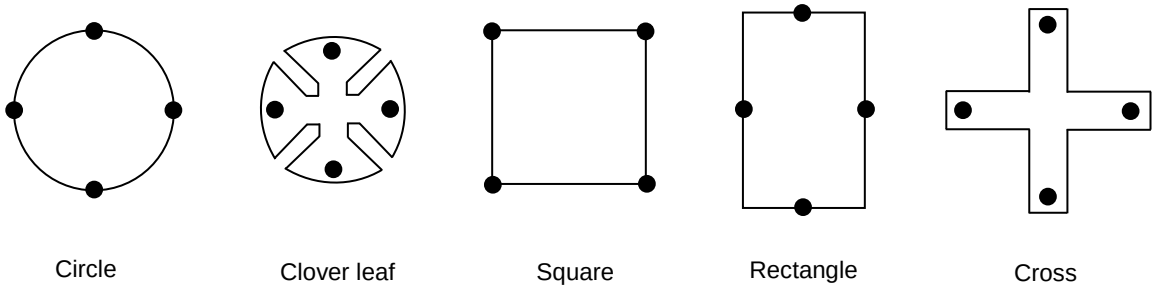

Figure 4.5 – Common designs of VDP test structures. Black dots illustrate the measurement contact points.

Contact size and placement can have significant effects on the accuracy of measurements. Ideally, contacts would be infinitely small and introduce no error. However, this is not practical as voltages required to drive a current between such contacts would be extremely high and not realistic. Designs such as the cross and clover leaf somewhat overcome this by isolating the contacts from the active region, using four separated paths to the centre and allowing for larger contacts. For a non-square substrate, moving contacts to the midpoint along the edges rather than the corners will also work. R. Chwang *et al* examined several sizes of both square and triangular shaped contacts on square samples by electrolytic tank experiment and calculation [4.4]. Figure 4.6 shows the VDP design.

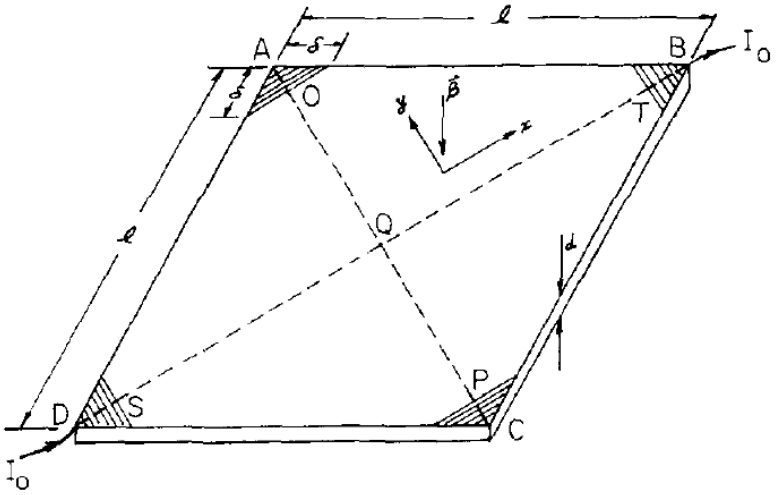

Figure 4.6 – Square sample with triangle ohmic contacts formed on the corners, R. Chwang *et al*.

Their results show the use of triangular contacts for a square VDP design produces reasonable accuracy depending on the contact size. For example, if the contact edge size δ is 1/8 the sample edge the Hall correction factor is less than 10%. This provides a good measurement setup for square samples in cases where more intricate VDP designs are less practical due to processing requirements, material, time constraints etc. For the cross and clover leaf designs shown in Figure 4.5, less than 1% error is possible [4.5].

4.2 Transmission Line Measurement

Transmission Line Measurement or Transfer Length Measurement (TLM) is a technique used to determine the contact resistance (R_c) between a metal and semiconductor [4.6]. The method employs a series of ohmic metal contacts fabricated in line with increasing gap size between each contact, presented in Figure 4.7. In this example five square contacts are spaced apart by 1 - 4 µm gaps. Each gap represents a network of resistances that are illustrated in Figure 4.8. Here, R_1 and R_2 represent the contact resistance between the metal and semiconductor and in theory these values should be equal. The resistance between these contacts, R_3, is determined by the conductivity of the substrate for a given gap size. Increasing or decreasing the distance between contacts will vary the value of R_3, while R_1 and R_2 should remain the same. As such, each gap can provide a value which when plotted against distance can be used to ascertain not only the contact resistance R_c, but also the substrate sheet resistance per unit area (R_s). An example plot is shown in Figure 4.9.

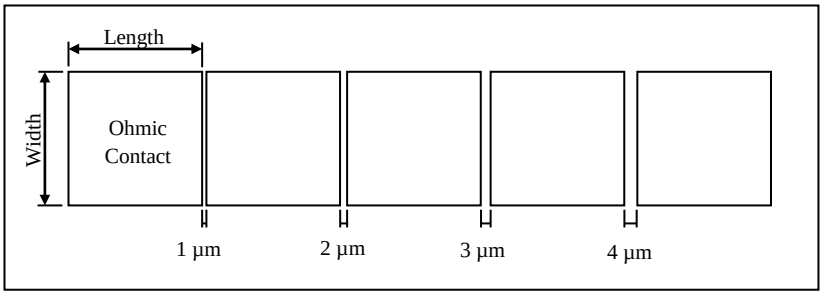

Figure 4.7 - TLM pattern with increasing gap distances

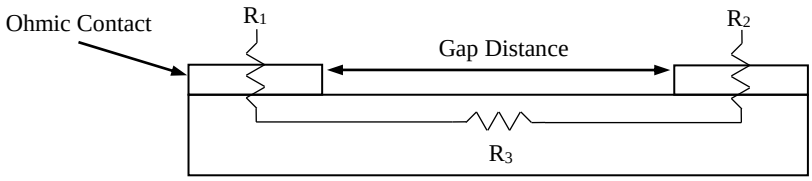

Figure 4.8 - The TLM gap transistor network.

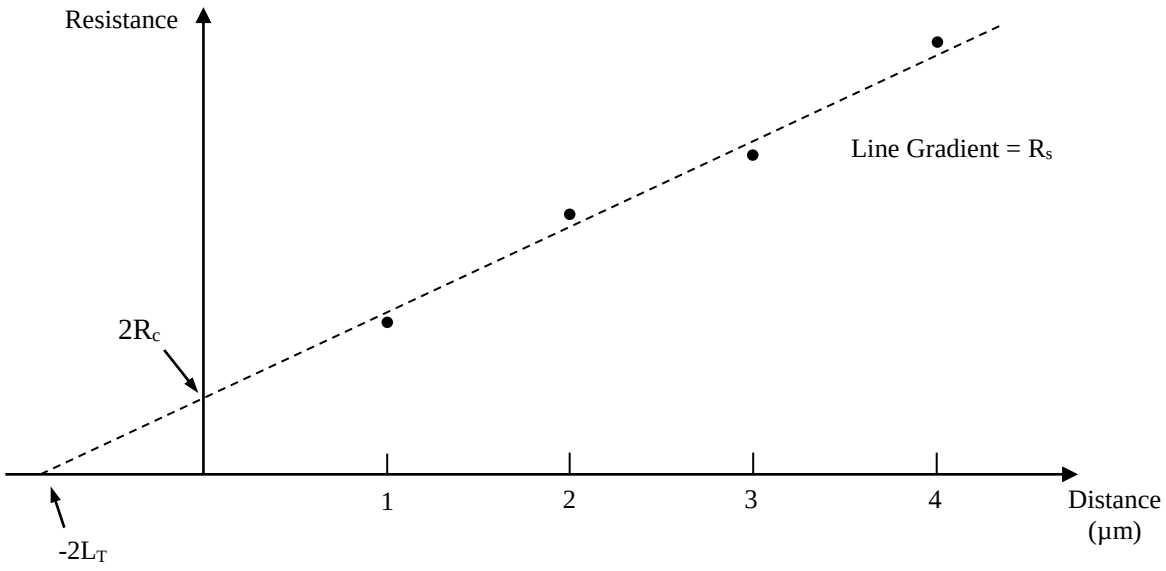

Figure 4.9 - Plot of resistance with gap distance from a typical TLM structure.

Here, the gradient of the line yields the sheet resistance of the substrate (Ω/□). The negative x-axis intercept represents 2 times the transfer length (L_T). Extrapolating the trend line backwards to the point where gap size equals zero (y-axis intercept) provides the total contact resistance, $2R_c$, for both contacts.

4.3 Atomic Force Microscopy

In both fabrication and sample characterisation a method of accurate surface profiling is desirable to view surface topology, roughness and also deposited film thickness. Atomic Force Microscopy (AFM) is a branch of Scanning Probe Microscopy (SPM) in which three-dimensional profiles are formed using a physical probe to scan the target material [4.7]. The AFM process makes use of a small cantilever equipped with a sharp pyramidal shaped probe located at the tip, often made from silicon. This probe is moved across the surface in a raster like pattern while a feedback mechanism measures the vertical displacement of the cantilever tip caused by changes in the surface. This is achieved by reflection of a laser off the reverse side of the cantilever and monitored by a photodiode array. The differential feedback from the laser is then used to form a topographical height map of the surface. To minimise damage to both the tip and the material being scanned, modern AFMs are equipped with a tapping mode in which the cantilever oscillates at a high frequency in order to "tap" the surface rather than be in constant contact. Figure 4.10 shows an illustration of an AFM setup.

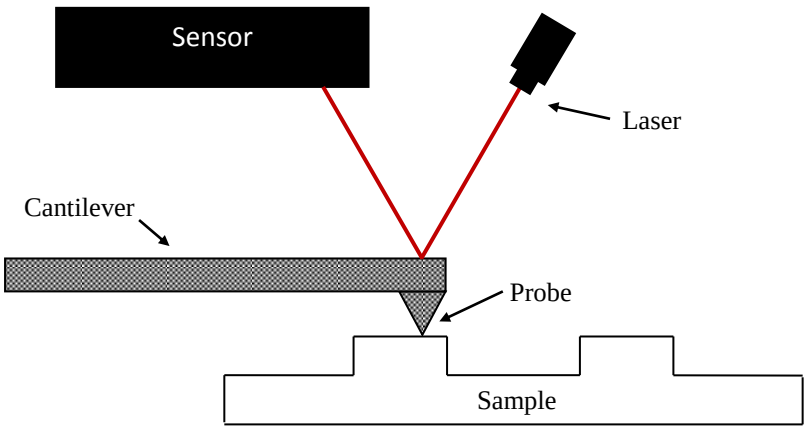

Figure 4.10 - Illustration of an AFM setup.

The AFM technique, while capable of sub-nm resolution, is primarily limited by the physical dimensions of the probe tip and its ability to conform to the topology of the surface being scanned. For example, attempting to measure a deep narrow trench in which the probe cannot fit as the pyramidal shape of the probe will prevent the apex reaching the bottom and into corners. As such AFM is generally more suited to height measurements rather than lateral distances and is not capable of mapping over hanging features. As well as the measurement of features such as film thickness, roughness values can also be extracted from the assessed profile independent of sample topology. The average roughness (Ra) is the arithmetic mean of the ordinate values Z within the sampling length. When Z is taken over a discrete number of measurement points, Ra can be expressed as:

$$Ra = \frac{1}{N}\sum_{i=l}^{N} Z_i$$

Here N is the number of measurement points in a given sampling length L. This is illustrated graphically in Figure 4.11. The centre line is the trace that the probe would measure according to its movement along a perfectly flat surface. If the regions below the centre line are placed above it, the Ra value is then the mean height of the resulting profile.

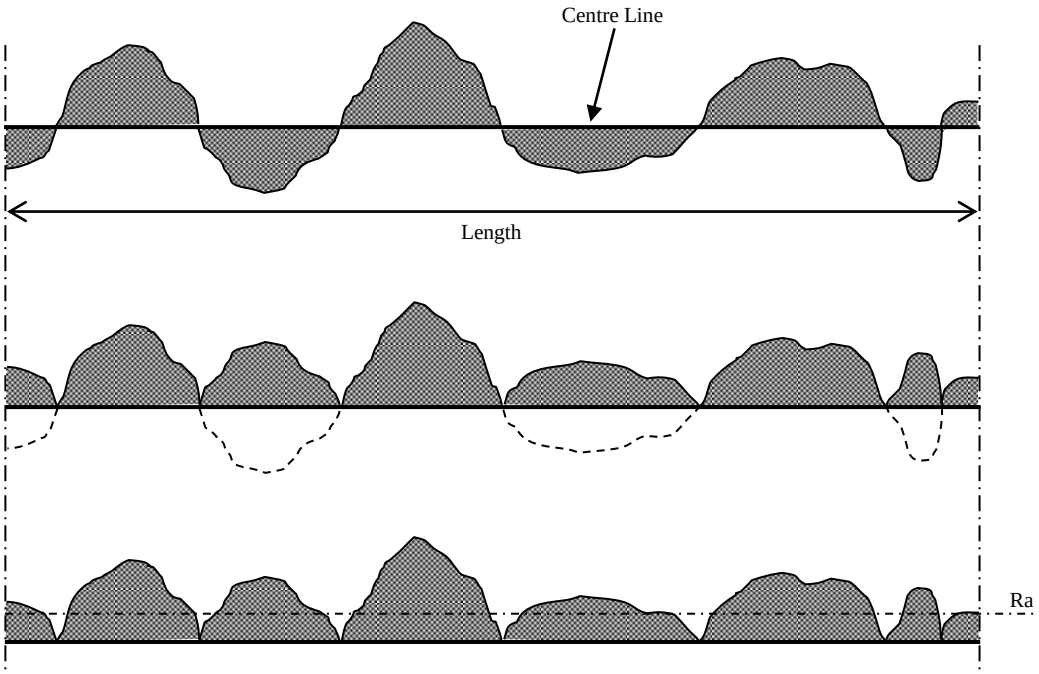

Figure 4.11 - Graphical derivation of Ra.

Since Ra is an average over a given sampling length the resulting value is less influenced by the presence of infrequent features on the surface, such as dirt or scratches. The measured value of Ra does not give any information as to the shape of the surface and as such it is possible to obtain similar Ra values for very different profiles.

The value Rq is the root mean square of the ordinate values Z for a given sampling length and is expressed as:

$$Rq = \sqrt{\frac{1}{N}\sum_{i=l}^{N} Z_i^2}$$

Unlike Ra, Rq grants additional influence to the numerically higher measured values of surface height and thus is more representative of a sample with less frequent features. While Rq can be skewed by anomalies foreign to the sample surface such as dirt, it is more representative of a surface with features such as pillars. Rq also has an advantage in that phase effects from electrical filters are negated and is often more useful for assessing the optical quality of a surface. The difference between Ra and Rq mathematically is exampled below.

$$Ra = \frac{Z_1 + Z_2 + Z_3 + \cdots Z_N}{N}$$

$$Rq = \sqrt{\frac{Z_1^2 + Z_2^2 + Z_3^2 + \cdots Z_N^2}{N}}$$

4.4 Chapter Summary

Techniques used in this work for the characterisation and measurement of hydrogen terminated diamond have been detailed. Primarily, Hall measurement is employed to inspect surface conductivity of substrates and the quality of surface termination is also indirectly verified by measurement of surface conductivity, due to an inability to directly detect hydrogen termination. TLM measurements serve to quantify surface conductivity while providing additional information with regards to contact resistance of metal contacts. A branch of microscopy, AFM, is also detailed as a means to profile diamond surfaces

with sub-nanometre precision. The following chapter presents fabrication processes for various measurement structures employed in this work, with particular attention to the fabrication constraints imposed by the hydrogen terminated diamond surface.

References

[4.1] E. H. Hall, "Elementary lessons in physics; mechanics (including hydrostatics) and light", H. Holt, (1894).

[4.2] L. J. van der Pauw, "A method of measuring specific resistivity and Hall effect of discs of arbitrary shape" Philips Research Reports, 13, (1958).

[4.3] I. Miccoli, F. Edler, H. Pfnür and C Tegenkamp, "The 100th anniversary of the four-point probe technique: the role of probe geometries in isotropic and anisotropic systems", Journal of Physics: Condensed Matter, 27, (2015)

[4.4] R. Chwang, B. J. Smith: and C. R. Crowell, "Contact size effects on the van der Pauw method for resistivity and hall coefficient measurement", Solid-State Electronics, 17, (1974)

[4.5] J. M. David and M. G. Buehler., "A numerical analysis of various cross sheet resistor test structures", Solid-State Electronics, 20, (1977)

[4.6] G. K. Reeves, H. B. Harrison, "Obtaining the specific contact resistance from transmission line model measurements", IEEE Electron Device Letters, 3, (1982)

[4.7] R. K. Leach, "Good Practice Guide No. 37: The Measurement of Surface Texture using Stylus Instruments", National Physical Laboratory Publications (UK), (2016)

5 Fabrication

In this chapter, fabrication details for the formation of devices and measurement structures on hydrogen terminated diamond are presented. Primarily, van der Pauw designs for Hall effect measurements made up the majority of electrical test structures produced. However, structures for determining contact resistance, gate leakage and FET devices were also made following processing details described in this chapter.

5.1 Electron Beam and Photo Lithography

In modern fabrication technology, the primary means of creating micro and nano-scale features are both photo and electron beam lithography [5.1]. Photolithography is a process by which the target substrate is coated with a photosensitive compound known as resist. The photo-resist weakens under ultraviolet radiation to the point at which it can be selectively removed in a solution. By coating a surface with resist (typically spun on to generate a conformal coating) and placing a mask on top; the resist can be exposed to pre-determined patterns. This is often referred to as contact lithography as the mask contacts the resist. After exposure to light, developing the sample in a solution removes the exposed areas of resist leaving behind the design embossed in unexposed resist. This technique can achieve resolutions on the microscopic scale. The process is illustrated in Figure 5.1.

An alternative process is electron beam lithography. Here electrons are used in place of light to pattern radiation sensitive resist, weakening exposed areas in a similar way to photolithography. Unlike photolithography there is no mask, instead an electron beam is precisely controlled by software and writes the pattern with raster style movement. Photolithography is considerably cheaper to implement than the complex systems required for controlled electron beam exposure. It is also much faster and more suited to mass producing multiples of the same pattern. However, for patterns which may be frequently altered the need to produce a new mask each time is impractical. The most significant

distinction between both methods is ultimately the minimum feature size that can be achieved. Photolithography is limited by the minimum feature size attainable to that of the light's wavelength and diffraction effects from the masking material, while electron beam lithography can achieve nanometre precision [5.1].

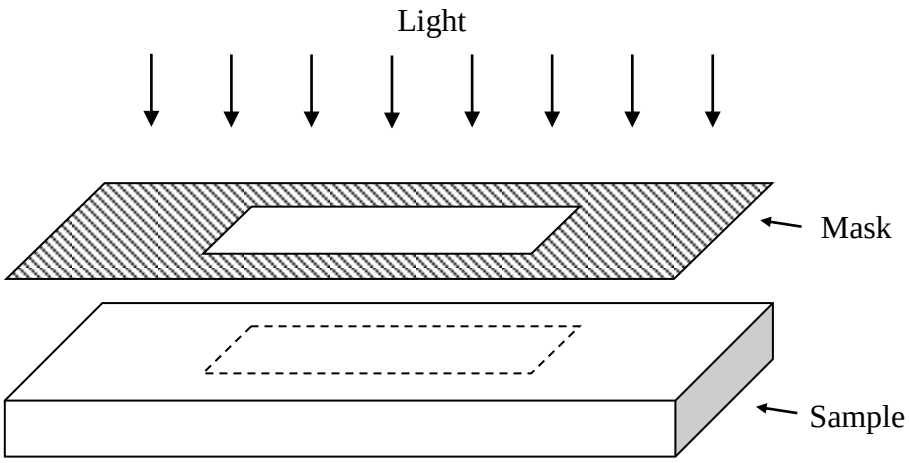

Figure 5.1 – Illustration of photolithography, selectively exposing a resist coated sample to light through a patterned mask.

One of the most common uses of resist once patterned by photo or electron beam lithography is to fill the exposed (patterned) areas with a chosen material. This is achieved by a process known as "lift-off", in which any remaining unexposed resist is removed in a solution after deposition of the desired pattern material. This material is often, but not limited to, metal. To create a "lift-off" profile, the resist consists of two layers, a layer directly on the substrate surface which is more susceptible to radiation topped with a thinner layer less susceptible to radiation. After lithography and subsequent development in a solution to remove the exposed resist, an overhang profile is formed as shown in Figure 5.2.

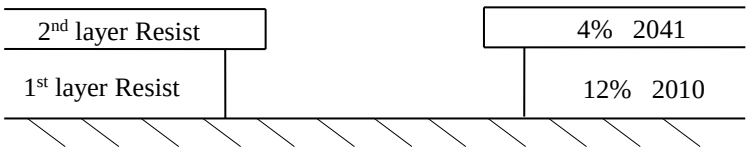

Figure 5.2 - Example cross section of a sample coated with resist after patterning.

This overhang becomes vital when depositing the desired material from which the pattern is to be formed, illustrated as metal in Figure 5.3. Due to the height of the resist and the overhang profile the deposited metal does not form a continuous film, resulting in regions where a wet chemical solution may access the resist and remove it.

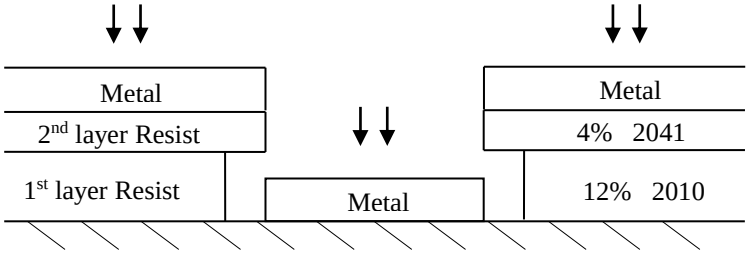

Figure 5.3 - Example cross section of a metallised sample.

As remaining resist is removed in a solution the deposited metal on top is also removed or "lifted-off". The result leaves behind only deposited metal in the desired pattern, Figure 5.4.

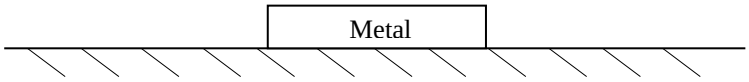

Figure 5.4 - Example cross section after lift-off.

The process of lift-off can be influenced in several ways. Perhaps most importantly, the thickness of the deposited material must not exceed the profile formed by the resist as illustrated in Figure 5.3. Otherwise the deposited material will form a continuous film over the lift-off profile and prevent a wet solution from accessing the resist. In cases where the deposited material nears the thickness limit of what can be successfully lifted-off by the resist profile being used, a feature known as "flags" will often form whereby additional material is left behind at the edges of the deposited pattern. This flagging effect also occurs when using an unoptimized resist bi-layer and or inadequate development process for the exposed resist.

5.2 Metallisation and Oxide Deposition

Thin films of material can be deposited by a variety of techniques, such as thermal and electron beam evaporation, sputtering and atomic layer deposition. The majority of material deposition performed in this work made use of electron beam and thermal evaporation systems built by Plassys, models MEB 400S and 400. These systems contain multiple crucibles for *in-situ* evaporation of different materials, suitable for substrates up to 150 mm with a cryo-pumped main chamber and load lock that reaches pressures of ~1 $\times 10^{-7}$ mbar. The 400S is used for the deposition of various metals and makes use of an electron beam source. The beam created by the electron gun is magnetically focused onto a target made of the desired deposition material, scanning in a raster pattern to generate localised heating and achieve a temperature at which the material sublimates. The Plassys 400 is equipped with a resistive element for thermal evaporation and is used exclusively for oxide materials to avoid metal/oxide contamination, illustrated in Figure 5.5. The deposition material is placed in a tungsten "boat" clamped between two electrodes. The material for deposition can be heated by passing a current through the boat, generating resistive heat with relatively precise control. For both systems, the thickness of the deposited film is monitored with a quartz crystal by measuring the resonant frequency of the crystal as evaporated material coats it.

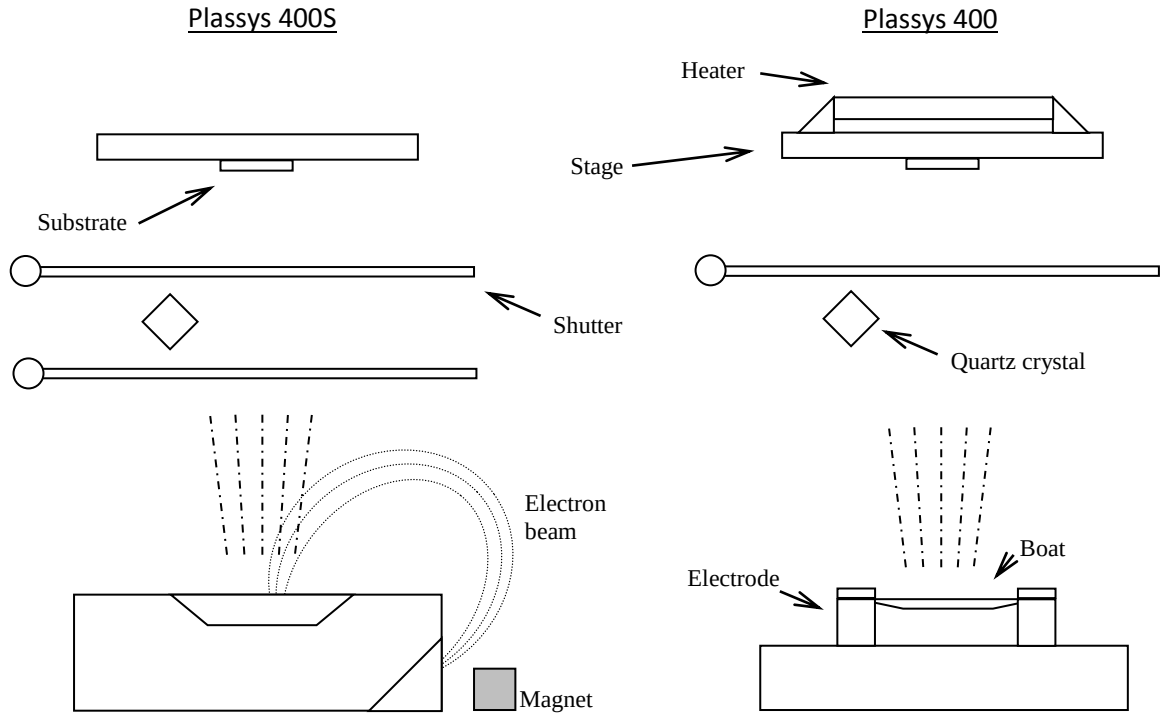

Figure 5.5 - Diagrams illustrating the Plassys 400/400S evaporation tools.

5.3 VDP & TLM Formation

Due to the sensitivity of the hydrogen terminated diamond surface, a layer of gold is firstly deposited onto the sample by electron beam evaporation. This metal layer protects the surface from subsequent processing steps which may disrupt the hydrogen termination. With the gold sacrificial layer in place, resist can then be spun on the sample for electron beam lithography. Alignment markers are written around the gold layer and a subsequent level of lithography is used to define isolation areas. The gold is selectively etched in these isolation regions using a solution of potassium iodide, leaving behind sections of gold from which ohmic contacts will be formed. At this stage, the isolation regions are exposed to O_2 plasma, replacing the hydrogen termination with oxygen. This removes the negative electron affinity in these areas and prevents surface transfer doping, effectively removing surface conductivity. The resist used in most of this work consists of a bi-layer 12% 2010 and 4% 2041 PMMA, baked for a minimum of 20 minutes at 120°C. This bi-layer works well both as a mask and for lift-off. The gold structures are then etched again to expose what are to be the active conduction regions between ohmic contacts. The process is illustrated in Figure 5.6.

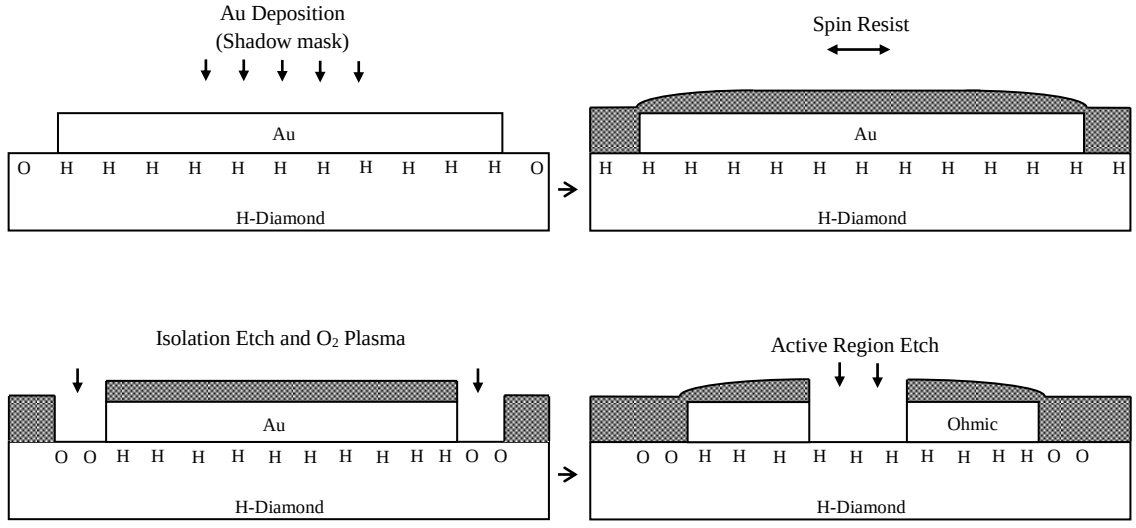

Figure 5.6 - Illustration of VDP fabrication on hydrogen terminated diamond. After deposition of gold using a shadow mask, resist is spun and the gold etched with potassium iodide to reveal regions to be isolated with O_2 plasma. The active region between ohmic contacts is then etched to form a working atmospheric VDP.

Wet etching gold in this manner to form ohmic contacts prevents the diamond surface from being exposed to resist which can be difficult to fully remove [5.2]. Exposure of the diamond surface to potassium iodide (KI_2) has shown no detrimental effect with regards to observed surface conductivity, whereas attempts to remove resist history from the surface using O_2 or SF_6 plasma disrupted the hydrogen termination. Figure 5.7 shows images of a lithographically defined VDP structure consisting of ohmic contacts overlapped by bond pad metal. These pads are made up of titanium capped with gold to provide a more robust probing solution. Here the active region in the centre of the four contacts remains covered in gold and has not yet been etched. Figure 5.8 shows the same group of VDP structures after etching of the gold covering the active region. The resist has not yet been removed, showing the lithographically defined window. At this stage the resist is then removed in an acetone bath kept at a temperature of 50ºC and later rinsed in isopropanol.

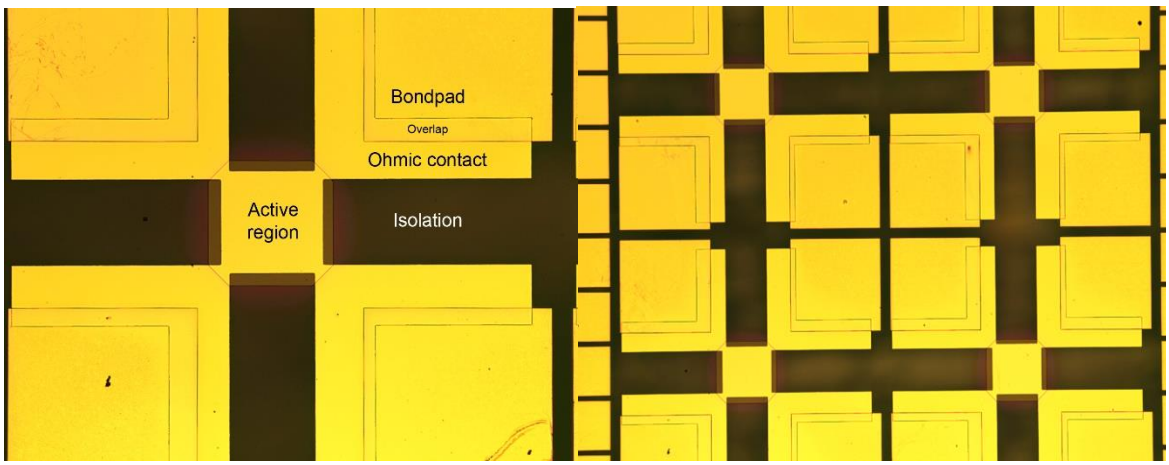

Figure 5.7 – Electron beam defined VDP structures. The active region in the centre of each structure has not yet been etched.

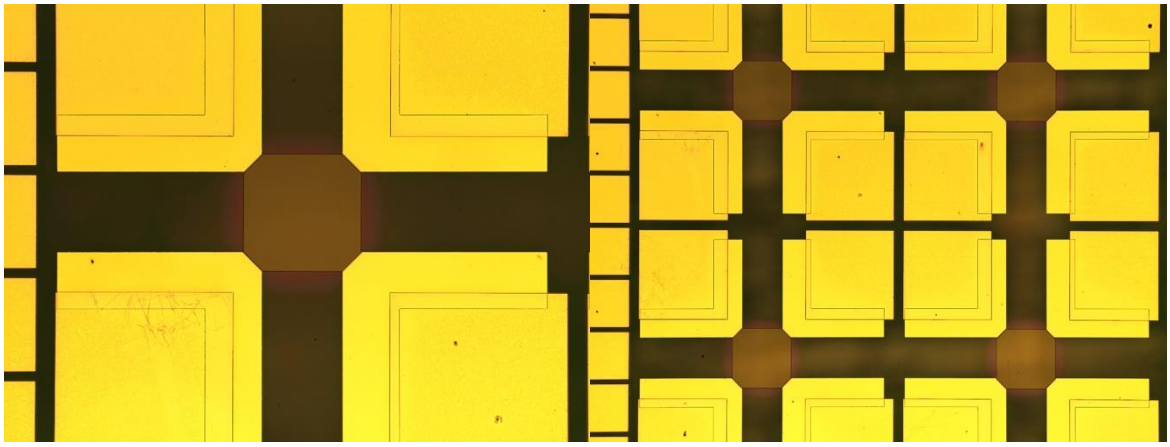

Figure 5.8 - Completed electron beam defined VDP structures.

During fabrication of designs requiring multiple levels of lithography, often active region wet etching with KI_2 would result in incomplete removal of the gold film as illustrated in Figure 5.9. The appearance of the gold after etching suggests masking of the metal by another medium, preventing full removal with the KI_2 solution. The most likely explanation is incomplete removal of the resist used in lithography [5.2]. After each consecutive layer of lithography, it is essential to thoroughly remove residual resist from the gold surface to prevent accumulation of a mask on the gold which prevents successful wet etching. This masking effect is more prone to occur after each successive level of lithography.

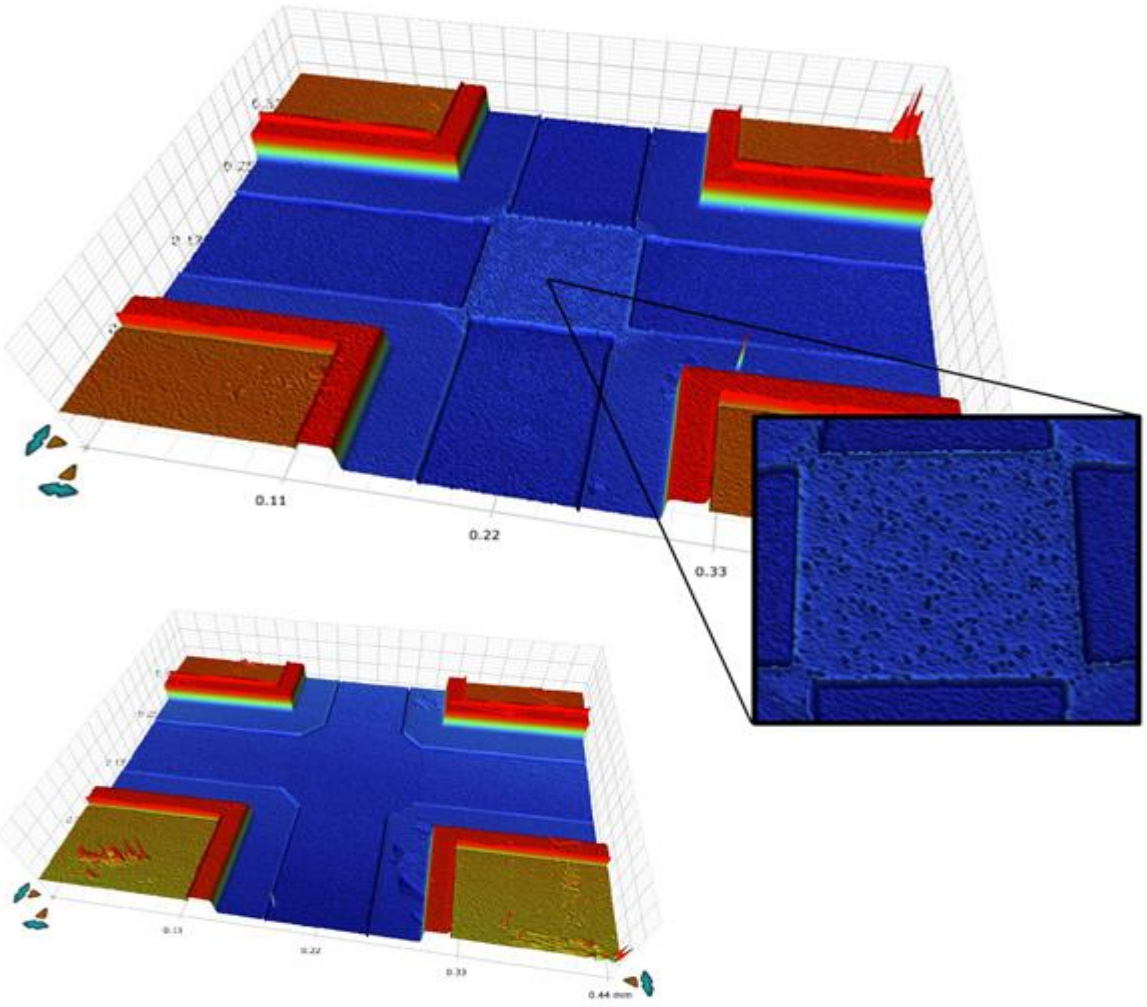

Figure 5.9 – Optical 3D images of a VDP structure fabricated on diamond, taken using a Bruker ContourGT Optical Profiler. Top image shows an incomplete active region etch. Image below shows a properly etched active region.

As discussed in Chapter 4, a streamlined van der Pauw structure can be prepared avoiding these lithography and fabrication steps by applying silver to the corners of a sample, roughly forming four symmetrically spaced contacts [5.3, 5.4]. This is illustrated in Figure 5.10.

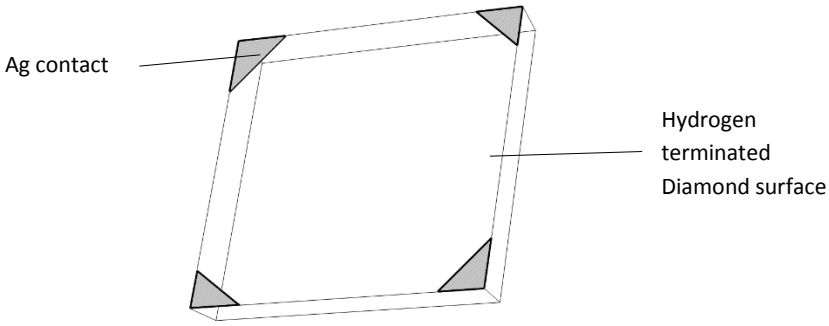

Figure 5.10 – Diagram of a diamond sample with silver applied to corners, forming a VDP test structure.

For the purpose of making 'large area' ohmic contacts to H-diamond silver contacts show a sufficiently low resistance and linear response [5.5]. Use of this simplified VDP structure minimises the risk of incurring contamination on the diamond surface using standard processing techniques such as exposure to resists, solvent chemicals and electron beam. Removal of hydrogen termination has previously been reported after exposure to electron beam, though at much higher doses than used in this work [5.6].

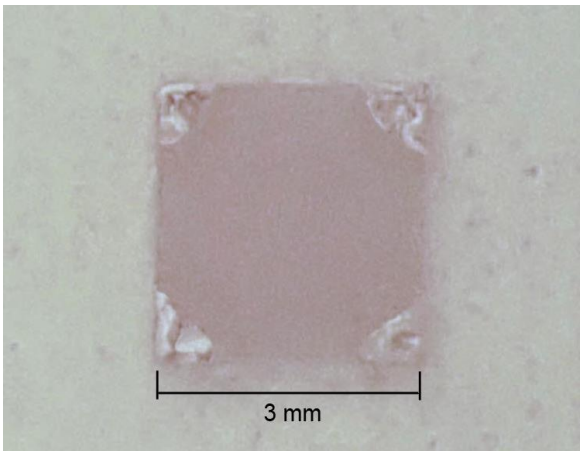

Figure 5.11 – Image of a 3 mm^2 diamond sample with silver applied to corners, forming a VDP test structure.

5.4 FET Gate Definition

So far, the use of a gold sacrificial layer, lithography and KI_2 wet etch has been discussed for the fabrication of structures on diamond with minimal exposure of the hydrogen terminated diamond surface to the various processing steps. Structures such as a VDP and TLM have good tolerance when it comes to undercut produced by the gold wet etch. For FET devices, however, the source to drain gap is determined by this undercut. FET devices fabricated in this work were formed by electron beam lithography, a patterning technique discussed previously in this chapter. Producing a sub 500 nm gate length on diamond with a controlled source drain gap first required process development. For development purposes, a 4.5 mm^2 diamond sample was first coated with 80 nm gold by way of electron beam evaporation at a chamber pressure of 2×10^{-6} mbar. The sample was then coated with the same PMMA bi-layer discussed previously and patterned by electron beam lithography. Figure 5.12 shows two microscope images of the gate pattern used. Here the resist has been developed and the gold wet etched with KI_2. Optimising the etchant concentration and temperature allowed for precise control of the undercut. Using a 10:1 H_2O:KI_2 mixture with a solution temperature of 60ºC resulted in a uniform 2 µm undercut when submerged for 30 seconds (Figure 5.12a). Reducing this time to 15 seconds resulted in a ~1 µm undercut creating a ~2 µm source drain gap depending on the gate length (Figure 5.12b). For structures in which the undercut is undesirable, such as TLM gaps, a short etch time of 10 seconds was found to produce an undercut of < 1 µm while still clearing out the 80 nm gold.

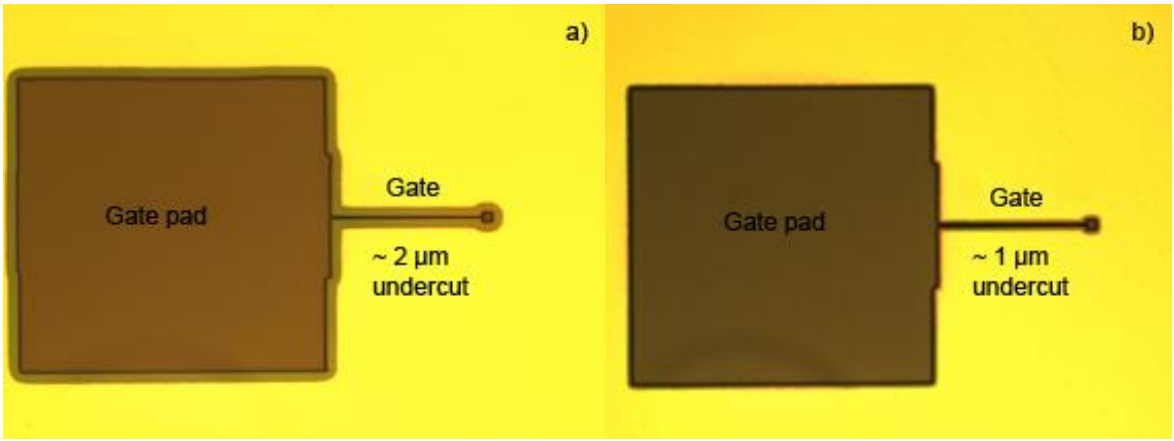

Figure 5.12 – Electron beam defined gates with contact pads on Au coated diamond.

The same resist profile used to etch the source-drain gap is also used to lift-off the gate metal. While writing the gate itself, the contact pad for probing (which connects to the gate) is also written. Due to the gate pad being significantly larger in area than the gate itself, two different sets of parameters when writing with electron beam are used, namely exposure dose and beam spot size. Figure 5.13 - shows a gate after deposition and lift-off using an 80 nm thick gate stack consisting of titanium, platinum and gold.

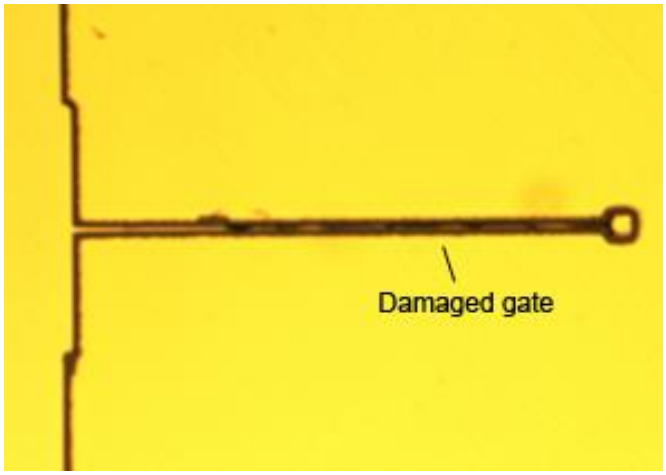

Figure 5.13 – Electron beam defined gate with contact pad after metalisation and lift off.

The gate dose was 1600 μCcm^{-2} with a beam spot size of 8 nA and a Variable Resolution Unit (VRU) of 10. The contact pad which the gate connects to was written with a dose of 1500 μCcm^{-2}, spot size 32 nA and a VRU of 32. Here the gate appears damaged, likely due to a poor lift-off resist profile as a result of inadequate exposure dose. Figure 5.14 shows another gate after lift-off using the same resist bi-layer and gate metal thickness.

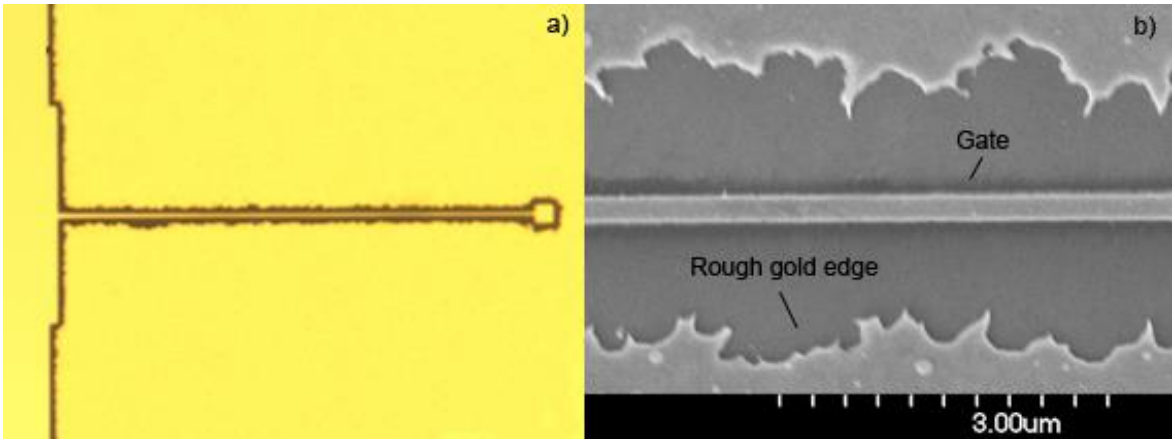

Figure 5.14 – E-beam defined gate with contact pad after metalisation and lift off.

Here the gate dose has been increased to 2100 μCcm^{-2} with an 8 nA spot size and a VRU of 10. Optical (5.14a) and Scanning Electron Microscope (SEM) (5.14b) imaging showed a well defined gate after lift-off. From the SEM image the gate length measures to be approximately 225 nm. The ohmic contacts formed by the source-drain wet etch prior to deposition of the gate metal show a rough, uneven profile. This phenomenon was commonly observed using a slower KI_2 etch at room temperature. Increasing the etch rate with a less dilute solution and higher temperature of 60^{o}C produced a smoother edge to the gold contacts. Figure 5.15 below shows a rendered AFM scan of a transistor gate combining both the optimised gate lithography and optimised gold wet etch, which resulted in smoother gold side walls and a well-defined gate. This is important for the source drain gap to minimise field concentrations at points along the uneven edge. Further optimisation to reduce the sidewall roughness is likely possible, but was not explored further in this work.

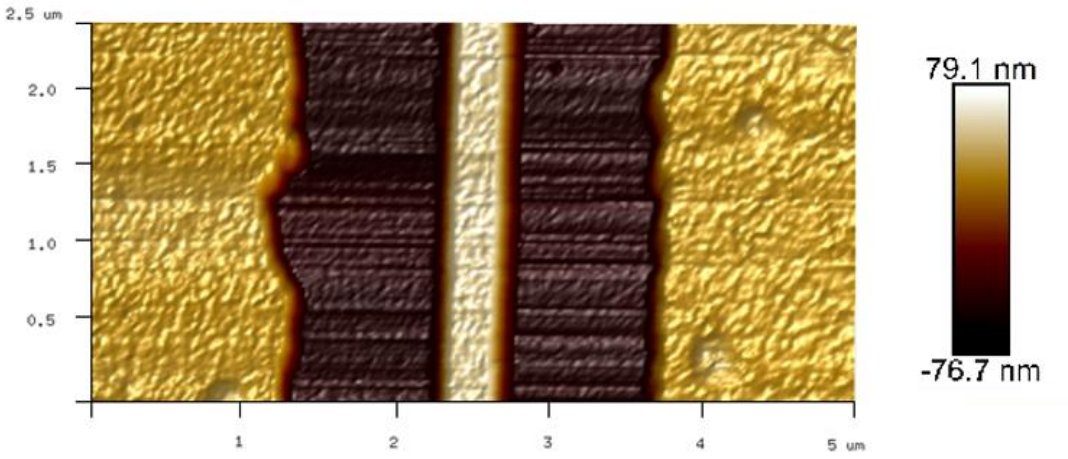

Figure 5.15 - 5 μm by 2.5 μm AFM render of an ebeam defined gate combining both the optimised dose and Au wet etch.

5.5 Chapter Summary

Formation of devices and structures which exploit the surface properties of hydrogen terminated diamond were discussed. A specific approach to fabrication on H-diamond is required as result of the hydrogen termination itself, which is easily degraded or even removed by exposure to various fabrication techniques typically used. The formation of both ohmic and gate contacts are shown, as well as the producion of van der Pauw

measurement structures. The following chapter contains the bulk of research presented in this thesis, utilising fabrication and measurement techniques discussed thus far.

References

[5.1] I. Brodie and J. J. Muray, "The Physics of Micro/Nano-Fabrication", New York: Plenum, (1992)

[5.2] D. S. Macintyre, O. Ignatova, S. Thoms and I. G. Thayne, "Resist residues and transistor gate fabrication," Journal of Vacuum Science and Technology B, 27, (2009)

[5.3] K. G. Crawford, L. Cao, D. Qi, A. Tallaire, E. Limiti, C. Verona, A. T. S. Wee and D. A. J. Moran, "Enhanced surface transfer doping of diamond by V_2O_5 with improved thermal stability", Applied Physics Letters, 108, (2016)

[5.4] R. Chwang, B. J. Smith: and C. R. Crowell, "Contact size effects on the van der Pauw method for resistivity and hall coefficient measurement", Solid-State Electronics, 17, (1974)

[5.5] M. C. Rossi, F. Spaziani, S. Salvatori, and G. Conte, "Electronic properties of hydrogen and oxygen terminated surfaces of polycrystalline diamond films" Physica Status Solidi (a), 199, (2003)

[5.6] F. Maier, M. Riedel, B. Mantel, J. Ristein and L. Ley, "Origin of Surface Conductivity in Diamond", Physics Review Letters, 85, (2000)

6 Surface Acceptor Results

Since the establishment of the surface transfer doping model for hydrogen terminated diamond exposed to ambient air, researchers have sought means of replacing the naturally occurring surface adsorbates with alternative electron acceptors. Some alternative materials are explored in this chapter, as mentioned previously in Chapter 3, including measurements of stability with time and at elevated temperatures. Issues that arose concerning sourcing of consistent, high quality hydrogen terminated diamond material used for this work is also discussed.

6.1 Hydrogen Termination

A mixture of hydrogen and oxygen termination is most common for naturally occurring diamond, due to earth's atmosphere [6.1]. CVD grown diamond is usually left H-terminated due to the presence of hydrogen in the chamber to suppress graphitic formation. Grown CVD diamond typically exhibits high levels of surface roughness and is usually then polished which in turn removes any H-termination. Perhaps the earliest method of terminating diamond with hydrogen is described by Emanuel in 1873 and involves mechanical polishing of diamond using olive oil as a lubricant [6.2]. Later it was observed using Low Energy Electron Diffraction (LEED) that diamond surfaces polished in this manner exhibit H-termination, the olive oil acting as the source of hydrogen. This method of H-termination however is not particularly consistent or repeatable. An important 1993 paper by Ando *et al* outlined a method of hydrogen termination by way of heating the diamond substrate and exposing it to a gas mixture containing hydrogen and an inert carrier [6.3]. This work explored the importance of substrate temperature in relation to achieving maximum hydrogen termination at ~900^{o}C, starting with an oxygen terminated surface. It is however important to avoid any graphitic formation on the surface at such temperatures, a process affected by vacuum pressure.

In Chapter 2 and 3, the importance of hydrogen termination in diamond surface conductivity was explored. Unfortunately, the resources required for the hydrogen termination of diamond were not readily available for the duration of this thesis, resulting in a reliance on collaborative parties. While the author is exceptionally grateful for these efforts, the lack of in-house control over this process greatly limited the scope by which this process could be understood and optimised. In this work hydrogen termination of the diamond surface was carried out in collaboration with the University of Paris 13 and Cardiff University. Both sources of H-termination differed in approach, process details outlined in the table below.

	Cardiff	**Paris**
Pressure	95 mbar	66 mbar
Power	3 kW	2.1 kW
Temperature	600°C	600°C
Time (minutes)	5	30

Table 6.1 – Process details of two hydrogen termination procedures used to H-terminate diamond samples in this chapter.

Both sources of H-termination used a purpose-built CVD diamond reactor with microwave plasma capability. Cardiff opted for a higher power process at 3 kW with a short exposure time of 5 minutes. The reasoning behind this high power and short time was to try to minimise damage to the diamond surface while still producing good hydrogen coverage. Conversely, the process at Paris made use of a much longer exposure time of 30 minutes with a lower power of 2.1 kW. Substrate temperature for both processes was maintained at roughly 600°C and measured by pyrometer. H-terminated samples arriving back at Glasgow were then given a solvent clean in acetone followed by IPA using an ultrasonic bath to remove any contaminants accrued during transit. Verifying the quality and consistency of hydrogen termination is challenging, due to the difficulty in detecting atomic hydrogen. Techniques often used to detect hydrogen termination, such as Scanning Tunnelling Microscope (STM) and LEED were not available [6.4, 6.5]. As such, the hydrogen termination of diamond samples in this work was primarily quantified by surface conductivity measurements.

It is essential to maintain a clean and somewhat consistent surface prior to any attempts at hydrogen termination. Ideally, the crystal plane would be atomically smooth with no

imperfections or impurities. However, due to available polishing and growth technologies this was not possible. The simplest bond that a diamond surface carbon atom can form is to hydrogen [6.6]. The resulting polar surface will be rapidly polluted via airborne contaminants -or contact with other materials- which bond strongly to the surface. This sort of surface contamination cannot be removed by basic chemical solvents such as acetone, but rather require aggressive acid cleaning at high temperatures to ensure a clean surface. Therefore, a two-step cleaning process was established, based upon a process developed by the ISDD Optics; Detector and Electronics Group at ESRF, illustrated in Figure 6.1.

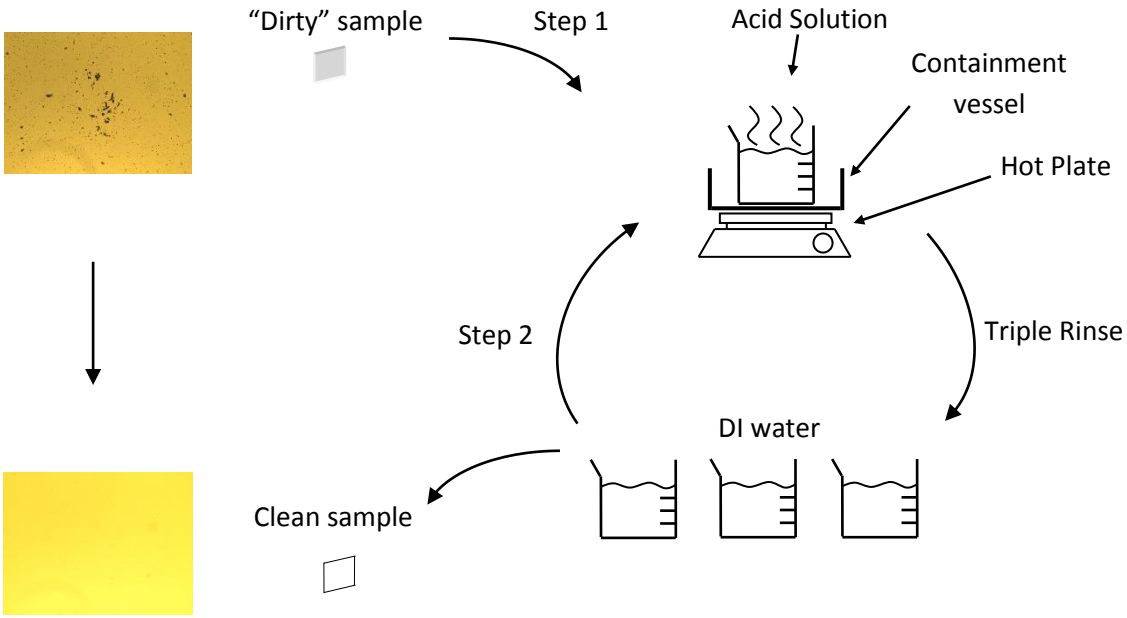

Figure 6.1 - Process flow of diamond acid cleaning.

Firstly the sample is placed in a mixture of freshly prepared aqua regia HNO_3:HCl 1:1, which is then placed on a hotplate and allowed to boil for >10 minutes. Once cooled the sample is removed from the solution and triple rinsed in DI water. This process removes any metal trace contaminants from the surface, as well as any hydrocarbon and oxygenated compounds. Next the sample is placed in a mixture of H_2SO_4:HNO_3 3:1 and boiled (~240^{o}C) for >10 minutes, again triple rinsed in DI water. This last step removes any lingering particle matter from the highly polar surface and leaves it oxygen terminated, ready to be hydrogen terminated via microwave plasma. This acid cleaning process is particularly important after polishing, to remove graphitic contaminants and other matter used in the polishing process. After cleaning, samples were inspected optically and by AFM.

To illustrate the variation seen in surface conductivity between samples in this work after hydrogen termination, an overview of Hall measurements for 13 H-terminated CVD diamond samples doped by air exposure are shown in Table 6.2.

Sample	Polish source	Termination source	Sheet resistance Ω/□	Carrier concentration /cm²	Mobility cm²/Vs
A	E6	Paris	8700	1×10^{13}	69
B	E6	Paris	71750	1.2×10^{12}	71
C	E6	Paris	39490	1.8×10^{12}	86
D	E6	Paris	58270	2.7×10^{12}	40
E	SP	Paris	16030	1.0×10^{13}	39
F	DPS	Cardiff	17320	1.3×10^{13}	28
G	DPS	Cardiff	15750	1.1×10^{13}	38
H	DPS	Cardiff	14990	1.1×10^{13}	38
I	DPS	Cardiff	25180	5.8×10^{12}	43
J	DPS	Cardiff	19340	6.3×10^{12}	51
K	DPS	Cardiff	22920	1.4×10^{13}	26
L	DPS	Cardiff	15980	1.2×10^{12}	32
M	DPS	Cardiff	12840	2.6×10^{12}	18

Table 6.2 - Compiled Hall measurements of 13 single crystal hydrogen terminated diamond samples exposed to air.

Each sample was prepared at different intervals over the duration of the author's PhD and vary in source of polishing, hydrogen termination and growth. All single crystal CVD diamond substrates listed were supplied by Element Six (E6). Samples A - D were scaife polished by E6 and sample E by Stone Perfect (SP), which were subsequently hydrogen terminated at the University of Paris 13. Samples F - M were polished by Diamond Product Solutions (DPS) and H-terminated at the University of Cardiff. All polished samples - despite polishing source- showed variable mobility coupled with widely varied carrier concentration. No clear relationship between surface roughness and mobility/carriers after polishing was observed. However, samples with the smoothest surfaces polished by DPS (~ 0.4 nm Ra) tended to exhibit the lowest mobility. Variation in carrier concentration will be impacted by hydrogen coverage of the surface and the composition of atmospheric adsorbates, in accordance with the surface transfer doping model discussed in Chapter 2. The presence and concentration of surface defects, introduced during growth and polishing, are possible factors in poor surface conductivity. The majority of electrical

measurements for surface transfer doped H-diamond shown in this chapter vary substantially between samples likely due to inconsistent hydrogen termination and or other variation in surface quality between samples. In Chapter 7, the conditioning of the diamond surface is explored and some preliminary results show varied parameters during the hydrogen termination process can yield large improvements in surface conductivity and surface roughness. This work to improve the hydrogen termination and surface conditioning was performed somewhat in parallel to and after the surface acceptor work done in this chapter. As such, all samples in this chapter were polished and hydrogen terminated as described in section 6.1.

6.2 Surface Transfer Doping

6.2.1 Air

Air exposure has traditionally been used as a surface acceptor medium for hydrogen terminated diamond [6.7], as explored in Chapter 3. Generally, all hydrogen terminated diamond samples in this work are first characterised with air exposure. This not only provides a starting point for subsequent measurements during experimentation but also gives an indication of hydrogen termination and or substrate quality. However, it should be noted there was no control over the composition of atmospheric species on the sample surface, relying on spontaneous adsorption when exposed to air. Therefore, variation in air doping between samples is likely without a more systematic study to control environmental conditions. To observe the general stability of air induced surface conductivity, a CVD diamond sample was polished and exposed to air after hydrogen termination, details of which can be found in Table 6.3.

VENDOR	ORENTATION	POLISH SOURCE	TERMINATION SOURCE	SIZE
E6	[100]	DPS	Paris	3 mm^2

Table 6.3 – Details of a CVD diamond sample used for air induced surface transfer doping experiments.

This sample was characterised using a Nanometric Hall measurement system (detailed in Chapter 4) over a period of 17 days as shown in Figure 6.2. To minimise disruption of the surface adsorbates, a VDP structure was formed by applying silver to the sample corners, a

method discussed in Chapter 5. Over time the hole carrier concentration can be seen to fluctuate around 1.1 $\times 10^{13}$ cm^{-2} with a deviation of approximately 5%. Sheet resistance shows a similar deviation of 4.6%. The sample was at all times stored in the same location within a class 10,000 clean room with a consistent room temperature in the range of 21.6-22.2^{o}C and typical humidity of 45% +/- 1% RH. While the source of this variation is unclear, it is likely attributed to instability in the composition of atmospheric species on the sample surface which are responsible for generating carriers within the diamond. Poor thermal stability of air doping is well documented [6.8], very little literature currently exists on the general stability of air doping over extended periods of time in a controlled environment.

To inspect the impact of elevated temperature on air-exposed H-diamond, Hall measurements were performed on two H-diamond samples doped by air exposure from room temperature to 300^{o}C (Figure 6.3). One sample was measured in ambient atmosphere, while the other was measured in a low vacuum of 60 mTorr. For the air-doped sample measured in ambient atmosphere, increasing temperature above 200^{o}C caused sheet resistance to increase above 1 $\times 10^{7}$ Ω/□ due to rapidly decreasing carrier concentration leading to the sample becoming unmeasurable. Hall measurements for the air-doped sample measured in a low vacuum showed significantly improved thermal stability compared to the one measured in atmosphere. However, a steady decrease in carrier concentration was still observed resulting in a sheet resistance increase of ~81%. Mobility for the sample measured in vacuum increases with increased temperature as carrier density decreases, however for the sample measured in ambient atmosphere the mobility decreases with increased temperature. Figure 6.4 shows sheet resistance for these two samples up to 300^{o}C with the cool down period returning the stage to room temperature and measurements taken 5 days after with the chamber vented. Repeat measurements performed after the atmosphere exposed sample was cooled back down to room temperature in air indicated the substrate permanently retained this unmeasurably high sheet resistance. A much ‘slower’ degradation in sheet resistance was observed with increased temperature for the sample measured in vacuum as attributed to the absence of air. Subsequently, this sample retained a decreased but measurable level of conductivity at 300^{o}C. The substrate was then cooled back down from 300^{o}C to room temperature in the same low-vacuum environment while measurements of sheet resistance were periodically taken during the cooling process. Little change in the sheet resistance was observed during this cool-down process.

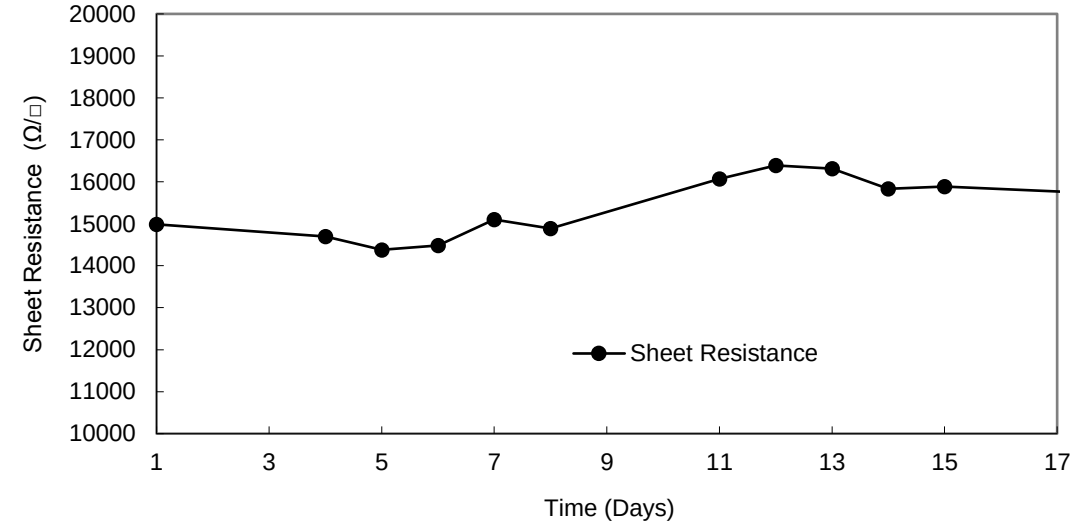

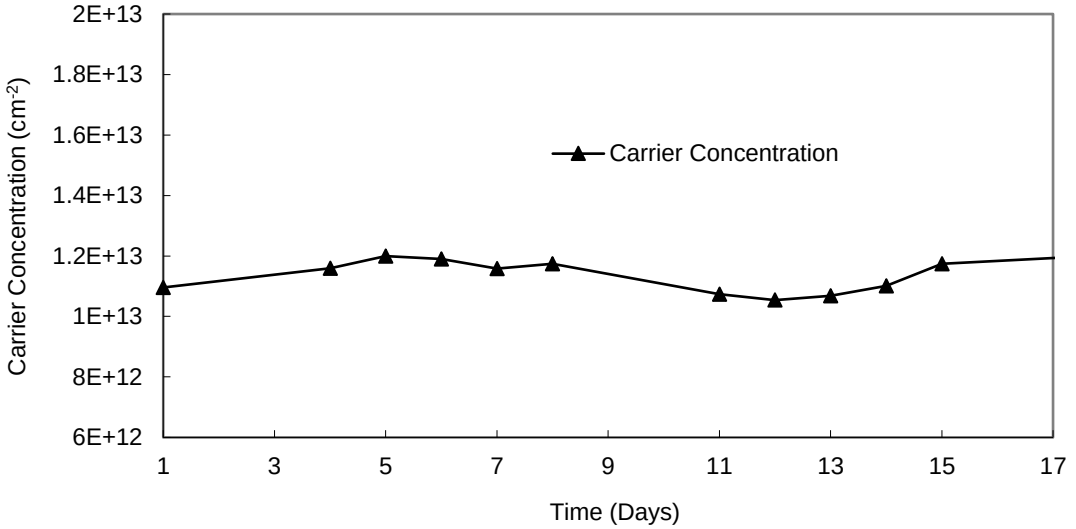

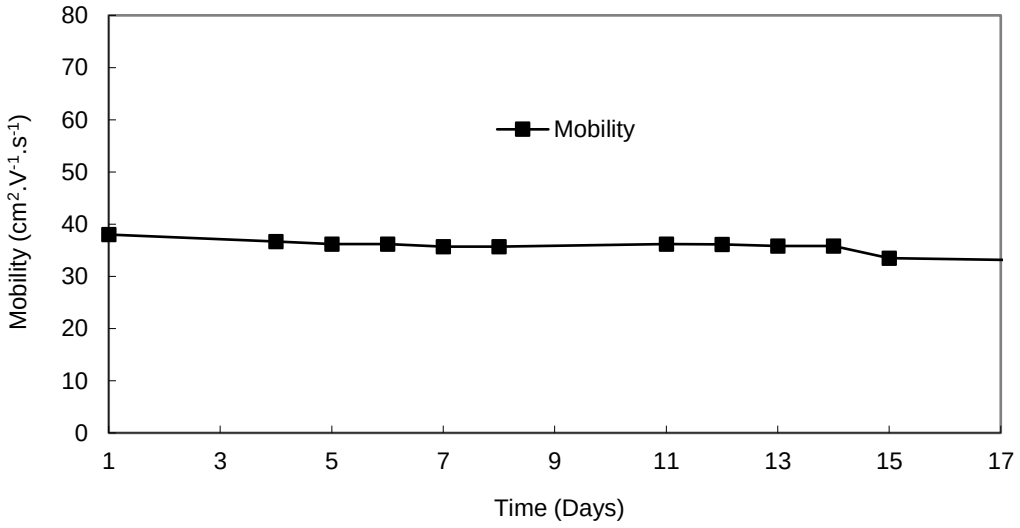

Figure 6.2 - Hall measurements over time for an air exposed H-diamond sample.

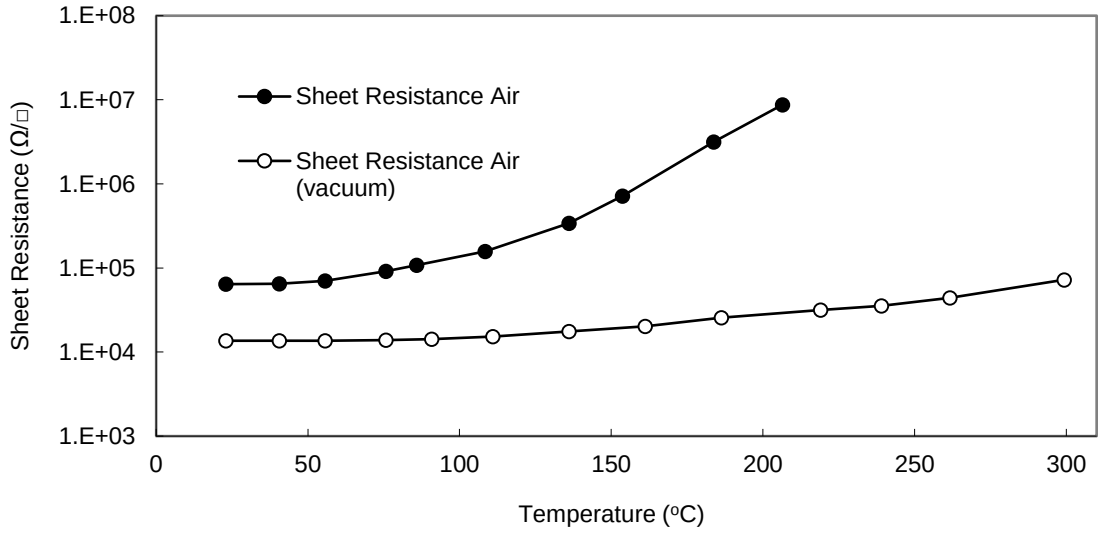

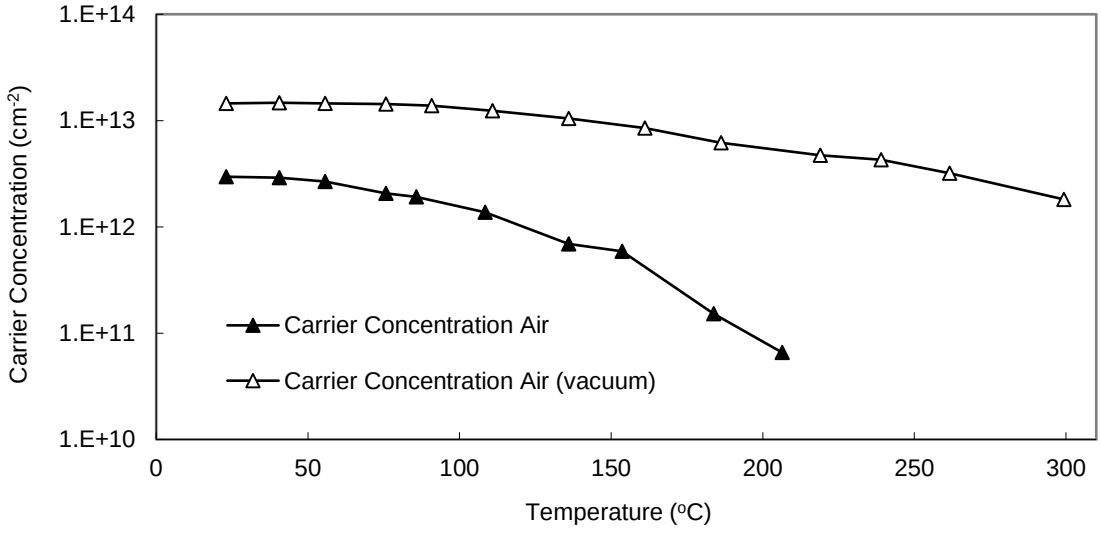

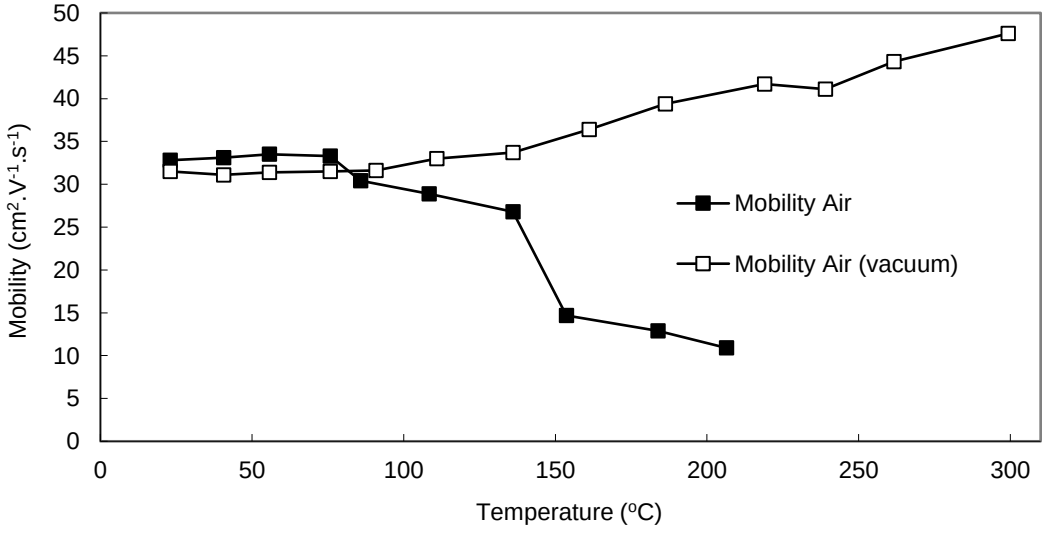

Figure 6.3 - High temperature Hall measurements up to 300°C for two air exposed H-diamond samples, one in ambient atmosphere and the other in vacuum.

The measurement system was then vented once the substrate had reached room temperature and the sheet resistance measured periodically for 5 days with the substrate exposed once again to ambient atmosphere. An immediate and notable reduction in sheet resistance (~50%) was observed following re-exposure to air. This decrease continued for ~ 21 hours following re-exposure of the sample to air before saturating for the remainder of the measurement period. Surface transfer doping in H-diamond using ambient air as a surface acceptor is well known to exhibit poor thermal stability. Previous work has demonstrated that annealing H-diamond in high vacuum at ~ 400^{o}C removes any conductivity that is attributed to previous exposure to air [6.8]. In this work, it was also found that the conductivity in the H-diamond returned after it was once again exposed to ambient air at room temperature. The recovery in conductivity observed following re-exposure to air indicated that the increase in sheet resistance observed at 400^{o}C under vacuum was attributed to desorption of atmospheric species from the H-diamond surface rather than removal of hydrogen. Experiments at higher temperatures in this work indicated that a temperature of at least 700^{o}C is required for desorption of the chemisorbed hydrogen in high vacuum. Conversely, H-diamond was found to begin to lose hydrogen from the surface when heated in ambient air at much lower temperatures closer to ~200^{o}C [6.8], due to oxidation of the surface. These findings agree well with the results shown here, whereby the degradation in conductivity observed at elevated temperatures is due to a combination of partial oxidation of the diamond surface as well as desorption of adsorbed atmospheric species. For the sample measured in ambient atmosphere, oxidisation of (and hence partial removal of hydrogen from) the diamond surface most likely resulted from heating of the substrate up to 300^{o}C in ambient air. Therefore, the conductivity did not recover when the substrate was re-exposed to ambient air. Conversely for the sample measured in vacuum, the degradation in conductivity observed up to 300^{o}C was substantially reduced in comparison and recovered substantially if not completely when re-exposed to ambient air. These results suggest that the surface hydrogen coverage remains mostly intact during heating in a low vacuum of 60 mTorr and the observed increase in sheet resistance was predominantly attributed to partial removal of surface acceptor species during heating.

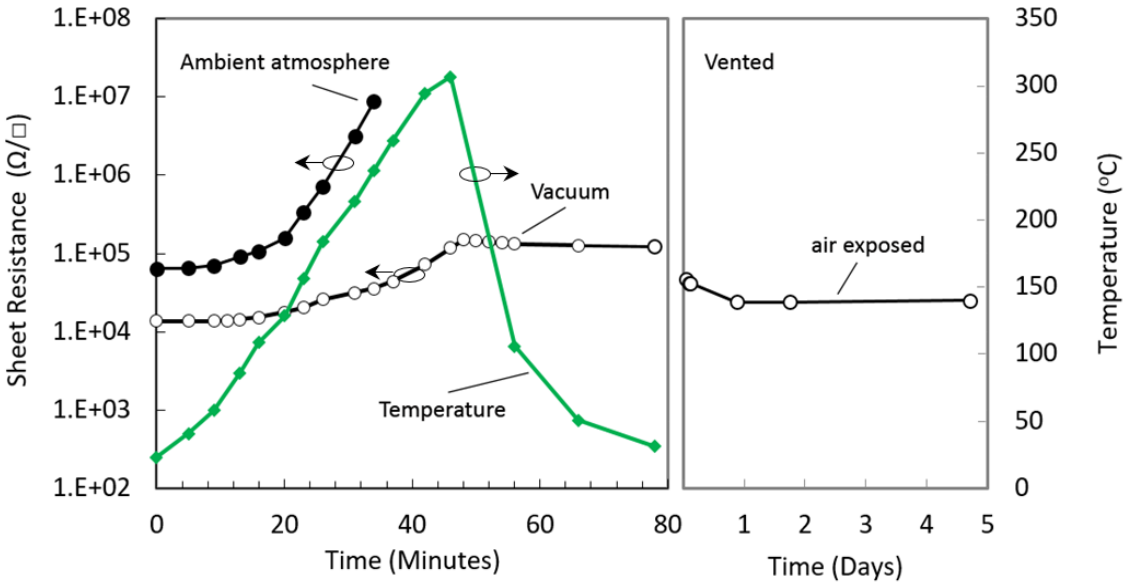

Figure 6.4 – High temperature sheet resistance measurements up to 300°C for two air exposed H-diamond samples, one in ambient atmosphere and the other in vacuum.

6.2.2 Molybdenum Trioxide as a Surface Acceptor

As discussed in Chapters 2 & 3, several high electron affinity transition metal oxides are expected to be capable surface electron acceptors on hydrogen terminated diamond. Owing to its electron affinity of ~6.9 eV, MoO_3 has a conduction band minimum more than 2.8 eV below the hydrogen-terminated diamond valence band maximum, making electron transfer from the diamond to MoO_3 energetically favourable [6.9]. To investigate the potential doping efficiency of MoO_3 on H-diamond, Hall measurement was performed on a van der Pauw test structure. To remove the possibility of electron beam exposure effecting the hydrogen termination, a simplified VDP formation utilising silver contacts was used as described in Chapter 5. Details of the substrate used can be found in Table 6.4.

VENDOR	ORENTATION	POLISH SOURCE	TERMINATION SOURCE	SIZE
E6	100	DPS	Paris	3 mm^2

Table 6.4 – Details of a CVD diamond sample used for MoO_3 induced surface transfer doping experiments.

After VDP formation, 100 nm of MoO_3 was deposited onto the sample by thermal evaporation using the Plassys 400 evaporator described in Chapter 5. While 100 nm of

oxide is in theory likely thicker than necessary to induce surface transfer doping at the H-diamond interface, this thickness was initially chosen to mitigate possible external environmental effects on the oxide film. Table 6.5 below shows results both before and after MoO_3 deposition.

	Sheet Resistance kΩ/□	Mobility cm^2/Vs	Sheet Carrier Concentration $/cm^2$
Before MoO_3 Deposition	17	28	1.3×10^{13}
After MoO_3 Deposition	6	17	6.6×10^{13}

Table 6.5 - Van der Pauw measurements prior to and post MoO_3 deposition.

The results show a carrier concentration increase of roughly 400% compared to atmosphere induced surface transfer doping, when using MoO_3. Subsequently, sheet resistance was reduced by ~67% and mobility fell ~40%, following a commonly reported relationship between carrier density and mobility in surface transfer doped diamond [6.10]. The sample was repeatedly measured for 17 days post MoO_3 deposition and showed gradual degradation to the improvements seen, shown in Figure 6.5.

The origin of the degradation observed with time for MoO_3 encapsulated H-diamond may likely be attributed to sensitivity of the oxide layer to atmosphere; MoO_3 has been shown to be highly sensitive to air exposure resulting in a decrease of Work Function (WF) due to partial reduction at the oxide surface [6.11]. This decrease in WF is consistent with a reduction in carriers based upon reduced band bending at the diamond:oxide interface. Arun Kuruvila *et al* performed a similar study whereby surface transfer doping of graphene using 5 nm thick layers of V_2O_5 and MoO_3 were inspected for the fabrication of light emitting diodes [6.12]. Their findings also show similar degradation in surface transfer doping of MoO_3 and V_2O_5 after exposure to air and note a greater stability of V_2O_5 compared to MoO_3. Their work showed prolonged air exposure of MoO_3 can lead to a reduced WF of 5.1 eV, a significant reduction from 6.9 eV. Therefore, the degradation in surface transfer doping by MoO_3 over time seen here is believed to be at least partly attributed to exposure to atmosphere.

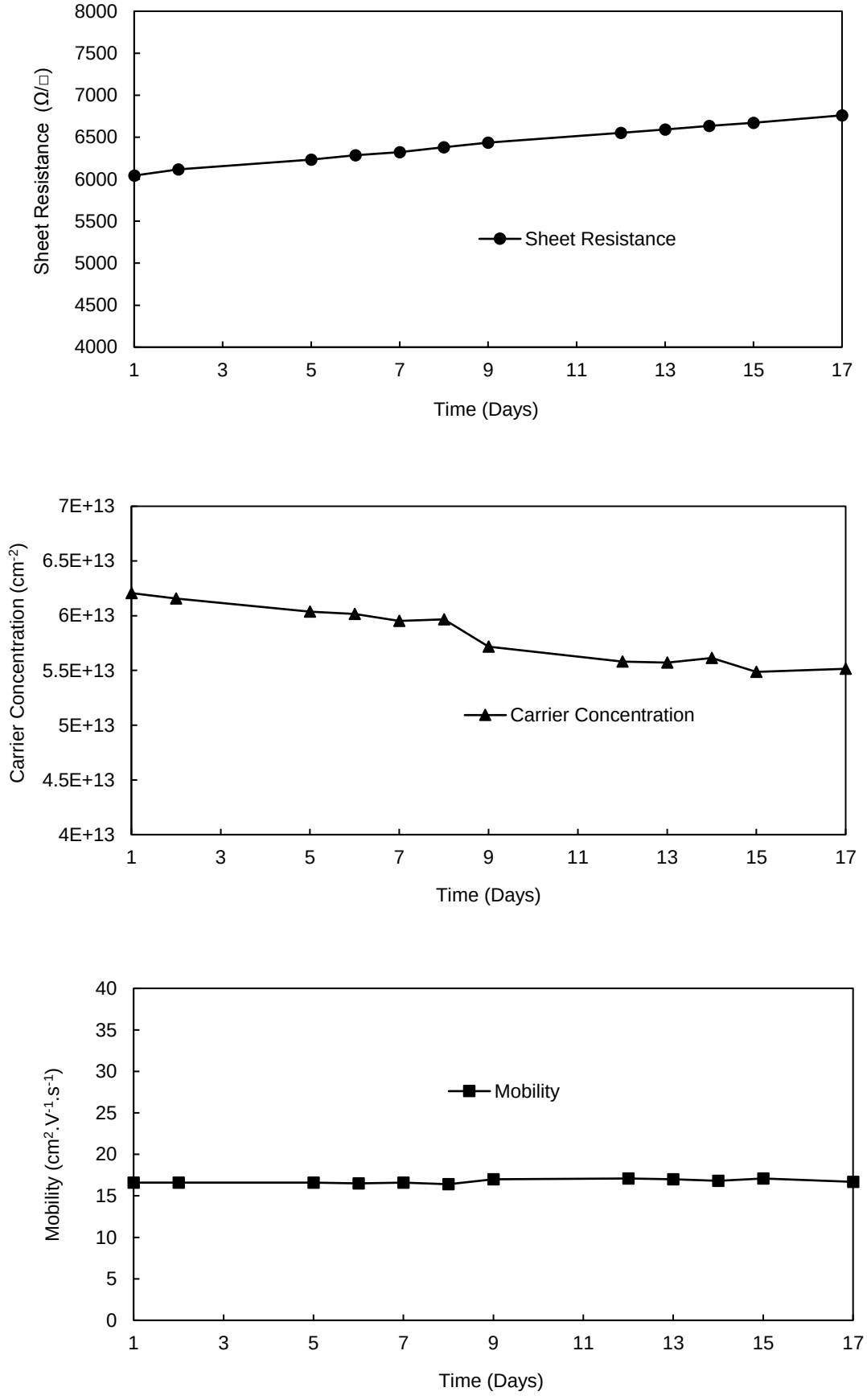

Figure 6.5 - Hall measurements taken over 17 days for a MoO_3 encapsulated H-diamond sample.

However, atmospheric adsorbents on the diamond surface prior to encapsulation could also be related to this effect prompting the need for their removal *in-situ* before deposition. Interestingly, Hall mobility remained largely stable for the MoO_3 doped sample over the 17-day period despite the degradation seen in carrier concentration.

MoO_3 deposition on H-diamond was repeated with a 200°C *in-situ* anneal prior to deposition, to observe the potential effects on doping stability after annealing the diamond surface prior to oxide deposition. Details of the sample used are shown in Table 6.6.

VENDOR	ORENTATION	POLISH SOURCE	TERMINATION SOURCE	SIZE
E6	100	E6	Paris	4.7 mm^2

Table 6.6 – Details of a CVD diamond sample used for MoO_3 induced surface transfer doping with a 200°C *in-situ* anneal.

VDP formation was performed using electron beam lithography with 80 nm thick gold contacts, as described in Chapter 5. The anneal of 200°C *in-situ* was performed in Plassys 400 immediately prior to deposition, maintaining a stage temperature of 200°C for one hour. The sample was returned to near room temperature (~27°C) in vacuum before deposition commenced. Notably, the anneal of 200°C resulted in no visible damage to the gold contacts. Additionally, Chapter 8 contains preliminary results showing improved contact resistance after annealing. Table 6.7 shows results both before and after MoO_3 deposition.

200°C anneal	Sheet Resistance kΩ/□	Mobility cm^2/Vs	Sheet Carrier Concentration $/cm^2$
Before MoO_3 Deposition	71	70	1.2×10^{12}
After MoO_3 Deposition	14	43	1×10^{13}

Table 6.7 - Van der Pauw measurements prior to and post MoO_3 deposition with a 200°C *in-situ* anneal of the diamond surface prior to deposition.

Here the starting values for surface conductivity exhibited a substantial difference in air induced surface transfer doped carrier concentration and mobility when compared to the previous sample. While unclear why, this difference may be attributed to inconsistent

hydrogen termination, the composition of atmospheric species on the surface or processing variation between samples. After MoO_3 deposition with a 200°C *in-situ* anneal, sheet resistance was reduced from 71 to 14 kΩ/□ with a carrier density increase from 1.2 $\times 10^{12}$ to 1 $\times 10^{13}$ cm^{-2}. Due to the already low starting value of carrier concentration an increase of roughly 760% after MoO_3 deposition was observed, however the after value of 1 $\times 10^{13}$ cm^{-2} induced by MoO_3 is relatively close to typical values seen for air exposed H-diamond surfaces. Degradation of carrier concentration was observed over the first 3 days while exposed to atmosphere at a rate similar to what was seen with the previous sample that received no anneal, indicating the 200°C anneal had little or no effect in reducing the degradation. Sixty-nine hours after deposition of MoO_3 and subsequent exposure to atmosphere, 50 nm of SiN was deposited to encapsulate the MoO_3 film via ICP CVD with the parameters: SiH_4/N_2 at a flow rate of 7.2/6 sccm, 100 W coil power and a pressure of 4.3 mTorr at room temperature. This approach was taken to determine if encapsulating the MoO_3 film from atmosphere would prevent further degradation. At ninety-five hours, the carrier concentration and sheet resistance stabilise at 5.5 $\times 10^{12}$ cm^{-2} and 25 kΩ/□ respectively with no further degradation observed, as plotted in Figure 6.6. Mobility increased slightly to 46 cm^2/Vs. A measurement directly after SiN deposition would have been ideal, however was not possible at the time due to laboratory access. It is therefore unknown if the measurement taken at 95 hours would have shown the same results if taken directly after SiN deposition. The apparent continued decline in carrier concentration prior to the 95-hour mark may be attributed to surface moisture being encapsulated by the SiN and thus absorbed between the time of SiN deposition and the sample stabilising. Also possible is the nature of the ICP CVD process when forming the SiN layer may have damaged the H-diamond:oxide interface somehow, reducing the systems doping capability. Structural stress may also have been introduced by the SiN film, though it's unclear what effect this would have on the MoO_3 induced charge transfer.

Another H-diamond sample was prepared to investigate MoO_3 deposition on H-diamond, increasing the anneal temperature to 300°C *in-situ*. Details of the sample used can be found in Table 6.8.

VENDOR	ORENTATION	POLISH SOURCE	TERMINATION SOURCE	SIZE
E6	100	E6	Paris	4.7 mm^2

Table 6.8 – Details of a CVD diamond sample used for MoO_3 induced surface transfer doping with a 300°C *in-situ* anneal.

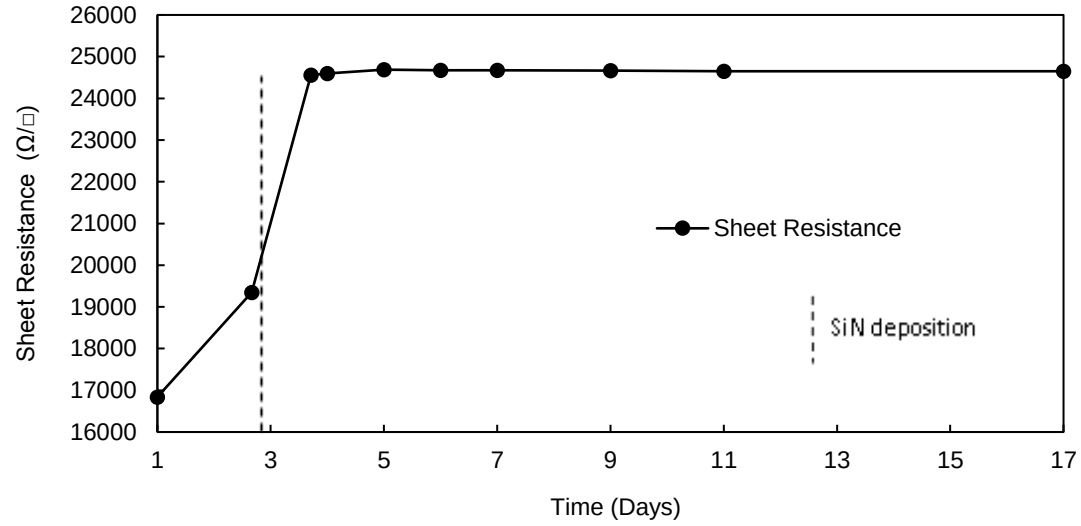

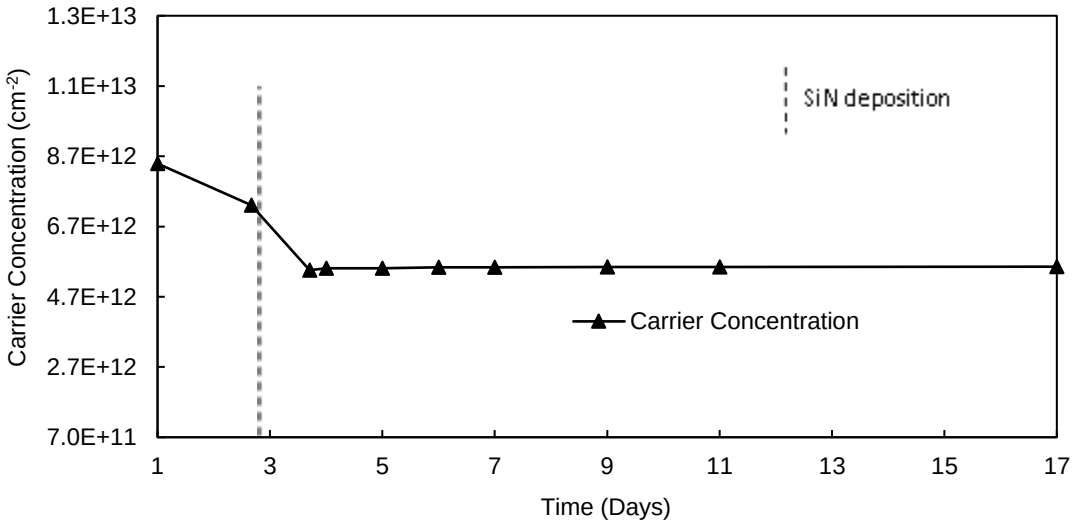

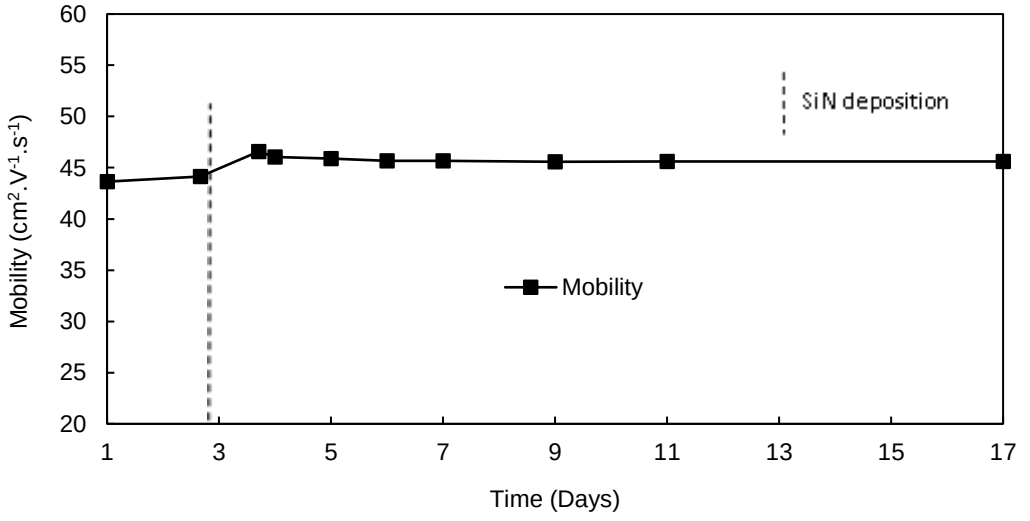

Figure 6.6 - Hall measurements taken over 17 days for a MoO_3 encapsulated H-diamond sample with a 200°C *in-situ* anneal of the diamond surface prior to deposition. At 69 hours, 50 nm SiN was deposited on top of the MoO_3 film.

A VDP structure was formed using silver contacts on the sample corners and the *in-situ* anneal increased to 300°C to evaluate the impact of higher anneal temperature on doping efficiency and stability. Results before and after MoO_3 deposition are shown in Table 6.9.

300°C anneal	Sheet Resistance kΩ/□	Mobility cm^2/Vs	Sheet Carrier Concentration $/cm^2$
Before MoO_3 Deposition	58	40	2.7×10^{12}
After MoO_3 Deposition	12	28	1.9×10^{13}

Table 6.9 - Van der Pauw measurements prior to and post MoO_3 deposition with a 300°C *in-situ* anneal of the diamond surface prior to deposition.

A low starting carrier concentration for air induced surface transfer doping resulted in a large increase of roughly 600% after MoO_3 deposition with an after value of 1.9×10^{13} cm^{-2}, close to the previously seen value of 1×10^{13} cm^{-2} induced by MoO_3. Hall measurements were taken over a 17-day period, as plotted in Figure 6.7. Stability was improved over time when compared to previous MoO_3 doping experiments. With a 300°C anneal prior to deposition, sheet resistance increased by 9% after 17 days, by comparison without annealing the sheet resistance increased by 12% over the same period and for the same film thickness. If the degradation seen is caused by atmospheric molecules on the diamond surface, then the higher *in-situ* anneal temperature may be the cause of this improved stability due to desorption of atmospheric species from the diamond surface prior to MoO_3 deposition [6.8].

The anneal temperature *in-situ* prior to MoO_3 deposition was then increased to 400°C for another H-diamond substrate. Details of the sample used are shown in table 6.10.

VENDOR	ORENTATION	POLISH SOURCE	TERMINATION SOURCE	SIZE
E6	100	E6	Paris	4.7 mm^2

Table 6.10 – Details of a CVD diamond sample used for MoO_3 induced surface transfer doping with a 400°C *in-situ* anneal.

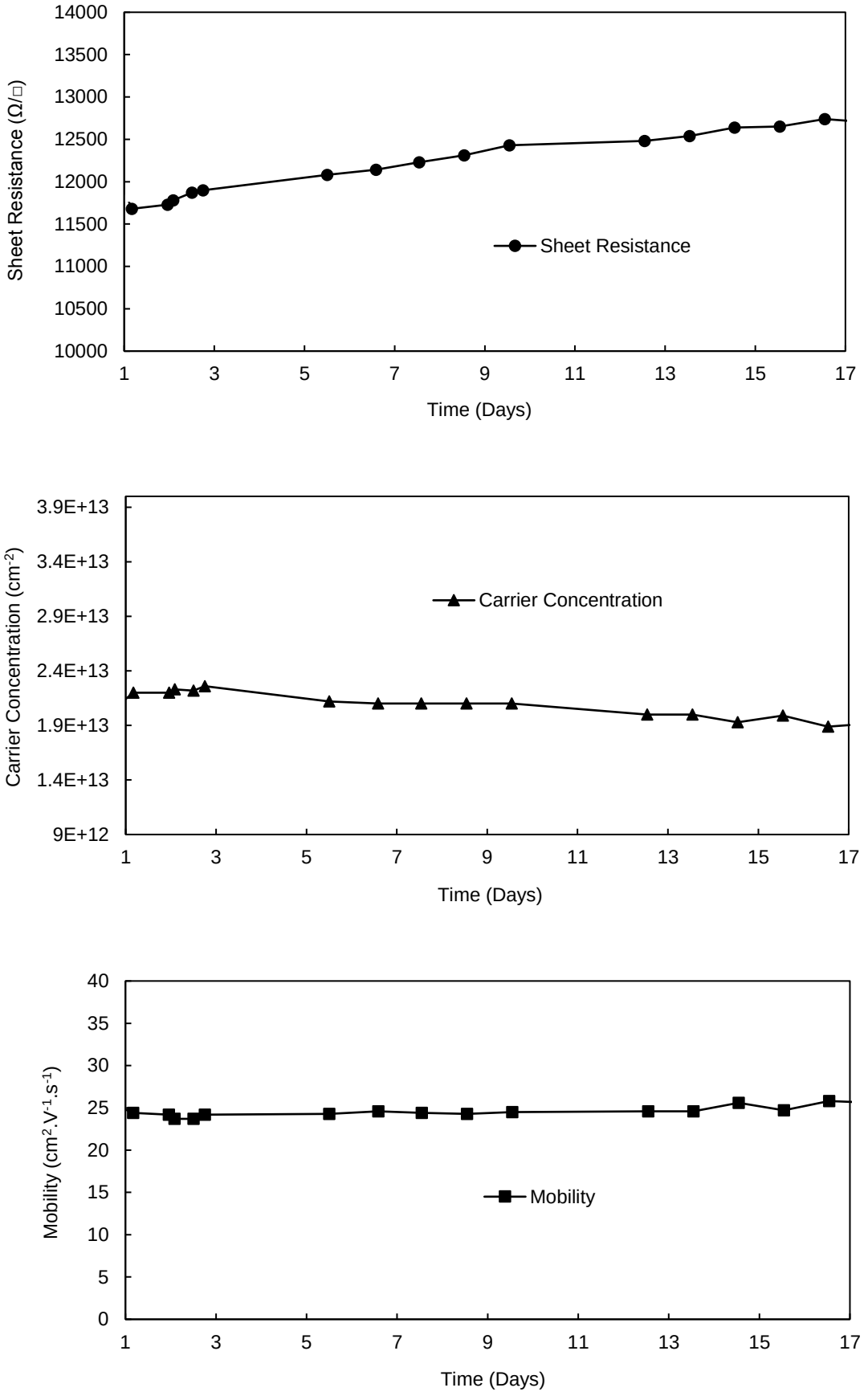

Figure 6.7 - Hall measurements taken over 17 days for a MoO_3 encapsulated H-diamond sample with a 300°C *in-situ* anneal of the diamond surface prior to deposition.

The VDP test structure was formed using silver contacts on the sample corners. Notably, silver appears to be robust at 400°C showing no visible damage or large increase in resistance while probing, as indicated during Hall measurements. Likewise, 400°C in vacuum should according to the previous high temperature Hall measurements for air doped H-diamond (and per the literature) be sufficient to fully desorb any atmospheric species from the diamond surface in vacuum without disrupting the hydrogen termination [6.8]. Results before and after MoO_3 deposition are shown in Table 6.11.

400°C anneal	Sheet Resistance kΩ/□	Mobility cm^2/Vs	Sheet Carrier Concentration $/cm^2$
Before MoO_3 Deposition	16	39	1×10^{13}
After MoO_3 Deposition	7	36	3×10^{13}

Table 6.11 - Van der Pauw measurements prior to and post MoO_3 deposition with a 400°C *in-situ* anneal of the diamond surface prior to deposition.

After MoO_3 deposition, carrier concentration was seen to increase from 1×10^{13} to 2.5×10^{13} cm^{-2}. Mobility decreased from 39 to 36 and as such sheet resistance fell from 16 to 7 kΩ/□. Continued Hall measurements over a period of 17 days are plotted in Figure 6.8. These results show a significant improvement in the stability of the surface transfer doping diamond:oxide system resulting from the use of a 400°C *in-situ* anneal prior to oxide deposition. The resultant doping is also substantially more stable with time than that observed for air-exposed H-diamond without MoO_3 encapsulation. These results suggest that degradation in the transfer doping mechanism seen previously is predominatly related to encapuslation of residual adsorbed material under the oxide layers rather than exposure of their outer surface to atmosphere. However, given the reported atmospheric sensitivity of these oxide films, their encapsulation (with, for example, inert dielectric layers) may be essential to ensure longer term stability, particularly for films thinner than 100 nm.

To evaluate the thermal stability of MoO_3 encapsulation compared to air-exposed H-diamond, Hall measurements were performed on the same sample shown in Figure 6.8, increasing the stage temperature in steps from 23-300°C. This is plotted in Figure 6.9.

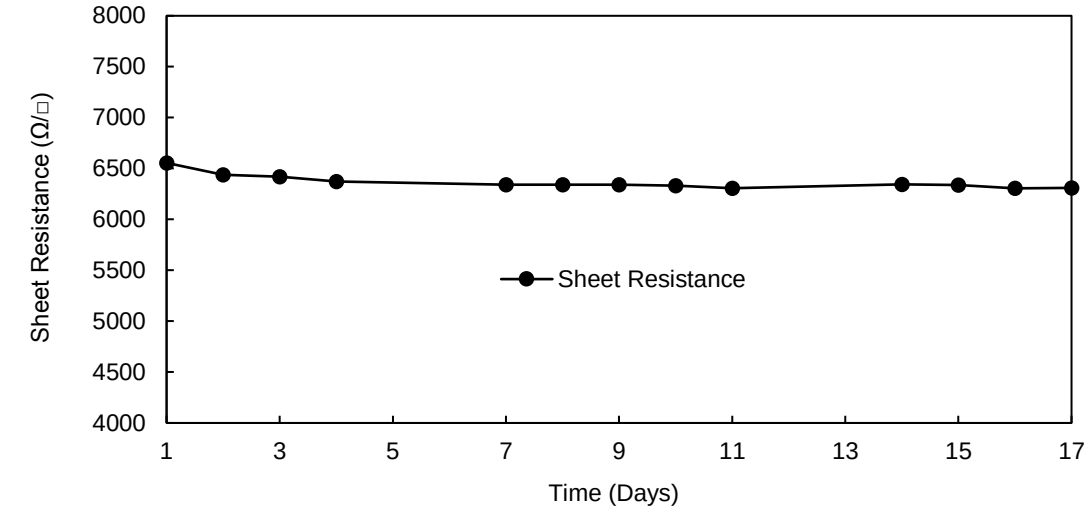

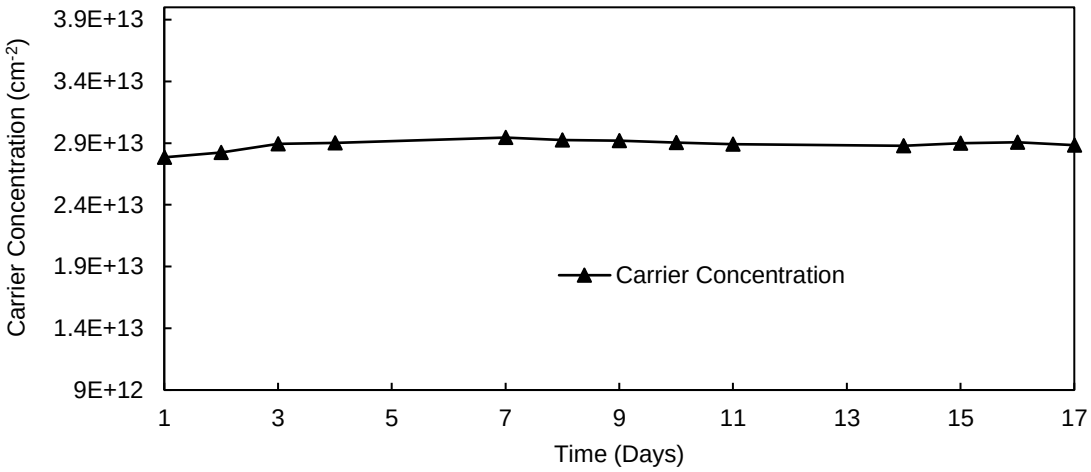

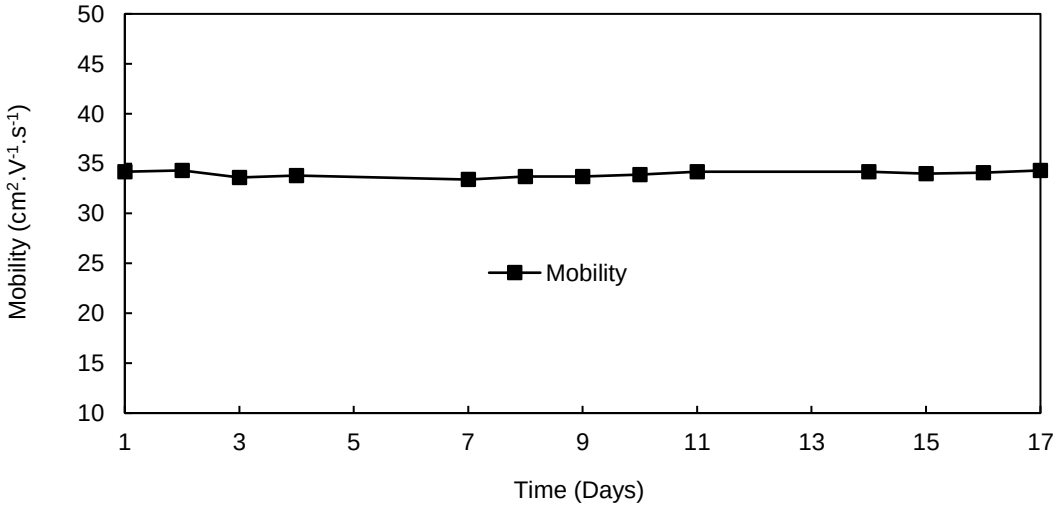

Figure 6.8 - Hall measurements taken over 17 days for a MoO_3 encapsulated H-diamond sample with a 400°C *in-situ* anneal of the diamond surface prior to deposition.

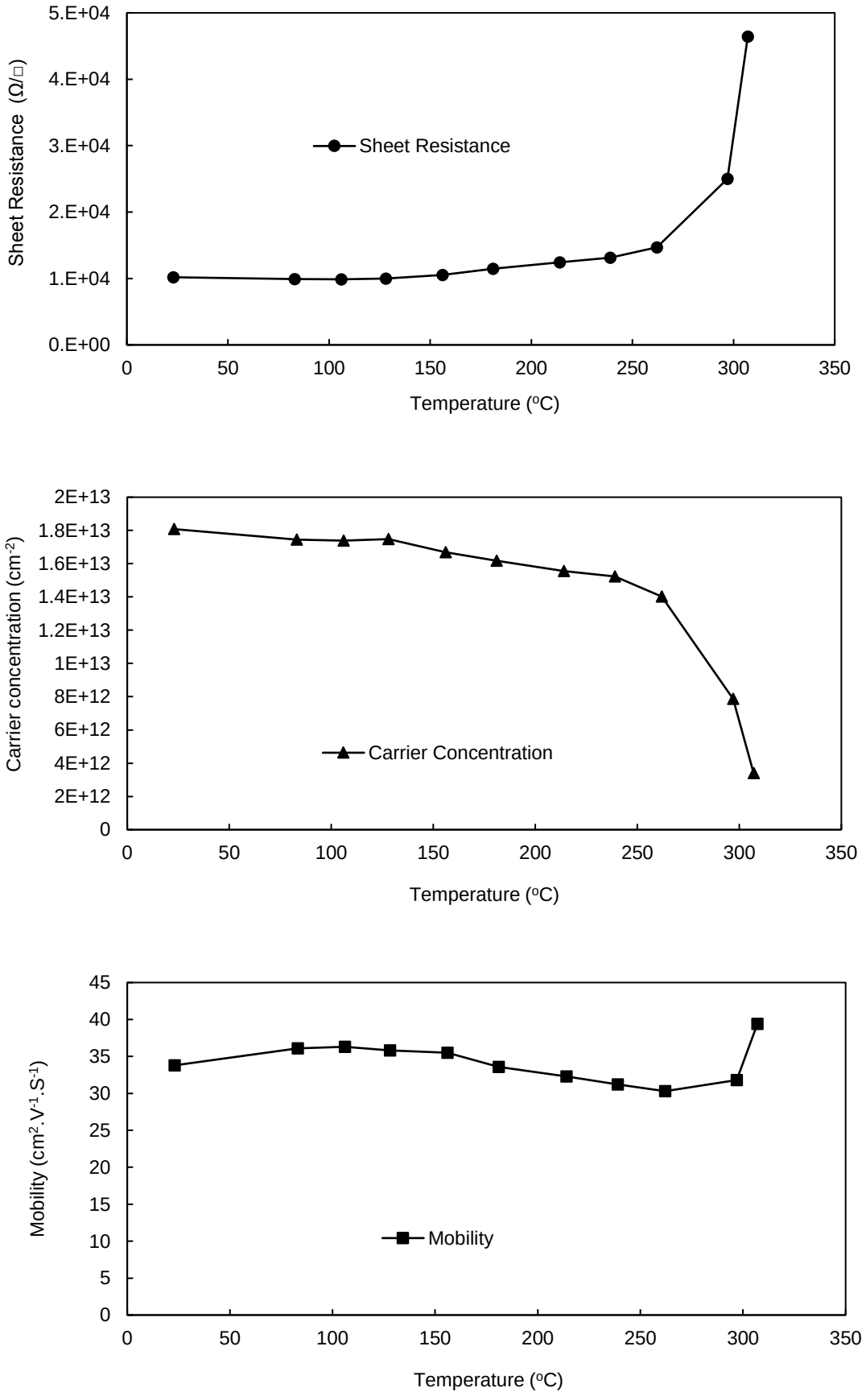

Figure 6.9 – High temperature Hall measurements in ambient atmosphere up to 300°C for a MoO_3 encapsulated H-diamond sample with a 400°C *in-situ* anneal of the diamond surface prior to deposition.

The results show doping efficiency of MoO_3 decreases with elevated temperatures in ambient atmosphere, upwards of 150-200^oC. Higher than 200^oC sheet resistance begins to rise sharply and the degradation remained after cooling back down to room temperature. Hall measurements following the same temperature profile were repeated for another H-diamond sample coated with 100 nm MoO_3 with 400^oC *in-situ* annealing prior to deposition. This sample however was measured in a vacuum of 60 mTorr as opposed to ambient air. Following this, the sample was then coated with ~600 nm hydrogen silsesquioxane (HSQ) to encapsulate the MoO_3 film and measured again up to 300^oC in ambient atmosphere. Details of this sample can be found in Table 6.12.

VENDOR	ORENTATION	POLISH SOURCE	TERMINATION SOURCE	SIZE
E6	100	DPS	Paris	3 mm^2

Table 6.12 – Details of CVD diamond sample used for MoO_3 induced surface transfer doping with a 400^oC *in-situ* anneal at variable temperatures vacuum and in air.

In contrast to the MoO_3 encapsulated sample measured in ambient atmosphere (Figure 6.9), high temperature measurements in vacuum showed significantly improved stability with relatively small degradation seen in sheet resistance (Figure 6.10). This observed stability despite falling carrier density is due to increasing mobility, maintaining a mostly steady sheet resistance up to 300^oC. After cooling down to room temperature and venting the chamber, HSQ was used to encapsulate the MoO_3 film. The HSQ layer was spun at a speed of 2000 rpm and baked on a hot plate for 2 minutes at 80^oC resulting in a ~600 nm thick layer. Hall measurements taken before and after applying the HSQ showed no change in conductivity of the H-diamond surface. With MoO_3:HSQ encapsulation, the sample was measured from room temperature up to 300^oC in ambient atmosphere to compare with previous measurements in vacuum and atmosphere without encapsulation of the MoO_3 film. Isolating the MoO_3 from atmosphere with HSQ showed significant improvement in stability at temperatures up to 300^oC (Figure 6.10), however greater degradation occurred compared to measurements in vacuum. Figure 6.11 shows sheet resistance measurements for MoO_3 in ambient atmosphere, vacuum and with HSQ encapsulation in ambient atmosphere including the cool down period in which the stage is returned to room temperature.

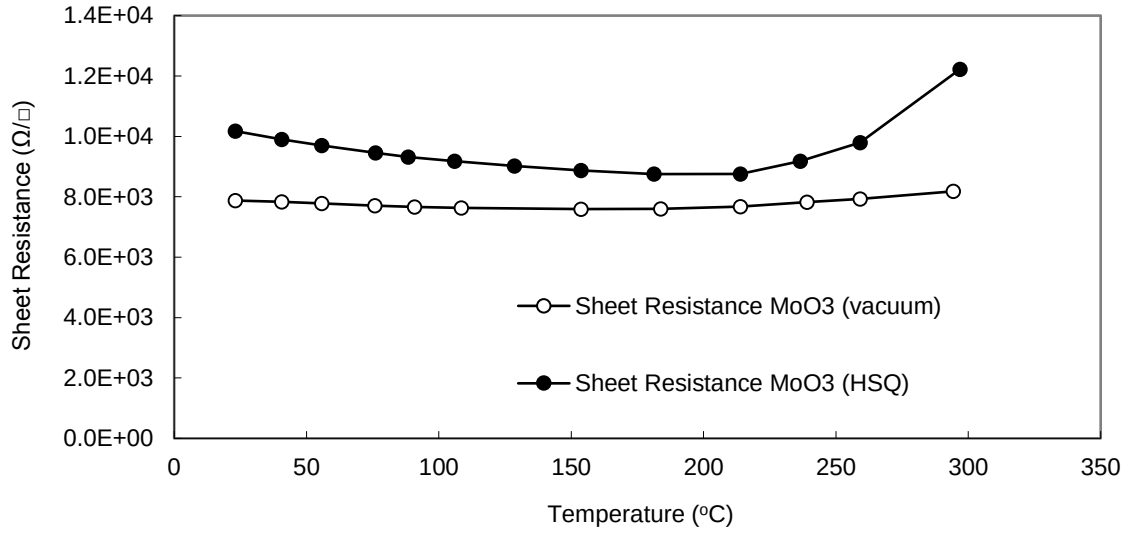

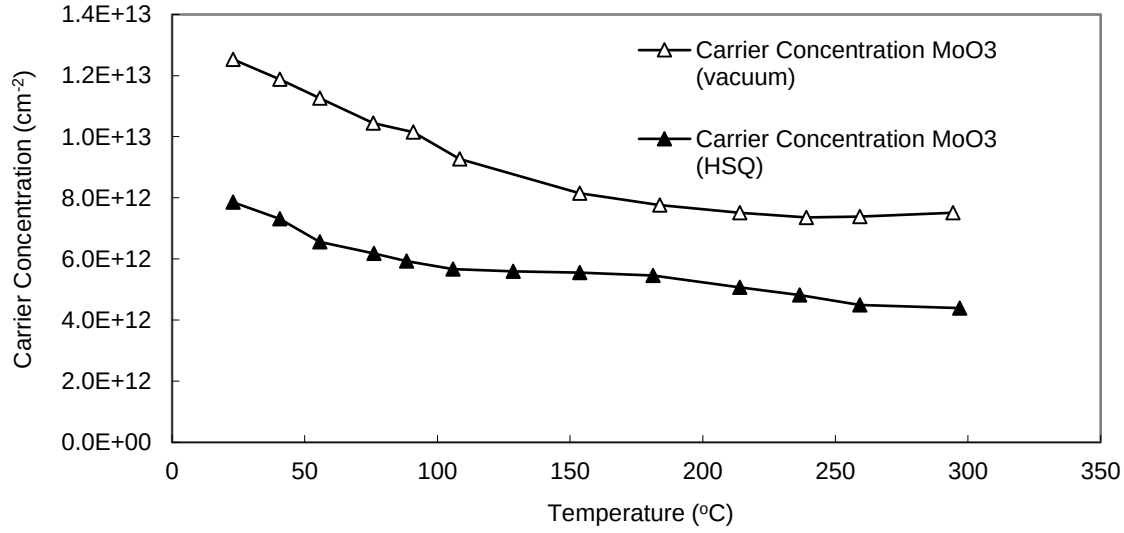

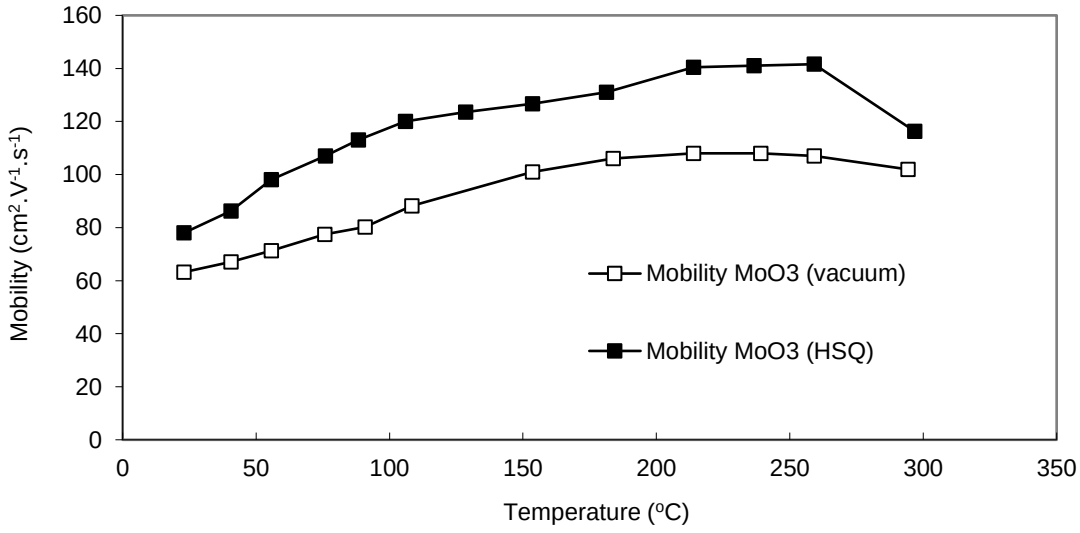

Figure 6.10 – High temperature Hall measurements in vacuum up to 300°C for a MoO_3 encapsulated H-diamond sample with a 400°C *in-situ* anneal of the diamond surface prior to deposition.

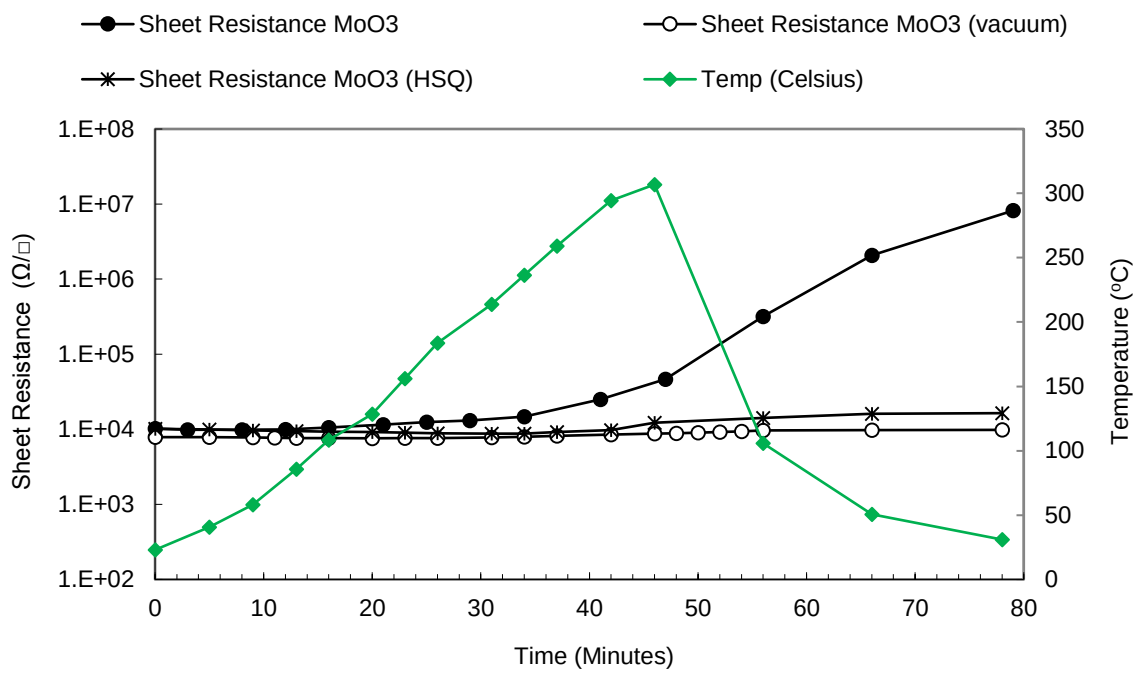

Figure 6.11 – Sheet resistance measurements up to 400°C with cool-down period for MoO_3 surface transfer doped samples and an air induced surface conductivity sample.

After returning the measurement system to room temperature, the air exposed MoO_3 sample did not recover any of its lost surface conductivity, indicating a lasting change to the diamond:oxide surface transfer doping system. While the diamond substrate is unlikely to be effected by an elevated temperature 300°C, the surface hydrogen termination and or oxide stoichiometry is possibly more sensitive. When heated in vacuum the surface conductivity induced by MoO_3 remains largely stable up to 300°C with only a slight increase in sheet resistance after cooling down. While the vacuum used here was relatively low due to limitations of the equipment, measurements in ultra-high vacuum may further prevent the observed drop in carrier density. Measurements for the 600 nm HSQ encapsulated MoO_3 doped sample measured in ambient air show degradation is still observed after cooling down, with sheet resistance roughly doubled, however the effect is vastly reduced compared to that of un-encapsulated air exposed MoO_3 measurements. While 600 nm HSQ may not be sufficient to prevent complete loss in conductivity, these results suggest a robust form of encapsulation would preserve the surface transfer doping mechanism induced by MoO_3 at high temperatures.

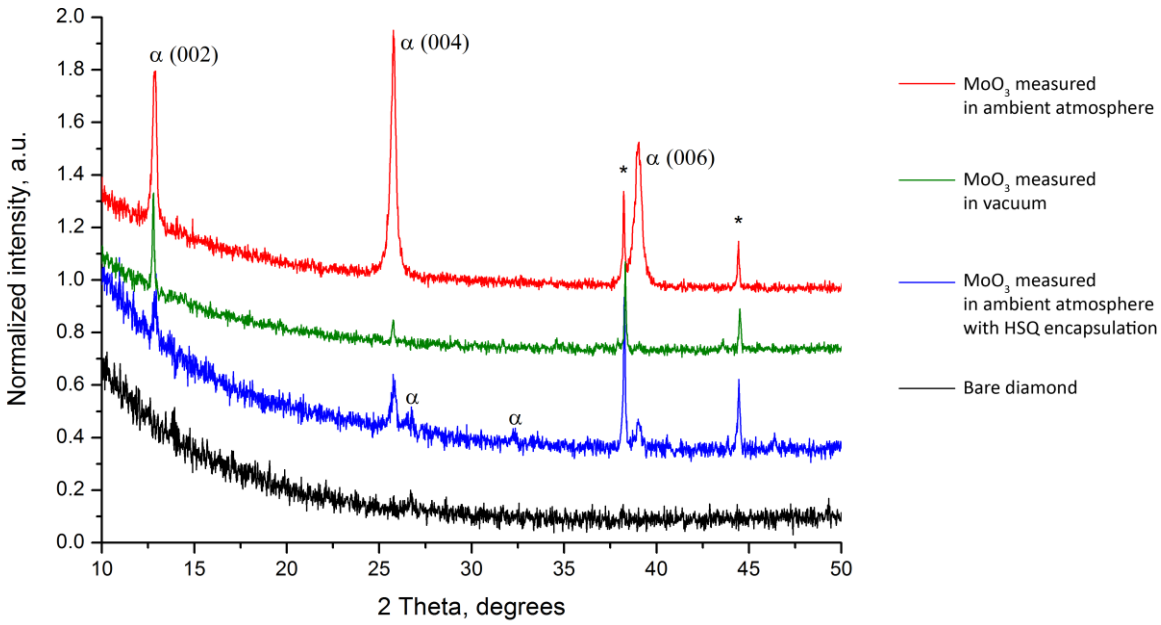

Figure 6.12 - X-ray diffraction patterns of MoO_3 films after Hall measurements. The reflections marked with asterisks originate from the silver contacts on the sample corners.

X-ray diffraction studies were carried out on the samples used in Figure 6.11 to identify any potential changes in the MoO_3 film structure associated with heating of the substrates up to 300°C in both ambient air and low vacuum. This was done in collaboration with Dr Alexey Ganin of the School of Chemistry at The University of Glasgow. All diffraction experiments were carried out *ex-situ* after the Hall measurements were completed. Figure 6.12 shows the normalised diffraction pattern for the MoO_3 coated H-diamond samples. As a base line comparison, diffraction measurement of a bare un-encapsulated diamond substrate is also plotted. The reflections marked with asterisks originate from the silver contacts and were used as internal standard for normalisation of the intensity of the evaluated samples. There was a significant difference in the intensity of MoO_3 peaks indicating that the crystallinity of the films changes depending on the conditions during high temperature measurements. For the sample measured in ambient atmosphere, only 00*l* reflections associated with an orthorhombic MoO_3 α-phase [6.13] were observed indicating that the MoO_3 film was highly oriented along *c*-axis of the film. Similarly, the diffraction pattern of the sample measured in low vacuum displayed only 00*l* reflections of α-phase suggesting a strongly oriented film. However, the intensity of the reflections is significantly lower than compared with the sample measured in ambient air, which is indicative of lower crystallinity. Protecting MoO_3 with HSQ still yields a crystalline film, although lacking strong preferred orientation as evident by additional reflections which are still attributed to the α-phase. These results suggest increased crystallinity of the MoO_3

film occurs independently of exposure to ambient atmosphere during high temperature measurements and is likely not related to loss in surface transfer doping for atmosphere exposed films.

So far all surface transfer doping experiments utilising MoO_3 as a surface electron acceptor have used 100 nm thick films. As mentioned previously, 100 nm was initally chosen to mitigate the effects of external enviormental factors and is likely significantly thicker than what should be necessary to achieve full charge transfer across the diamond:oxide interface [6.9]. To investigate the effects of using a thinner oxide, three nomically intentical H-diamond samples were prepared for Hall measurement with silver contacts, details of the samples in Table 6.13 below.

VENDOR	ORENTATION	POLISH SOURCE	TERMINATION SOURCE	SIZE
E6	100	DPS	Paris	3 mm^2

Table 6.13 – Details of three nominally identical diamond samples used for different film thicknesses of MoO_3 induced surface transfer doping with *in-situ* annealing prior to deposition.

MoO_3 was deposited on each sample with a 400^{o}C *in-situ* anneal prior to deposition, using the oxide thicknesses 10, 30 and 100 nm. Figure 6.13 shows Hall measurements over a period of 43 days with trend line for these three different thicknesses of MoO_3 on H-diamond. Carrier density for these samples was significantly higher than seen previously for MoO_3 doped H-diamond, due to an improved hydrogen termination process discussed in the next chapter. Sheet resistance measurements for 100 nm MoO_3 appear very stable over the measurement period, as is consistent with previous results showing the importance of a 400^{o}C anneal prior to deposition. However, 10 nm of oxide shows gradual degradation in carrier density and increased sheet resistance after 10 days, continuing over the same period despite the 400^{o}C *in-situ* anneal performed. Carrier density similarly degraded for the 30 nm film over time, however at a much slower rate. As discussed previously, MoO_3 has shown to be sensitive to air exposure, lowering the oxide work function. These results suggest films of MoO_3 when used to surface transfer dope H-diamond will degrade over time when exposed to air, with a delayed effect depending on thickness of the oxide film. As such, appropriate passivation of the MoO_3 film is neccesary, especially for use in actual devices such as a FET where thinner oxide is likely desirable to reduce seperation between the gate and sub-surface 2DHG, allowing for better control of the channel.

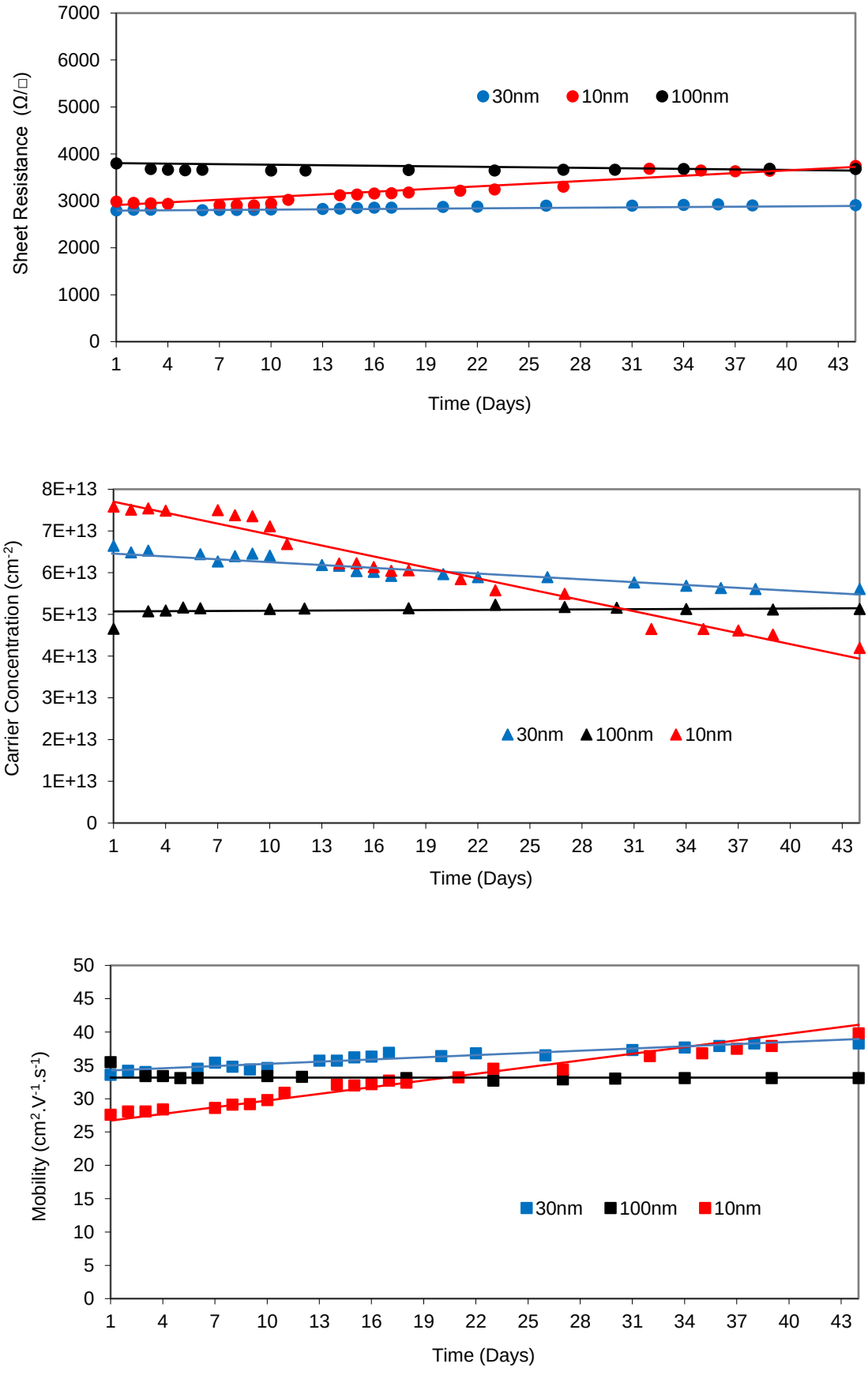

Figure 6.13 - Hall measurements taken over a period of 36 days for three different thicknesses of MoO_3 on H-diamond, 10, 30 and 100 nm. The diamond surface was annealed at 400°C *in-situ* prior to deposition of oxide.

6.2.3 Vanadium Pentoxide as a Surface Acceptor

Studies of MoO_3 as a surface acceptor on hydrogen terminated diamond first took place at The University of Glasgow, showing great success as shown in the previous section. In continuation of this work, other transition metal oxides were experimented with. V_2O_5 possesses an electron affinity of ~6.3 eV, theoretically high enough induce surface transfer doping in H-diamond as discussed in Chapter 2 [6.12, 6.14]. In replication of the original MoO_3 experiment, 100 nm V_2O_5 was thermally deposited onto a hydrogen terminated CVD diamond sample with no prior annealing of the diamond surface. Details of the sample used can be found in Table 6.14.

VENDOR	GRADE	ORENTATION	POLISH SOURCE	TERMINATION SOURCE	SIZE
E6	Optical	100	DPS	Cardiff	3 mm^2

Table 6.14 – Details of CVD diamond sample used for V_2O_5 induced surface transfer doping with no *in-situ* anneal prior to deposition.

Hall measurements were extracted via the simplified VDP method as described previously, employing silver contacts on the sample corners. Table 6.15 shows results both before and after V_2O_5 deposition with no annealing of the diamond surface.

No anneal	Sheet Resistance kΩ/□	Mobility cm^2/Vs	Sheet Carrier Concentration $/cm^2$
Before V_2O_5 Deposition	15.8	37.6	1.1×10^{13}
After V_2O_5 Deposition	5.2	22.1	5.5×10^{13}

Table 6.15 - Van der Pauw measurements prior to and post V_2O_5 deposition with no prior annealing of the diamond surface.

After deposition sheet resistance fell from 15.8 to 5.2 kΩ/□, as carrier density increased from 1.1×10^{13} to 5.5×10^{13} cm^{-2} and mobility decreased from 37.6 to 22.1 cm^2/Vs. The improvement seen here is very similar to that of MoO_3 without annealing, showing a small difference of ~400 Ω in comparison. Figure 6.14 shows Hall measurements over 17 days for the same V_2O_5 coated H-diamond sample.

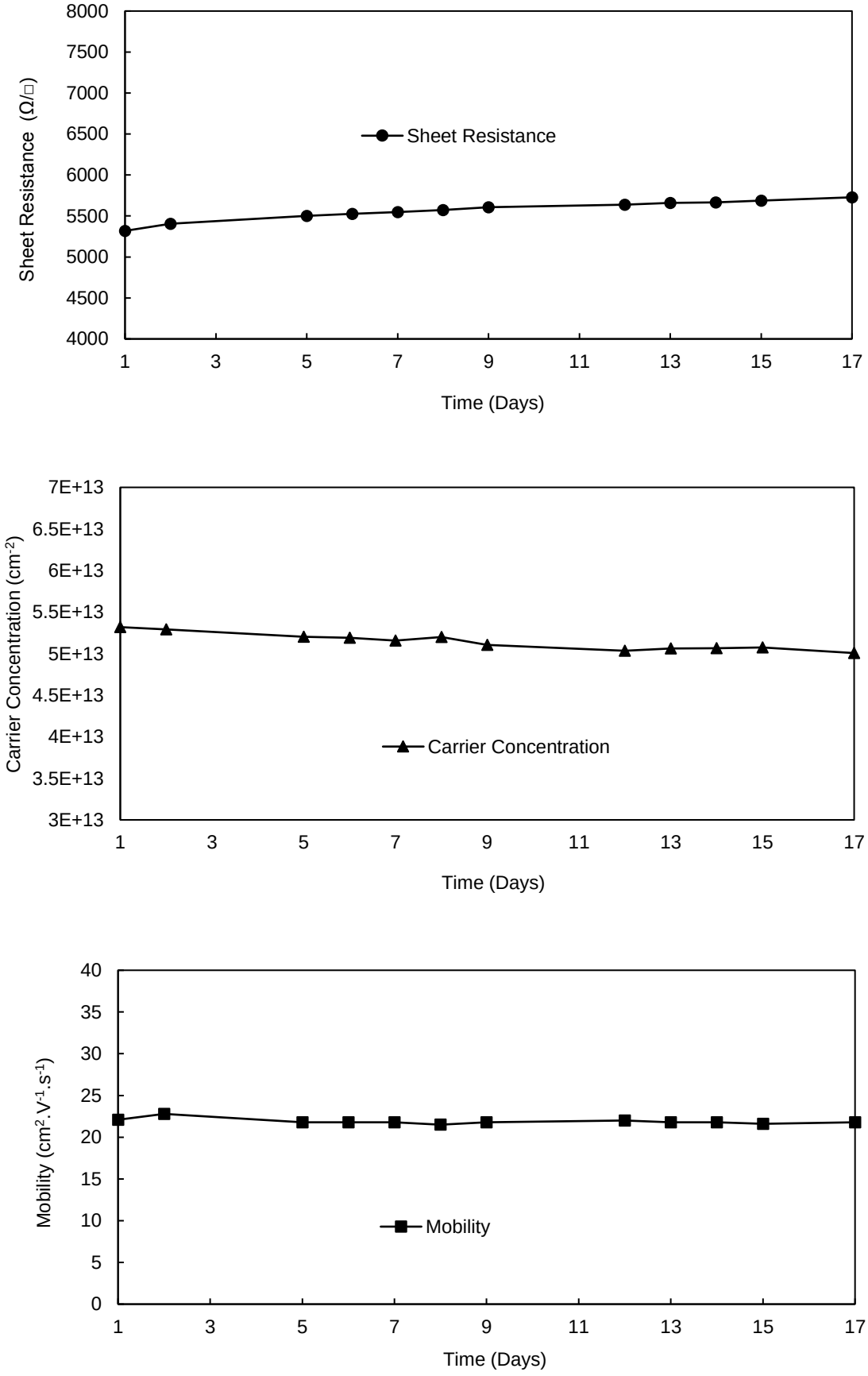

Figure 6.14 - Hall measurements taken over 17 days for a V_2O_5 encapsulated H-diamond sample with no prior annealing of the diamond surface.

Measurements over time show a gradually increasing sheet resistance, as carriers decrease and mobility remains largely unchanged. An accelerated rate of degradation was observed however for MoO_3 encapsulation in comparison with V_2O_5, without prior annealing of the diamond surface. Both MoO_3 and V_2O_5 have been shown to also induce transfer doping in thin film graphene structures [6.12], in which the doping efficiency and the stability in air of V_2O_5 outperformed that of MoO_3 [6.11, 6.12, 6.15]. This agrees with results seen here, suggesting V_2O_5 may provide a more robust transfer doping solution.

Depostion of 100 nm V_2O_5 on H-diamond was then performed with a 1 hour 400°C *in-situ* anneal of the diamond surface prior to deposition. Similar to the experiments performed using MoO_3, this was done to investigate the effect on stability of surface conductivity induced by V_2O_5 encapsulation. Sample details can be found in Table 6.16 below.

VENDOR	GRADE	ORENTATION	POLISH SOURCE	TERMINATION SOURCE	SIZE
E6	Optical	100	DPS	Cardiff	3 mm^2

Table 6.16 – Details of CVD diamond sample used for V_2O_5 induced surface transfer doping with *in-situ* annealing prior to deposition.

Hall measurements were extracted using the silver contact method as described previously, employing contacts on the sample corners. Table 6.17 shows results both before and after V_2O_5 deposition with annealing of the diamond surface prior to deposition.

400°C anneal	Sheet Resistance kΩ/□	Mobility cm^2/Vs	Sheet Carrier Concentration $/cm^2$
Before V_2O_5 Deposition	25.2	42.8	5.8×10^{12}
After V_2O_5 Deposition	7.9	18.3	4.3×10^{13}

Table 6.17 - Van der Pauw measurements prior to and post V_2O_5 deposition with surface annealing.

After V_2O_5 deposition, sheet resistance was reduced from 25 to 8 kΩ/□. Carrier density increased from 5.8×10^{12} to 4.3×10^{13} cm^{-2} and mobility decreased from 43 to 18 cm^2/Vs.

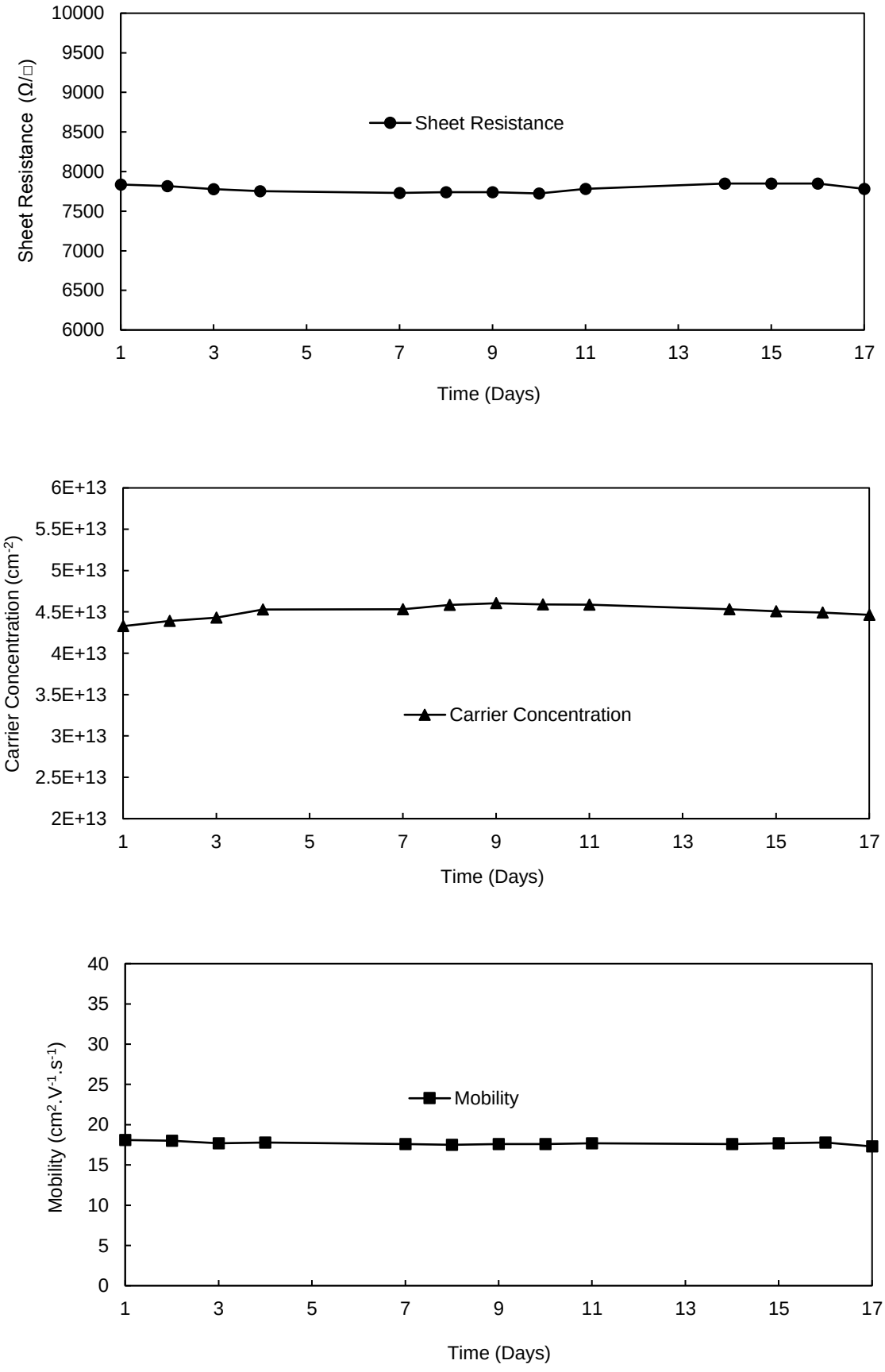

Figure 6.15 - Hall measurements taken over 17 days for a V_2O_5 encapsulated H-diamond sample with a 400°C *in-situ* anneal of the diamond surface prior to deposition.

Compared to the previous V_2O_5 result with no surface annealing, sheet resistance for this sample is 4 kΩ higher. However, the initial value in air of 25 kΩ/□ indicates the hydrogen termination of this sample may have been inferior. Figure 6.15 shows Hall measurements taken over a period of 17 days for this sample. Similar to the results for MoO_3, annealing the diamond surface substantially reduced degradation in carrier concentration over time for the V_2O_5 doped H-diamond. This sample with a 400°C pre-anneal and V_2O_5 encapsulation was then used for high temperature Hall measurements in ambient atmosphere after the initial 17-day measurement period, increasing the stage temperature in steps from 23-300°C and then back to room temperature shown in Figure 6.16.

The results show doping efficiency of V_2O_5 decreases with elevated temperatures in air, upwards of 150-200°C. Higher than 200°C sheet resistance begins to rise sharply and the degradation seen is lasting after cooling down to room temperature. Sheet resistance measurements following the same temperature profile were repeated for another H-diamond sample coated with 100 nm V_2O_5 with 400°C *in-situ* annealing prior to deposition. This sample was measured following the same temperature profile up to 300°C in a low vacuum of 60 mTorr after which it was coated with 600 nm HSQ to encapsulate the V_2O_5 film and measured again up to 300°C in ambient atmosphere. Details of this sample can be found in Table 6.18.

VENDOR	GRADE	ORENTATION	POLISH SOURCE	TERMINATION SOURCE	SIZE
E6	Optical	100	E6	Cardiff	3 mm^2

Table 6.18 – Details of CVD diamond sample used for V_2O_5 induced surface transfer doping high temperature measurements with *in-situ* annealing prior to deposition.

Figure 6.17 shows the measurements for V_2O_5 from room temperature up to 300°C in vacuum and encapsulated with HSQ. Similar to results seen for MoO_3 (Figure 6.10), measurements in vacuum showed significantly improved stability with relatively small degradation compared to V_2O_5 measured in ambient atmosphere. This observed stability despite falling carrier density is due to increasing mobility, maintaining a mostly steady sheet resistance up to 300°C. Following the same process as in Figure 6.10, HSQ was used to encapsulate the V_2O_5 film. The HSQ layer was spun at a speed of 2000 rpm and baked on a hot plate for 2 minutes at 80°C resulting in a ~600 nm thick layer.

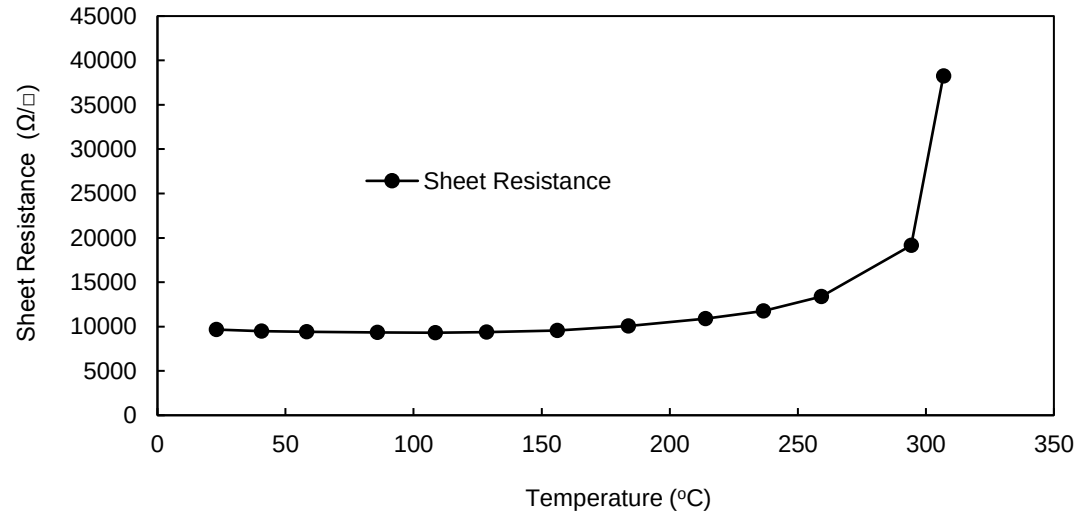

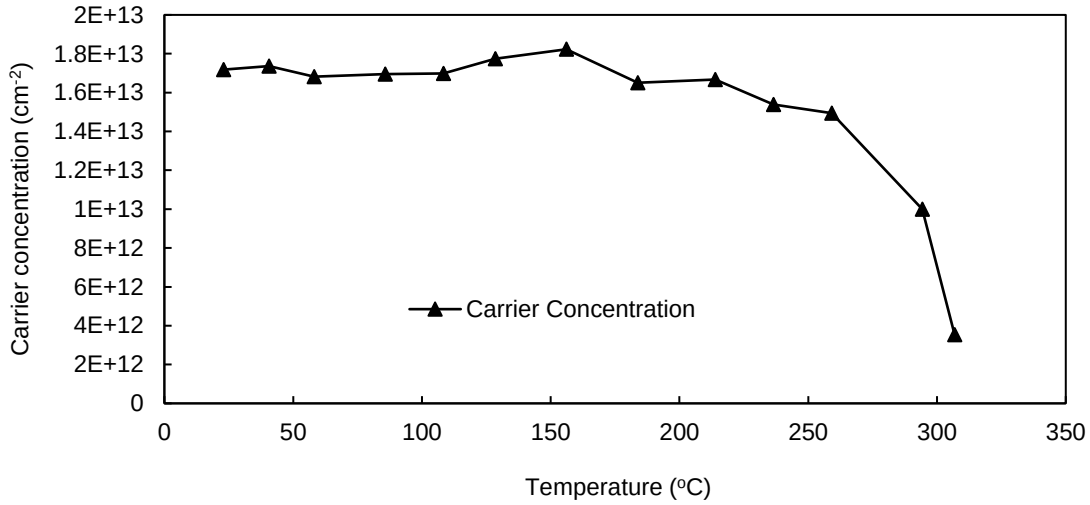

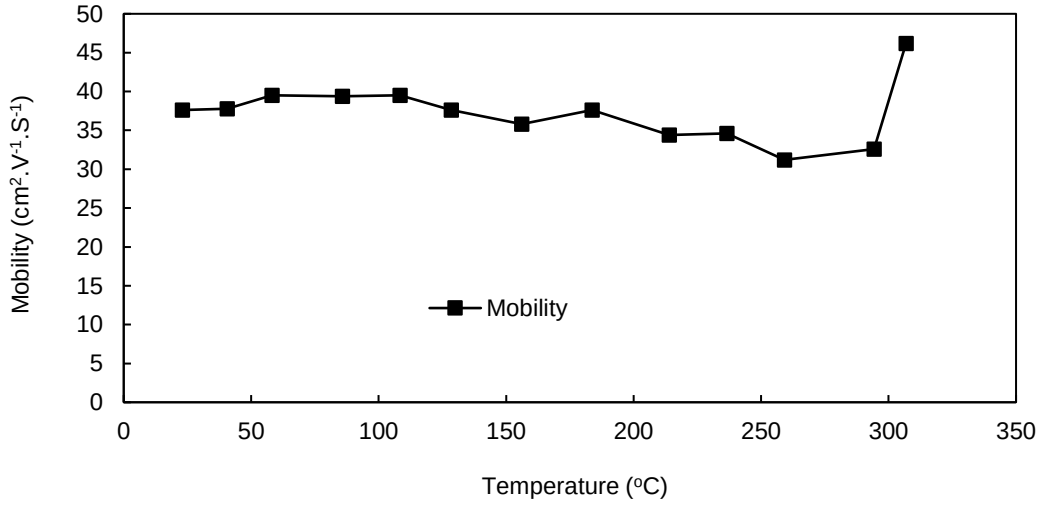

Figure 6.16 - High temperature Hall measurements in air up to 400°C for a V_2O_5 encapsulated H-diamond sample with a 400°C *in-situ* anneal of the diamond surface prior to deposition.

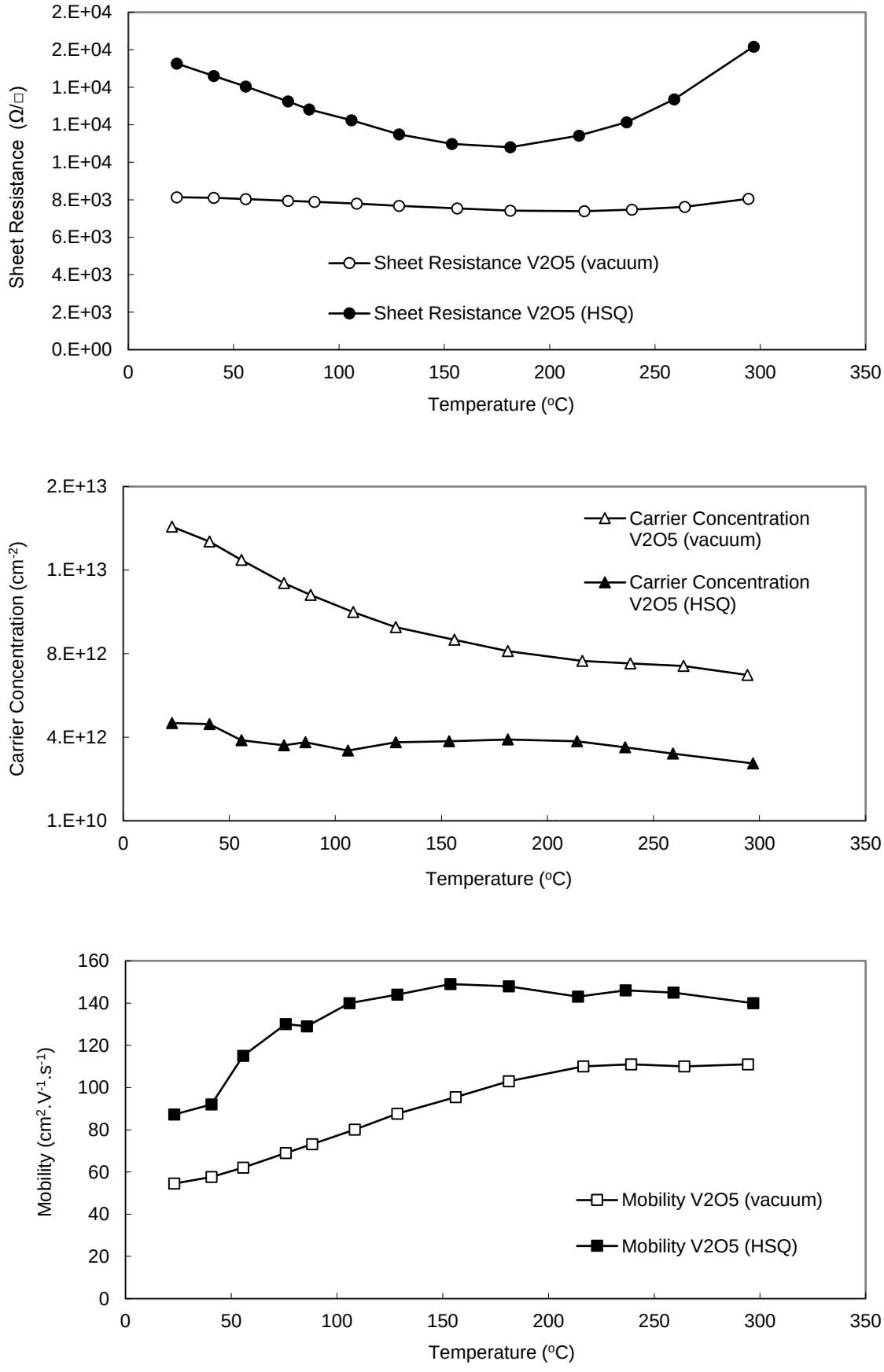

Figure 6.17 – High temperature Hall measurements in vacuum up to 300°C for a V_2O_5 encapsulated H-diamond sample with a 400°C *in-situ* anneal of the diamond surface prior to deposition.

Hall measurements taken before and after applying the HSQ showed no change in conductivity of the H-diamond surface. With the V_2O_5 film encapsulated by HSQ, the sample was measured from room temperature up to 300^{o}C in ambient atmosphere to compare with previous measurements in vacuum and in ambient atmosphere without encapsulation of the oxide. Isolating the V_2O_5 from atmosphere with HSQ showed significant improvement in stability at temperatures up to 300^{o}C (Figure 6.17), however greater degradation occurred compared to measurements in vacuum. Figure 6.18 shows sheet resistance measurements for V_2O_5 in ambient atmosphere, vacuum and with HSQ encapsulation in ambient atmosphere including the cool down period in which the stage is returned to room temperature.

After returning the measurement system to room temperature, the air exposed V_2O_5 sample did not recover any of its lost surface conductivity. This behaviour is near identical to that of MoO_3, suggesting the diamond surface termination to be the common factor in observed conductivity loss at high temperatures. The V_2O_5 sample encapsulated with HSQ showed similar degradation to that of MoO_3 with HSQ. These results suggest that adequate encapsulation of the oxide with a robust material will prevent conductivity loss at temperatures up to 300^{o}C. In this instance the relativily small degradation seen in the HSQ:oxide samples may be due to the thickness or material of the capping layer being insufficent to completely isolate the sample from atmosphere. Likewise, the VDP structure employed here using the sample corners as contacts may leave the film edges exposed resulting in incomplete encapsulation of the oxide.

Like MoO_3, XRD measurements were performed on the samples used in Figure 6.18 to inspect any thermally induced structural change to the V_2O_5 films (Figure 6.19). In contrast to the XRD measurements performed on MoO_3 films, only reflections associated with the silver contacts are visible in these results. Therefore, the V_2O_5 films appeared to remain amorphous after heating to 300^{o}C in air, vacuum and with HSQ encapsulation in air. These results suggest V_2O_5 is substantially less structurally sensitive to the effects of elevated temperatures in both vacuum and atmosphere when compared with MoO_3 films of the same thickness. XRD results after applying high temperatures suggest there is little correlation between any thermally-induced physical modification to the oxide films and the electrical results achieved for both MoO_3 and V_2O_5.

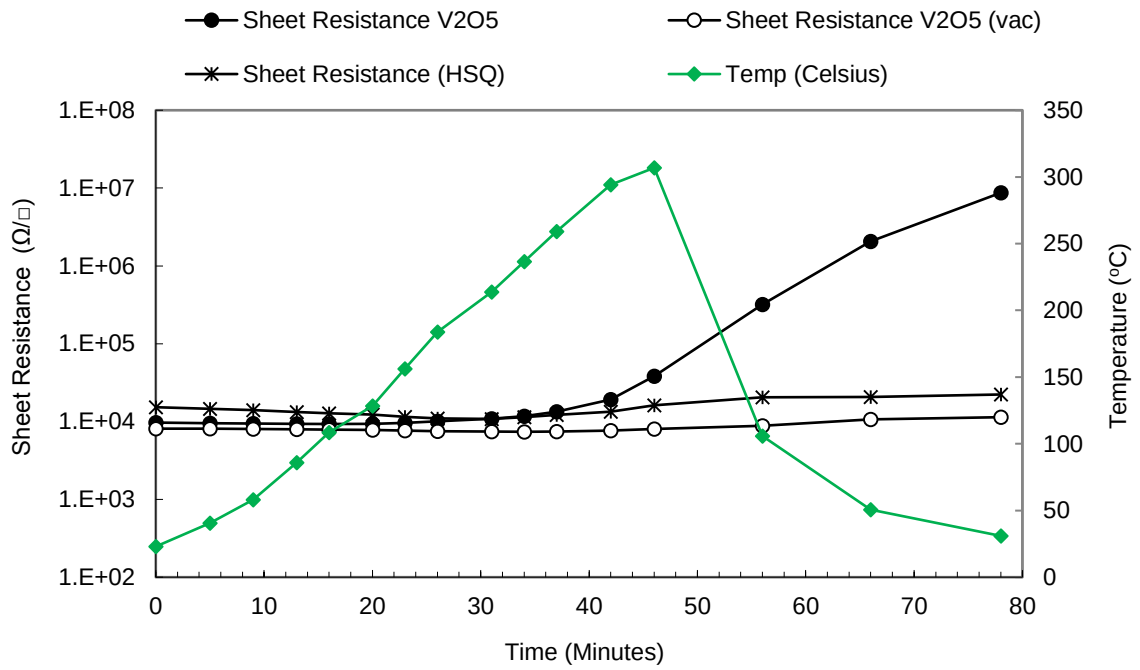

Figure 6.18 - Sheet resistance measurements up to 400°C with cool down period for V_2O_5 surface transfer doped samples and an air induced surface conductivity sample.

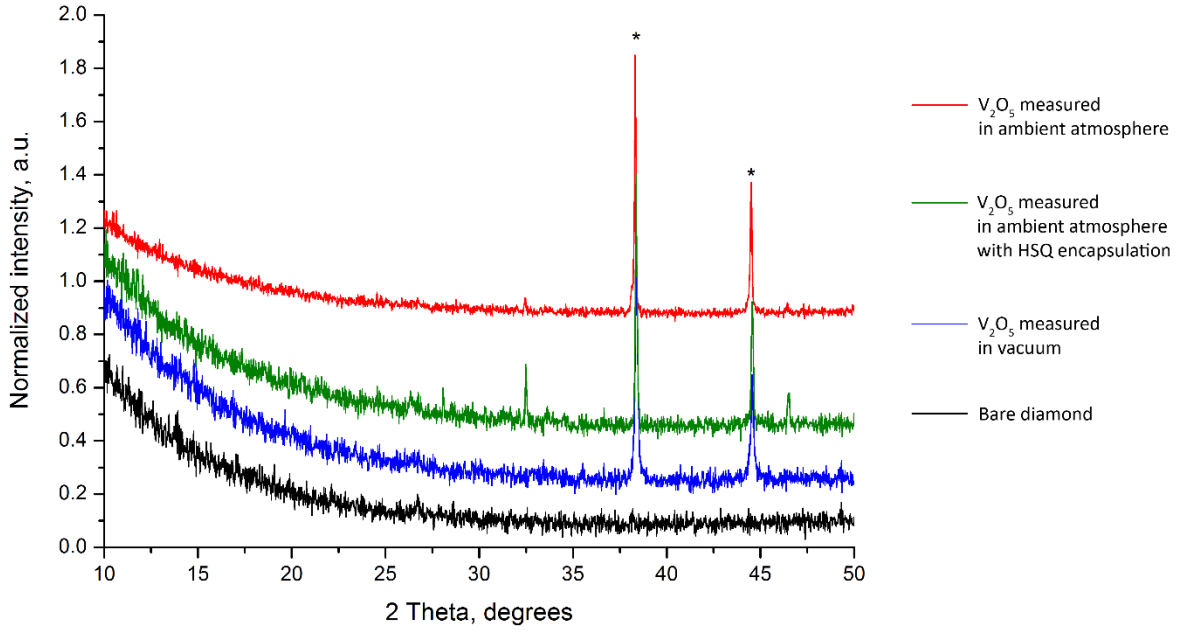

Figure 6.19 - X-ray diffraction patterns of V_2O_5 films after Hall measurements. The reflections marked with asterisks originate from the silver contacts on the sample corners.

To investigate the effects of using thinner oxide V_2O_5 films, three nomically intentical H-diamond samples were prepared for Hall measurement with silver contacts following the same process used for MoO_3 (Figure 6.13). Details of the samples used are shown in table 6.19.

VENDOR	GRADE	ORENTATION	POLISH SOURCE	TERMINATION SOURCE	SIZE
E6	Optical	110	DPS	Cardiff	3 mm^2

Table 6.19 – Details of three nominally identical diamond samples used for different film thicknesses of V_2O_5 with *in-situ* annealing prior to deposition.

V_2O_5 was deposited on each sample with a 400^{o}C *in-situ* anneal prior to deposition, using the oxide thicknesses 10, 30 and 100 nm. Figure 6.20 shows Hall measurements over a period of 38 days with trend line for these three different thicknesses of V_2O_5 on H-diamond. Sheet resistance measurements for 30 and 100 nm thick V_2O_5 appear largely stable over the measurement period, as is consistent with previous results showing the importance of a 400^{o}C anneal prior to deposition. However, 10 nm of oxide shows gradual degradation in carrier density and increased sheet resistance after roughly 17 days, continuing over the same period despite the 400^{o}C *in-situ* anneal performed. As shown previously for MoO_3, V_2O_5 appears to be sensitive to air exposure. These results suggest films of V_2O_5 when used to surface transfer dope H-diamond will degrade over time when exposed to air, with a delayed effect depending on thickness of the oxide film. However, here 30 nm thick V_2O_5 demonstrated improved stability compared to 30 nm thick MoO_3, as is consistent with previous results suggesting V_2O_5 to be less impacted by atmosphere than MoO_3. Regardless, appropriate passivation of the oxide film appears neccesary for consistent long term performance.

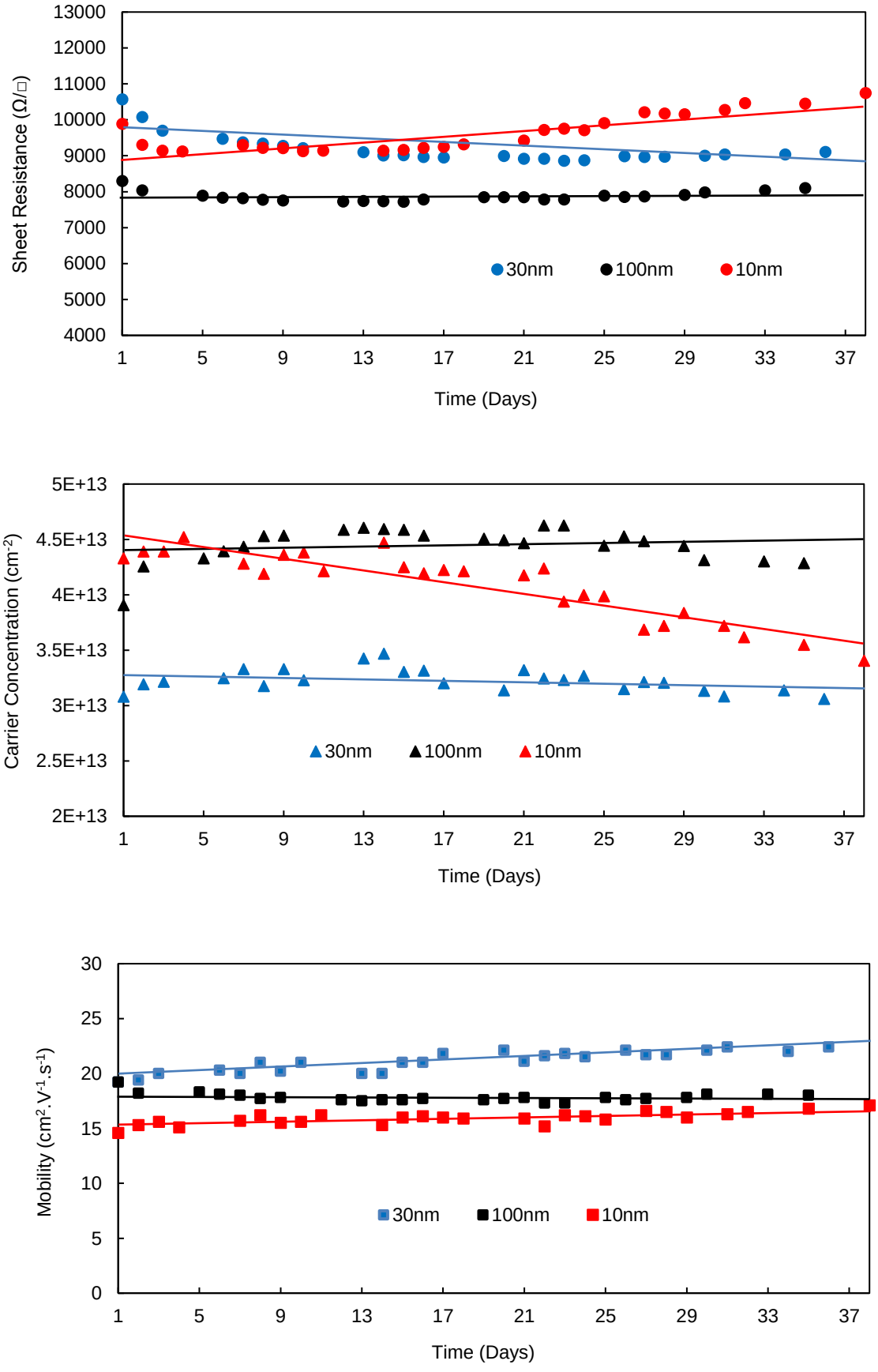

Figure 6.20 - Hall measurements taken over a period of 36 days for three different thicknesses of V_2O_5 on H-diamond, 10, 30 and 100 nm. The diamond surface was annealed at 400°C *in-situ* prior to deposition of oxide.

6.2.4 Tungsten Trioxide as a Surface Acceptor

A promising transition metal oxide that should induce surface transfer doping on H-diamond is tungsten trioxide (WO_3), due to its high electron affinity of 5.1-6.4 eV [6.11, 6.16]. A hydrogen terminated diamond sample was prepared with silver contacts on the corners following the VDP formation method described in Chapter 5. Details of the sample used can be found in Table 6.20.

VENDOR	GRADE	ORENTATION	POLISH SOURCE	TERMINATION SOURCE	SIZE
E6	Optical	100	DPS	Cardiff	3 mm^2

Table 6.20 – Details of CVD diamond sample used for WO_3 induced surface transfer doping with no *in-situ* anneal prior to deposition.

As previous results have shown the importance of removing atmospheric adsorbates from the diamond surface, a 400°C *in-situ* anneal was performed prior to deposition of 100 nm WO_3 by the same thermal evaporation outlined in Chapter 5. Hall measurements taken before and after WO_3 deposition are shown in Table 6.21.

400°C anneal	Sheet Resistance kΩ/□	Mobility cm^2/Vs	Sheet Carrier Concentration $/cm^2$
Before WO_3 Deposition	16	32	1.2×10^{13}
After WO_3 Deposition	8.9	23.8	3×10^{13}

Table 6.21 - Hall measurements prior to and post WO_3 deposition with a 400°C *in-situ* anneal of the diamond surface prior to deposition.

After WO_3 deposition sheet resistance decreased from 16 to 9 kΩ/□, as carrier concentration increased from 1.2×10^{13} to 3×10^{13} cm^{-2} and mobility fell from 32 to 24 cm^2/Vs. Hall measurements taken over 17 days for this sample are plotted in Figure 6.21. These preliminary results for WO_3 induced surface transfer doping on H-diamond suggest WO_3, while capable as an electron acceptor material, is far less stable in atmosphere than either MoO_3 or V_2O_5 for an equivalent film thickness of 100 nm.

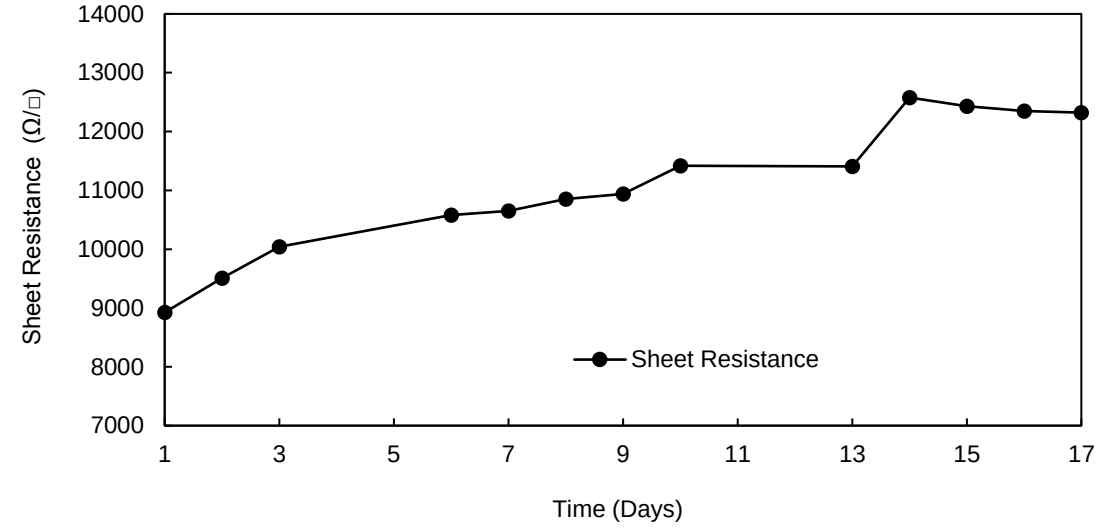

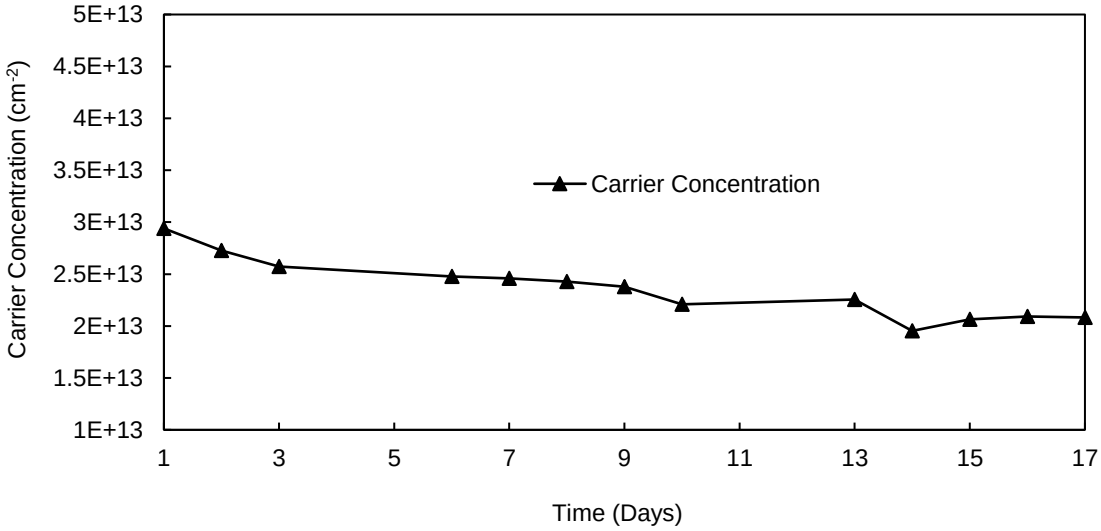

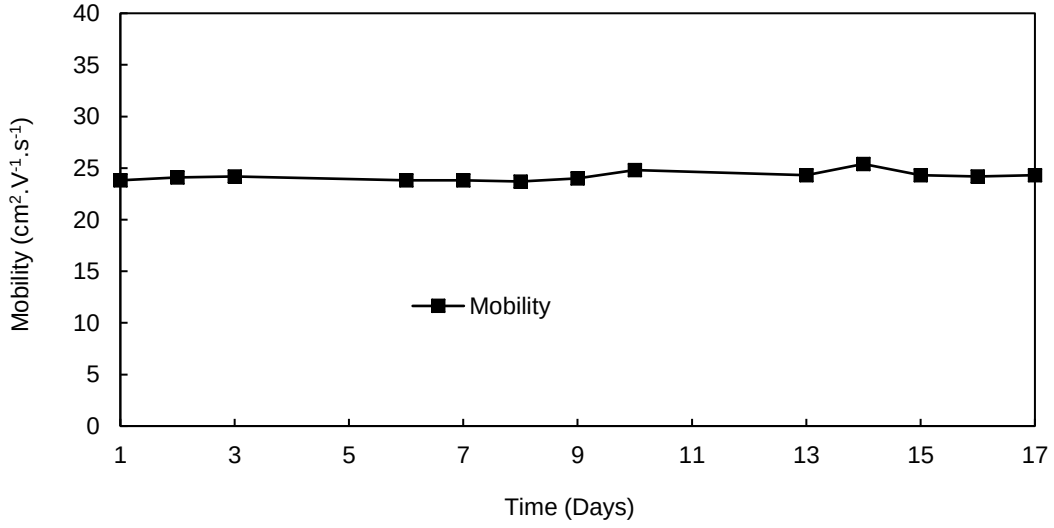

Figure 6.21 - Hall measurements taken over 17 days for a WO_3 encapsulated H-diamond sample with a 400ºC *in-situ* anneal of the diamond surface prior to deposition.

To examine the stability of varied WO_3 film thickness, two nominally identical samples were prepared using silver contacts on the sample corners. Details of the samples used can be found in Table 6.22. Figure 6.22 shows Hall measurements over a period of 32 days with trend line for these three different thicknesses of WO_3 on H-diamond, 10, 30 and 100 nm.

VENDOR	GRADE	ORENTATION	POLISH SOURCE	TERMINATION SOURCE	SIZE
E6	Optical	100	DPS	Cardiff	3 mm^2

Table 6.22 - Details of three nominally identical diamond samples used for different film thicknesses of WO_3 induced surface transfer doping with *in-situ* annealing prior to deposition.

Sheet resistance measurements for all three thicknesses of WO_3 showed gradual degradation over the time period measured. Rate of loss in carrier density was roughly the same for each thickness of oxide, in contrast to the MoO_3 and V_2O_5 results where thicker oxide was observed to be more stable with time.

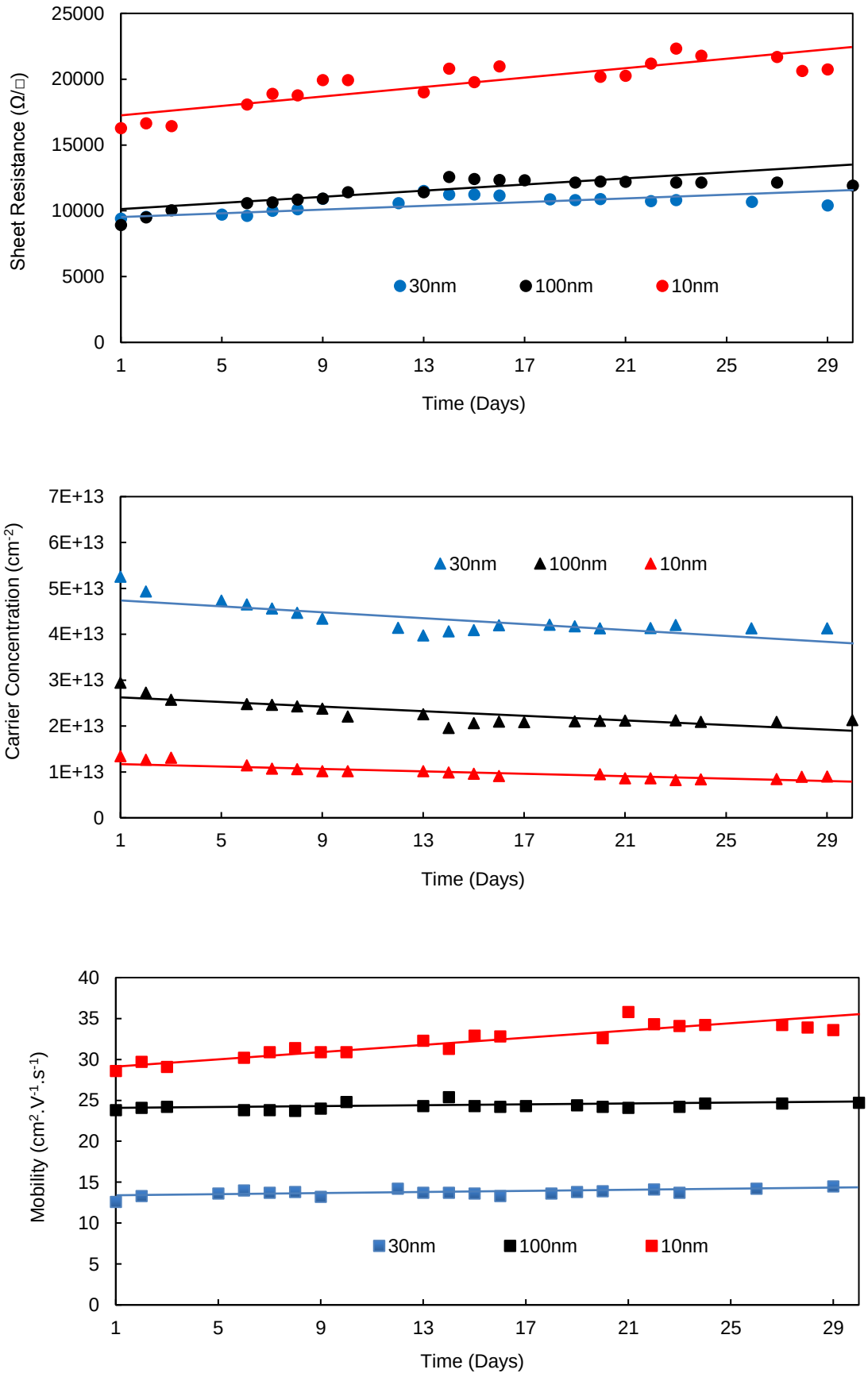

Figure 6.22 - Hall measurements taken over a period of 32 days for three different thicknesses of WO_3 on H-diamond, 10, 30 and 100nm. The diamond surface was annealed at 400°C *in-situ* prior to deposition of oxide.

6.3 Chapter Summary

Experimentation of surface transfer doping on hydrogen terminated diamond for three different high electron affinity transition metal oxides demonstrated excellent improvements in surface conductivity and stability. Both MoO_3 and V_2O_5 with *in-situ* annealing of the diamond surface prior to deposition showed superior stability over time in comparison to air induced surface conductivity, however preliminary trials using WO_3 showed poor stability despite prior annealing of the diamond surface. The thermal stability of MoO_3 and V_2O_5 as surface transfer dopants shows vastly greater potential with appropriate isolation of the oxide from atmosphere. The same improvement in carrier density was achieved for thicknesses down to 10 nm for each oxide; MoO_3, V_2O_5, and WO_3. However, WO_3 likely requires *in-situ* encapsulation of the oxide to retain maximum charge transfer. The ability to incorporate thinner oxide layers is an important factor when designing FET devices. While the surface transfer doping potential of MoO_3 and V_2O_5 are similar, V_2O_5 appears to be more robust both over time and in elevated temperatures up to 300^{o}C. Temperature effects for WO_3 on H-diamond were not investigated due to time constraints, sample availability and the apparent inherent instability of the transfer doping oxide.

References

[6.1] S. J. Sque, R. Jones and P. R. Briddon, "Structure, electronics, and interaction of hydrogen and oxygen on diamond surfaces", Physics Review Letters B, 73, (2006)

[6.2] C. Bandis and B. B. Pate, “Photoelectric emission from negative-electron-affinity diamond (111) surfaces: Exciton breakup versus conduction-band emission”, Physics Review Letters B, 52, (1995)

[6.3] T. Ando, M. Ishii, M. Kamo and Y. Sato, “Thermal hydrogenation of diamond surfaces studied by diffuse reflectance Fourier-transform infrared, temperature-programmed desorption and laser Raman spectroscopy”, Journal of the Chemical Society, Faraday Transactions, 89, (1993)

[6.4] A. J. Mayne, G. Dujardin, “STM Characterization of Hydrogenated Diamond Surfaces”, New Diamond and Frontier Carbon Technology, 15, (2005)

[6.5] H. Kawarada, “Hydrogen-terminated diamond surfaces and interfaces”, Surface Science Reports, 26, (1996)

[6.6] J. Ristein, “Electronic properties of diamond surfaces -blessing or curse for devices?”, Diamond and Related Materials, 9, (2000)

[6.7] C. J. H. Wort and R. S. Balmer, “Diamond as an electronic material”, Materials Today, 11, (2008)

[6.8] F. Maier, M. Riedel, B. Mantel, J. Ristein and L. Ley, “Origin of Surface Conductivity in Diamond”, Physics Review Letters, 85, (2000)

[6.9] S. A. O. Russell, L. Cao, D. Qi, A. Tallaire, K. G. Crawford, A. T. S. Wee, D. A. J. Moran, “Surface transfer doping of diamond by MoO_3: A combined spectroscopic and Hall measurement study”, Applied Physics Letters, 113, (2013)

[6.10] H. J. Looi, R. B. Jackman, J. S. Foord, “High carrier mobility in polycrystalline thin film diamond”, Applied Physics Letters, 72, (1998)

[6.11] I. Irfan, H. J. Ding, Y. L. Gao, D. Y. Kim, J. Subbiah, and F. So, “Energy level evolution of molybdenum trioxide interlayer between indium tin oxide and organic semiconductor”, Applied Physics Letters, 96, (2010)

[6.12] A. Kuruvila, P. R. Kidambi, J. Kling, J. B. Wagner, J. Robertson, S. Hofmann and J. Meyer, “Organic light emitting diodes with environmentally and thermally stable doped graphene electrodes”, Journal of Materials Chemistry C, 2, (2014)

[6.13] W. Chang, X. Qi, J. Kuo, S. Lee, S. Ng, D. Chen, “Post-deposition annealing control of phase and texture for the sputtered MoO_3 films”, CrystEngComm, 13, (2011)

[6.14] K. G. Crawford, L. Cao, D. Qi, A. Tallaire, E. Limiti, C. Verona, A. T. S. Wee and D. A. J. Moran, “Enhanced surface transfer doping of diamond by V_2O_5 with improved thermal stability”, Applied Physics Letters, 108, (2016)

[6.15] J. Q. Zhong, H. Y. Mao, R. Wang, J. D. Lin, Y. B. Zhao, J. L. Zhang, D. G. Ma, and W. Chen, "Ionization potential dependent air exposure effect on the MoO_3/organic interface energy level alignment", Organic Electronics, 13, (2012)

[6.16] M. Kroger, S. Hamwi, J. Meyer, T. Riedl, W. Kowalsky, and A. Kahn, "Role of the deep-lying electronic states of MoO_3 in the enhancement of hole-injection in organic thin films", Applied Physics Letters, 95, (2009)

7 Diamond Surface Conditioning

After CVD growth of diamond, substrates are typically polished due to extensive roughness of the surface as mentioned in Chapter 6.1 [7.1]. The most common diamond polishing technique is to hold the diamond sample against a high-speed rotating wheel coated with diamond powder, called a scaife wheel [7.2]. All samples polished in this work were done so in this way and performed by external sources. Many factors, such as the rotation speed of the wheel, balance of both the wheel and the holding mechanism, composition of diamond powder etc., can cause significant variation in quality and appearance of a polished sample. The transfer doping mechanism used to generate charge carriers in hydrogen terminated diamond occurs at the interface between the diamond surface and an adjacent material, as discussed in Chapter 2. This process is likely influenced by increased values of surface roughness, polishing induced crystal damage and reduced hydrogen coverage which may impact the electrical performance [7.3]. Bulk dislocations can occur during crystal growth, while surface damage may occur from polishing [7.4]. In this chapter methods of etching the diamond surface are investigated with the aim of providing greater control over surface topology, roughness and the removal of potential sub-surface damage caused during polishing.

7.1 Chlorine Etching

A 4.5 mm^2 CVD diamond sample of orientation [100] provided by Element Six is shown in Figure 7.1 after a high temperature acid clean, described in Chapter 6. This 5 µm AFM scan shows the surface which has also been polished by E6. This presentation with distinct polishing grain is typical of samples polished by scaife wheel, showing the direction of the wheel's rotation following the grain. The scan shows an average surface roughness (Ra) of 0.74 nm with the route mean squared (Rq) of the surface being 1 nm. Despite a high temperature acid clean, what appears to be contaminants are still present on the surface. In this instance Rq is significantly higher due to the apparent surface contaminants, while Ra will average out these tall "pillar" like features.

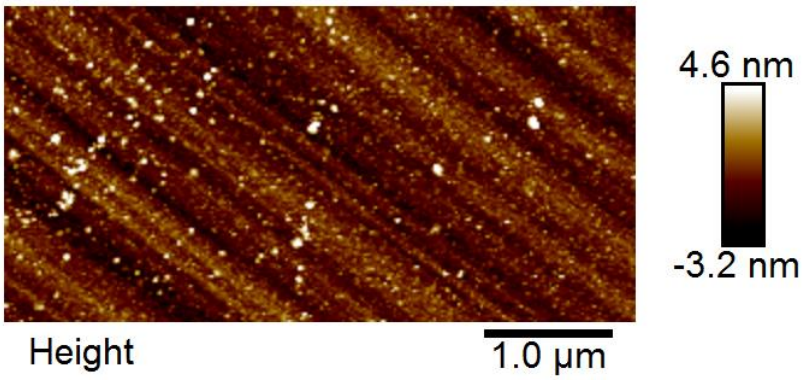

Figure 7.1 - 5 µm AFM scan of a CVD diamond surface after polishing. Image Ra 0.74 nm and Rq 1 nm.

A process for removal of diamond layers by way of Reactive Ion Etching (ICP) using Cl_2 + Ar was developed, based on work done at the University of Strathclyde [7.5]. The ICP parameters used were as follows; chamber pressure 5 mTorr, stage temperature 20ºC, coil power 400 W, Cl_2 Flow Rate 40 sccm and Ar Flow Rate 25 sccm. Etch rate for this recipe was measured as approximately 10 nm per minute using a NiCr mask, in close agreement with C. L. Lee *et al* [7.5]. The etching mechanism of diamond using Ar + Cl_2 plasma is reported to be:

$C + Cl_2 \rightarrow CCl_x$.

Ar ions sputter the diamond surface enabling the reaction of chlorine with carbon atoms to form the volatile etch product CCl_x. The sample in Figure 7.1 was subjected to 10 minutes of ICP etching using the above recipe, results of which are shown in Figure 7.2.

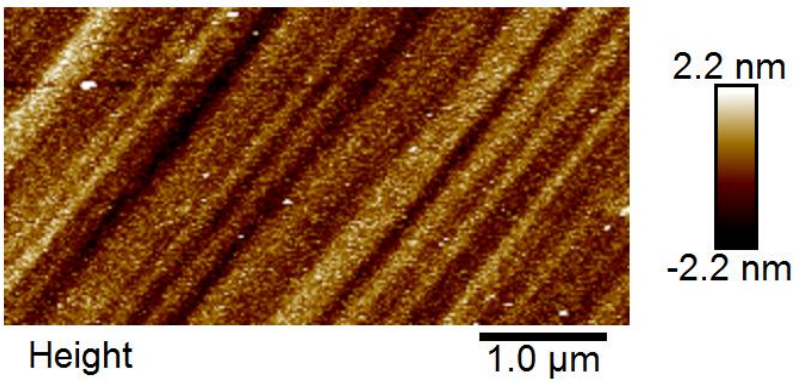

Figure 7.2 – 5 µm surface scan after 10 minutes ICP Cl_2 + Ar etching. Image Ra 0.47 nm and Rq 0.64 nm.

After 10 minutes etching the surface Ra was reduced from ~0.6 nm to ~0.5 nm. Notably there was also a large reduction in the appearance of tall "pillar" like features, possibly indicating isotropic etching (where the etch is not completely unidirectional) or a faster etch rate of these surface features. Figure 7.3 shows the same sample after a further 240 minutes of ICP etching. To prevent a build-up of etch product in the chamber the process was done in cycles of 10 minute intervals with a 2-minute N_2 purge of the chamber between etching.

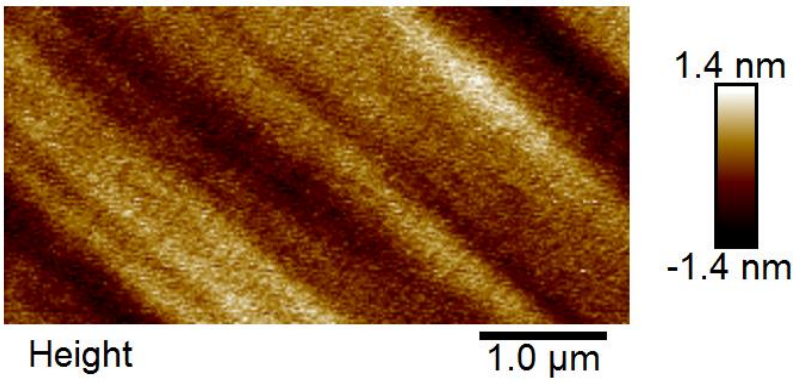

Figure 7.3 – 5 µm surface scan after 250 minutes ICP Cl_2 + Ar etching. Image Ra 0.34 nm and Rq 0.42 nm.

After a combined 250 minutes of ICP etching with Ar + Cl_2 the surface Ra was further reduced to ~0.3 nm with an Rq of ~0.4 nm. As well as lowering surface roughness, the reduction in delta between Ra and Rq for this sample shows the isotropic smoothing effect of the Ar + Cl_2 etch. Peaks and troths are widened and reduced in depth, resulting in a flatter surface over the same area and complete removal of surface contaminants like those seen in Figure 7.1. The etch rate of 10 nm per minute for this recipe is not optimised, resulting in extensive etch times. Further work could be done to improve upon this etch rate, taking care to maintain the surface smoothing effect.

7.2 Oxygen Etching

As in the previous section, Figure 7.4 below shows a polished sample from E6 after high temperature acid cleaning. This surface scan exhibits an Ra of ~0.5 nm and an Rq of ~0.9 nm. Again, tall pillar like features can be seen on the surface further increasing the delta between Ra and Rq.

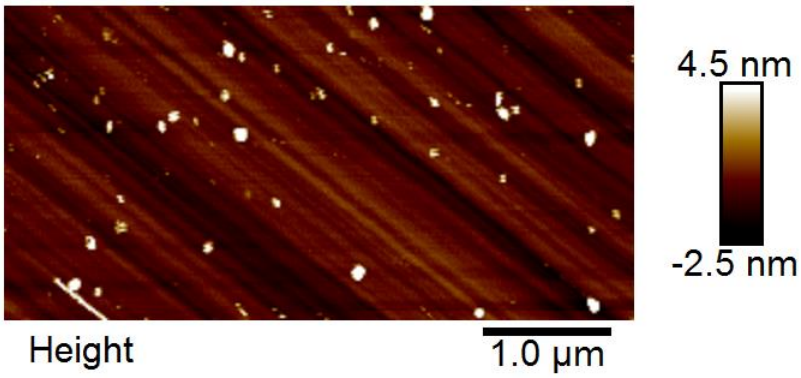

Figure 7.4 - 5 µm AFM scan of a CVD diamond surface after polishing. Image Ra 0.53 nm and Rq 0.93 nm.

Reactive Ion Etching (RIE) using a mixture of Ar + O_2 was explored as an additional etch step after etching with Ar + Cl_2 [7.6]. The motivation for this O_2 etch was to remove any possible Cl_2 contamination of the diamond surface and to also improve etch rates if the surface roughness was not adversely effected. Figure 7.5 shows the sample after 240 minutes of Ar + Cl_2 etching, following the same recipe as in the previous section. A 3D render of the surface is also shown for illustrative purposes.

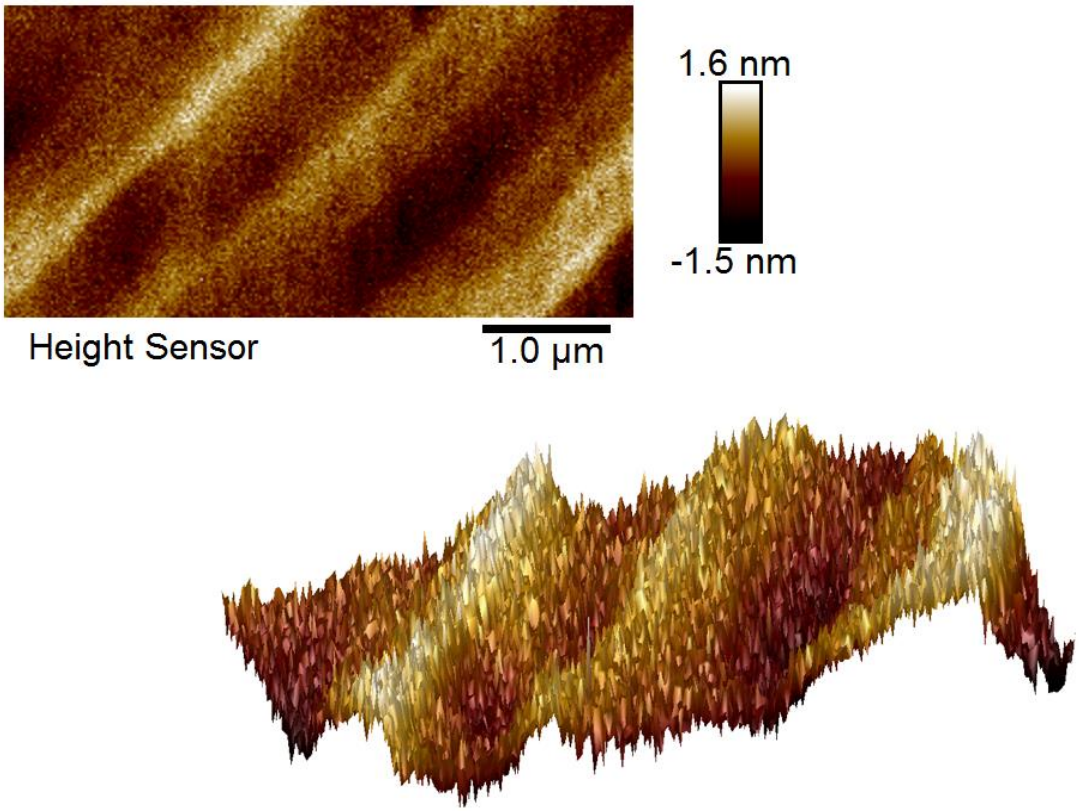

Figure 7.5 – Surface AFM scan of a polished CVD diamond sample with values Ra 0.36 nm and Rq 0.45 nm. 3D render of the surface topology is shown.

After 240 minutes of Ar + Cl_2 the surface is significantly smoother with an Ra of ~0.4 nm and an Rq of ~0.5 nm. Again, the large reduction in delta between Ra and Rq is due to the removal of tall surface features common after scaife polishing. Also, the grain of the surface has been widened as seen previously. This sample was then etched a further 8 minutes with Ar + O_2 to examine the effects of O_2 plasma on the already smoother diamond surface after Cl_2 etching [7.6]. The RIE parameters used were as follows; chamber pressure 20 mTorr, stage temperature 22°C, RF power 200 W, O_2 Flow Rate 40 sccm and Ar Flow Rate 10 sccm. Etch rate for this recipe was measured as approximately 25 nm per minute using a S1818 resist mask, a rate significantly faster than the Ar + Cl_2 recipe. Figure 7.6 shows the same sample after 8 minutes of Ar + O_2 etching, removing approximately 200 nm from the top surface.

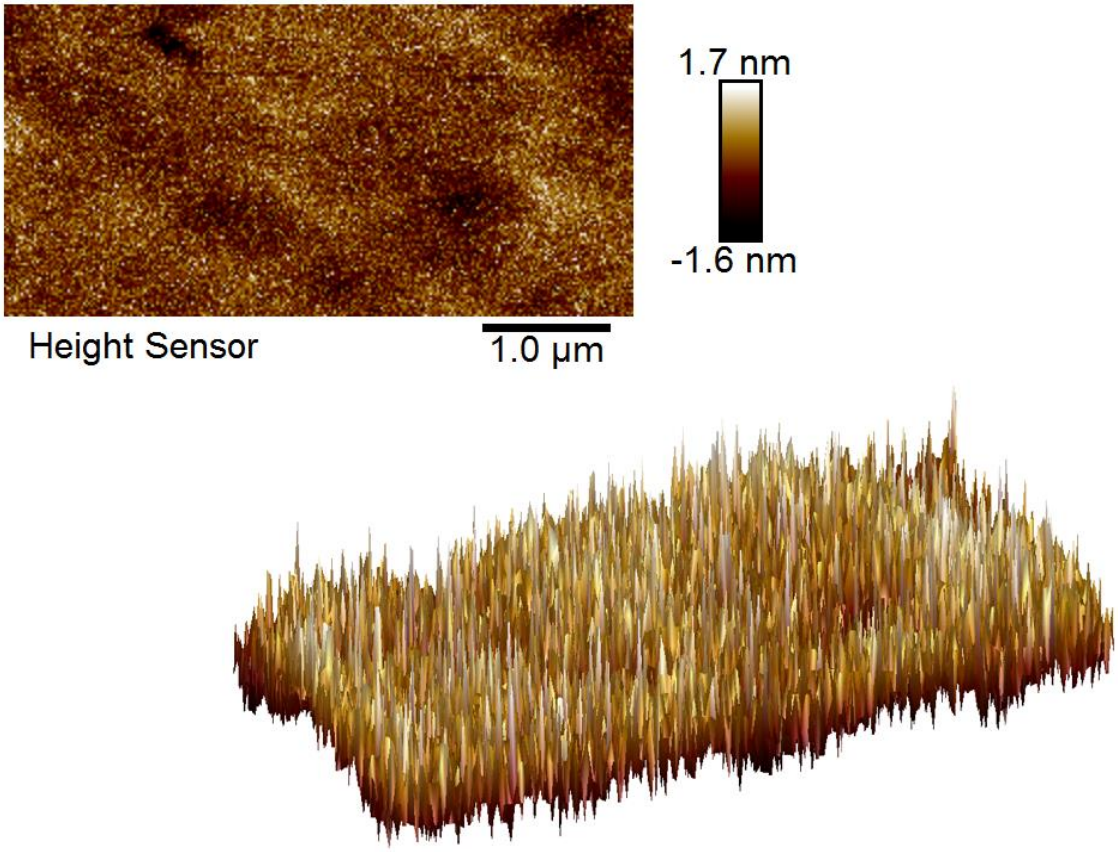

Figure 7.6 – Surface AFM scan of an 8 minute Ar + O_2 etched CVD diamond sample with values Ra 0.36 nm and Rq 0.46 nm. 3D render of the surface topology is shown.

After etching with Ar + O_2 the sample Ra and Rq remained largely unchanged, indicating the smoother surface first achieved with Cl_2 etching can be maintained while removing further surface layers with O_2 plasma. Figure 7.5 and 7.6 include 3D renders of the associated surface AFM scan. Significant difference in surface topology can be seen despite the similar values for Ra and Rq. While Cl_2 plasma appears to have an isotropic effect of etching and widening the existing polishing grain, O_2 plasma mottles the surface completely removing existing surface features.

Due to the improved etch rate using Ar + O_2, this process becomes more viable for etching the diamond surface while using a masking material. Figure 7.7 shows an optical image of a CVD diamond sample after O_2 plasma was used to etch a pattern into the diamond surface. In this instance the sample identification number, university name and NEDDS (Nano-Electronic Diamond Devices and Systems) group logo was patterned with photolithography prior to etching. An AFM scan with step depth of approximately 206 nm is shown.

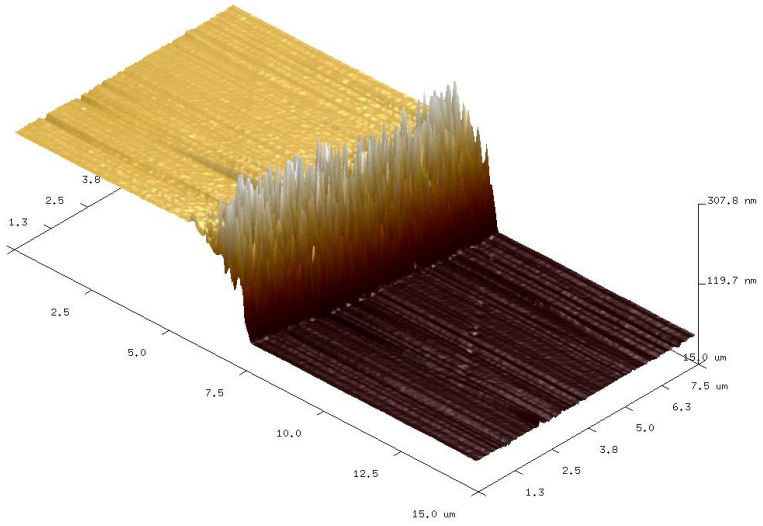

Figure 7.7 - Optical image of a CVD diamond sample, embossed with sample name via photolithography defined etching. Step etched into a CVD diamond substrate ~206 nm deep using an 8 minute Ar + O_2 RIE etch.

7.3 Etching and Hydrogen Termination

To investigate the potential benefits of etching the diamond surface post polish and prior to hydrogen termination, three nominally identical CVD diamond samples were hydrogen terminated after being etched for various durations. These samples were provided unpolished by E6 with (100) surface orientation and were 3 mm^2 in size. Figure 7.8 below shows a 5 µm scan of the diamond surface after high temperature acid cleaning.

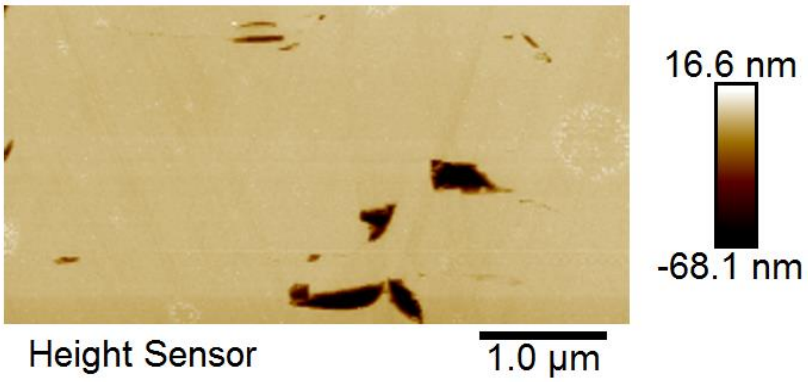

Figure 7.8 – Unpolished CVD diamond sample with an Ra of 3 nm and Rq of 9.6 nm.

Large vacancies in the diamond surface can be seen, with typical depth of roughly 130 nm depending on location measured. This illustrates the need for polishing to provide a level surface. All three samples were then polished together using a scaife polishing wheel by an external company called Stone Perfect. The samples, designated C1, 2 and 3 are shown in Table 7.1 below alongside roughness values after polishing. Typical Ra values after polishing range from approximately 0.6 to 0.7 nm. Figure 7.9 shows AFM scans for these samples after polishing.

Sample	Polish	Ra (nm)	Rq (nm)
C1	Scaife	0.71	0.88
C2	Scaife	0.68	0.85
C3	Scaife	0.63	0.88

Table 7.1 – Samples C1-3 roughness values after polishing by Stone Perfect.

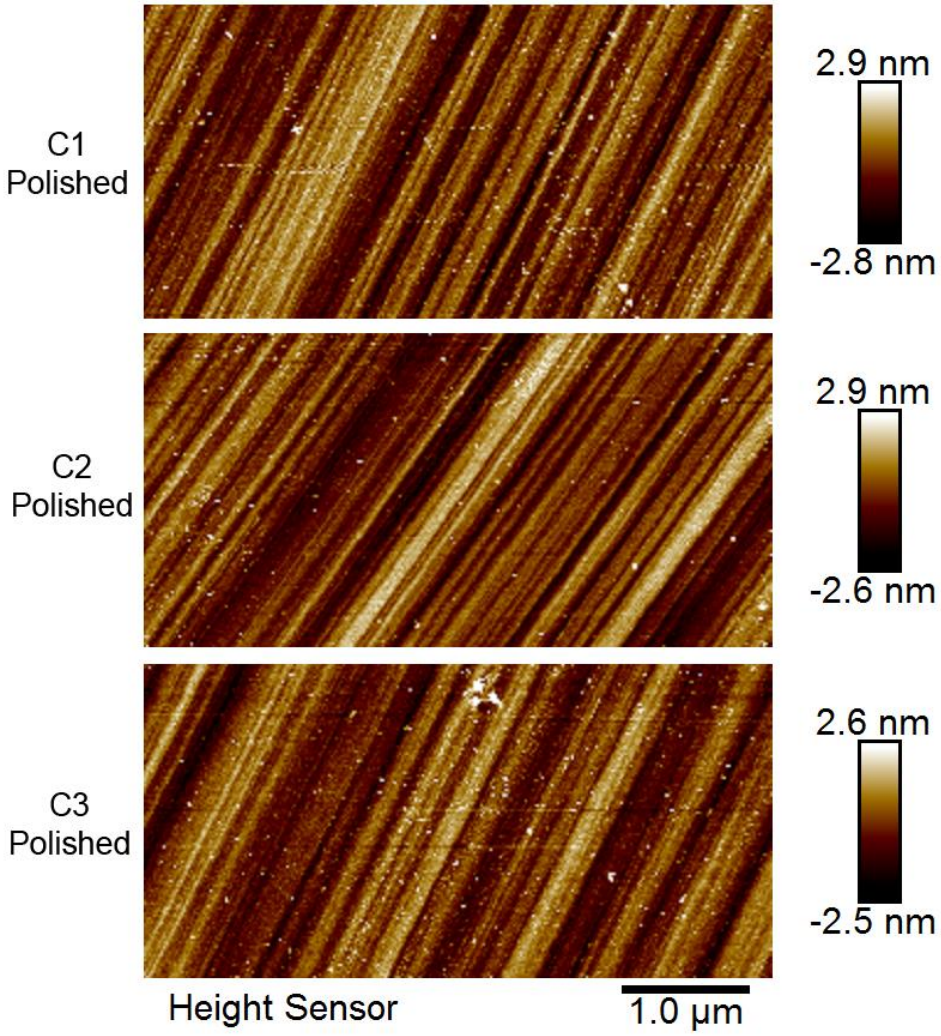

Figure 7.9 – AFM scans of C1-3 after polishing by Stone Perfect.

These samples were then etched using ICP with the Ar + Cl_2 recipe described earlier in this chapter. Etch time was varied for the three samples, removing approximately 600 nm, 3 µm and 4.2 µm respectively. Roughness values after etching are shown in Table 7.2.

Sample	Etch depth	Ra (nm)	Rq (nm)
C1	600 nm	0.43	0.56
C2	3 µm	0.40	0.54
C3	4.2 µm	0.33	0.41

Table 7.2 – Samples C1-3 roughness values after Ar + Cl_2 etching.

Surface Ra of the samples was reduced to between approximately 0.3 to 0.4 nm for the same scan area, with the lowest Ra produced by C3 after 4.2 µm of etching. AFM scans after etching are shown in Figure 7.10.

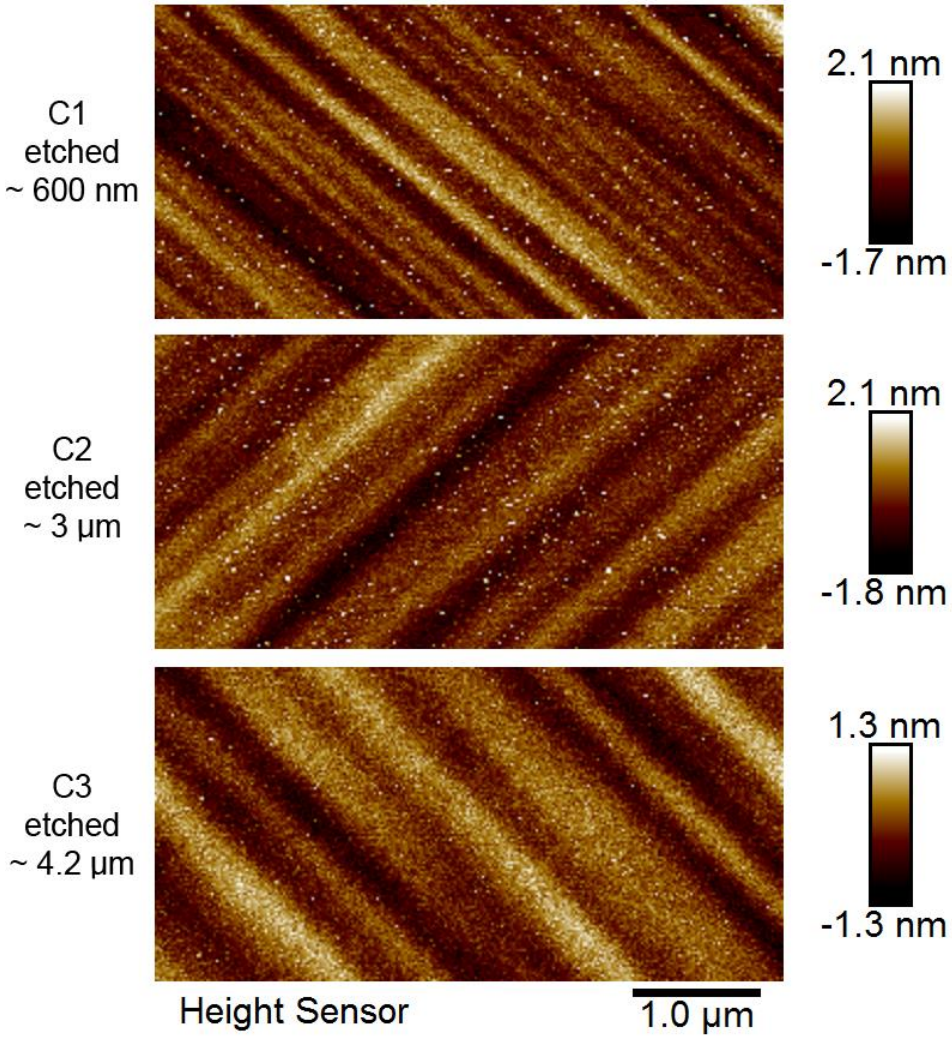

Figure 7.10 – AFM scans of C1-3 after Ar + Cl_2 etching.

An increase in grain width was observed across all three samples, becoming more pronounced as etch depth increases. A progressive reduction in surface roughness is seen as etch time increases, with C3 showing the least amount of tall peak like features on the surface. All three samples were then hydrogen terminated in Cardiff following the parameters outlined in Chapter 5. Roughness values after hydrogen termination are shown in Table 7.3.

Sample	H-termination	Ra (nm)	Rq (nm)
C1	Cardiff	0.42	0.52
C2	Cardiff	0.33	0.4
C3	Cardiff	0.33	0.42

Table 7.3 - Samples C1-3 roughness values after hydrogen termination at Cardiff.

After hydrogen termination Ra was largely maintained for all three samples, ranging from approximately 0.3 to 0.4 nm. Figure 7.11 shows AFM scans for these samples after hydrogen treatment.

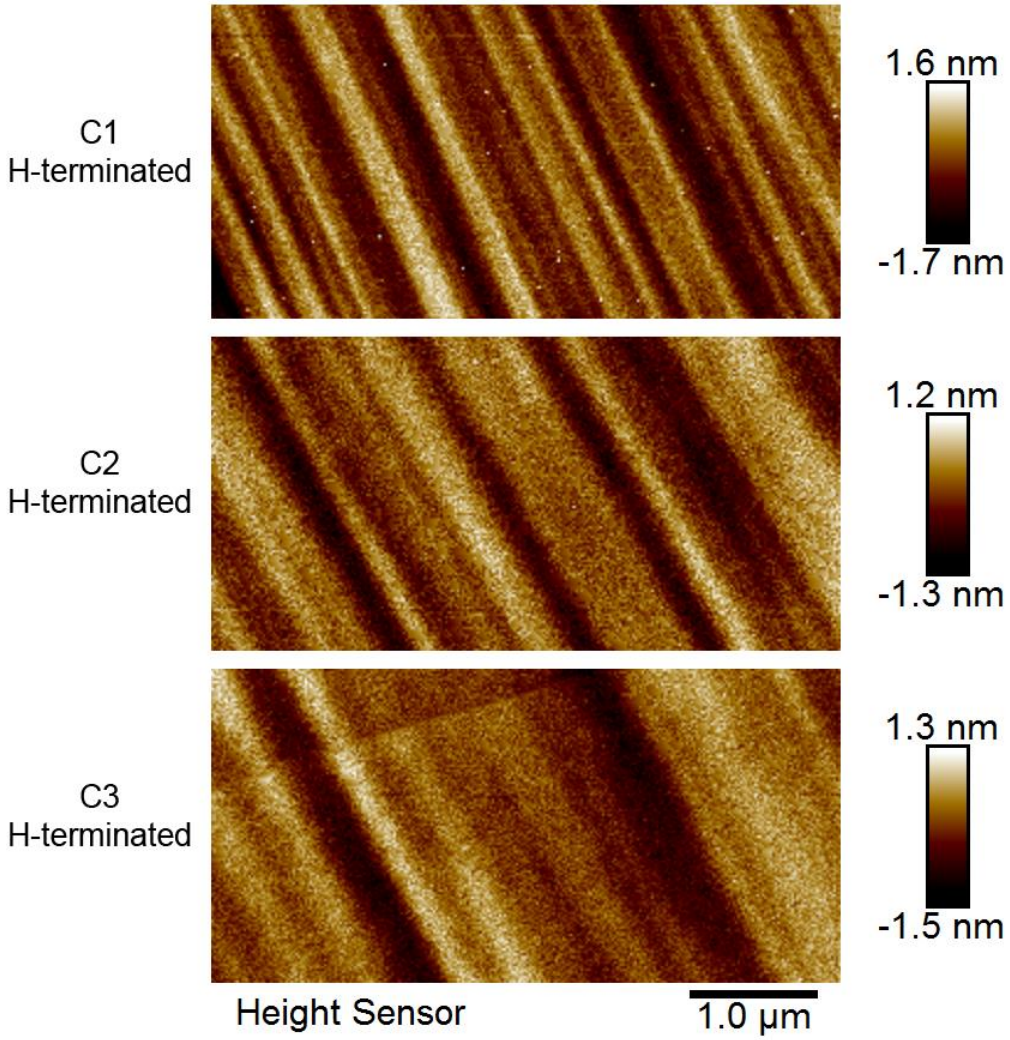

Figure 7.11 - AFM scans of C1-3 after hydrogen termination in Cardiff.

Hall measurements were then performed on these samples to ascertain the quality of hydrogen termination after etching of the surface. Silver contacts were applied to the sample corners following the method outlined in Chapter 5. Measurements of sheet resistance, carrier concentration and mobility are shown in Table 7.4 for each sample. This includes values with the diamond surface exposed to air and after encapsulation with 100 nm MoO_3 using a 400°C *in-situ* anneal process established in Chapter 6.

Sample (doping)	Approx. Etch depth	Sheet Resistance kΩ/□	Mobility cm^2/Vs	Sheet Carrier Concentration cm^{-2}
C1 (air)	600 nm	19.8	26.5	1.19×10^{13}
C2 (air)	3 µm	84.5	4.21	1.75×10^{13}
C3 (air)	4.2 µm	36.5	11.3	1.52×10^{13}
C1 (MoO_3)	600 nm	16.6	16.6	2.27×10^{13}
C2 (MoO_3)	3 µm	32.2	6.15	3.153×10^{13}
C3 (MoO_3)	4.2 µm	12.8	12.8	3.788×10^{13}

Table 7.4 – Hall measurements for samples C1-3 after hydrogen termination. Measurements while exposed to air and after deposition of 100 nm MoO_3 are shown.

With the diamond surface exposed to air, C1 showed the lowest sheet resistance at ~20 kΩ/□ with C2 showing the highest at ~85 kΩ/□. All three samples showed relatively similar carrier concentrations ranging from ~1.2 to 1.5 $\times 10^{13}$ cm^{-2}. As such, large variation in carrier mobility was responsible for the significant differences in sheet resistance between samples. C1 showed the highest mobility with the lowest carrier density, following a commonly observed trend for surface transfer doped H-diamond [7.7, 7.8]. Likewise, C2 showed the lowest mobility with the highest carrier density. Electrical comparison of samples doped by air exposure is somewhat unreliable, due to the spontaneous nature of surface adsorbent accumulation on the diamond surface [7.3]. Likewise, composition of these surface acceptors is difficult to control. Therefore, 100 nm MoO_3 was deposited on all three samples simultaneously with a 400°C *in-situ* anneal. After MoO_3 deposition, all three samples showed significantly lower sheet resistance as is consistent with previous results [7.8]. The observable range in carrier concentration seen extended to ~2.3 - 3.8 $\times 10^{13}$ cm^{-2} and follows a trend of increasing carrier density with increased etch depth. After MoO_3 encapsulation, C1 still showed the highest mobility and

C2 the lowest despite disproportional changes in carrier density between samples. These results suggest etching of the surface may improve charge transfer to a surface acceptor material, however in this case mobility was low possibly due to increased scattering somehow caused by the etch [7.3].

An additional three E6 CVD diamond samples were scaife polished by an external company called Diamond Product Solutions (DPS). These samples were nominally identical with a size of 3 mm^2 and surface orientation of [100]. The samples were then etched, this time the Ar + Cl_2 step was followed by a Ar + O_2 etch to a combined depth of roughly 3.4 µm. Each sample was then hydrogen terminated in Paris following the process outlined in Chapter 6. However, to investigate improving the termination process the plasma power density was varied for each sample. These three samples are designated A1, 2 and 3 and the power used was 1.5, 2.1 and 2.6 kW respectively. Table 7.5 shows roughness values for these samples after polishing, ranging from ~0.7 to 0.9 nm Ra. Figure 7.12 shows AFM scans of the diamond surface after polishing.

Sample	Polish	Ra (nm)	Rq (nm)
A1	Scaife	0.71	0.89
A2	Scaife	0.92	1.2
A3	Scaife	0.85	1.0

Table 7.5 – Roughness values for diamond samples A1-3 after polishing.

Polishing done by DPS showed a significantly different surface topology with no visible grain typical of scaife polishing. The reason for this unusual presentation is unclear, as DPS do not share specific details of their polishing process. One possibility is the use of a specific variation in the composition of diamond dust in the polishing process to avoid surface damage. Differences in rotation speed and or applied force could also produce a surface with less visible polishing features. The surface after polishing by DPS still shows sub-nanometre roughness with no large surface vacancies seen in unpolished samples.

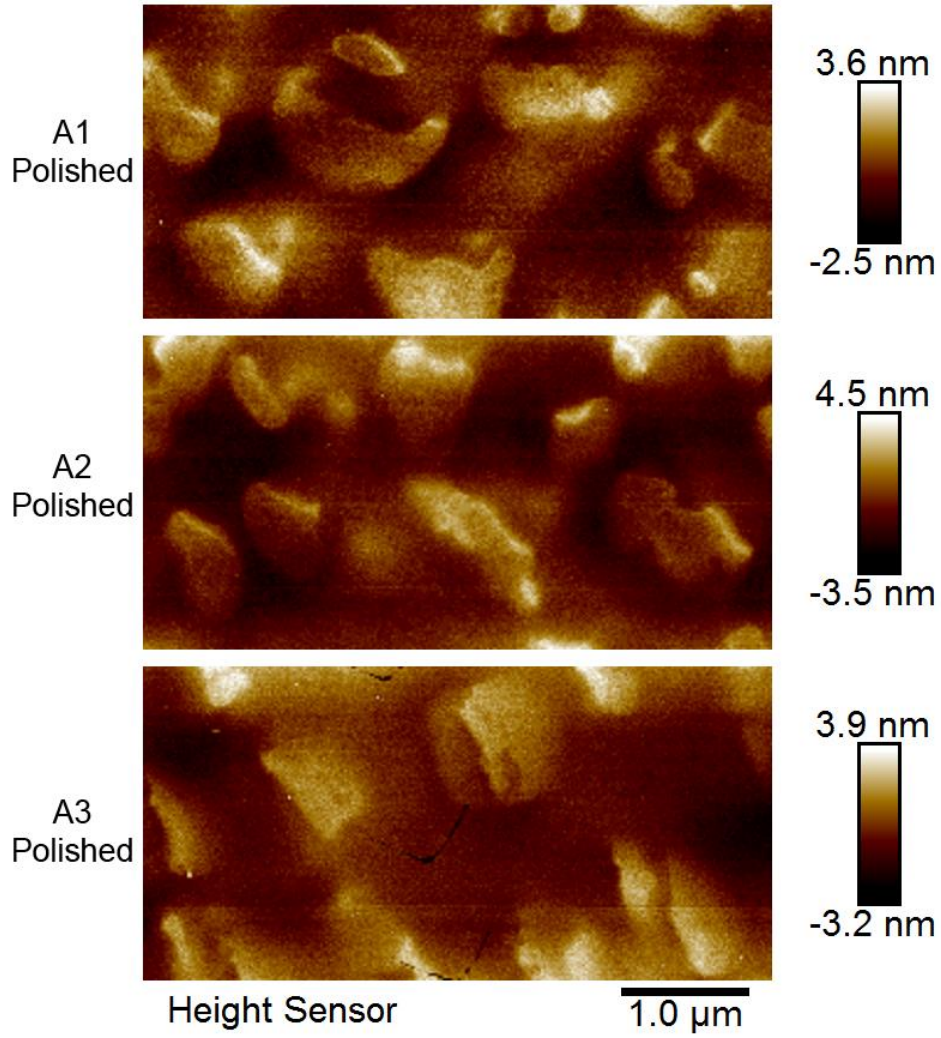

Figure 7.12 – AFM scans of A1-3 after polishing by Diamond Product Solutions.

The samples were then etched to a depth of ~ 3 µm using the Ar + Cl_2 process detailed earlier in this chapter. Roughness values for each sample are shown in Table 7.6 below.

Sample	Etched (Cl_2)	Ra (nm)	Rq (nm)
A1	~ 3 µm	0.42	0.53
A2	~ 3 µm	0.44	0.55
A3	~ 3 µm	0.44	0.56

Table 7.6 – Roughness values for diamond samples A1-3 after etching with Ar + Cl_2.

After etching surface roughness average was reduced to roughly 0.4 nm for all three samples with relatively small difference between Ra and Rq. AFM scans for these samples are shown in Figure 7.13.

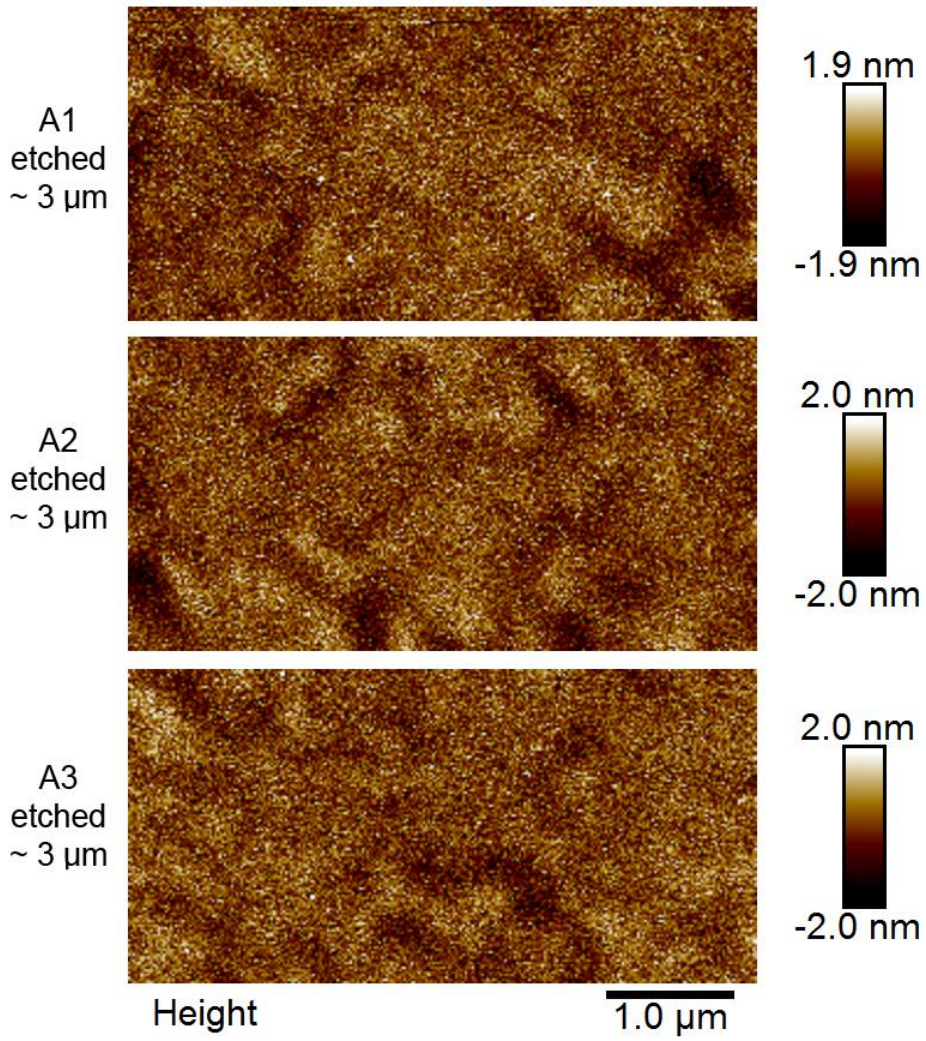

Figure 7.13 – AFM scans of A1-3 after Ar + Cl_2 etching to a depth of roughly 3 µm.

The surface topology for these samples after etching with Ar + Cl_2 differs from what was seen previously using this process. While Ra and Rq values remain similar, the surface appears more uniform due to the absence of polishing features. However, some of the initial polishing features can still be seen. These samples were then etched again to a depth of roughly 400 nm using the Ar + O_2 process detailed previously. Roughness values for each sample are shown in Table 7.7 and Figure 7.14 shows AFM scans of the surface after etching.

Sample	Etched (O_2)	Ra (nm)	Rq (nm)
A1	~ 400 nm	0.21	0.26
A2	~ 400 nm	0.21	0.26
A3	~ 400 nm	0.24	0.3

Table 7.7 – Roughness values for diamond samples A1-3 after etching with Ar + O_2.

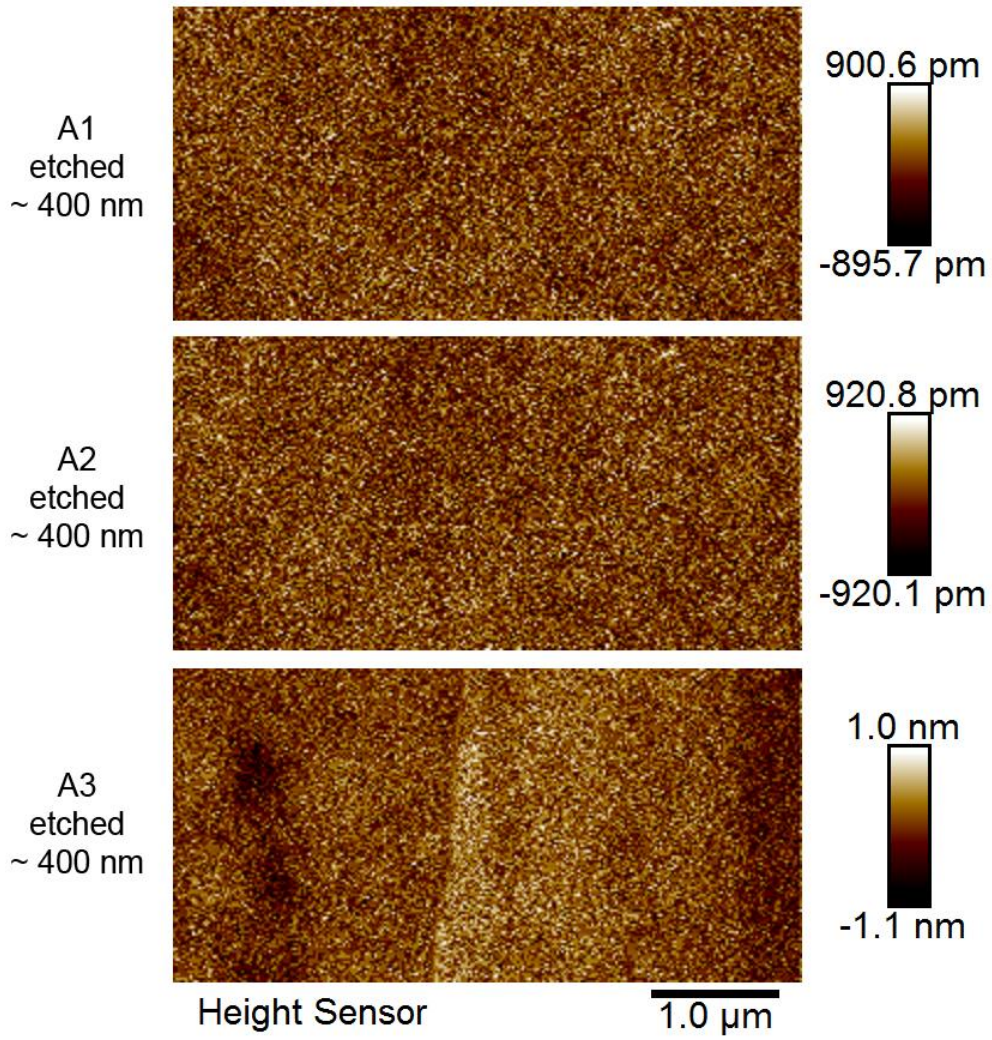

Figure 7.14 – AFM scans of A1-3 after Ar + O_2 etching to a depth of roughly 400 nm.

After further etching with Ar + O_2, surface Ra was reduced to roughly 0.2 nm with small difference between Ra and Rq indicating a very smooth profile. Surface features formed after polishing, as can be seen in Figure 7.12, are completely removed. These samples demonstrated the smoothest surfaces produced thus far.

Each sample was treated with hydrogen plasma in Paris, as noted in Chapter 6. Previously, the hydrogen termination process at the University of Paris 13 used a plasma power density of 2.1 kW. To investigate the effect of varying this parameter, sample A1 was treated with a lower power of 1.5 kW, for sample A2 the usual power of 2.1 kW and for A3 a higher power of 2.6 kW. All samples were treated for the same duration of 30 minutes. Table 7.8 shows roughness values for these samples after hydrogen termination using the varied powers.

Sample	H-termination	Ra (nm)	Rq (nm)
A1	Paris (Low)	0.21	0.31
A2	Paris (Med)	1.2	1.6
A3	Paris (High)	1.3	1.6

Table 7.8 – Roughness values for diamond samples A1-3 after etching with Ar + O_2.

Using the lower power, sample A1 showed no difference in Ra with a small increase in Rq. Whereas samples A2 and A3 showed significantly increased values of roughness using the higher power hydrogen treatment. Interestingly, both samples A2 and A3 exhibited very similar values of roughness despite A3 receiving a higher power treatment than A2. Figure 7.15 shows AFM scans for each sample after hydrogen treatment.

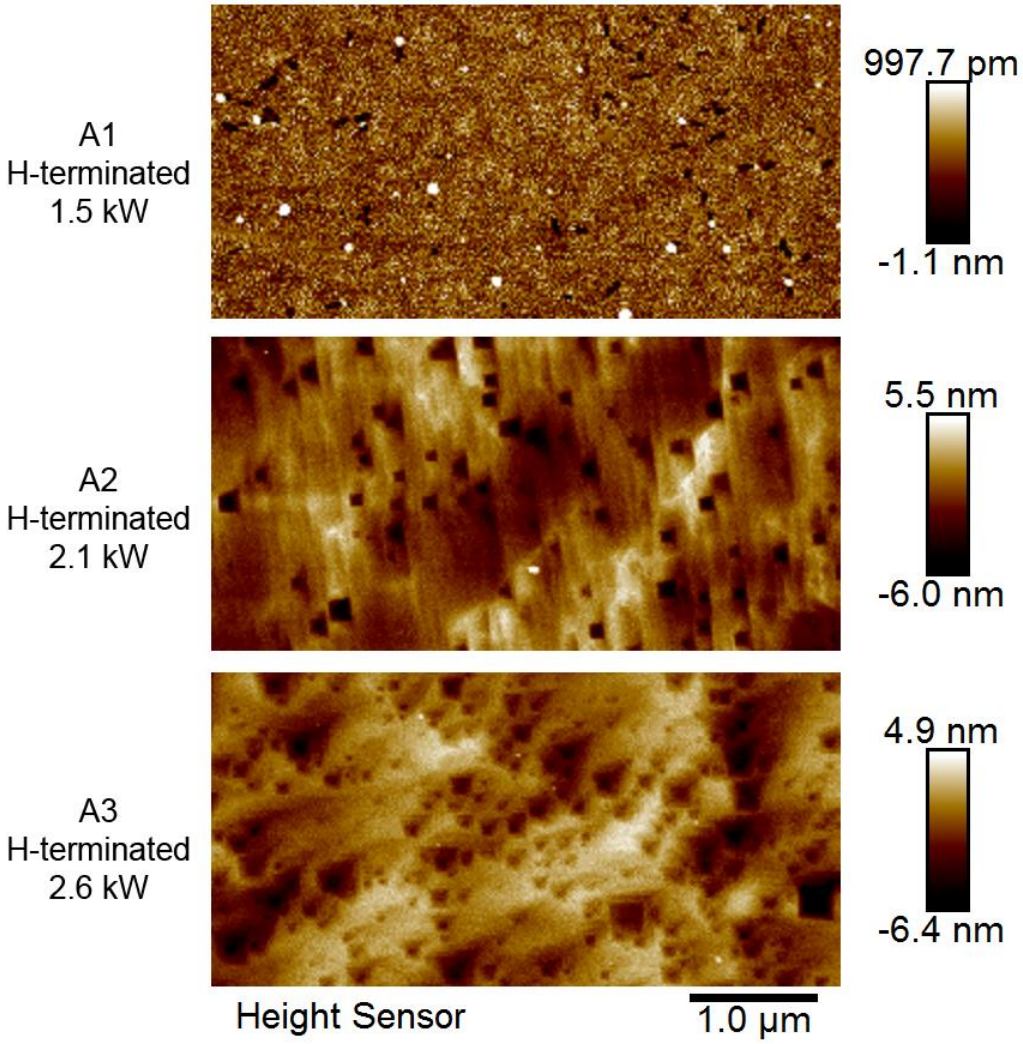

Figure 7.15 - AFM scans of samples A1-3 after hydrogen termination at the University of Paris 13.

After hydrogen treatment using the varied power process, surface topology varied significantly between samples. A1 remained largely unchanged with slight roughening of the surface. In contrast, samples A2 and A3 show significant roughening with the formation of visible pits on the surface. In comparison to the previous hydrogen termination experiment shown in Figure 7.11, the hydrogen termination process for these samples done in Paris used a 30 minute exposure time, significantly longer than the 5 minutes used in Cardiff. Despite the high-power process used in Cardiff, no pits formed on the surface as seen here. As such both exposure time and power density appear to influence pitting of the surface after hydrogen termination. The nature of these pits is discussed in the following section.

Hall measurements were taken for each sample after hydrogen termination, employing silver contacts on the sample corners. Electrical properties in air and after deposition of 100 nm MoO_3 are shown in Table 7.9. Prior to oxide deposition, samples were annealed at 400°C *in-situ* for 1 hour.

Sample (doping)	Termination Power (kW)	Sheet Resistance kΩ/□	Mobility cm^2/Vs	Sheet Carrier Concentration $/cm^2$
A1 (air)	1.5	100	-	-
A2 (air)	2.1	20.8	26.6	1.13×10^{13}
A3 (air)	2.6	10	56.4	1.1×10^{13}
A1 (MoO_3)	1.5	10	15.4	4×10^{13}
A2 (MoO_3)	2.1	6.16	25.7	3.9×10^{13}
A3 (MoO_3)	2.6	4.56	31.1	4.4×10^{13}

Table 7.9 – Hall measurements for samples A1-3 after hydrogen termination using varied power. Measurements while exposed to air and after deposition of 100 nm MoO_3 are shown.

With the diamond surface exposed to air, A3 exhibited the lowest sheet resistance of 10 kΩ/□, half that of A2. Results when doped by air for the high and medium power samples A3 and A2 differ primarily in mobility, as both samples showed near identical carrier concentration. Sample A1 demonstrated an unmeasurable carrier density/mobility and an extremely high sheet resistance of ~100 kΩ/□ in air. The reason for this is unclear and may be due to the lower power treatment being insufficient to terminate the surface with hydrogen. However, results with the diamond surface exposed to air can be highly variable due to the uncontrolled composition of atmospheric adsorbents [7.3]. After deposition of MoO_3, all three samples showed a large reduction in sheet resistance as seen previously [7.8]. A3 maintained the highest surface conductivity of the three samples, with both the highest carrier density and mobility. Sample A2 showed similar numbers with a sheet resistance roughly 26% higher than A3. Sample A1, however, demonstrated a vast reduction in sheet resistance with a final value after MoO_3 encapsulation of 10 kΩ/□. Carrier density for A1 was near identical to A2, but with a lower mobility of ~15 cm^2/Vs. This vast improvement in surface conductivity for A1 while encapsulated with a solid controlled transfer dopant suggests relativity good hydrogen termination of the diamond surface. It is also possible that the anneal of 400°C prior to deposition benefited the conditioning of A1's surface. The anneal may have helped desorb matter from the diamond

surface that disrupted charge transfer between the diamond valence band to an adjacent material. Due to the low power hydrogen termination process and thus minimal etching of the surface, as seen in Figure 7.15, samples A2 and A3 may have avoided this problem. In summary, results after deposition of a controlled surface electron acceptor material suggest increased power density during hydrogen termination can yield large improvements in surface conductivity for etched diamond samples. This may be due to improved hydrogen termination of the surface and or etching of the surface during hydrogen treatment. By comparison, sheet resistances as low as 1 kΩ/□ have been reported for hydrogen terminated diamond in a 20,000-ppm NO_2 environment [7.9] and elsewhere 2.7 kΩ/□ after MoO_3 deposition [7.10].

7.4 Surface Pitting

As can be seen in the previous section, Figure 7.15, diamond when hydrogen terminated by a microwave plasma can often develop pits on the surface. A CVD diamond sample acquired from and polished by Element Six was cleaned in boiling acid, a process described in the previous chapter. Figure 7.16 shows an AFM scan of the sample surface.

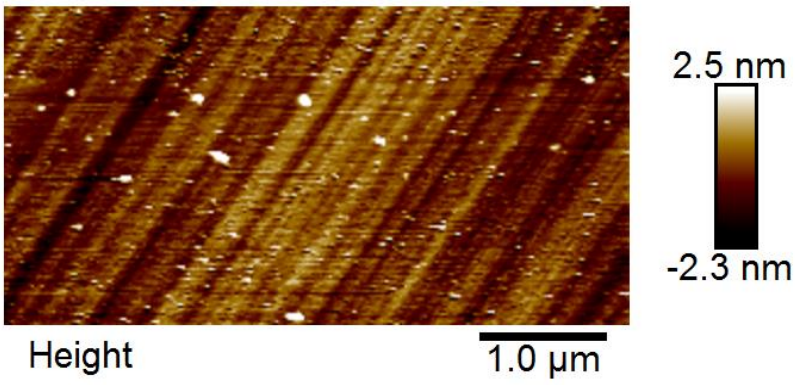

Figure 7.16 - AFM surface scan of a diamond sample after scaife polishing and acid cleaning. Ra 0.51, Rq 0.72.

After cleaning, the surface exhibits a distinct grain indicating the direction of the scaife wheel as is typical of scaife polishing. The Ra value for this 5 µm scan was ~0.5 nm with an Rq value of ~0.7 nm. For a surface topology like this, the Rq value will usually be higher than the Ra value as Rq accounts more for troughs and or peaks. Figure 7.17 shows

the same sample after hydrogen treatment of the surface in Paris, following parameters described in Chapter 6.

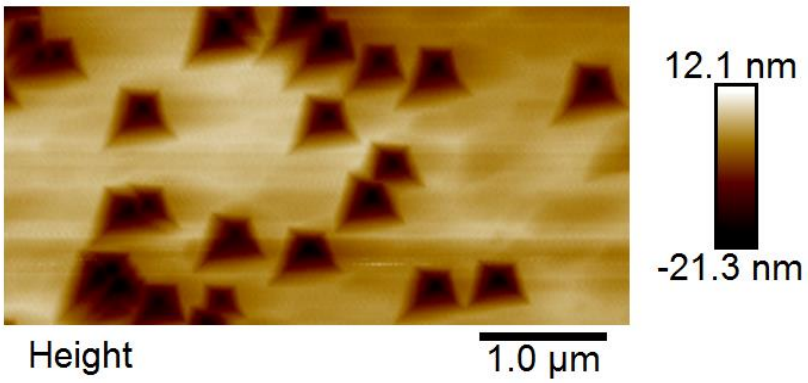

Figure 7.17 - AFM surface scan of a diamond sample after scaife polishing and hydrogen termination. Ra 3.5, Rq 4.7.

Etch pits of slightly varying size and depth can be seen to have formed on the surface, increasing the image Ra to greater than 3 nm. This is a persistent phenomenon seen on hydrogen terminated diamond samples [7.4, 7.11]. After hydrogen termination, the diamond surface often exhibits etch pits. Figure 7.18 shows a cross section of a pit taken from Figure 7.17, which has formed after hydrogen termination.

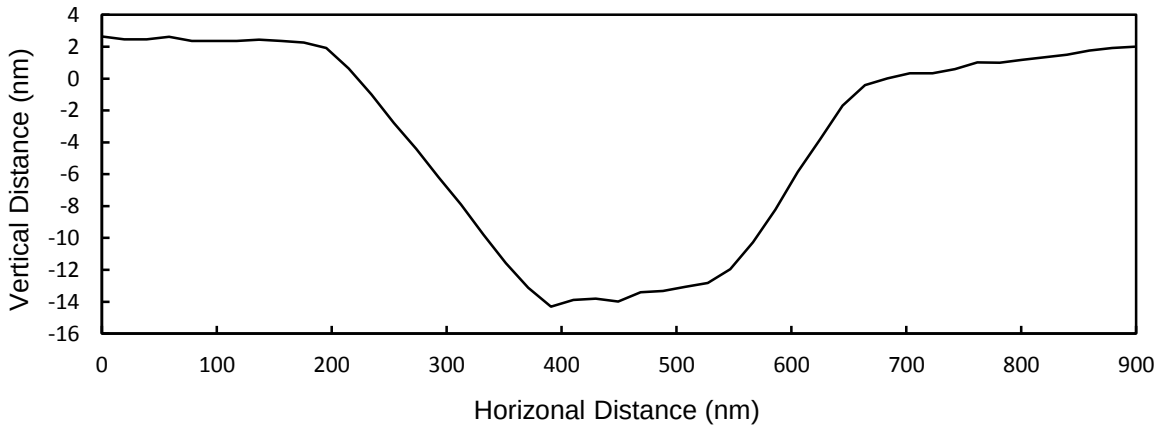

Figure 7.18 – Cross section of a pit on the surface of a hydrogen terminated sample. Approximate depth of 16 nm and width 461 nm.

A cross sectional analysis of five different pits showed an average depth of 18 nm and width of 451 nm. Figure 7.19 shows a 3D render of the same AFM scan shown in Figure 7.17. An inverted 3D render is shown underneath, illustrating the shape of the pits.

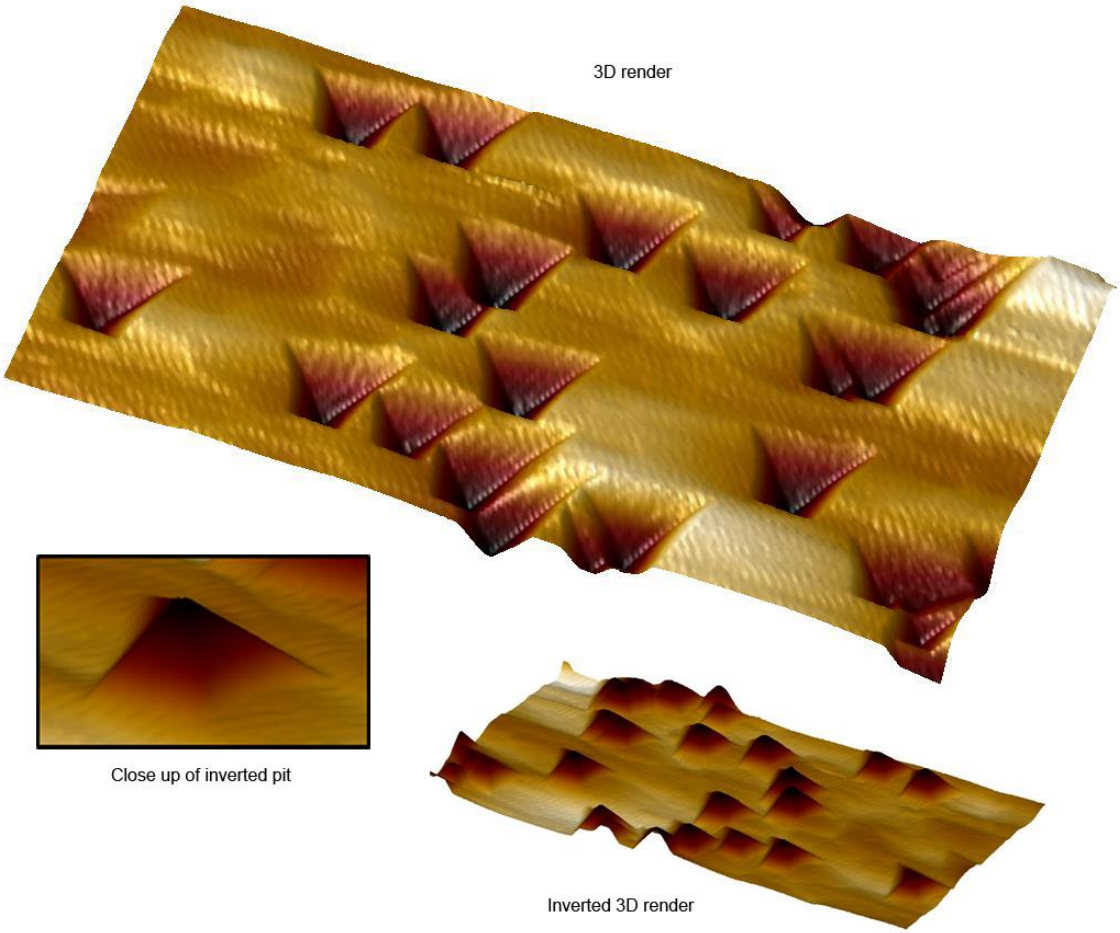

Figure 7.19 – 3D render of the hydrogen terminated diamond surface after pit formation, inverted render shown to illustrate pit shape.

The etching of pits on the surface of diamond after hydrogen treatment is a known phenomenon; work by M. Naamoun *et al* showed defects at the surface can be revealed by H_2/O_2 etching with relatively low amounts of oxygen [7.4]. They also found these defects present as pits in the form of hollow inverted pyramids. Their work concluded two main sources of these pits; firstly, crystal dislocations at the surface introduced by polishing and secondly, dislocations that originate from defects in the bulk of the material. These non-sp^3 bonded defects at the surface are susceptible to etching by hydrogen plasma. Defects such as dislocations and stacking faults are common in both synthetic and natural diamond [7.12]. For CVD diamond films grown on High Pressure High Temperature (HPHT) substrates, defects in the HPHT substrate have been shown to translate into the grown CVD film. Gaukroger *et al* demonstrated HPHT substrates with surface damage would produce dislocations in grown CVD films [7.12] and Martineu *et al* found stacking faults in HPHT diamond substrates would result in a higher density of dislocations [7.13].

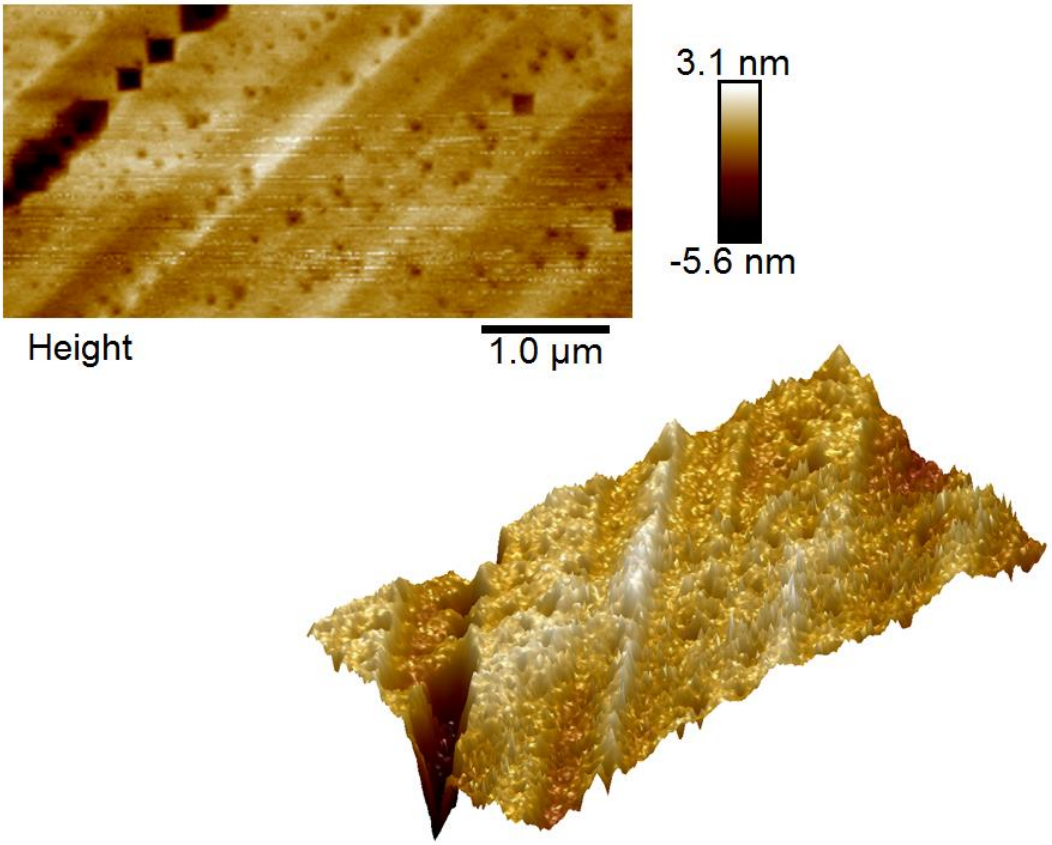

Figure 7.20 – 5 µm surface AFM render after hydrogen termination.

Figure 7.20 shows an AFM scan and 3D render of a polished E6 CVD diamond sample after hydrogen termination in Paris. The polishing grain of the surface can clearly be seen, as well as etched pits following the grain indicating damage caused by polishing. Etch pits caused by bulk dislocations can be reduced by acquiring higher quality diamond substrates with less defects. Whereas polishing induced defects can potentially be reduced by etching the surface after polishing, a process explored previously in this chapter. After initial observations of this pitting effect post hydrogen termination, attempts were made to reduce or remove these etch pits with Ar + Cl_2 etching. This chemistry was selected as it has previously shown to have a smoothing effect on the diamond surface. Figure 7.21 shows another hydrogen terminated diamond sample with surface pits similar to that shown in Figure 7.20. This sample was provided and polished by E6, hydrogen terminated in Paris and acid cleaned prior to AFM inspection.

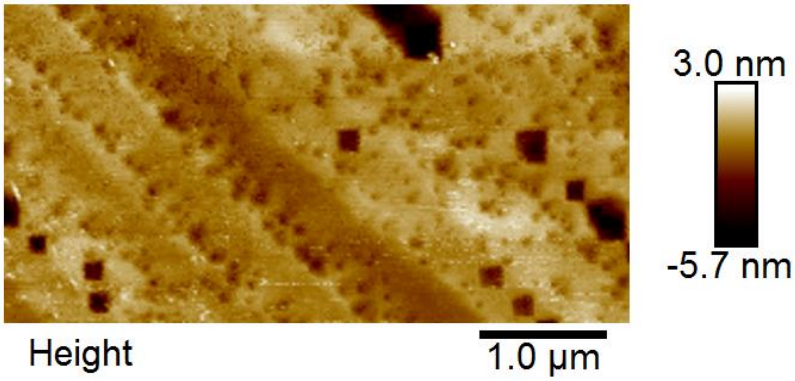

Figure 7.21 – AFM scan of a diamond surface after high temperature acid cleaning. Ra 0.64, Rq 0.96.

Again, the hydrogen plasma treatment revealed surface damage caused by polishing. Figure 7.22 shows the same sample after 30 minutes of Ar + Cl_2 etching following the process recipe detailed earlier in this chapter.

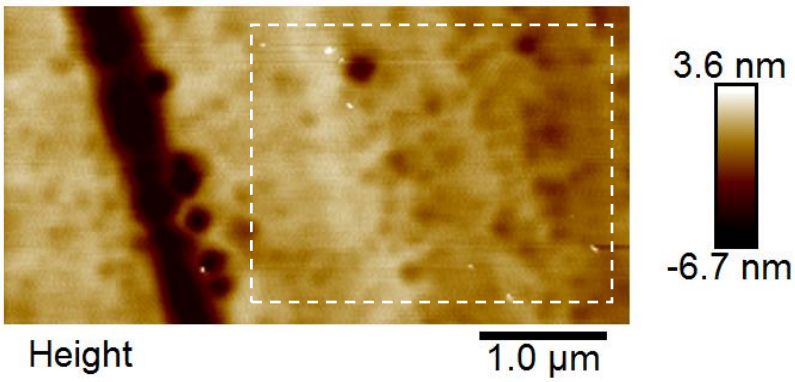

Figure 7.22 – 5 µm surface scan after 30 minutes Cl_2 + Ar etching. Ra 1.2, Rq 1.7. Selected region, Ra 0.46, Rq 0.64.

Presentation of pits remained largely unchanged, however the edges of pits became less defined due to the smoothing effects of Ar + Cl_2 etching. Figure 7.23 shows this sample after a further 240 minutes Ar + Cl_2 etching.

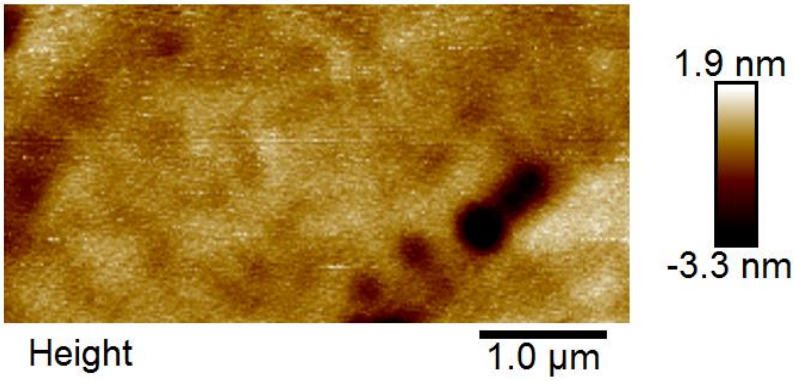

Figure 7.23 – 5 µm surface scan of after 240 minutes Cl_2 + Ar etching. Ra 0.39, Rq 0.59.

Surface Ra is significantly reduced to ~0.4 nm. Additionally, pits are widened and reduced in depth. Figure 7.24 below shows a 1 µm AFM scan of a pit on this sample prior to any etching. A 3D render is shown for illustration.

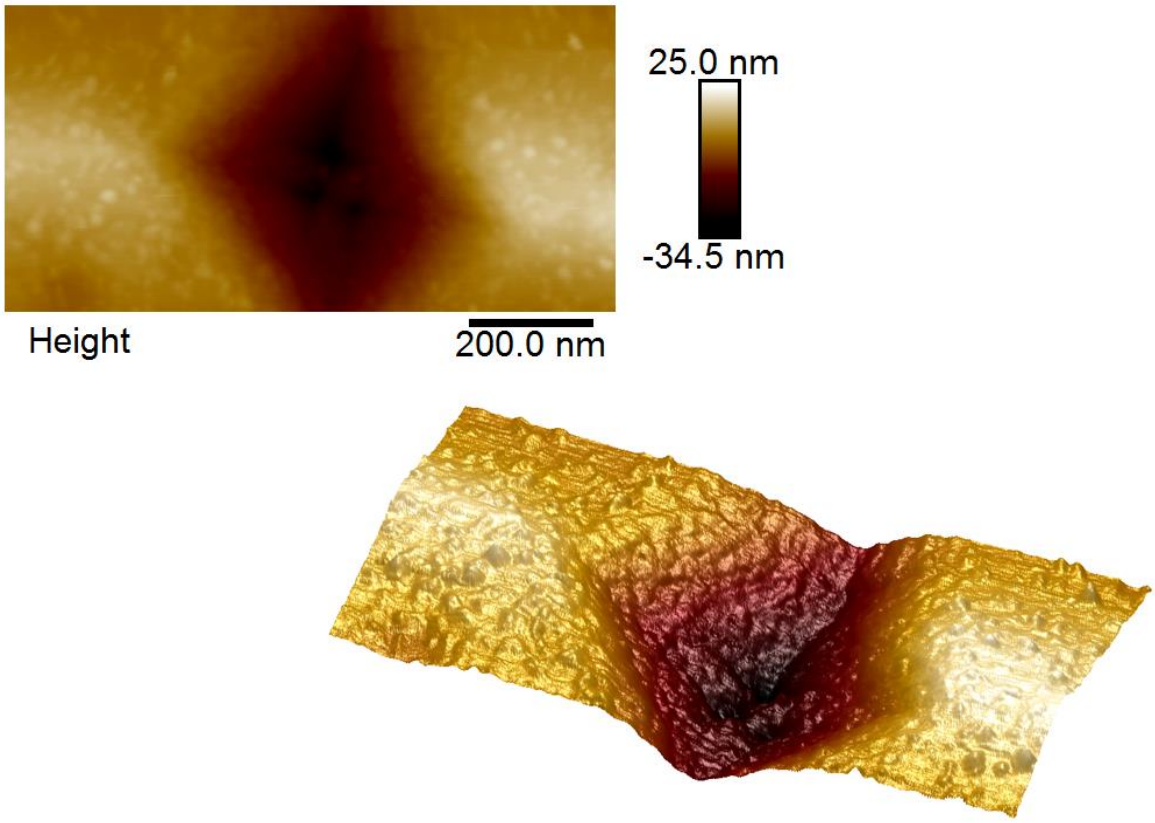

Figure 7.24 – 1 µm surface scan of a surface pit after hydrogen termination.

Shown in Figure 7.25 is a pit on the same sample after a combined 270 minutes of Ar + Cl_2 etching. Scan size was increased from 1 µm to 1.7 µm due to the pit becoming wider, the scale of the Z axis is kept the same for visual comparison with Figure 7.24.

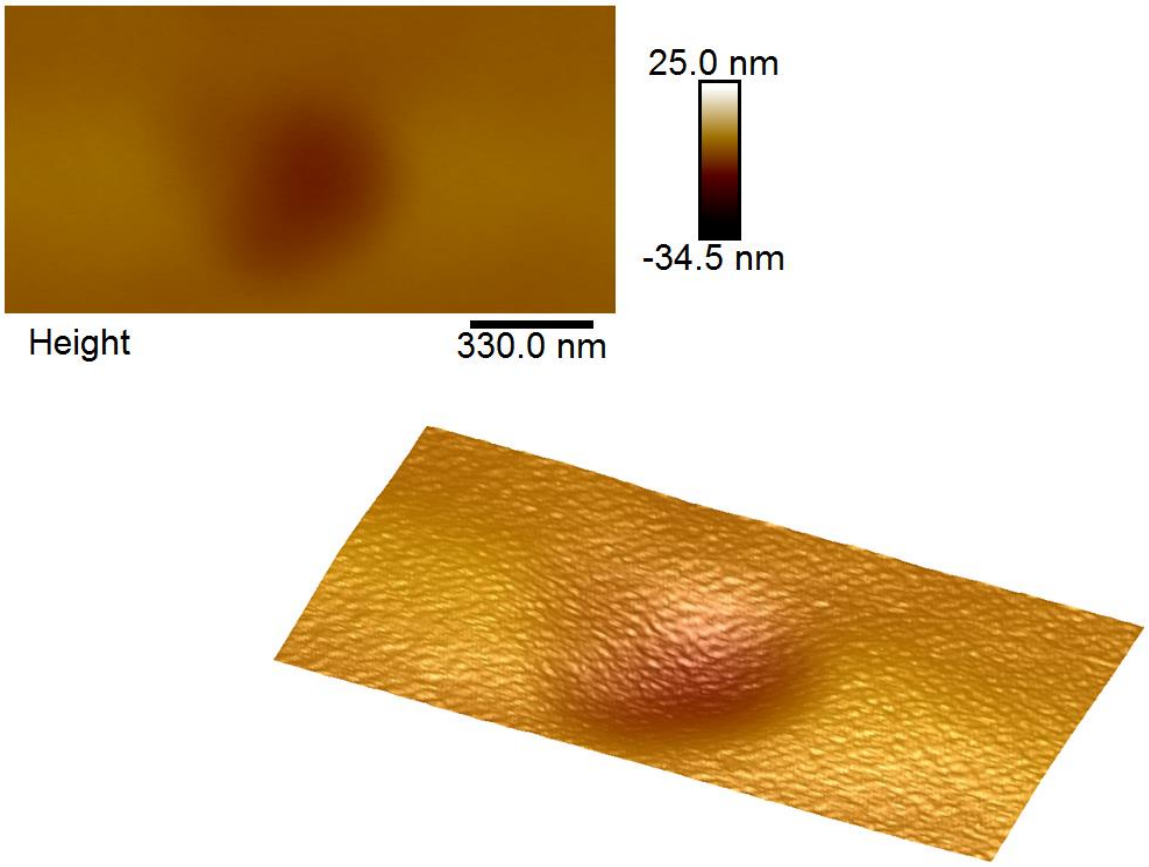

Figure 7.25 - 1.7 µm surface scan of a pit after 270 minutes Ar + Cl_2 etching.

While the pits are not completely removed, further etching with Ar + O_2 would likely result in a relatively flat surface as demonstrated earlier in this chapter. This shows a possible strategy of etching away defects at the surface with hydrogen plasma followed by Ar + Cl_2 etching to flatten the surface after removal of defects.

7.5 Chapter Summary

This chapter has primarily focused on the condition of CVD single crystal diamond surfaces after mechanical polishing. In parallel to work done in Chapter 6, techniques for etching diamond surfaces were developed using both RIE and ICP, removing several microns from the top surface and reducing roughness to values as low as 2 angstroms. The ability to pattern diamond surfaces, using this etching process, was also demonstrated. Polishing defects revealed by exposure to hydrogen plasma were inspected by AFM and removed by etching the diamond surface. Hydrogen termination experiments, varying the hydrogen plasma density, were carried out on pre-etched diamond surfaces and the resulting conductivity of the surface quantified by Hall measurement. The results demonstrated greatly reduced sheet resistance when combined with a surface transfer doping oxide such as MoO_3, compared to that seen previously. The next chapter details preliminary work investigating the incorporation of a surface transfer doping oxide into a hydrogen terminated diamond device.

References

[7.1] A. Gicquel, K. Hassouni, F. Silva, J. Achard, "CVD diamond films: from growth to applications", Current Applied Physics, 1, (2001)

[7.2] J. R. Hird, J. E. Field, "Diamond polishing", Proceedings of the Royal Society A, 460 (2004)

[7.3] C. Nebel, "Surface transfer-doping of H-terminated diamond with adsorbates", New Diamond and Frontier Carbon Technology, 15, (2005)

[7.4] M. Naamoun, A. Tallaire, F. Silva, J. Achard, P. Doppelt, A. Gicquel, "Etch-pit formation mechanism induced on HPHT and CVD diamond single crystals by H_2/O_2 plasma etching treatment" Physica Status Solidi, 209, (2012)

[7.5] C. L. Lee, E. Gu, M. D. Dawson, I. Friel, G. A. Scarsbrook, "Etching and micro-optics fabrication in diamond using chlorine-based inductively-coupled plasma" Diamond and Related Materials, 17, (2008)

[7.6] P. W. Leech, G. K. Reeves & A. Holland, “Reactive ion etching of diamond in CF_4, O_2, O_2 and Ar-based mixtures”, Journal of Materials Science, 36, (2001)

[7.7] H. J. Looi, R. B. Jackman, J. S. Foord, “High carrier mobility in polycrystalline thin film diamond”, Applied Physics Letters, 72, (1998)

[7.8] S. A. O. Russell, L. Cao, D. Qi, A. Tallaire, K. G. Crawford, A. T. S. Wee, D. A. J. Moran, “Surface transfer doping of diamond by MoO_3: A combined spectroscopic and Hall measurement study”, Applied Physics Letters, 113, (2013)

[7.9] T. Yoshiteru, K. Shiraishi, M. Kasu, H. Sato, “Mechanism of hole doping into hydrogen terminated diamond by the adsorption of inorganic molecule”, Surface Science, 609, (2013)

[7.10] C. Verona, W. Ciccognani, S. Colangeli, E. Limiti, Marco Marinelli, and G. Verona-Rinati, “Comparative investigation of surface transfer doping of hydrogen terminated diamond by high electron affinity insulators”, Journal of Applied Physics, 120, (2016)

[7.11] N. Tsubouchi, Y. Mokuno, S. Shikata, “Characterizations of etch pits formed on single crystal diamond surface using oxygen/hydrogen plasma surface treatment”, Diamond and Related Materials, 63, (2016)

[7.12] M. P. Gaukroger, P. M. Martineau, M. J. Crowder, I. Friel, S. D. Williams, and D. J. Twitchen, “X-ray topography studies of dislocations in single crystal CVD diamond”, Diamond and Related Materials, 17, (2008)

[7.13] P. M. Martineau, M. P. Gaukroger, K. B. Guy, S. C. Lawson, D. J. Twitchen, I. Friel, J. O. Hansen, G. C. Summerton, T. P. G. Addison, and R. Burns, “High crystalline quality single crystal CVD diamond”, Journal of Physics: Condensed Matter, 21, (2009)

8 Incorporation into FET Devices

So far, the work outlined in this thesis has centred around the diamond surface transfer doping model. Investigations of hydrogen termination, surface acceptor material and their associated stability have been shown. Topology of the diamond surface has been studied and methods for improving roughness have been developed. The end goal of these individual components is to incorporate the advances they offer into actual electronic devices. In this chapter, fabrication of test structures looking at contact resistance, gate leakage and finally a basic DC FET device is shown. This work was done in parallel to that of Chapter 7, as such the improved hydrogen termination process detailed there was unfortunately not employed for substrates in this chapter. The FET device fabricated here serves only as a preliminary test, attempting to incorporate a surface transfer doping oxide into a gated device.

8.1 TLM & Gate Measurements

Transmission Line Measurement or Transfer Length Measurement (TLM) is a technique used to determine both the contact resistance between a metal and semiconductor and the sheet resistance of the substrate. The method employs a series of ohmic metal contacts fabricated in line with increasing gap distance between each contact, as discussed in Chapter 4. Figure 8.1 shows TLM structures fabricated on a hydrogen terminated diamond substrate, each contact is 100 µm wide gold with a film thickness of 80 nm and was defined by electron beam lithography. Firstly, a sacrificial layer of gold 80 nm thick was deposited onto a hydrogen terminated diamond substrate. After spinning and patterning resist on top of the gold layer, a wet etch is used to selectively etch around the contacts, a process described in Chapter 5.

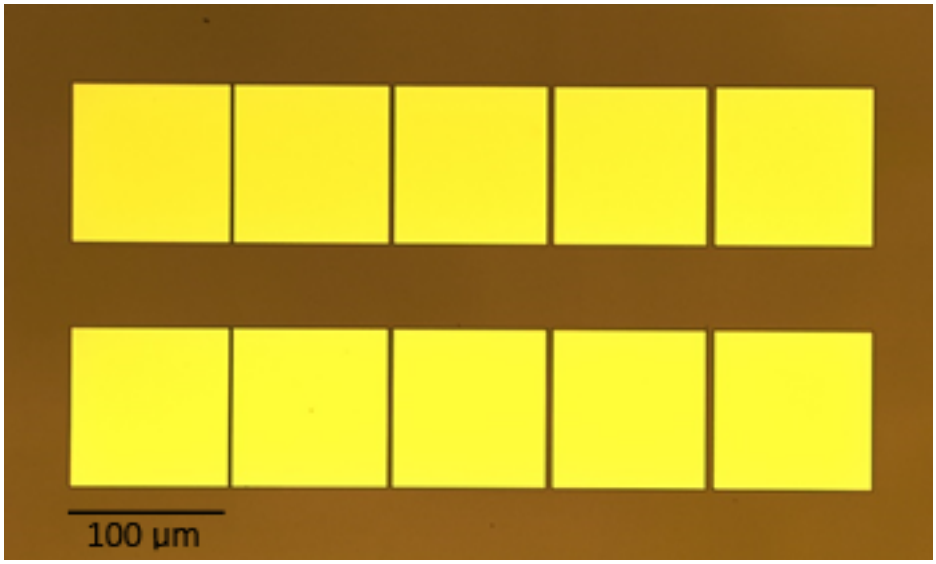

Figure 8.1 - TLM structures on H-diamond. Gap sizes from left to right; 1, 2, 3 and 4 µm.

To investigate the effect of both a 400ºC anneal and deposition of MoO_3 on the ohmic contact resistance, TLM measurements were performed before MoO_3 encapsulation (with the H-diamond surface exposed to air) and after. Details of all samples used in this chapter are shown in Table 8.1 below.

VENDOR	ORENTATION	POLISH SOURCE	TERMINATION SOURCE	SIZE
E6	110	DPS	Cardiff	4.5 mm^2

Table 8.1 – Origin and preparation details of CVD diamond samples used in this chapter.

Measurements from three TLM structures with the sample surface exposed to air and with MoO_3 encapsulation are plotted in Figure 8.2. TLM measurements when doped by air for this sample showed an average contact resistance of 33 Ω.mm and a sheet resistance of 12 kΩ/□. The sample was then annealed at 400ºC for 1 hour *in-situ* and allowed to cool down to roughly room temperature prior to deposition of 100 nm thick MoO_3.

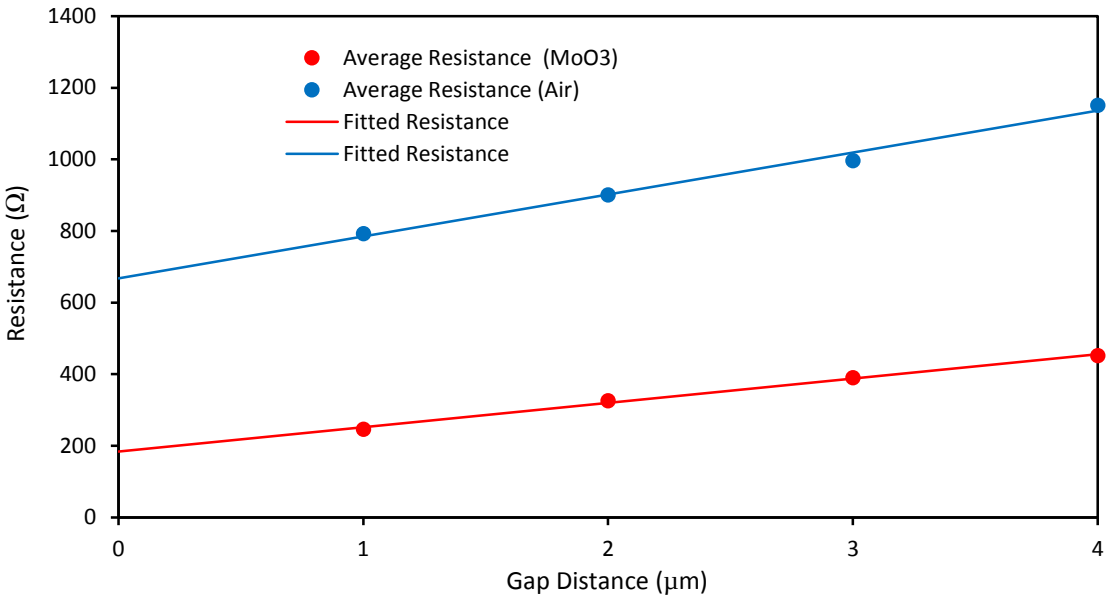

Figure 8.2 – Averaged resistance measurements of three TLM structures before and after a 400°C *in-situ* anneal and encapsulation with 100 nm MoO_3.

As shown previously in Chapter 6, this *in-situ* anneal is required to desorb atmospheric species from the diamond surface. The results after MoO_3 deposition showed a greatly reduced contact resistance down to 9 Ω.mm and reduced sheet resistance of 7 kΩ/□. While the reduction in sheet resistance after MoO_3 deposition was both expected and consistent with results observed from prior Hall measurements, the vast improvement in contact resistance from 33 to 9 Ω.mm was not. The explanation for this reduction in contact resistance by way of a 400°C anneal was unclear, yet may be due to modification of potential atmospheric adsorbates encapsulated under the gold. Investigation of this nature prior to use of MoO_3 has been limited due to disruption of air doping by elevated temperatures. However, both the ohmic contact and sheet resistance were reduced following the MoO_3 encapsulation process using a 400°C *in-situ* anneal stage as is required to remove atmospheric species from the diamond surface and prevent a reduction in the oxide work function at the oxide:diamond interface. Figure 8.3 shows an IV plot for a 1 µm gap before and after MoO_3 encapsulation.

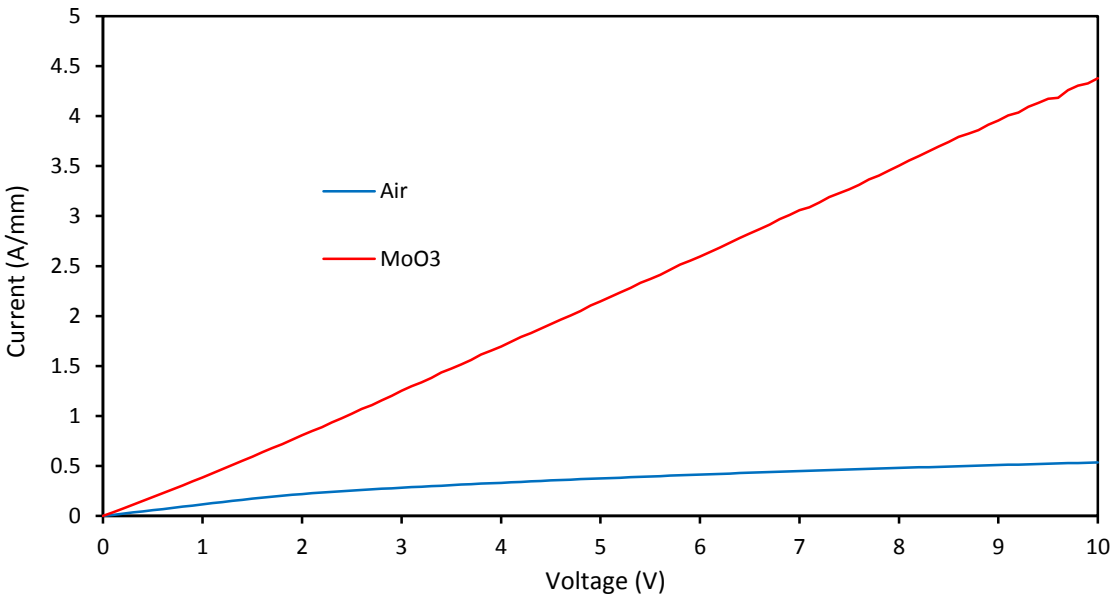

Figure 8.3 – IV measurement for a 1 µm gap before and after encapsulated with 100 nm MoO_3.

Gate test structures were fabricated on hydrogen terminated diamond to investigate the effects of both a 400°C *in-situ* anneal and deposition of 100 nm MoO_3 on a gate contact. The test structures were defined by electron beam lithography, using a sacrificial gold layer 80 nm thick and wet etching to form a circle with 100 µm diameter. Keeping the same resist profile used for wet etching, 20 nm aluminium, 20 nm platinum and 40 nm gold were then deposited and lifted-off, a process described in Chapter 5, to form a circular gate contact surrounded by a ohmic metal contact. As discussed in Chapter 3, aluminium forms a Schottky contact on hydrogen terminated diamond due to its low work function [8.1]. Platinum served as a buffer layer to prevent mixing of the other two metals during the anneal stage. An optical image of the test structure is shown in Figure 8.4 and details of the diamond substrate used are shown in Table 8.2. IV measurements were performed on the gate test structure before and after deposition of 100 nm MoO_3 using a 400°C *in-situ* anneal for 1 hour prior to encapsulation. The results are shown in Figure 8.5.

Prior to the 400°C anneal and MoO_3 deposition process, a typical IV characteristic is achieved for the gate test structure when exposed to air as shown in Figure 8.5. This includes a very pronounced increase in gate leakage current for gate voltage < -1.5 V. Following a 400°C anneal of the test structure and encapsulation with 100 nm MoO_3, the peak gate current is reduced approximately four orders of magnitude compared to its pre-encapsulation value (at V = -2V). While the exact mechanism for reduction in gate leakage

is unclear, it is possibly attributed to the 400°C anneal. Previous work suggests an oxide forms under the Al gate contact, possibly due to the presence of oxygen on the diamond surface prior to deposition [8.2]. It is possible the resistance of this oxide layer is improved post anneal.

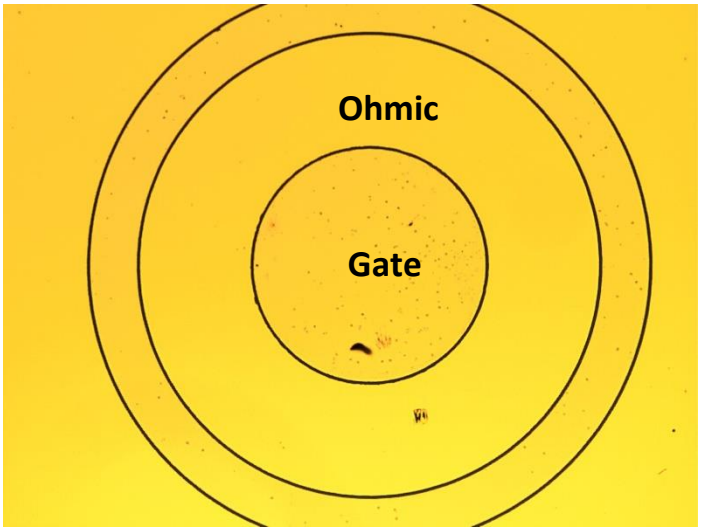

Figure 8.4 - Optical image a gate diode test structure. The central circular gate contact is 100.

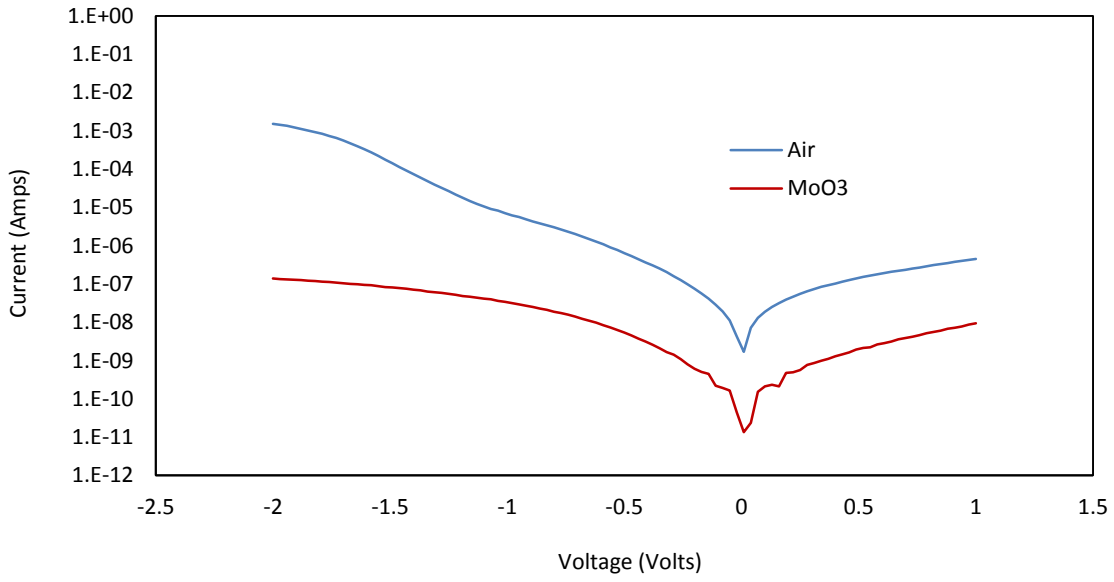

Figure 8.5 - IV measurements showing gate leakage vs applied gate voltage for the gate diode.

8.2 FET Measurements

Basic DC FET devices were fabricated on hydrogen terminated diamond in an attempt to incorporate the enhancements in surface conductivity and stability achieved with MoO_3 encapsulation. VDP and TLM test structures were also included on the same sample to inspect contact resistance and sheet resistance of the substrate. The design was fabricated by electron beam lithography. Ohmic contacts were formed from 80 nm thick gold using a wet etch process outlined in Chapter 5. Isolation of the surface was achieved by exposing the diamond surface to O_2 plasma and verified by probing two predefined ohmic contacts which yielded no measurable current. Bond pads consisting of 20 nm titanium and 100 nm gold were then designed to overlap the ohmic contacts for more robust probing. The source drain gap was defined by a controlled wet etch to be ~2 µm wide, a process also detailed in Chapter 5, and the gate consisted of 20 nm aluminium, 20 nm platinum and 40 nm gold. The sample was then encapsulated with 100 nm MoO_3 after being annealed for 1 hour at 400^{o}C *in-situ*. Figure 8.6 below shows a 3D optical render and optical image of a completed transistor with a 425 nm gate length and a width of 25 µm.

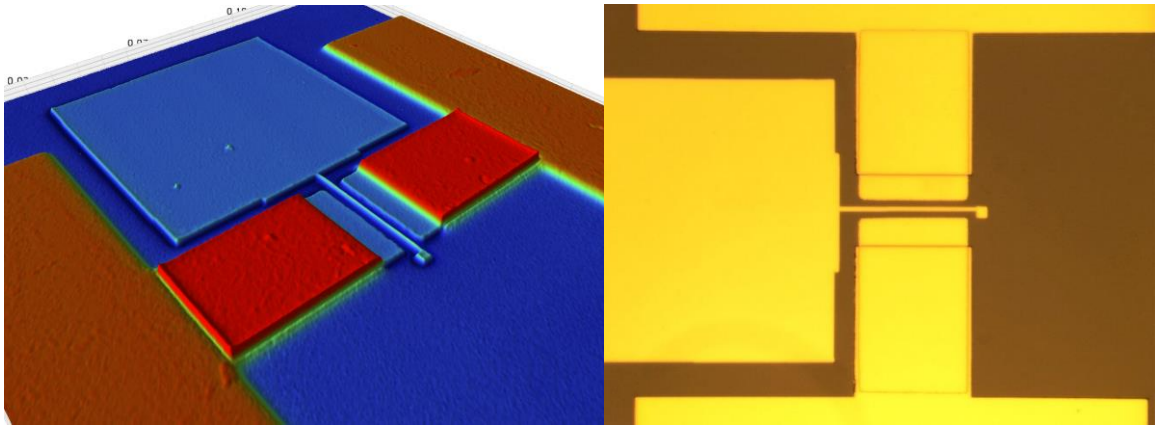

Figure 8.6 - 3D render taken using a Bruker ContourGT Optical Profiler (left) and optical microscope image of a completed FET device on H-diamond (right).

Test structures and devices were measured before and after MoO_3 encapsulation for comparison purposes. Initial I_dV_d measurement of a FET device doped by air exposure is shown in Figure 8.7 and an I_dV_g plot is shown in Figure 8.8.

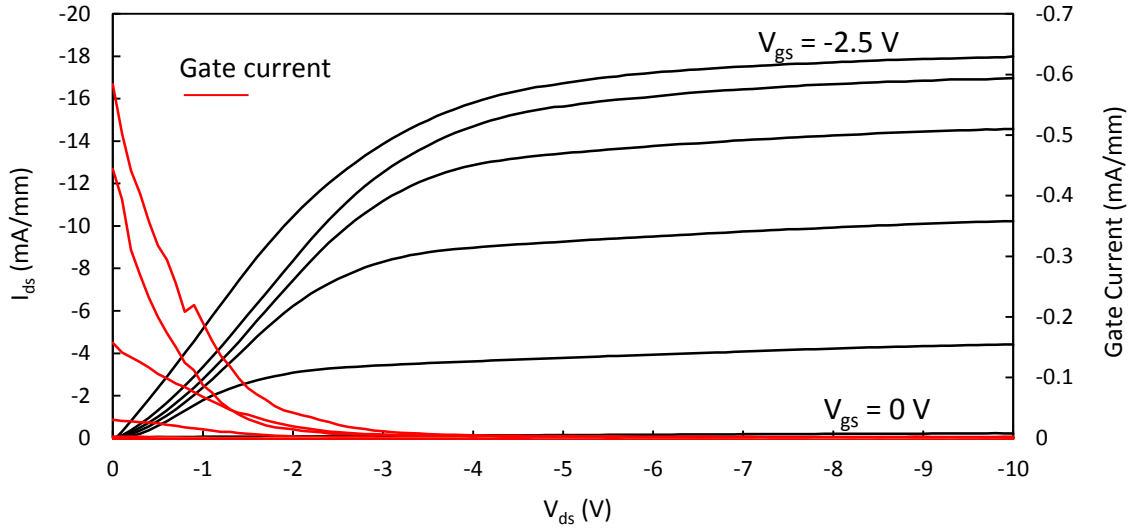

Figure 8.7 - Output characteristics for a 425 nm L_g FET.

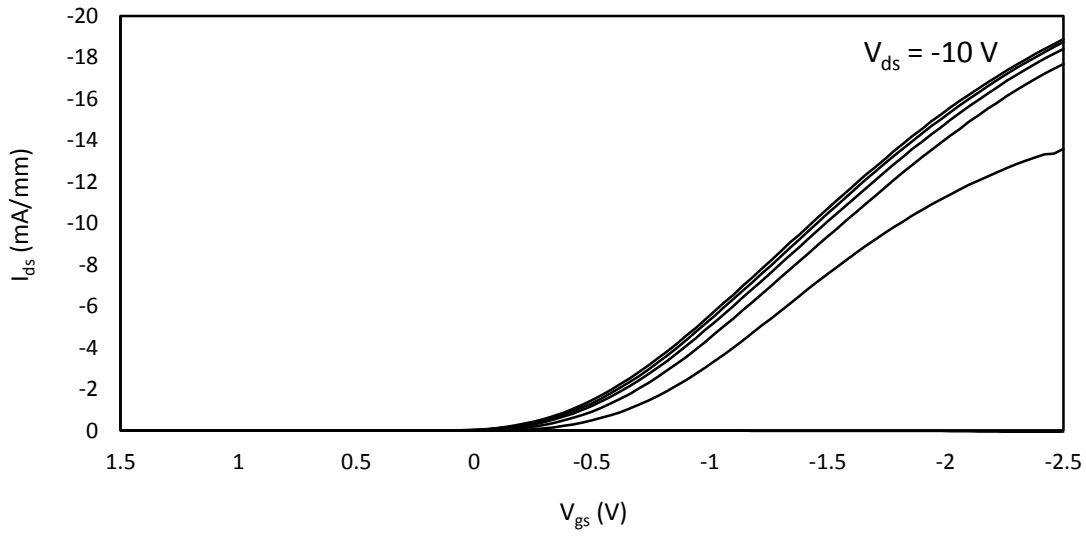

Figure 8.8 - Transfer characteristics for a 425 nm L_g FET.

The device was measured with a drain voltage from 0 to -10 V and a gate voltage from -2.5 to 1.5 volts in steps of 0.5 and exhibited good modulation of the channel with low gate leakage current. However, the maximum I_d for this device was low, ~18 mA/mm compared to typical values of 150 - 300 mA/mm reported elsewhere [8.3]. This low drain current is likely attributed to poor hydrogen-termination which would result in reduced carrier concentration and mobility. Unfortunately, as discussed in Chapter 6, the dependency on external collaboration for this fundamental processing stage limited control and understanding of the hydrogen termination. The slope of the linear region and not quite saturation of drain current indicates a large value of R_{on}, suggesting high sheet and contact resistance. The threshold voltage appears to be roughly between 0 and -0.5 V, however the

range of gate voltage applied was not extended beyond this to avoid damaging the device prior to MoO_3 deposition. Similarly, the drain voltage was not extended beyond -10 V to avoid irreversible damage attributed to breakdown. Due to the relatively large gate length of 425 nm, the device is off at 0 V gate voltage and hence shows enhancement mode operation. This is caused by the formation of a depletion region large enough to fully deplete the channel at zero gate bias. Measurable gate current was seen at V_{ds} = 0 V, however beyond 4 V drain bias there was no notable gate leakage. Figure 8.9 shows I_dV_d measurement of the same FET after encapsulation with 100 nm MoO_3 and Figure 8.10 shows an adjacent FET on the same substrate.

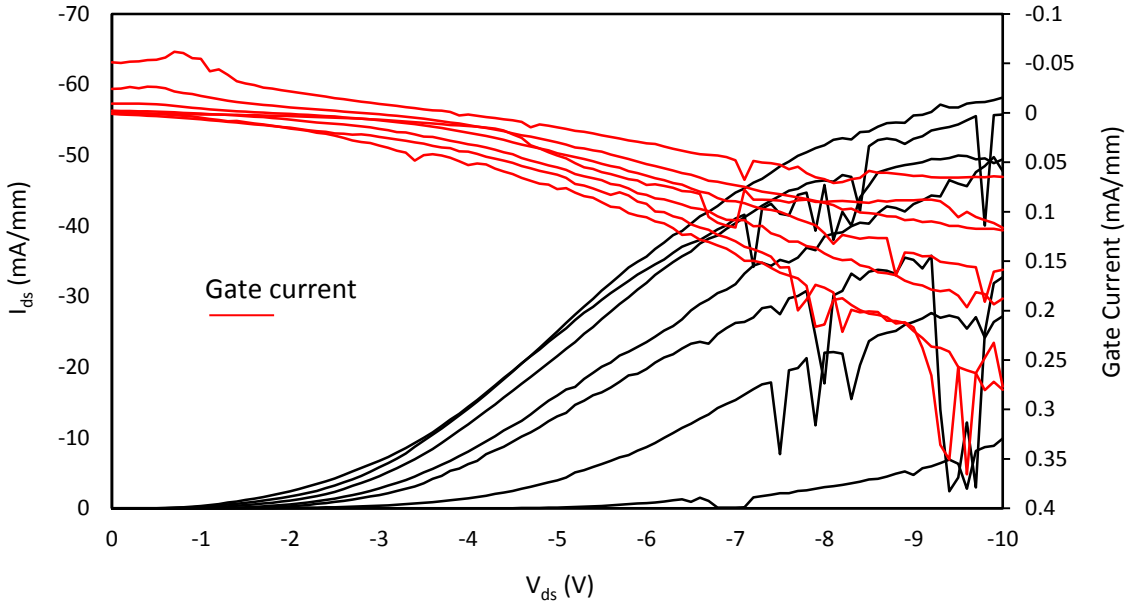

Figure 8.9 - Output characteristics of the FET shown in Figure 8.7 after an *in-situ* anneal of 400°C and encapsulation with 100 nm MoO_3.

The I_dV_d response of devices following MoO_3 deposition varied substantially, but it appeared the gate contact had been damaged in some way in each case. Figure 8.9 shows a small amount of gate modulation with a significantly increased maximum I_d current of ~60 mA/mm. Figure 8.10 shows an adjacent device that demonstrated little to no gate control with an even higher maximum I_d current of ~120 mA/mm. This observed difference in drain current between Figure 8.9 and 8.10 suggests modification of the H-diamond:gate interface perhaps caused by the 400°C anneal. Direction of the gate current has also reversed, peaking at a drain bias of -10 V. Optical inspection of the sample at this stage showed no visible damage or otherwise visible abnormality of the devices.

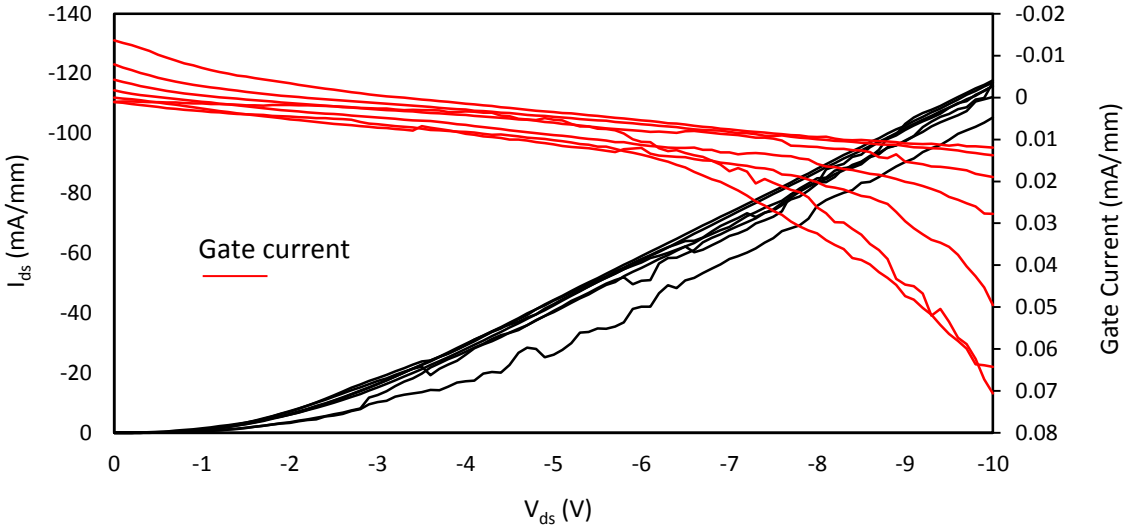

Figure 8.10 - Output characteristics of an adjacent FET after an *in-situ* anneal of 400°C and encapsulation with 100 nm MoO_3.

Hall measurements were taken both before and after MoO_3 encapsulation, shown in Table 8.2.

400°C	Sheet Resistance kΩ/□	Mobility cm^2/Vs	Sheet Carrier Concentration $/cm^2$
Before MoO_3 Deposition	47.8	106	1.2×10^{12}
After MoO_3 Deposition (resist history)	11.6	39.4	1.4×10^{13}

Table 8.2 - Hall measurements taken before and after MoO_3 encapsulation.

With the sample doped by air exposure, a sheet resistance of 48 kΩ/□ was measured with a mobility of 106 cm^2/Vs and a carrier concentration of 1.2×10^{12} cm^{-2}. After annealing *in-situ* for 1 hour at 400°C and deposition of 100 nm MoO_3 the same VDP showed a sheet resistance of 12 kΩ/□ with a reduced mobility of 40 cm^2/Vs and an increased carrier concentration of 1.4×10^{13} cm^{-2}. It should be noted however, the VDP active region prior to oxide encapsulation was exposed to PMMA resist. This was unavoidable due to the sequence of fabrication steps required when both etching the gold and depositing a gate metal. The resist residue left could not be removed without disrupting the surface hydrogen termination.

TLM measurements were performed before and after MoO_3 encapsulation, as shown in Figure 8.11. Measurements with the diamond surface doped by air exposure exhibited an average contact resistance of 90 Ω.mm and a high sheet resistance of 48 kΩ/□, in close agreement with Hall measurements taken prior to MoO_3 encapsulation. After an *in-situ* anneal and MoO_3 deposition, TLM measurements showed an average contact resistance of 28 Ω.mm and a high sheet resistance of 27 kΩ/□. This sheet resistance was more than double that shown by Hall measurement. However, as with the VDP active region, the TLM gaps were exposed to resist history which will likely hamper proper contact between the oxide and H-diamond surface.

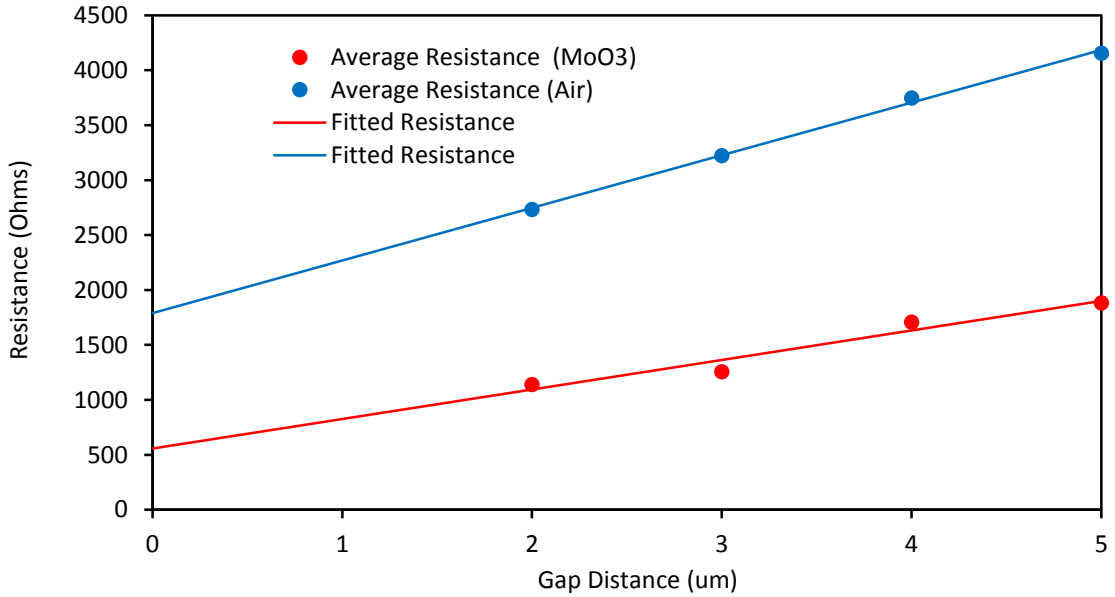

Figure 8.11 - Resistance measurements of TLM structures on an air exposed sample, showing each gap size.

The integration of MoO_3 into FETs has been demonstrated to be beneficial to the ohmic contact and diamond encapsulated regions of devices as expected from the results shown in this chapter and Chapter 6. Although previous results suggest that the gate contact is not degraded by deposition of MoO_3 utilising a 400°C *in-situ* anneal, operation in the gate region of the device is found to change dramatically after MoO_3 deposition. The encapsulation of a metal/semiconductor interface with a dielectric material should in principle not alter the intrinsic operation of the gate interface. However, detailed capacitance-voltage characterisation is likely required to explore the full impact of both oxide encapsulation and the 400°C anneal on the gate contact. After electrical characterisation, the sample with FET devices was recycled using the high temperature

acid cleaning process described in Chapter 6 to remove metal and oxide from the diamond surface. Figure 8.12 shows surface fluorescence of this sample taken using a DiamondView imaging tool after cleaning.

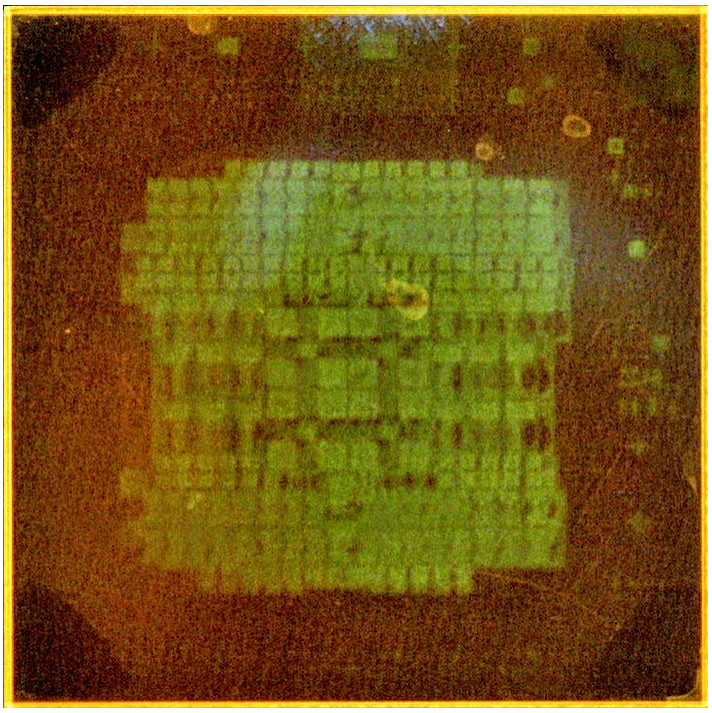

Figure 8.12 - DiamondView imaging after recycling. Fabricated pattern is visible, despite optical microscope inspection showing a clean surface.

The orange fluorescence is typical of CVD grown diamond. Strong phosphorescence in the form of the fabricated pattern can be seen. This phenomenon has never previously been observed for diamond samples recycled by acid cleaning after fabrication, however previous samples fabricated with gold, titanium and aluminium were also not annealed at 400^{o}C for 1 hour. This suggests the metal contacts may have diffused into the diamond during the 400^{o}C annealing stage. Titanium carbide (TiC) contacts have been reported to form at temperatures as low of 400^{o}C given a long enough anneal [8.4]. This is consistent with improvements seen previously in contact resistance after annealing and may explain the gate behaviour seen in devices after MoO_3 deposition.

8.3 Chapter Summary

Preliminary results incorporating the transition metal oxide MoO_3 into a FET device has been presented. From lessons learned previously in Chapter 5 & 6, this entailed the use of a high temperature anneal to maximise performance potential. A systematic approach, investigating the addition of MoO_3 and its effects on individual components of a FET was taken. Deposition of MoO_3 with an *in-situ* anneal was found to not only improve conductivity of the surface, but also reduce contact resistance of gold on hydrogen terminated diamond. A basic DC FET was fabricated and exhibited typical transistor like behaviour despite low conductivity of the substrate due to poor hydrogen termination. After deposition of MoO_3 with an *in-situ* anneal, the drain current of devices was significantly increased as is consistent with previous results. However, the gate contact was degraded in some form resulting in little to no modulation of the channel. This appears to be a consequence of the 400^{o}C anneal prior to MoO_3 deposition. As such, it is likely necessary that the maximum acceptable thermal budget of FET devices fabricated on H-diamond is increased before incorporating both MoO_3 and V_2O_5 when using a high temperature anneal. This may be possible through use of a different gate metal or inclusion of a dielectric material under the gate. Alternatively, removal of adsorbents from the diamond surface prior to oxide deposition without the use of a high temperature anneal may be a solution.

References

[8.1] M. Aoki and H. Kawarada, "Electric Properties of Metal/Diamond Interfaces Utilizing Hydrogen-Terminated Surfaces of Homoepitaxial Diamonds", Japanese Journal of Applied Physics, 33, (1994)

[8.2] M. Kasu, K. Ueda, H. Kageshima and Y. Yamauchi, "Gate interfacial layer in hydrogen-terminated diamond field-effect transistors," Diamond and Related Materials, 17, (2008)

[8.3] D. A. J. Moran, O. J. L. Fox, H. McLelland, S. Russell, and P. W. May, "Scaling of Hydrogen-Terminated Diamond FETs to Sub-100-nm Gate Dimensions" IEEE Electron Device Letters, 32, (2011)

[8.4] T. Tachibana, B. E. Williams, and J. T. Glass, “Correlation of the electrical properties of metal contacts on diamond films with the chemical nature of the metal-diamond interface. II. Titanium contacts: A carbide-forming metal”, Physical Review B, 45, (1992)

9 Conclusions and Future Work

The success of surface transfer doped hydrogen terminated diamond for use in electronics has primarily been hindered by issues of stability. The biggest achievement of work presented in this thesis has been to significantly advance the efficiency and stability of transfer doped diamond through the use of alternative surface passivation techniques. A systematic study of three high electron affinity transition metal oxides, MoO_3, V_2O_5 and WO_3 deposited on hydrogen terminated diamond revealed vastly superior thermal and atmospheric stability over previous methods involving diamond surfaces doped by air exposure. Verified by Hall measurement, these oxides significantly reduce sheet resistance to values as low as ~ 3 kΩ/□ by boosting carrier densities up to ~7.5 $\times 10^{13}$ cm^{-2}. Hall measurement of thicknesses down to 10 nm showed initially stable transfer doping for all three surface acceptor materials tested. Longer term stability of carrier density was shown to necessitate annealing of the diamond surface *in-situ* prior to oxide deposition for MoO_3 and V_2O_5, due to sensitivity of the material to atmosphere. Similarly, encapsulation of these oxides is recommended, especially for thinner layers to prevent degradation. High temperature operation was demonstrated up to at least 300°C with MoO_3 and V_2O_5 when suitably isolated from air, a significant improvement over air exposed diamond surfaces which begin to lose carriers at temperatures as low as 50°C.

This process of transfer doping couples itself intimately with the surface of diamond. As such, parallel investigation into the conditioning of diamond surfaces produced techniques for removing surface defects produced by polishing damage and improving material roughness. This was achieved by both RIE and ICP etching, using tailored gas mixtures based on oxygen and chlorine. The quality of hydrogen termination for diamond surfaces etched in this way was also explored, showing increased plasma density during the termination process produced superior surface conductivity when coupled with a transition metal oxide such as MoO_3.

Preliminary work incorporating the improvements offered by MoO_3 into a hydrogen terminated diamond FET was shown. The deposition process developed for MoO_3 involves the use of a 400°C anneal to maximise stability, as such the effects of this anneal were initially investigated for both ohmic and gate contacts. Initial IV measurements indicated no negative consequence and for ohmic contacts showed improved contact resistance. The FET device produced displayed typical transistor like behaviour including modulation of the channel with the diamond surface doped by air exposure. Drain current was relatively low due to high sheet resistance likely caused by poor hydrogen termination. Results after deposition of MoO_3 with prior annealing of the substrate demonstrated significantly increased drain current as expected. However, modulation of the channel was almost completely lost, possibly due to effects of the anneal on the gate:diamond interface.

Surface transfer doped diamond for electronics is an emerging technology, with much work still to be done. Continued study and development of optimal hydrogen termination on single crystal diamond is fundamental. Ideally, this would include measurement capabilities to detect and quantify the quality of surface termination. Study of surface reconstruction can indicate termination species, while XPS measurement of negative electron affinity will confirm the presence of a hydrogen terminated surface. While hydrogen is difficult to detect, analysis of an oxygen terminated surface or lack thereof may also indicate successful hydrogen termination. Hall measurements of carrier density and mobility measurements could also be coupled with measurements of surface roughness and defect profiles to explore the effect of surface conditions on carrier transport within the diamond. This will produce new insights into the optimisation of surface transfer doped diamond, specifically preparation and hydrogen termination of the diamond surface for optimal performance. Contact resistance may be reduced by improving the hydrogen termination process, reducing density of states at the surface. Greater insights into the formation of a 2DHG in diamond will be gained through investigation of the diamond surface and the impact of roughness and crystal orientation.

Future endeavours to produce a FET device which incorporates transition metal oxides such as MoO_3 must first deal with the issue of adsorbents on the diamond surface. If removed by high temperature annealing, as shown here, the device design must allow for an appropriate thermal budget. This is further complicated by choices of MESFET (Metal on Semiconductor) or MISFET (Metal Insulator Semiconductor) design, placing the surface acceptor material under the gate or not. Coupled with a greater understanding of the hydrogen terminated diamond surface, fabrication techniques can be further developed

to maintain optimal surface conditions, such as intact hydrogen termination and minimal surface contamination. As part of this process, both ohmic and gate contacts can be examined and improved upon. Effects of annealing contacts would be characterised and incorporation of transition metal oxides used to boost performance and stability over previously reported devices. Successful devices can also be tested for use in harsh environments, such as varied temperatures and exposure to radiation. Previous results have shown encapsulation of MoO_3 and V_2O_5 to be necessary for optimal stability. As such, robust encapsulation materials such as SiN and Al_2O_3 should also be examined.

Despite the challenges presented by working with the hydrogen terminated diamond surface, significant advances are being made. Improvements to surface preparation and specifically tailored device designs will inevitably unlock diamonds potential.